

**DEVELOPMENT OF THREE DIMENSIONAL
SILICON MICRO- AND NANO-MACHINING**

SARA AZIMI

(B. Sc. University of Tehran)

A THESIS SUBMITTED

FOR THE DEGREE OF DOCTOR OF PHILOSOPHY

DEPARTMENT OF PHYSICS

NATIONAL UNIVERSITY OF SINGAPORE

2013

Abstract

A novel process for fabricating true, three-dimensional (3D) silicon and porous silicon components at micro- and nano-scale dimensions has been developed and presented in this thesis. Using this process, structures which can be two- and three-dimensional, free-standing, arbitrary-shaped, or curved, and with features at multiple heights, and combined at micro- and nano-scale dimensions are fabricated in a single etch step. This process is based on high-energy ion irradiation, such as 100 keV to 2 MeV protons and helium ions, of p-type silicon wafers. Ion irradiation alters the hole current flow during subsequent electrochemical anodization, allowing the anodization rate to be slowed/stopped for low/high fluences. For moderate fluences the anodization rate is selectively stopped only at depths corresponding to the high defect density at the end of ion range, giving a promising machining technique for true 3D silicon micro/nano-fabrication.

Two different modes of irradiation were used in this thesis. The first mode is the well-established proton beam writing (PBW), in which a small, focused ion beam spot is scanned over a sample area. This mode was used as a flexible approach for making prototypes for 3D silicon structures. A simple modification to the standard operation of a nuclear microprobe provided a means of solving the common problems of PBW, allowing rapid irradiation of large wafer areas, which may lead to mass production of multilevel true three-dimensional silicon and porous silicon components. In this large area mode, a uniform, defocused beam current of several hundred nanoamps was used in conjunction with a photoresist mask, patterned through ultraviolet, electron-beam, proton-beam, X-ray or two-

photon lithography depending on the pattern, resolution and the thickness of the required mask.

Fundamental aspects of this silicon machining work are also studied in this thesis, particularly the effects of patterned ion irradiation on the motion of current flowing through irradiated regions and porous silicon and surface roughness characterization. A new phenomena for current transport mechanism was observed during electrochemical anodization of low-fluence ion irradiated p-type silicon in which a hole diffusion current is highly funneled along the gradient of the modified doping profile towards the maximum ion induced defect density, so dominating the etching behaviour. At higher fluences a solid 3D silicon core can form. The effect of this phenomena and other parameters influencing the core shape and size are studied, and the most important factors identified, namely the ion energy, fluence, irradiation width, wafer resistivity and anodization current density. These fundamental studies was used to explain the anomalous behavior of surface roughness, photoluminescence and formation of different types of micro-, meso- and macro-porous silicon observed for different resistivities of irradiated wafers at different fluences.

Applications of this two- and three-dimensional machining process in different fields such as photonics, micro/nano fluidics, X-ray optics, micro/nano-electromechanical systems (M/NEMS), nano-scale depth machining, nanostencil masks fabrication and patterned silicon-on-insulator (SOI) fabrication are explored in this thesis. Further developing this innovative state-of-the-art silicon and porous silicon machining technique may lead to fabrication of highly compact custom-shaped 3D systems-on-a-chip to develop future micro- and nano-technologies.

Acknowledgements

One of the joys of completion is to look over the time past and remember all the memories, friends and family who have helped and supported me during the past four years of my life.

First and foremost, I would like to express my heartfelt gratitude to Professor Mark Breese, who is not only a tremendous supervisor but a dear friend who is inspirational, supportive, and patient. His attitude towards life and passion for research and science make him amazingly unique and a life time friend and advisor.

Warm thanks to all the CIBA members for all the great moments we shared during the past few years. In particular, I would like to thank past members of CIBA Isaac, Susan and Anna, and present members Kyle, Zhiya, Haidong, Jiao and Malli. Thanks for all the great times, nice discussions, all night long beam runnings (together with chitchats, having midnight dinners and watching movies) and the cheerful (and needful) coffee breaks, which are all unforgettable. I would also like to thank Mr Choo, Armin and Chammika for patiently teaching me the first and main task that should be accomplished at CIBA as soon as one joins, which is learning how to use the accelerator!

I am also grateful to Kambiz (from IMRE) for teaching me nano-imprinting and Sascha and Selvi (from SSLs) for teaching me X-ray lithography. Thank you for your great ideas and valuable discussions.

This thesis would never had been possible without the love and support of my family. I would like to deeply thank my parents, who raised me with a love of

science and craving for learning and exploring new things, for inspiring me and for their endless support through all the stages of my life. I would also like to thank my brother for always believing in me, and always being there for me, encouraging and supporting me in both my personal and academic life. Soheil, you are the best brother ever!

Lastly, I offer my regards to all of those, not mentioned by name, who helped and supported me in any respect during the completion of this thesis. Thank you all very much.

List of Publications

1. **S. Azimi**, Z. Y. Dang, J. Song, M. B. H Breese, E. Vittone, and J Forneris, Defect enhanced funneling of diffusion current in silicon, *Appl. Phys. Lett.* **102** 042102 (2013)
2. Z. Y. Dang, J. Song, **S. Azimi**, M. B. H Breese, J. Forneris, and E. Vittone On the formation of silicon wires produced by high-energy ion irradiation, *Nucl. Instrum. Methods in Phys. Res. B* **269** 32-40 (2013)
3. **S. Azimi**, M. B. H Breese, Z. Y. Dang, Y. Yan, Y. S. Ow, A. A. Bettiol, Fabrication of complex curved three-dimensional silicon microstructures using ion irradiation, *J. Micromech. Microeng.* **22** 015015 (2012)
4. **S. Azimi**, J. Song, Z. Y. Dang, M. B. H. Breese, Three-dimensional silicon micromachining, *J. Micromech. Microeng.* **22** 113001 (2012)
5. J. Song, Z. Y. Dang, **S. Azimi**, M. B. H Breese, J. Forneris, and E. Vittone, On the formation of 50nm diameter free-standing silicon wires produced by ion irradiation, *J. Solid-State Sci. and Technol.* **1** 66-69 (2012)
6. Z. Y. Dang, M. B. H Breese, G. R. Sánchez, **S. Azimi**, J. Song, H. D. Liang, A. Banas, V. T. Costa, R. J. M. Palma, Silicon-based photonic crystals fabricated using proton beam writing combined with electrochemical etching method, *Nanoscale Research Lett.* **7** 416 (2012)
7. Y. S. Ow, H. D. Liang, **S. Azimi**, M. B. H. Breese, Modification of porous silicon formation by varying the end of range of ion irradiation, *Electrochemical and Solid-State Lett.* **14** D45-D47 (2011)
8. **S. Azimi**, Y. S. Ow, M. B. H Breese, On the Dependence of the surface roughness of electrochemically anodized silicon on ion irradiation fluence, *Electrochemical and Solid- State Lett.* **13** H382-H384 (2010)

9. Y. S. Ow, S. Azimi, M. B. H Breese, E. J. Teo, and D. Mangaiyarkarasi, Effects of focused MeV ion beam irradiation on the roughness of electrochemically micromachined silicon surfaces, *J. Vac. Sci. Technol. B* **28** 500 (2010)
10. M. B. H. Breese, S. Azimi, Y. S. Ow, D. Mangaiyarkarasi, T. K. Chan, S. Jiao, Z. Y. Dang, D. J. Blackwood, Electrochemical anodization of silicon-on-insulator wafers using an alternating current, *Electrochemical and Solid-State Lett.* **13** H271-H273 (2010)
11. Y. S. Ow, M. B. H. Breese, S. Azimi, Fabrication of concave silicon micro-mirrors *Optics Express* **18** 14511-14518 (2010)
12. Y.S. Ow, M.B.H. Breese, Y.R. Leng, S. Azimi, E.J. Teo, X.W. Sun, Micromachining of amplitude and phase modulated reflective computer generated hologram patterns in silicon, *Nucl. Instrum. Methods in Phys. Res. B* **268** 1416–1421 (2010)

Contents

Abstract	i
Acknowledgements	iii
List of Publications	v
List of Figures	xiii
Chapter 1 : Introduction	1
1.1 Motivation.....	1
1.2 Silicon machining review.....	2
1.3 Objective	5
1.4 Thesis overview	6
Chapter 2 : Background	7
2.1 Electron beam writing.....	8
2.2 Focused ion beam technology	9
2.3 Proton beam writing (PBW)	10
2.4 Centre for Ion Beam Applications (CIBA)	12
2.4.1 Magnetic focusing.....	14
2.5 Modes of ion irradiation	15
2.5.1 PBW.....	16
2.5.2 Large area irradiation.....	17
2.6 Porous silicon (PSi) formation.....	18

2.6.1 Electrochemical anodization of silicon	19
2.7 Effect of ion beam irradiation on p-type silicon	25
2.7.1 General steps of micromachining silicon and PSi formation	27
2.8 Review of previous silicon/PSi micromachining work at CIBA.....	28
2.8.1 Distributed Bragg reflectors.....	29
2.8.2 Computer generated holography	32
2.8.3 Micromirrors – spherical surface patterning	34
2.8.4 Waveguides for silicon photonics	35
Chapter 3 : Electrochemical Anodization Setup.....	39
3.1 The immersion cell.....	39
3.2 The O-ring cell	43
3.2.1 Modified O-ring cell	44
3.3 Double sided cell.....	47
Chapter 4 : Different Effects of Irradiation Modes on Surface Roughness	51
4.1 Roughness of electrochemically anodized silicon surface	54
4.2 Focused ion beam irradiation roughness studies	56
4.2.1 Factors limiting roughness for focused beam irradiation.....	62
4.2.2 Removal of large-scale variations in anodization rate.....	64
4.3 Large area irradiation roughness studies.....	64
4.4 Summary	70

Chapter 5 : Diffusion Funnelling and Core Formation in Silicon	72
5.1 Defect enhanced funneling of diffusion current in silicon.....	73
5.1.1 Experimental results of current flow around irradiated areas	74
5.1.2 Current flow around irradiated areas	77
5.1.3 Simulation of current flow around silicon irradiated areas	78
5.2 Factors influencing the core shape	84
5.2.1 Effect of ion energy on the core shape	85
5.2.2 Effect of ion fluence on the core shape	86
5.2.3 Effect of wafer resistivity on the core shape	88
5.3 Formation of extended cores.....	90
5.3.1 Evolution of surfaces due to high energy protons.....	91
5.3.2. Evolution of core shape	93
5.4 Photoluminescence and porosity of irradiated areas.....	97
5.5 Summary	104
Chapter 6 : Three-Dimensional (3D) Silicon Machining.....	106
6.1 Principles of 3D silicon machining using ion irradiation	107
6.2 Fabrication process of free standing 3D silicon structures.....	109
6.3 3D silicon machining using PBW	110
6.3.1 Dimensions of the free-standing silicon wires.....	113
6.3.2 Reducing the wire size by thermal annealing	114
6.4 Fabrication of complex 3D silicon structures using PBW.....	116
6.5 3D silicon micromachining using large area irradiation.....	118

6.5.1 UV-lithography	120
6.5.2 E-beam lithography.....	121
6.5.3 X-ray lithography.....	124
6.6 Summary	127
Chapter 7 : Curved and Multilevel 3D Silicon Structures.....	128
7.1 Fabrication of curved 3D silicon structures	128
7.1.2 UV lithography followed by thermal reflow of PMMA.....	130
7.1.3 Two-photon lithography	132
7.2 Multilevel 3D wires	135
7.2.1 Fabrication of two-level silicon structures.....	136
7.2.2 Fabrication of multilevel silicon structures.....	139
7.3 Summary	141
Chapter 8 : Micro- and Nano-Scale Applications of 3D Silicon Machining.....	142
8.1 Fabrication of silicon lines with nano-sized tips	142
8.2 Buried porous silicon channels	146
8.3 Arrays of buried 3D hollow channels	148
8.4 Precisely controlled 3D surface steps at micro and nano scale.....	152
8.4 Free-standing silicon structures	158
8.5 Combined 3D micro- and nano-scale mold for microfluidics	162
8.6 Summary	169

Chapter 9 : Studies of Silicon-on-Insulator Materials	171
9.1 Electrochemical anodization of SOI using an alternating current	172
9.1.1 Mechanism of electrochemical anodization of SOI using a.c.	173
9.1.2 Patterning SOI wafers using a.c. anodization cell	173
9.1.3 A.c and d.c anodization of bulk silicon.....	174
9.1.4 Line pattern fabrication on SOI wafers using large area irradiation...	175
9.1.5 Micromachining line patterns on SOI using a line focus.....	177
9.1.6 Summary	178
9.2 Formation of patterned SOI via ion irradiation on bulk silicon	179
9.2.1 Principle of fabrication of patterned SOI wafer using PBW.....	179
9.2.1.1 Fabrication process using PBW	180
9.2.1.2 Experimental results	182
9.2.2 Fabrication process using large area irradiation.....	185
9.2.3 Fabrication process using boron implantation	188
9.2.4 Summary	193
Chapter 10 : Conclusions	194
Bibliography.....	199

List of Figures

Figure 1-1 : (a),(b) An illustration showing the two primary steps for the fabrication of arbitrary 3D silicon structures using gray-scale lithography to form a nested mask. In (a), an exposed and developed photoresist from gray-scale lithography is used as a masking layer. In (b), the final RIE etched structure in silicon is shown using the masking layer from (a). (c) SEM image of an etched silicon structure resulting from a gray-scale nested mask and RIE etching. From [3].	3
Figure 1-2: (a) Schematic image of a device structure manufactured on CSOI wafer. Support pillars enable better diaphragm uniformity. ICP (Inductively Coupled Plasma) dry etching is used for device manufacturing. (b) Cross-sectional SEM of the delay line structure etched into a CSOI substrate. From [6].	4
Figure 2-1 : Comparison between (a) PBW, (b) FIB, and (c) electron beam writing on PMMA. This figure shows schematically the difference between the three techniques. The PBW and FIB images were simulated using SRIM [23] while the e-beam writing image was simulated using the Casino [24] software package. The advantage of PBW in terms of ability to penetrate deeper with minimal lateral broadening are clearly shown here. For a more realistic comparison, the energies for the simulations here are chosen to reflect the typical energy used for each technique respectively. From [22].	8
Figure 2-2: The Sirion scanning electron microscope (FEI Company) which also serves as platform for e-beam lithography located at Singapore Synchrotron Light Source (SSLS) clean room.	9
Figure 2-3 : (Left) CIBA singletron facilities. (Right) Schematics diagram of CIBA facilities: (a) the accelerator (b) 90° magnet (c) switching magnet (d) endstations.	13
Figure 2-4 : (a) Schematic of Oxford triplet lenses configuration used in the 10° beam line in CIBA. Working distance (WD) is 0.07m. (b) Cross sectional schematic design in a quadrupole lens. Blue arrows show the field lines inside the lens and green lines indicate the force on a positively charged particle travelling into the plane of the paper at different points (A to D) in the quadruple lens. Red arrows show the direction of the current flow in the coils to get desired magnetic polarity.	15
Figure 2-5 : SRIM simulation [30] of (a) trajectories versus depth and (b) defect distribution for 2 MeV protons in silicon by 2000 protons.	16
Figure 2-6 : Schematic of large area irradiation system based on a nuclear microprobe quadrupole multiplet focusing system.	18
Figure 2-7 : Electrochemical anodization setup for p-type silicon.	20
Figure 2-8 : Silicon dissolution in HF electrolyte scheme. From [45-46].	21
Figure 2-9 : Schematic drawing of the principle for the formation of the nano-/macroporous silicon network. Formation process includes the following stages: (A) migration of charge carriers in the bulk silicon to the electrolyte interface, (B) random pore nucleation and (C) pore formation and propagation. From [47].	22
Figure 2-10 : illustration of modification of the silicon bandgap during porous silicon formation as a result of the quantum confinement effect. See [46].	23
Figure 2-11 : Pore diameter and density for different types of porous silicon. From [44].	24
Figure 2-12 : Dopant spacing for different resistivity of p-type silicon wafers. From [48].	25

Figure 2-13 : Schematics of machining multilevel silicon structures. (a) Irradiating with various high energy ion beam fluences (b) Formation of PSi during subsequent electrochemical anodization in HF solution (c) PSi removal to reveal multilevel silicon structures.	26
Figure 2-14 : (a),(b). SRIM [23] plots of 400 and 700 keV H_2^+ ions incident on different thicknesses of photoresist (PR) on top of a 7- μm thick Si layer (shown in gray). (a) From left to right the PR thicknesses are 7 μm , 3 μm and 0 and trajectory plots show how far each ion penetrates through the layer structure. (b) Corresponding defect density. Both beam energies are shown, with the higher energy to the right. From [40].	29
Figure 2-15 : (a) Change in peak reflected wavelength of irradiated DBR versus proton fluence. (b) Patterned DBR formed by irradiating groups of four 10 μm wide pixels with different proton fluences prior to anodization. Other examples of patterned DBR structures such as (c) Dragon and (d) Henri Matisse's painting 'La Musique'. From [60].	30
Figure 2-16 : 3D patterned DBR arrays, (a) SEM, (b) high magnification optical micrograph showing the effect of white light illumination from the top and from the left sides of such pixels. (c),(d) low magnification optical micrograph of large areas arrays of patterned 3D DBR pixels. From [61].	31
Figure 2-17 : (a) SEM image of transferred binary amplitude CGH pattern in silicon irradiated with 600 keV helium ions at 5×10^{14} ions/ cm^2 . (b) to (d) show grey scale reconstructed holograms from binary amplitude CGH on silicon. From [67].	33
Figure 2-18 : (a) Optical, (b) SEM images of concave silicon surfaces. (c) Optical image of an array of concave surfaces with 20 μm diameter. (d) Optical image of a concave DBR mirror illuminated with white light, reflecting and focusing blue wavelengths. From [72].	35
Figure 2-19 : SEM images of SOPS strip waveguides (a) direct-write irradiated with 250 keV protons fluences of 7×10^{13} , 1×10^{14} , $1 \times 10^{15}/\text{cm}^2$, increasing from left to right. (b) plan and cross section views of similar SOPS waveguides fabricated using a large area irradiation fluence of $2 \times 10^{13}/\text{cm}^2$. (c) left: schematic diagram of the fabrication process of Bragg waveguides in silicon and right: cross section SEM image of Bragg cladding waveguide irradiated with a fluence of $2 \times 10^{15}/\text{cm}^2$. From [74-76].	37
Figure 3-1 : Immersion cell anodization setup.	40
Figure 3-2 : The preparation steps prior to electrochemical anodization: (a) Removing the native oxide of the backside of the wafer by immersing in a diluted HF solution. (b) Covering the entire backside of the wafer with Gallium-Indium eutectic paint and stick a copper wire to it. (c) Coating the back surface with epoxy to protect from HF. (d) Covering all the sides of the wafer with epoxy.	41
Figure 3-3 : (a) Schematic of cross sectional view of O-ring cell, the silicon wafer is placed between the cell opening and two platinum meshes are used as electrodes. (b) Designed cell.	44
Figure 3-4 : (a) Schematic of a modified cell where a copper slab is used for giving the back contact to the silicon sample. (b) Designed cell.	45
Figure 3-5: (a) Clearly pronounced edge effect in the form of a groove on the periphery of the porous region. Virtually the whole etch current is displaced to the groove region, with little etching of the central part of the sample (b) Schematic cross-sectional view of the cell designed for anodization of p-type silicon where the front opening is larger than the back side opening (c) Schematic of the cell showing the distribution of the electric field lines in the substrate. A metal ring with a positive bias can be placed on the sample surface for further improving the cell.	46
Figure 3-6 : (a) Moderate resistivity wafers irradiated with 1 MeV helium and a fluence of 5×10^{14} after anodization using conventional setup (left) and modified anodization setup (right), with 1 cm^2 opening. (b) Surface profile of the right-hand sample over its diameter after removing the PSi.	47

Figure 3-7 : (a) Schematic cross-sectional view of the anodization cell designed for making SOI wafers from bulk silicon wafers. Red arrows show the direction of hole current flow during the anodization. (b),(c) Frontside and backside designed slits respectively, which are added to the anodization cell in Figure 3-3 (b) where the wafer is placed.	48
Figure 3-8 : (a) Schematic of cross sectional view of anodization cell with direct contact, specially designed for making SOI. Red arrows show the direction of hole current flow during the anodization. (b) Designed cell.	49
Figure 4-1 : Cross sectional SEM and AFM image of anodized silicon sample (a) before (b) after megasonic cleaning.	52
Figure 4-2 : Schematic of the effect of ion irradiation of a well-defined region. (a) ion irradiation, (b) electrochemical anodization, (c) PSi removal.	53
Figure 4-3 : RMS roughness plotted as a function of PSi layer thickness for three resistivities ρ of silicon substrates. From [85].	55
Figure 4-4 : (a) rms roughness as a function of the current density used in PSi formation for 0.01 Ω .cm wafers (25% HF was used). Comparable decreases for the two layer thicknesses are observed. (b) rms roughness as a function of PSi layer thickness anodized at two different current densities. Although saturation is obtained in both cases the limiting value is reduced by a factor of 3 at a high current density. From [85].	56
Figure 4-5 : (a),(b) AFM images of two different sets of five adjacent 10 μm wide irradiated bars. The vertical direction of the focused beam during irradiation is shown by the white arrows. (c),(d) AFM line profiles across each pattern in (a) and (b) respectively. The vertical scales are 800 nm and 40 nm respectively.	58
Figure 4-6 : (a) Plot of RMS roughness versus fluence for the three samples shown in Figures 4.5 (a), (b) and 4.7, labeled 4.5a, 4.5b and 4.7 respectively. The AFM rms roughness values are extracted from $5 \times 5 \mu\text{m}^2$ areas. (b) Plot of the rms roughness vs fluence for two samples irradiated using uniform broad beam ion irradiation. Zero on horizontal axis means the rms roughness measured from the unirradiated background.	60
Figure 4-7 : (a),(b) SEM images of an irradiated pattern with five vertical bars with fluences of 2, 4, 6, 8, and 10×10^{15} protons/ cm^2 and overlapped with another five similarly irradiated horizontal bars. The horizontal and vertical bars are each 10 $\mu\text{m} \times 100 \mu\text{m}$ in dimensions. Each bar is spaced at 10 μm from each other except for the two bars with the highest fluence which were spaced at 20 μm for identification purpose. The vertical direction of the focused beam during irradiation is shown by the black arrow. (c), (d) AFM image and linescan across this structure.	61
Figure 4-8 : (a) Reduced PSi formation rate versus fluence. (b) Measured RMS roughness of an irradiated area versus number of frames used to achieve the same fluence in each case. Zero on horizontal axis means the RMS roughness was measured from the unirradiated background.	62
Figure 4-9 : RMS surface roughness versus helium ion fluence for three wafer resistivities, anodized using a current density of 50 mA/ cm^2 . (b). Anodized depth versus helium ion fluence for three wafer resistivities.	67
Figure 4-10 : Calculated change in resistivity versus MeV helium ion fluence for wafer resistivities of 0.02 Ω .cm, 0.5 Ω .cm and 5 Ω .cm.	68
Figure 4-11 : Variation of PL intensity versus helium ion fluence for 0.02 Ω .cm wafer resistivity, data reproduced from Ref. [89]. Roughness data for the same material from Figure 4-9 (a) is overlaid for comparison.	69
Figure 4-12 : AFM image and line profile of silicon surface relief pattern (a) from point (1) of roughness plot of Figure 4-11 which is irradiated with relatively low ion fluence and	

tends to form mesoporous silicon and (b) from point (2) of Figure 4-11 which is irradiated with relatively high ion fluence and tend to form microporous silicon. 70

- Figure 5-1 : (a) Cross-section SEM showing lines irradiated with 500 keV protons with different line fluence in 0.4 Ω .cm p-type silicon, which was subsequently anodized to a depth of 10 μ m at 40mA/cm² and then cleaved perpendicular to the lines. A higher magnification of the lowest Ψ is shown at the left. (b),(c) Optical and photoluminescence images of the same array of lines. The insets in (c) show the PL intensity across the lowest and highest Ψ cores. PL collected with a Nikon Eclipse microscope with excitation wavelength of 330-380nm, for an exposure time of 50 ms. 74
- Figure 5-2 : Cross-section SEMs of 0.02 Ω .cm p-type silicon line irradiated with 500 keV protons, with a range of Ψ 76
- Figure 5-3 : Porosity as a function of doping density for p-type (open symbols) and n-type (filled symbols) silicon electrodes anodized in 1:1 ethanoic HF at different current densities (as indicated). From [44]. 76
- Figure 5-4 : Cross-section SEMs of line irradiated in 0.02 Ω .cm p-type silicon irradiated with 1 MeV protons, with (a),(b) $\Psi = 3 \times 10^{10}$ /cm, 1.8×10^{11} /cm and (c)-(f) zoom-in view of $\Psi = 3 \times 10^{10}$ /cm, $\Psi = 6 \times 10^{10}$ /cm, $\Psi = 9 \times 10^{10}$ /cm and $\Psi = 1.8 \times 10^{11}$ /cm respectively. 77
- Figure 5-5: (a) Simulated electric potential using the COMSOL package [96]. Black arrows show the direction of the diffusion component of current. (b) Directions of the applied electric field and built in electric field at three different locations around the irradiated region labelled as (1)-(3) in (a). The magnitude and direction of the resultant electric field experienced by the anodization current is important in understanding the shape of the formed core. 78
- Figure 5-6 : (a) SRIM simulation map of the average vacancy distribution $v_G(x,y)$ per 30 keV He ion in silicon. (b) map of N_A^{eff} for a line irradiation for $\Psi = 4 \times 10^8$ /cm. This, and all following plots in 0.4 Ω .cm p-type silicon. (c) map of electric potential for $\Psi = 1 \times 10^7$ /cm. 79
- Figure 5-7 : Maps of potential (color scale on the right) and current streamlines for the (upper) drift component and (lower) total current flow for increasing values of (a) $\Psi = 10^5$ /cm, (b) 10^8 /cm, (c) 10^{10} /cm. 81
- Figure 5-8 : (a) Hole density and (b) total current density versus depth below the surface, for different Ψ 82
- Figure 5-9 : Simulations for single line irradiation with 250 keV protons in 0.4 Ω .cm silicon for $\Psi = 4 \times 10^{10}$ /cm, showing (a),(b) magnified maps of potential with superposed arrow plots of the drift and diffusion components of the anodization current where the lengths of the arrows are proportional to the modulus of the current components, (c), (d) low magnification maps of the five rightmost cores in an array of eight irradiated lines, with line period of 1.7 μ m, encompassing the outermost core at the right side to the central two at the left side, for $\Psi = 6 \times 10^8$ /cm. 83
- Figure 5-10 : Plot of proton range versus energy in silicon (b) Plot of defect density versus lateral distance across the end-of-range core for different proton energies in silicon... 86
- Figure 5-11 : Cross-section optical micrographs showing core sizes for surface line width and irradiated Ψ of 1 MeV protons of (a) 500 nm, 3×10^{10} /cm, (b) 1000 nm, 1×10^{10} /cm..... 87
- Figure 5-12 : Optical images showing wire cross-sections buried in PSi in 0.4 Ω .cm wafer after irradiation with 1MeV protons with a Ψ of (a) 1.5×10^{10} /cm, 3×10^{10} /cm, (b) 6×10^{10} /cm and 1.2×10^{11} /cm. 88
- Figure 5-13 : (a)-(h) Cross-section SEMs of cores formed in 0.02 Ω .cm p-type wafer by 1 MeV protons with Ψ of 1×10^{11} /cm, 2×10^{11} /cm, 3×10^{11} /cm, 5×10^{11} /cm, 6×10^{11} /cm, 8×10^{11} /cm, 1.5×10^{12} /cm, 2.4×10^{12} /cm respectively. 88

- Figure 5-14 : Cross-section SEM images showing cores formed in 0.4 Ω .cm p-type silicon wafer irradiated with 250 keV protons using (a) $\Psi=1\times 10^{10}/\text{cm}$ and (b) $\Psi=3\times 10^{10}/\text{cm}$ 89
- Figure 5-15 : Cross-section SEM images showing cores irradiated with (a) $\Psi=2\times 10^{10}/\text{cm}$ and (b) $\Psi=5\times 10^{10}/\text{cm}$ 250 keV protons in 0.02 Ω .cm p-type wafer..... 90
- Figure 5-16 : Cross-sectional SEMs of DBRs forms by irradiating 6 μm wide line, 2 mm in length with fluence of [(a)-(c)] $2\times 10^{15}/\text{cm}^2$ and [(d)-(f)] $4\times 10^{15}/\text{cm}^2$. (g) Measured ϕ versus anodization depth of the unirradiated background for fluences of $1\times 10^{15}/\text{cm}^2$, $2\times 10^{15}/\text{cm}^2$ and $4\times 10^{15}/\text{cm}^2$. From [61]..... 92
- Figure 5-17 : (a) Cross-section SEM (b) PL images of the same array of lines showing high porosity observed owing to the current funnelling at the low fluence regime of $4\times 10^{14}/\text{cm}^2$. The dashed box in (a) shows one of the end-of-range regions from which intense PL is observed in (b). PL was collected with a Nikon Eclipse microscope with excitation wavelength of 330-380nm, for an exposure time of 120 ms..... 93
- Figure 5-18 : Simulated drift and total current flow for a wide irradiation region of 12 μm , for 250 keV protons, generated using COMSOL [96]. 94
- Figure 5-19 : Cross-section SEMs showing core formation by irradiating with 1 MeV protons and design widths of (i),(ii),(iii) 5 μm , 10 μm and 17 μm with increasing proton fluencies of (a)-(f): $3\times 10^{14}/\text{cm}^2$, $6\times 10^{14}/\text{cm}^2$, $1\times 10^{15}/\text{cm}^2$, $2\times 10^{15}/\text{cm}^2$, $5\times 10^{15}/\text{cm}^2$, $8\times 10^{15}/\text{cm}^2$ respectively..... 95
- Figure 5-20 : Change in the extended core formed by increasing the fluence using high ion energy for (i) narrow (ii) wide irradiation regions. Depending on the irradiation width and depth, cores with sharp or flat top regions may be observed. The angles θ and ϕ both increase with fluence at a fixed width irradiation..... 96
- Figure 5-21: PL images of (a) 0.02, (b) 0.3, and (c) 3 Ω .cm resistivity p-type silicon wafers irradiated with a range of fluences at very large areas. The arrow points in the direction of increasing fluence for all three images. (a) Square patterns irradiated with fluences (doses) of 5×10^{12} , 1×10^{13} , 2×10^{13} , 5×10^{13} , up to $5\times 10^{15}/\text{cm}^2$. The locations of lower fluences irradiation are outlined by dotted squares, since no visible PL is produced. In (b) and (c), irradiations of 5×10^{11} , 1×10^{12} , 2×10^{12} , 5×10^{12} , up to $2\times 10^{13}/\text{cm}^2$ are displayed. (d) Measured PL intensity and (e) peak-wavelength emission as a function of dose from (a)-(c), for low (0.02 Ω .cm, solid line) and moderate-resistivity (0.3 Ω .cm, dotted line and 3 Ω .cm, dashed line) p-type silicon wafers. From [89]..... 98
- Figure 5-22 : From the irradiated region shown Figure 5-17 (a) PL intensity across and (b) perpendicular to the centre of the highest porosity (end-of-range) region for an exposure time of 30 ms. (c) Magnified SEM image of low fluence irradiated region. White arrow indicates the darkest region in the SEM referring to the highest porosity region..... 99
- Figure 5-23 : Cross-section SEM, and magnified view of the cores, showing 0.02 Ω .cm wafer irradiated with 1 MeV protons with different line width of 1, 3 μm with line fluence of $1\times 10^{11}/\text{cm}$ and $3.5\times 10^{10}/\text{cm}$ and line width of 5, 10, 17 μm with the a fluence of $1\times 10^{15}/\text{cm}^2$ respectively. (b),(c) Optical and PL images of the same array of lines. PL collected with a Nikon Eclipse microscope with excitation wavelength of 330-380 nm, for an exposure time of 60 ms. (d) PL intensity across the formed cores. (e) PL intensity perpendicular to the centre of the 10 μm core. 100
- Figure 5-24 : (a)-(c) Optical micrograph and PL image and intensity linescan collected for 30 ms across the top of the formed core in 0.02 Ω .cm wafer irradiated with 1 MeV protons with different line width of 1, 3 μm with line fluence of $5\times 10^{10}/\text{cm}$ and $1.5\times 10^{10}/\text{cm}$ and line width of 5, 10, 17 μm with the same fluence of $5\times 10^{14}/\text{cm}^2$ respectively after the removal of FOPS formed at the highest porosity regions. (d) PL intensity perpendicular to the centre of the 17 μm core, and (e) showing the respective SEM. (f) shows the same region before removing FOPS..... 103

Figure 5-25 : Cross-section SEMs of 0.02 Ω -cm wafer showing (a)-(d) 1 μm irradiated line Ψ of $1 \times 10^{11}/\text{cm}$, $2 \times 10^{11}/\text{cm}$, $5 \times 10^{11}/\text{cm}$ and $8 \times 10^{11}/\text{cm}$ respectively, and (e)-(i) 10 μm irradiated line with fluence of $3 \times 10^{14}/\text{cm}^2$, $6 \times 10^{14}/\text{cm}^2$, $2 \times 10^{15}/\text{cm}^2$, $5 \times 10^{15}/\text{cm}^2$ and $8 \times 10^{15}/\text{cm}^2$ respectively..... 104

Figure 6-1: (a) SRIM simulation[30] of (top) trajectories versus depth and (bottom) defect distribution for 1MeV protons in silicon. (b) schematic showing the damage profile and deflected hole current around high defect region during anodization. At suitable fluences, the total hole current bends round the high defect region and flows through the lower defect region. 108

Figure 6-2 : Schematics of the processes involved in fabricating free standing 3D structures using (a) as an example, 1MeV proton irradiation for wires and 2MeV protons with a high Ψ for supporting walls, (b) anodization to produce PSi around the cores and (c) removal of the PSi leaving a free-standing structure. 110

Figure 6-3 : Optical image of embedded silicon wires in PSi layer. The supporting walls appeared bright as they are not etched hence not embedded in PSi and they are very smooth. The fluence used for irradiating them is high enough to form the PSi on top of these regions. Figure 6-4 (a) shows the same sample after removing the PSi. 111

Figure 6-4 : SEM images of 3D machined arrays of free standing cores forming various shapes, supported by heavily irradiated silicon walls in a 0.4 Ω .cm wafer. (a),(b) show wires and their close-up views. 112

Figure 6-5 : Free-standing silicon wires formed in a 0.4 Ω .cm wafer and irradiated with: (a) $2 \times 10^{10}/\text{cm}$, (b) $4 \times 10^{10}/\text{cm}$, (c) $8 \times 10^{10}/\text{cm}$, (d) $1 \times 10^{11}/\text{cm}$, (e) $2 \times 10^{11}/\text{cm}$, (f) $4 \times 10^{11}/\text{cm}$ 114

Figure 6-6 : Silicon wire (a) before (b) after oxidation..... 115

Figure 6-7 : 3D silicon nano-wires achieved after oxidation and removing the PSi..... 115

Figure 6-8 : (a) 3D machined wheel with a pillar for support. (b) grid formed by irradiation with 250 keV protons. (c) and (d) 3D star and butterfly irradiated by 500 keV protons. 117

Figure 6-9: Free-standing 3D silicon spring fabricated with PBW. Silicon spring (a) before (b) after oxidation. (c) Large view of the silicon spring after oxidation. 118

Figure 6-10 : Schematics of the processes involved in fabricating free-standing 3D structures using (a) broad uniform irradiation over a sample covered with a desired resist pattern. The resist is thick enough to stop the incoming ions completely. (b) anodization to produce PSi around the cores, leaving the cores intact. The PSi can be removed if desired, to make free-standing 3D structures. 119

Figure 6-11 : Silicon machining using UV lithography pattern in conjunction with large area irradiation. 121

Figure 6-12 : Cross-section SEMs of (a) 1 μm thick e-beam patterned PMMA resist on top of 0.4 Ω -cm wafer, and (b) silicon cores formed inside the PSi after irradiation with $\Psi=1.3 \times 10^9/\text{cm}$ using 50 keV protons and anodization. (c) shows plane view SEM of free-standing wires after removing the PSi. 123

Figure 6-13 : Cross-section SEMs of individual cores in 0.02 Ω -cm wafers irradiated with 50 keV protons with varying period and line fluence. 124

Figure 6-14 : (a),(b) show SEMs of a 150 μm thick PMMA layer patterned using X-ray lithography. (c) Cross-section SEM images of a core formed 16 μm deep inside the sample irradiated with 1 MeV protons and a Ψ of $1.6 \times 10^{10}/\text{cm}$ after anodization. (d),(e) Cross-sectional SEMs of larger cores formed using X-ray lithography patterns and large area irradiation facility with fluence of $1.2 \times 10^{15}/\text{cm}^2$ and $8 \times 10^{14}/\text{cm}^2$ respectively. The wide silicon region in (d) needs to be etched for longer time to be completely undercut. 125

Figure 7-1 : Schematics of the processes involved in fabricating curved free-standing 3D wires using (a) 1MeV proton irradiation for wires and 2MeV protons with a high Ψ for supporting walls, (b) anodization to produce P <i>Si</i> around the cores and (c) removal of the P <i>Si</i> leaving a free-standing structure.....	129
Figure 7-2 : (a) SEM images of an example failure in fabrication of curved 3D wires due to the sharp angle (θ) between the resist pattern and the wafer surface. The red curved line shows an example of the place of the curved wires which are broken and removed. (b) magnified view of such failure with the red line indicating the location of the resist line pattern during the irradiation.....	130
Figure 7-3 : PMMA resist pattern (a) before (b) after thermal reflow.....	131
Figure 7-4 : SEM of curved wires fabricated via PBW of lines over the resist pattern shown in Figure 7-3 (b). The arrow indicates in the bend in the wires following the resist profile on the surface of the wafer.	131
Figure 7-5 : Example of a failed fabrication of curved 3D wires due to the step at the edge of the resist pattern, $\Psi=1\times 10^{10}/\text{cm}$. (d) shows the resist line used on the sample to modify the end-of-range defects.	133
Figure 7-6 : Curved 3D free-standing silicon wires, $\Psi=5\times 10^{10}/\text{cm}$	134
Figure 7-7 : Cross-sectional SEMs of free-standing silicon cores fabricated with (a) $5\times 10^{10}/\text{cm}$ and (b) $8\times 10^{10}/\text{cm}$ protons. (c),(d) show the cores after oxidation respectively.	135
Figure 7-8 : Schematics of the processes involved in fabricating multilevel free-standing 3D wires using (a) 250 keV and 1 MeV proton irradiation for wires and 2 MeV protons with a high Ψ for supporting walls, (b) anodization to produce P <i>Si</i> around the cores and (c) removal of the P <i>Si</i> leaving a free-standing structures.....	136
Figure 7-9 : (a) A schematic of a two level silicon wire array created with four irradiation combinations of Ψ and energy, where the thin/thick lines indicates a low/high fluence. Deep wires (shown in blue) are formed by irradiation with 1 MeV protons with a low Ψ of $1\times 10^{10}/\text{cm}$ in portions [c,d] and high Ψ of $5\times 10^{10}/\text{cm}$ in portions [e,f]. Shallow wires (shown in red) are formed by irradiation with 250 keV protons with a low Ψ of $1\times 10^{10}/\text{cm}$ in portions [d,f] and a high Ψ of $7\times 10^{10}/\text{cm}$ in portions [c,e]. (b) SEM showing the resultant 3D line array. (c)-(f) SEMs showing close up view of each combination, with same lettering as in Figure 7-9 (a),(b).....	137
Figure 7-10 : Two-level array of parallel wires fabricated using 0.02 Ω .cm silicon wafer.	138
Figure 7-11 : Schematic showing fabrication of multilevel 3D silicon structures using a single ion energy. (a) the beam is scanned in line orthogonal to the page, resulting in (b) end-of-range cores at different depths.....	140
Figure 7-12 : SEM image showing the change in the depth of the free-standing multilevel silicon wires following the resist profile on the surface of the wafer. The white arrow is indicating the increase in depth of the wires.	141
Figure 8-1 : (a) SRIM plot showing defects versus depth for 450 KeV protons in silicon. (b) A cross sectional SEM image of a photoresist with sloping sidewalls on silicon. (c) - (d) schematics showing the fabrication of silicon lines with nano-sized tips. (c) shows how photoresist with sloping sidewalls may change and bring the end of range of ions nearer to the silicon surface. (d) shows the anodization process and how with continued anodization, sharp silicon tips forms as P <i>Si</i> continues to form inwardly.	143
Figure 8-2 : (a)-(d) show cross sectional SEM images of multilayer P <i>Si</i> irradiated with fluences $2\times 10^{13}/\text{cm}^2$, $2\times 10^{14}/\text{cm}^2$, $1\times 10^{15}/\text{cm}^2$ and $2\times 10^{16}/\text{cm}^2$ respectively. Green trapezium indicates the locations of the photoresist during the irradiation. In (d) the fluence was high enough to completely stop P <i>Si</i> formation.	144
Figure 8-3: Silicon line structures after the removal of P <i>Si</i> with KOH.....	145

- Figure 8-4 : (a)-(b) Schematics showing the processes used to achieve buried PSi channels formation. (a) shows a multilevel photoresist pattern on silicon. (b) shows how ions are completely stopped by the thickest PR step while their end of range is brought nearer to the surface by the second PR step. (c) shows the formation of the buried PSi channel. 146
- Figure 8-5 : (a) Optical image of multilevel photoresist patterned on silicon. The thickest photoresist step is where two PR lines overlap. (b) shows a plan view SEM image of the sample. PSi forms only from the regions previously covered with the thickest resist while buried PSi channels are achieved when PSi formation starts to undercut the shallowly irradiated silicon areas under the second resist step (c) A cross-section SEM image of the irradiated and anodized sample. (d) A magnified cross-sectional SEM image of the irradiated and anodized sample. Red arrows indicate the planes where PSi formation is confined. Sample in (c) and (d) were intentionally over-anodized to demonstrate PSi undercutting all irradiated regions..... 147
- Figure 8-6 : Cross-sectional SEMs showing (a) various dimensions of hollow channels formed inside a PSi layer and magnified view of hollow channels with a width of (b) $\sim 1 \mu\text{m}$ (c) $10 \mu\text{m}$ and (d) $17 \mu\text{m}$ within the depth of $16 \mu\text{m}$ of PSi. 150
- Figure 8-7 : cross-section SEM images showing a silicon rod inside a hollow channel within the PSi layer by using slightly higher line fluences (a),(b) $\Psi = 6 \times 10^{10} / \text{cm}^2$ and irradiated width of $5 \mu\text{m}$ and $1 \mu\text{m}$ respectively (c) $\Psi = 1.8 \times 10^{11} / \text{cm}^2$ and irradiation width of $3 \mu\text{m}$ 151
- Figure 8-8 : Plane optical micrograph of an array of parallel, hollow channels (dark regions) at a depth of $16 \mu\text{m}$ inside a transparent FOPS layer. 152
- Figure 8-9 : (a),(b) Different step heights formed across a $4 \mu\text{m}$ wide region irradiated 2 MeV proton fluence of $5 \times 10^{14} / \text{cm}^2$ and $2.5 \times 10^{15} / \text{cm}^2$ respectively. (c) SEM image of checkerboard silicon surface pattern, having many different heights. Fabricated with irradiating two sets of crossing bars, each with fluences of $2, 4, 6, 8$ and 10×10^{15} protons/ cm^2 using 2 MeV protons. 153
- Figure 8-10 : AFM images and line profiles across adjacent $10 \mu\text{m}$ wide bars showing (a) $\sim 10 \text{ nm}$ and (b) $\sim 30 \text{ nm}$ step height. 154
- Figure 8-11 : (a) Optical micrograph, (b) before and (c) after thermal annealing AFM images and line scans of surface relief pattern of $10 \mu\text{m}$ squares of four different heights, created using large area irradiation with 1 MeV proton fluences in orthogonal directions of 1 and 1.1×10^{15} protons/ cm^2 . (d) 3D AFM images before (top) and after (bottom) thermal annealing, showing the smoothing effect of thermal annealing. 155
- Figure 8-12 : SEM images of (a),(b) the machined four level silicon (c),(d) transferred to polycarbonate resist by nano-imprinting. 157
- Figure 8-13 : (a) Schematic of producing undercut, detached silicon microstructures, where the PSi etch front undercuts the irradiated regions, forming curved surfaces. (b) optical micrograph of the photo resist mask pattern used for fabrication of the grid. (c)-(d) Free-standing silicon fabricated over a $5 \times 5 \text{ mm}^2$ area using this process, (c) the free-standing silicon grid resting on a tweezers. (f) SEM image of many silicon bars resting on the underlying silicon surface, though completely detached from it. 159
- Figure 8-14 : Schematics showing fabrication process of free-standing nano-structures using large area beam irradiation setup in conjunction with a patterned photoresist mask which is thick enough to stop the incoming ions (a) low energy irradiation to produce end-of-range defects at the openings of the e-beam lithography patterned photoresist (b) higher energy ions with a high fluence to completely stop anodization at the openings of the UV lithography patterned photoresist (c) electrochemical anodization to form PSi around and undercut the high defected regions. (d),(e) Optical and SEM images showing free-standing nano-wires supported by a coarse free-standing micro-grid after the PSi is removed, making the whole structures free-standing. (f) SEM image of

similarly prepared free-standing silicon structures showing the spacing between the silicon nano-wires can vary.....	160
Figure 8-15 : Schematic diagram of proposed geometries of the conductivity sensor with a nano-fluidic microchip electrophoresis design and idea.	163
Figure 8-16 : Schematics showing silicon cross-section in two perpendicular directions (a) by using a single ion energy irradiation and vary the fluence, 3D structures with different cross-sectional dimensions, changing from tens of micron to tens of nanometers can be fabricated. The lateral dimension can be controlled by the irradiation design width. (b) PSi forms during the electrochemical anodization, leaving only high defected regions intact. (c) The PSi is removed using a diluted KOH solution.	164
Figure 8-17: SEMs of machined structures after anodization and removal of the PSi, showing a 10 μm long nano-ridge placed in between a 400 μm long micro-ridge. A second, separate nano-ridge parallel to the actual one is for better studying the shape of the ridge.	164
Figure 8-18 : SEMs showing (a) silicon micro-ridge connected to nano-ridge (b) high magnification of the nano-ridge, and insert shows AFM line profile across the nano-ridge. (c),(d) transferred patterns to PC after nano-imprint lithography, showing micro- and nano-channels with sharp edges and straight lines.....	166
Figure 8-19 : SEM images showing sharp nano-ridge fabricated by using 1 MeV protons and $\Psi=4\times 10^{11}/\text{cm}^2$, and the same energy protons with a fluence of $2\times 10^{17}/\text{cm}^2$ was used to produce micro-ridges. (b) insert shows AFM line profile across the nano-ridge indicating a very sharp tip of the ridge.....	167
Figure 8-20 : Schematic showing imprinting and sealing of nano-channel with an identical PC sheet.	167
Figure 9-1 : Schematic of the a.c. anodization process. (a) Proton irradiation through a thick, patterned PMMA layer (shown in black) results in a patterned SOI device layer. (b) Teflon cell (shown in black) for a.c. anodization of SOI wafer. This cell is similar to Figure 3.3 but here a.c. voltage instead of d.c. voltage is used. (c) Removal of PSi producing a patterned SOI device layer.	174
Figure 9-2 : AFM line profiles 10 $\Omega\cdot\text{cm}$ p-type bulk silicon anodized in a.c. and d.c. modes, offset for clarity. The inset shows the AFM image of the a.c. anodized wafer.	175
Figure 9-3 : Cross-section SEMs of the central portion of the a.c. anodized SOI wafer at different magnifications.	176
Figure 9-4 : Cross-section SEMs of the a.c. anodized SOI wafer close to the cell edge. (a) shows the non-uniform lateral anodization, (b) shows the deep groove forming at the cell edge.	176
Figure 9-5 : AFM image of a single irradiated line in SOI after a.c. anodization, using a line focus of 2 MeV protons.	178
Figure 9-6: Schematics of the processes involved in fabricating patterned SOI wafer using (a) 250 keV and 1MeV proton irradiation, (b) anodization to produce PSi around the irradiated regions, red dashed arrows show the hole current flow and (c) thermal annealing to oxidized the PSi layer.	182
Figure 9-7 : Patterned SOI wafer formed by 1 MeV with a low fluence of $1\times 10^{15}/\text{cm}^2$ to form the bottom layer, and 250 keV protons with a high fluence of $2\times 10^{16}/\text{cm}^2$ to form the top layer.....	183
Figure 9-8 : Two levels of irradiation connected to each other by using 250 keV protons with a fluence of $2\times 10^{16}/\text{cm}^2$ and 1 MeV protons with a fluence of (a) $2.5\times 10^{15}/\text{cm}^2$ and (b) $5\times 10^{15}/\text{cm}^2$	184

Figure 9-9 : SEM cross-sectional images showing only the bottom irradiation with the same irradiation and anodization conditions as (a) Figure 9-8, (b) and (c) Figure 9-9 (a),(b) respectively..... 184

Figure 9-10 : Cross-section SEMs of 600 keV helium ion irradiation with a fluence of $1 \times 10^{15}/\text{cm}^2$ and 1 MeV protons with a fluence of (a) $7 \times 10^{14}/\text{cm}^2$ and (b) $1.4 \times 10^{15}/\text{cm}^2$. The irradiated top silicon regions are lifted during the cleaving of the sample. 185

Figure 9-11 : Schematics showing the fabrication process of SOI wafer using large area high-energy ion irradiation for directing the hole current during electrochemical anodization in the sample. 186

Figure 9-12 : Attempt to fabricate SOI wafer. Cross-section SEM of one side of the wafer (a) and magnified view of it (b). (c) Magnified SEM showing the undercut irradiated regions. 187

Figure 9-13 : Resistivity as a function of effective dopant density for p-type silicon at 300°K. From [143]. 188

Figure 9-14: (a) SRIM simulation [23] showing the penetration depth of 300 keV boron (blue) and 100 keV helium (red). (b),(c) Tilted cross-section SEMs of silicon implanted with 300 keV boron and irradiated with a line pattern (d) High magnification cross-section SEM of the sample. 189

Figure 9-15 : Optical images comparing 5 Ω .cm wafer irradiated with a line pattern using 1 MeV helium (a) without boron implantation (b) with 300 keV implanted boron which allows an easy and fast undercutting of the irradiated regions by forming a conducting path..... 190

Figure 9-16 : (a) SRIM simulation [23] showing the penetration depth of 50 keV boron (blue) and 100 keV helium (red). (b) Tilted and (c),(d) normal cross-section SEMs of this sample irradiated with a line pattern. (e) Optical image showing top view of array of such irradiated lines. Silicon layers appear colourful as they are very thin..... 191

Figure 9-17 : SRIM simulation [23] showing the penetration depth of 50 and 200 keV boron (shown in blue) and 100 keV helium (shown in red). (b) Tilted cross-section SEM of silicon implanted with 50 and 200 keV boron and irradiated with a line pattern, showing a thin macroporous silicon layer formed on the top surface of the irradiated wafer. (c) Optical image showing top view of array of such irradiated lines..... 192

Chapter 1 : Introduction

1.1 Motivation

Recent developments in micro- and nano-fabrication technologies have opened up new opportunities in many diverse and different fields, such as integrated circuits, solar cells, microfluidics, optoelectronics, microsensors, etc, which has contributed to a new phase for developments of miniaturized and low cost devices. Although a variety of different materials can be used, silicon has been the material of choice because of the availability of wide range of manufacturing facilities developed for integrated circuits, its compatibility with integrated circuit fabrication technologies, and being a semiconductor with unique mechanical and optical properties.[1] Silicon is a preferred material for microelectronics not only because of the semiconductor properties but also because of the readily-formed high-quality electrical insulator, silicon dioxide, on the wafer which can be used for silicon surface passivation and protecting the silicon wafer during processing. Being extremely strong, together with its other mechanical properties, makes silicon desirable for micromechanical systems, such as cantilevers, membranes, resonators, pressure sensors, etc. Hence, microelectromechanical systems (MEMS) have expanded in many different directions: microfluidics, microacoustics, biomedical microdevices, BioMEMS, RF MEMS, PowerMEMS to name a few. Silicon is also widely used for optoelectronic devices such as light detectors, waveguides and mirrors.

The integration of all these enabling technologies can lead to miniature, multi-functional systems on a single chip. Hence, in the past decade researchers have been motivated to investigate even smaller structures, nano-devices, for

further miniaturization and to take advantage of the exceptional properties of nano-scale structures. In addition, developing novel and innovative ways to achieve three-dimensional (3D) integrated systems can improve the devices' performance and packing density as well as adding the ability of fabricating custom-shaped structures. Such highly compact 3D systems-on-a-chip offer abundant possibilities and applications for developing future micro/nanotechnologies in many different fields.

1.2 Silicon machining review

Silicon machining technology is the ability of etching desired structures in silicon wafers. The two fundamental types of silicon etching processes are “wet” (liquid-phase) and “dry” (plasma/gas-phase) etching. In the wet etching process, isotropic etchants like Hydrofluoric acid (HF), HNA (HF/Nitric/Acetic acid), and Nitric acid (HNO_3), with the same etching rate in all the directions, or anisotropic etchants like Potassium hydroxide (KOH) and Tetramethylammonium hydroxide (TMAH), with orientation-dependent etching rates, can be used. In the gas-phase, dry etching with a corrosive gas like XeF_2 is used to isotropically etch silicon substrates. In plasma-based dry etching, typically isotropic removal of exposed surfaces is achieved using a plasma of reactive gases such as fluorocarbons, chlorine, boron trichloride, and sometimes with the addition of nitrogen, argon, helium and other gases. Deep Reactive-Ion Etching (DRIE) is one of the most commonly used dry etching methods for silicon fabrication, especially for making high aspect ratio structures.

Two main techniques for the DRIE process [2] are the Bosch process and the cryogenic process. In the Bosch process, two steps alternate repeatedly to achieve vertical structures on silicon. The first step is isotropic plasma etching,

which is usually performed with a SF_6 plasma. The next step is chemical deposition of an inert passivation layer with the aid of C_4F_8 gas in a plasma. When these two steps repeat after each other, the passivation layer prevents the sidewalls from being etched, while because of the presence of directional ions in the plasma, the passivation layer is removed from the bottom surface. The alternating nature of this process results in scalloped sidewalls. The other main DRIE technique is the cryogenic process. This technique uses a mixture of SF_6/O_2 gasses to form the plasma while the sample is held at cryogenic temperatures (around -100°C). At such temperatures a SiO_xF_y passivation layer forms on the silicon sidewalls, while because of the presence of directional ions in the plasma that bombards the bottom surface, this layer will not form on the bottom surfaces and active components of the plasma can etch the silicon at the bottom surface. Because of non-alternating nature of this process, the sidewall roughness can be very low.

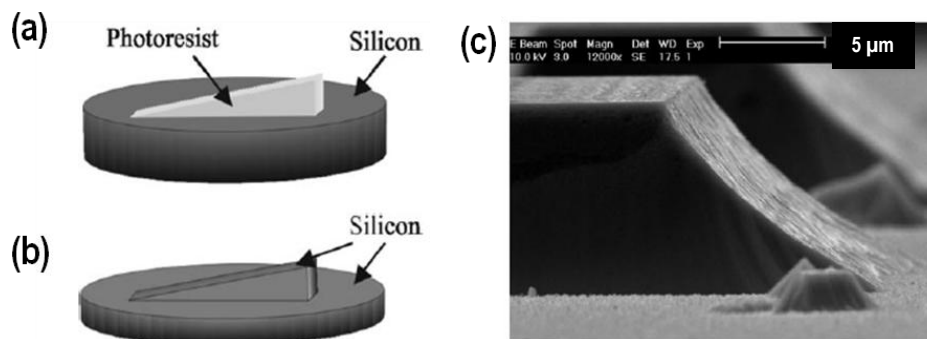


Figure 1-1 : (a),(b) An illustration showing the two primary steps for the fabrication of arbitrary 3D silicon structures using gray-scale lithography to form a nested mask. In (a), an exposed and developed photoresist from gray-scale lithography is used as a masking layer. In (b), the final RIE etched structure in silicon is shown using the masking layer from (a). (c) SEM image of an etched silicon structure resulting from a gray-scale nested mask and RIE etching. From [3].

Fabricating complex, arbitrary-shaped silicon structures in 3D is of great importance for different mechanical, electronic, and optical devices. Various techniques have been described in the literature for 3D silicon micro/nanofabrication. Surface machining which uses deposited thin films or SOI wafers may be used [4-5]. The top layer is selectively etched using mask patterns,

then the sacrificial layer is removed, producing free-standing silicon structures. This approach uses SOI (silicon-on-insulator) wafers which makes it expensive, or depositing polysilicon layers which results in non-crystalline silicon structures. The Cavity-SOI (CSOI) technique uses a thin wafer bonded with another wafer having pre-etched cavities for making free-standing structures on bulk silicon. The 3D structures are etched in the thinned device layer above the cavities located in the handle wafer.[6] Focused ion beams (FIB) [7-8] are used for silicon surface milling by scanning the beam over the sample to etch arbitrary shape patterns. 3D fabrication is possible using a FIB combined with other methods [9-11].

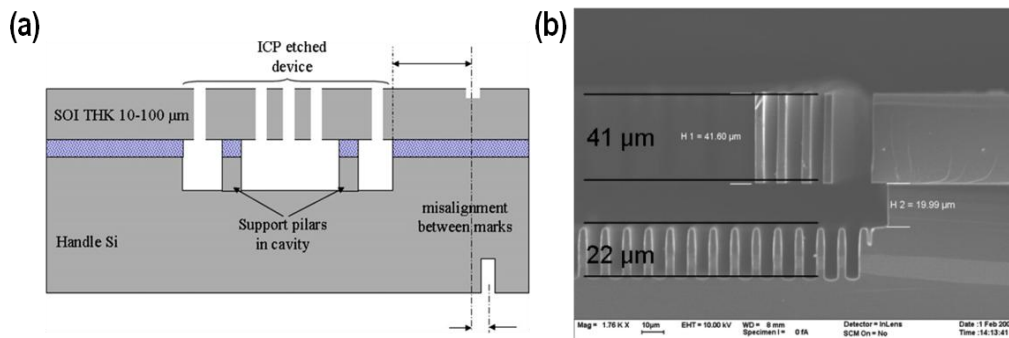


Figure 1-2: (a) Schematic image of a device structure manufactured on CSOI wafer. Support pillars enable better diaphragm uniformity. ICP (Inductively Coupled Plasma) dry etching is used for device manufacturing. (b) Cross-sectional SEM of the delay line structure etched into a CSOI substrate. From [6].

Both surface machining and FIB techniques are unable to fabricate 3D structures within the bulk of the wafer. The most common method for bulk silicon micro/nano-machining is DRIE [2], used for making structures with vertical side walls [12]. However, it is limited in fabricating complex 3D structures. Other techniques such as gray scale, multiple lithography, or controlling the degree of under-etching can help to make curved silicon structures [3, 13-15]. In gray-scale lithography, the gradient height profiles in a photoresist mask are transferred to the silicon substrate using anisotropic RIE, Figure 1-1 [16]. Deliberate modulation of the mask pattern openings define the etch depth variation in the RIE lag-based method [17-18]. Controlling the process parameters such as power density, gas

flows and timings in a sequential DRIE process will also result in the desired deep vertical etching with controlled under-etching and recovery, yielding 3D features on a silicon substrate [14]. For fabricating free-standing structures on bulk silicon using DRIE, SOI wafers [19] or CSOI technology [6] may be used, introducing additional flexibility though at a high wafer cost and complexity, Figure 1-2. In addition, complex 3D structures can be constructed indirectly by combination of machining different parts and assembly processes [20-21].

Despite the existing fabrication processes described above, making more complex structures, such as arbitrary free-standing 3D structures at certain depths or multilevel structures in bulk silicon, are highly challenging. These techniques require multiple or unconventional processes and show major limitations in the fabrication of complex 3D geometries. To overcome these limitations, there is a need to develop a simple and direct technique capable of fabricating complex, curved, multilevel, 3D structures in bulk silicon.

1.3 Objective

The main objective of this thesis is to develop such a technique for silicon micro- and nano-machining in bulk silicon using ion irradiation coupled with electrochemical anodization. This thesis also aims to study fundamental aspects of this process, including studying and modelling the effects of patterned ion irradiation on the motion of charge and current flowing through irradiated wafers and hence formation of 3D silicon structures as well as characterization of surface roughness. The final aspect of this thesis is to apply this unique 3D machining technique across a range of various applications such as M/NEMS, photonics, optoelectronics, nanoscale depth machining and micro/nano-fluidics.

1.4 Thesis overview

Chapter 1 has described the motivation and objective of this thesis as well as review some common techniques for silicon micromachining and 3D silicon machining. Chapters 2 and 3 give an overview of electrochemical anodization of silicon, the effect of ion irradiation on silicon wafer and different electrochemical anodization setups used in this thesis.

Chapters 4 and 5 summarize fundamental studies and characterization which provide an important understanding of the basic mechanism and effect of ion irradiation on p-type silicon. Chapter 4 describes the effect of irradiation on the roughness and etching rate of anodized silicon surfaces having different resistivities, and hence formation of different types of porous silicon. Chapter 5 describes a new current transport mechanism observed during electrochemical anodization of ion irradiated p-type silicon, namely diffusion funnelling observed at low-fluence irradiation, and the formation of silicon cores at moderate-fluence irradiation.

Using this improved level of fundamental understanding, chapters 6-8 describe the development of a novel technique for true 3D silicon micro- and nano-machining via ion irradiation and electrochemical anodization. The results show this machining technique is able to fabricate complex, curved, multilevel, 3D silicon structures in bulk silicon. Chapter 8 presents what can be achieved with our developed 3D machining technique for various applications. Chapter 9 describes use of the same principles for electrochemical anodization of Silicon-on-Insulator (SOI) wafers as well as develop a new technique for fabricating patterned SOI wafers out of bulk silicon.

Chapter 2 : Background

Direct-write technologies currently used for micro- and nano-fabrication are generally based on charged particles that can be focused to nanometer dimensions, e.g. electrons (e-beam writing) and slow, heavy ions in focused ion beam (FIB) systems. Both these techniques are very successful, and as a result, e-beam writers and FIB instruments are commercially available.

Proton beam writing (PBW) [22] is a new direct-writing technique for patterning resist material at micro- and nano-dimensions by using a focused beam of MeV protons. Although the process is similar in many ways to direct-writing using electrons, it, offers several interesting and unique advantages. High-energy protons are more massive than electrons; therefore have deeper penetration in materials while maintaining a straight penetration path owing to their high momentum. This allows PBW to fabricate 3D, high aspect ratio structures with smooth and vertical sidewalls. Furthermore, proton irradiation can modify the resistivity at different depths in silicon, allowing machining and patterning of selective regions via subsequent electrochemical anodization.

A comparison between e-beam writing, FIB lithography and PBW is shown in Figure 2-1 and is briefly discussed in the following sections.

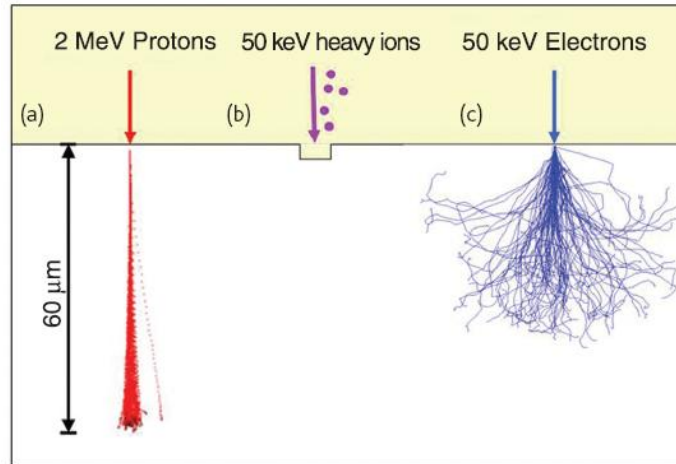


Figure 2-1 : Comparison between (a) PBW, (b) FIB, and (c) electron beam writing on PMMA. This figure shows schematically the difference between the three techniques. The PBW and FIB images were simulated using SRIM [23] while the e-beam writing image was simulated using the Casino [24] software package. The advantage of PBW in terms of ability to penetrate deeper with minimal lateral broadening are clearly shown here. For a more realistic comparison, the energies for the simulations here are chosen to reflect the typical energy used for each technique respectively. From [22].

2.1 Electron beam writing

E-beam writing [25] can be used for patterning resist films, by selectively removing either exposed or non-exposed region of the resist during the development process, depending on the type of the resist. In e-beam writing, when the electron beam interacts with the resist material, electron/electron collisions occur which result in large-angle multiple scattering of the electron beam. Therefore a pear-shaped ionization volume around the entry point of electrons into the resist is observed (Figure 2-1 (c)). For simulating the electron trajectories inside a material, Monte Carlo techniques such as the Casino software package [24] can be used. As an example, the penetration depth of a focused 50 keV e-beam is about 40 μm in the resist poly (methyl methacrylate) (PMMA) with a 20 μm lateral spread in the beam. Sub-100 nm e-beam writing therefore can only be achieved in very thin resist layers.

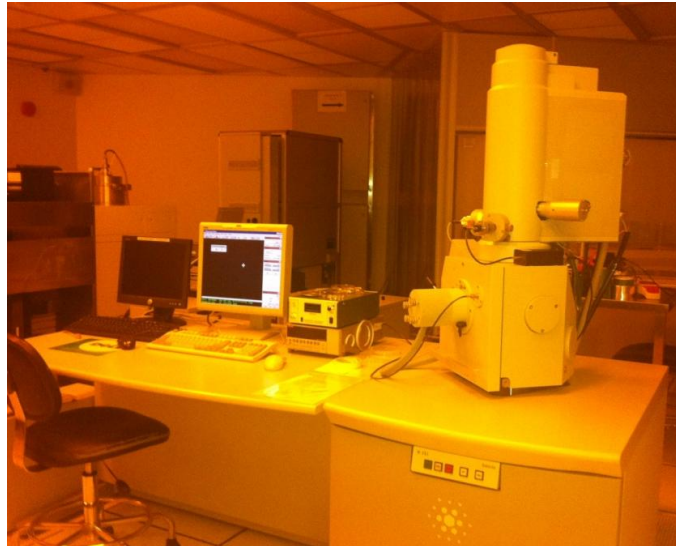


Figure 2-2: The Sirion scanning electron microscope (FEI Company) which also serves as platform for e-beam lithography located at Singapore Synchrotron Light Source (SSLS) clean room.

Despite the limitations of the resist thickness and small throughput, e-beam lithography is widely used as a commercial technique for maskless patterning of polymer resists. It can beat the diffraction limit of light and enables patterning features in the nanometer regime in a thin resist. In this thesis, e-beam lithography instrumentation as shown in Figure 2-2, is used as a mean of high resolution patterning of thin resist films (typically PMMA) on top of a silicon wafer, in conjunction with low energy proton irradiation for fabricating high resolution silicon structures. This allows the reduction of the size and the gap between the machined silicon structures as well as mass production of 3D nano-structures, which is discussed in chapter 6.5.2.

2.2 Focused ion beam technology

FIB [26] systems operate in a similar fashion to a SEM except, rather than a beam of electrons they use a focused beam of ions (usually gallium) that can be operated at low beam currents for imaging or high beam currents for site specific sputtering or milling (Figure 2-1 (b)).

FIB sputtering is based on momentum transfer between the incident heavy ions and the atoms close to the surface of the material. This results in structural and chemical changes as well as sputtering of atomic species from the surface. Monte Carlo techniques can be used to simulate the sputtering mechanism. The relatively slow material removal rate compared to e-beam writing in resists imposes limitations on FIB as a rapid fabrication technique, and hence FIB is generally confined to limited applications only.

2.3 Proton beam writing (PBW)

In the 1970's nuclear microprobes were developed to focus high momentum MeV ion beams. They are typically based on the use of quadrupole lens multiplets [27-28], briefly described in chapter 2.4.1, which provide a much stronger focusing action than axially symmetric lenses. Microprobes were mainly used for microanalysis using a range of ion beam techniques but more recently their use for direct writing and patterning of polymer resists for a range of applications was developed [22]. The PBW process uses a focused beam of high energy (MeV) protons. Although this process is similar to e-beam writing, it offers some unique advantages. Protons are approximately 1800 times more massive than electrons ($m_p/m_e \approx 1800$), therefore at high energies they have deeper penetration in resist materials and travel in an almost straight path. The trajectory of a MeV proton in a material depends on the interaction with both the electrons and nuclei in the material. For most of its path, the probability of interaction of a proton with an electron is a few orders of magnitude larger than for nuclear scattering. Because of the high mass difference between the proton and the material's electrons, individual collisions of a proton with electrons do not cause any significant deviation in the trajectory of a proton from a straight line path. In addition, as a result of the momentum difference, the energy transfer in each collision between a

proton and an electron is small and, hence, many thousands of collisions occur before a proton comes to rest in the material. The interaction of a proton beam inside resists can be summarized as follows:

1. The proton beam travels in a nearly straight line in materials apart from a small amount of end-of-range broadening which occurs when nuclear collisions are more likely to happen. This is a big advantage over e-beam lithography since the focused e-beam spreads rapidly when it enters the resist material, which makes it more difficult to fabricate high aspect ratio or three-dimensional structures.
2. The defect creation rate and energy deposition rate as the protons penetrate into the material are relatively constant along the path, at least for the initial portion of their trajectories. This is an advantage over other techniques such as X-ray and UV lithography, where an exponential reduction in dose occurs with depth.

For protons, the beam tends to remain well-collimated, with little lateral scattering until the ions slow down close to their end-of-range. The defect generation rate is more than ten times higher at the end-of-range compared to the trajectory closer to the surface [29]. By controlling the fluence within each point of an irradiated area, this property can be used to machine 3D silicon structures which are described in chapters 5-9.

3. The proton beam energy defines the penetration depth and end-of-range of the protons in a material. Their energy loss profile, trajectories and penetration depth can be simulated by means of Monte Carlo calculations, such as using computer code Stopping and Range of Ions in Matter (SRIM) [23, 30]. Hence, controlling the energy allows fabrication of multilevel structures in a resist layer or silicon wafer.

4. There are few high-energy secondary electrons produced in proton beam lithography, which prevents unwanted exposure of the resist (proximity effects). Unlike, for instance in e-beam lithography, where proximity effect occurs over a micron range because of a small but significant fraction of generated high energy secondary electrons.

PBW as a mean of resist lithography is well studied. In general, the primary mechanisms for patterning resist material are bond scissioning for positive resists such as PMMA, or cross-linking for negative resists such as SU-8. In positive resists the damaged regions can be removed by chemical development procedures to form the desired structures, whereas in negative resists undamaged regions of the resist are removed by chemical development and remaining cross-linked resists produce the final structures.

One of the primary differences of protons over e-beam writing is that energetic protons can induce atomic displacements in crystalline materials, such as silicon, which can change the local electrical properties. The work in this thesis is mainly based on this unique advantage of proton beam.

2.4 Centre for Ion Beam Applications (CIBA)

The process described in this thesis using high-energy ion beam irradiation is unique in fabricating complex 3D structures in a direct and flexible way in bulk silicon. The irradiation process using PBW involves focusing an ion beam to a spot size of tens or hundreds of nanometers. The focusing is based on using magnetic quadrupole lenses [27-28], which provide a much stronger focusing action than axially symmetric lenses. Microprobes were initially mainly used for microanalysis using a range of ion beam techniques but more recently their use for

direct writing and patterning of polymer resists and other materials for a range of applications was developed [22].

The 3.5 MV Singletron (High Voltage Engineering Europa) ion beam accelerator at CIBA produces high brightness, energetic ions. A Radio Frequency source first excites gas atoms, causing them to dissociate into ions. Using this process, various types of ions can be generated; however, in this thesis typically protons (H^+), molecular hydrogen ions (H_2^+) or singly-charged helium (He^+) are used. An electric field generated by the accelerator gradually accelerates the ions to the desired energy (Figure 2-3 (a)). For the work described in this thesis, energies mainly in the range of few hundred keV to 2MeV are used. The beam goes through a 90° magnet (Figure 2-3 (b)). This strong magnetic field imposes a Lorentz force on ions when passing through it. The strength of the magnetic field is adjusted so that only ions with the desired energy are bent by exactly 90° , so are able to pass through a small aperture after the magnet. Ions with higher or lower energies do not pass through this aperture, in this way we can precisely select the ion energy which is transported along the microprobe beam line.

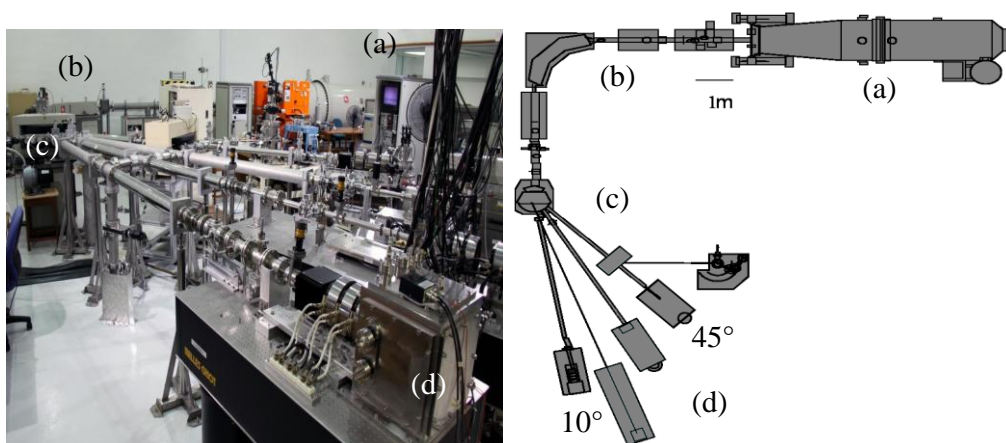


Figure 2-3 : (Left) CIBA singletron facilities. (Right) Schematics diagram of CIBA facilities: (a) the accelerator (b) 90° magnet (c) switching magnet (d) endstations.

The ion beam then passes through the switching magnet (Figure 2-3 (c)) to be directed in any of the desired five beam lines (Figure 2-3 (d)) for different

applications. For the work described in this thesis only endstations located at 10° and 45° are used for PBW and large area irradiation respectively (see chapter 2.5).

The ion beam profile can be monitored using a beam profile monitor located between the accelerator and 90° magnet. The ion beam current can be measured using a Faraday Cup, which intercepts all the charged ions. There are two Faraday Cups, one located after the accelerator, and the other just after the 90° magnet. In the whole acceleration and beam transport process the ions travel under a low vacuum pressure of $\sim 10^{-6}$ - 10^{-7} millibar) to the microprobe chamber where the samples are mounted for irradiation.

2.4.1 Magnetic focusing

The technology behind the focusing of electron beams is well established. A magnetic field parallel to the beam axis is produced by magnetic solenoids used in electron microscopes. As the electrons pass through the magnetic fringe fields at either end, a force towards the axis is induced. However, because of the large mass difference between electrons and protons, a stronger magnetic field is required to focus ions of the same energy. For example, the field strength required to focus 2 MeV protons is about 430 times stronger than that required to focus 20 keV electrons.

Magnetic quadrupole lenses are the most suitable strong focusing lens for MeV proton and alpha particles [31]. After the beam passes through the switching magnet it is focused with a high demagnification using a system of OM52 magnetic quadrupole lenses from Oxford Microbeams (Figure 2-4(a))[32-34]. A schematic design of a quadrupole lens is shown in Figure 2-4(b). The Oxford Triplet configuration consists of three magnetic quadrupole lenses, each consisting of four magnetic poles. The field is created by these four poles arranged

symmetrically in a N-S-N-S configuration about the axis and perpendicular to the beam direction. The blue lines in Figure 2-4(b) illustrate magnetic field lines. Owing to the symmetry, the field on the axis is zero, and the field strength increases proportionally to the distance away from the axis. The lenses focus the ion beam via the Lorentz force.

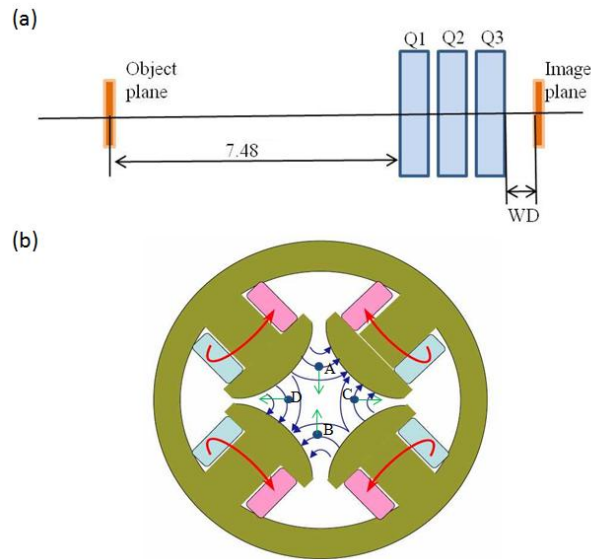


Figure 2-4 : (a) Schematic of Oxford triplet lenses configuration used in the 10° beam line in CIBA. Working distance (WD) is 0.07m. (b) Cross sectional schematic design in a quadrupole lens. Blue arrows show the field lines inside the lens and green lines indicate the force on a positively charged particle travelling into the plane of the paper at different points (A to D) in the quadrupole lens. Red arrows show the direction of the current flow in the coils to get desired magnetic polarity.

The quadrupole lenses have a length of 0.055 m, an aperture radius of 3.75 mm and spacing of 0.025 m between the lenses (Figure 2-4(a)). A demagnification of 220 and 70 in the horizontal and vertical directions respectively is achieved at the default working distance of 0.07 m. With this system of quadrupole lenses at the 10° beam line, CIBA has achieved a spot size of $35\text{nm} \times 75\text{nm}$ [22].

2.5 Modes of ion irradiation

Two main modes of irradiation have been used in this thesis for silicon machining:

2.5.1 PBW

The use of a microprobe to provide small MeV ion beam spot, which is then scanned over a small sample area is well established (see chapter 2.3), and used for microanalysis and also for PBW. Being very flexible, it enables high spatial resolution as well as direct variety of fluences to be used in the same area.

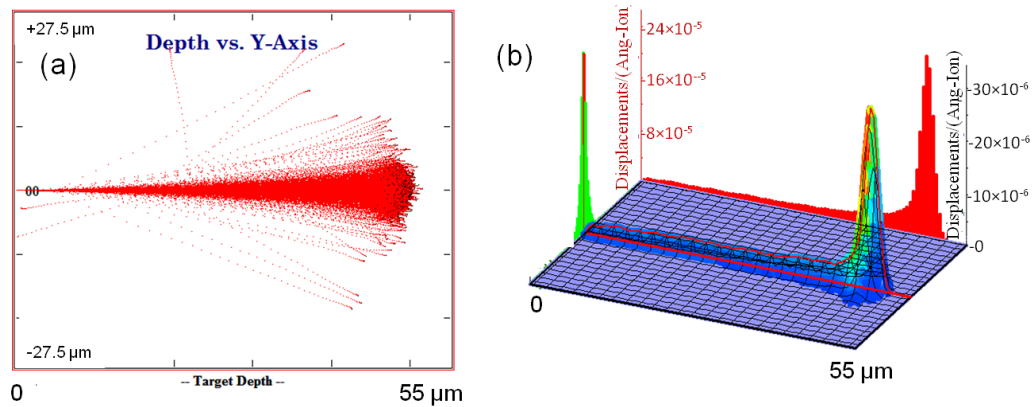


Figure 2-5 : SRIM simulation [30] of (a) trajectories versus depth and (b) defect distribution for 2 MeV protons in silicon by 2000 protons.

As an example, Figure 2-5 shows SRIM simulations [30] for 2 MeV protons penetrating silicon. The beam loses energy and eventually comes to rest at about 48 μm below the wafer surface. Along the proton path, lattice vacancies are created in crystalline silicon. Some of the energy is lost in collisions with the lattice atoms, resulting in them being displaced away from their lattice site, mainly forming a vacancy- interstitial pair, i.e. a Frenkel defect [23, 35-37]. Most of this lattice damage is produced at the end of range. According to SRIM calculations, a 2 MeV proton fluence of 5×10^{15} protons/cm² introduces a defect concentration of about 10^{19} vacancies/cm³ close to the silicon surface; however, it increases sharply to a maximum of 10^{20} vacancies/cm³ at the ion end-of-range [22]. This property is discussed further and made use of in chapter 5-9 to fabricate 3D structures in bulk silicon.

Scanning the focused beam in the desired pattern is done by deflecting the ion beam using a magnetic scan amplifier. Because of the different demagnification in the X and Y planes, the scan amplifier can be used to adjust the X to Y axis ratio and scan size independently. More complicated structures can be irradiated using the IonScan computer software package developed at CIBA [38-39]. The desired pattern should be drawn as a black and white pixelated image format which IonScan reads and then scans the required pattern according to the set scan size. IonScan is also able to control the dwell time at each irradiation point based on the pre-set desired fluence (number of ions/cm²). Using IonScan we can also set the number of frames, so different fluence irradiations can also be produced by repetitively scanning the focused beam a differing number of frames over each area. The dwell time is calculated based on the ion beam current in the chamber and the required fluence for each pattern. There is a beam blanking system controlled by IonScan which is located just before the switching magnet. The blanking system is used to blank the beam away by deflecting the beam out of the chamber when some parts of the pattern do not need to be irradiated. Using IonScan any complicated pattern can be irradiated.

2.5.2 Large area irradiation

Although PBW is very flexible, it does however suffer from the usual problems of all direct write processes, such as limited scan size (typically 1 mm), small throughput owing to the low beam current (typically a few picoamperes), and non-uniform irradiated areas if the beam current fluctuates.

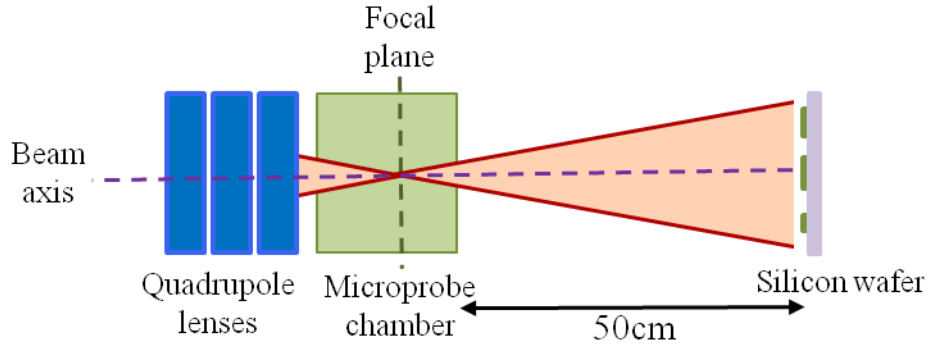


Figure 2-6 : Schematic of large area irradiation system based on a nuclear microprobe quadrupole multiplet focusing system.

A simple modification to the standard operation of a nuclear microprobe provides a means of solving these problems, allowing rapid irradiation of large wafer areas with high-energy ions [40]. Figure 2-6 shows a schematic of a standard microprobe lens multiplet focusing the beam in the chamber, as in normal operation. For large area operation the collimator and object apertures are opened wide to give a focused beam current of several hundred nanoamperes within the microprobe chamber. The wafer is positioned downstream of the chamber where the highly divergent beam exiting the quadrupole multiplet is uniformly distributed over a large area. For example, locating the sample about 50 cm downstream allows an irradiated area of more than $25 \times 25 \text{ mm}^2$. A MeV helium ion beam current of 500 nA delivers fluences of $\sim 10^{14}/\text{cm}^2$, typical of those required to form many micromachined components, in a few minutes. A further beneficial aspect of this irradiation mode is the irradiated beam uniformity is excellent, since any change in beam current equally affects the whole irradiated area. This will be discussed in detail in chapter 4.

2.6 Porous silicon (PSi) formation

The micromachining work in this thesis revolves around electrochemically anodization of silicon and porous silicon (PSi) formation. PSi is composed of arrays of pores with silicon skeleton walls, resemble a sponge-like structure with a

large surface-to-volume ratio. The size of the pores and the remaining silicon skeleton can change from few nm to μm depending on the wafer resistivity and electrochemical anodization conditions. PSi was first noticed by accident in 1956 by Uhlir at the Bell Labs, while developing a technique for electropolishing and shaping the surfaces of bulk silicon. In Bell Lab's notes they mentioned these rougher and somewhat porous areas with brown color in silicon simply as imperfect areas. These findings were used later in mid-1970's and 1980's mainly for the use of device isolation in integrated circuits [41-43], the process is described in chapter 9.2.1. These findings were not taken much further until in 1990 Leigh Canham at DERA (the UK's Defence Evaluation and Research Agency) discovered the emission of visible light from PSi by illuminating with an external UV light source at room temperature. This was attributed to the quantum confinement effect within the nanometer size silicon skeleton remaining after the electrochemical etching of silicon in an electrolyte containing Hydrofluoric Acid (HF). It was very important discovery, since silicon normally produce little photoluminescence owing to its indirect band gap. The discovery of this property motivated many PSi and silicon anodization studies over the past two decades.[44]

2.6.1 Electrochemical anodization of silicon

PSi is formed as a result of partial dissolution of silicon during electrochemical anodization in a HF electrolyte. The range of anodization mechanisms which can occur in p-type and n-type silicon are similar, except for p-type silicon the electrical holes are available within the wafer, hence by applying an external bias and forming an electric field inside the HF solution, holes start to migrate within the wafer towards the surface. However, for n-type silicon, electrical holes have to be generated by light illumination to break electron-hole pairs in the wafer. The rest of the anodization mechanism is similar to p-type wafers. In this thesis, for

simplicity, p-type silicon wafer is used for the micromachining process as it requires no external illumination.

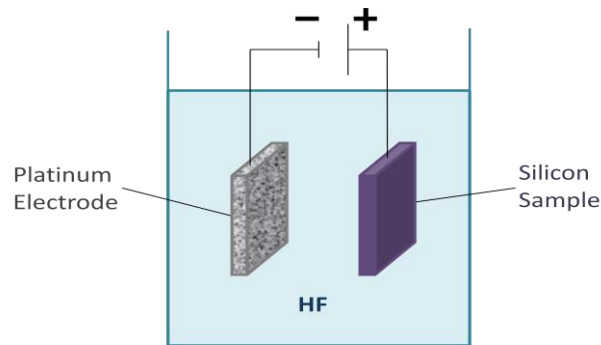


Figure 2-7 : Electrochemical anodization setup for p-type silicon.

Figure 2-7 shows the process of electrochemical anodization of p-type silicon, where a bulk silicon wafer together with a platinum electrode are immersed in a dilute HF solution. Platinum is used because it does not react with HF. The presence of electrical holes, which are readily available in p-type silicon, causes partial dissolution of the silicon wafer at the surface and the formation of PSi. The silicon wafer is the anodic electrode, so holes are driven from the back to the front surface of the wafer under influence of the applied electric field, facilitating the formation of PSi. The exact dissolution chemistries for PSi formation are still in question. There are different models proposed for describing the mechanism and formation of PSi. The most commonly accepted model [44-45] is explained here and shown in Figure 2-8 and Figure 2-9.

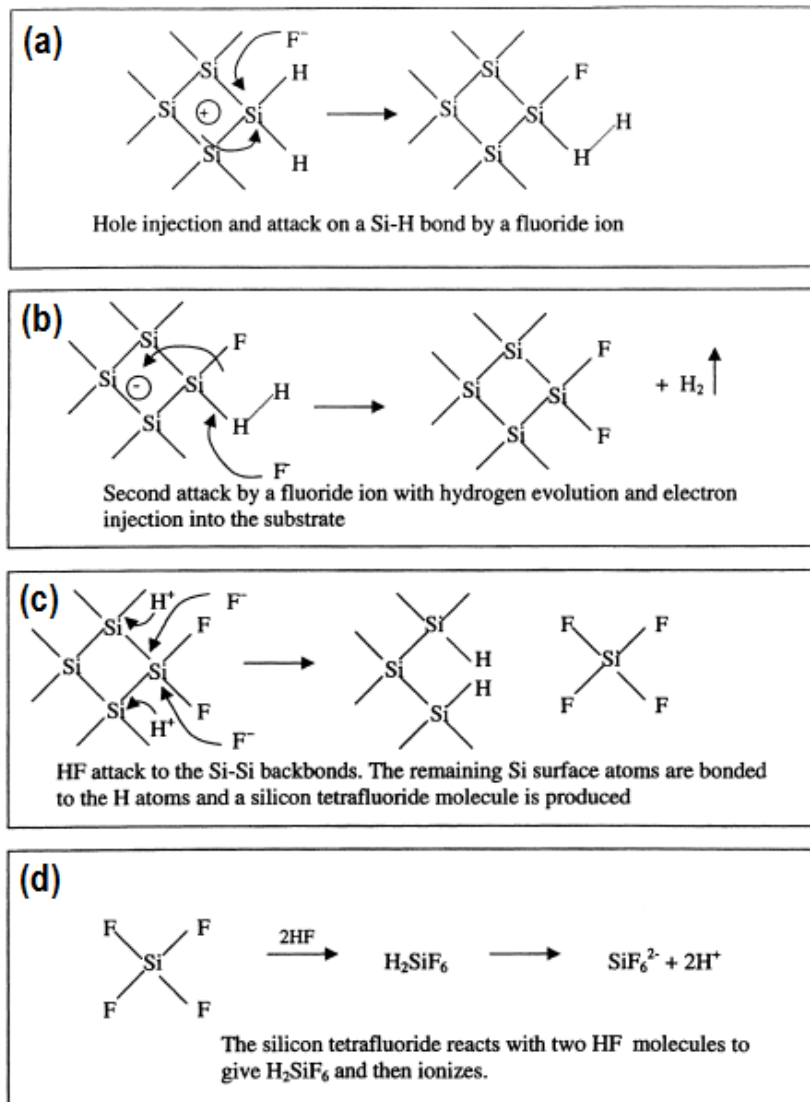


Figure 2-8 : Silicon dissolution in HF electrolyte scheme. From [45-46].

After applying a bias voltage, electrical holes migrate to the surface of the wafer and silicon atoms become bound to hydrogen atoms. The presence of electrical holes facilitates the nucleophilic attack of fluoride ions on silicon atoms. This process releases H^+ ions. After forming a silicon-fluorine bond, through attracting electrons from the silicon atom, the fluorine polarizes the bond (Figure 2-8 (a)). Therefore the other silicon bonds become weaker (Figure 2-8 (b)). The chance of being attacked by other F^- ions is higher for these atoms, and eventually all four bonds are made to fluorine atoms (Figure 2-8 (c)). A Silicon-Tetrafluoride

molecule (SiF_4) is released into the HF electrolyte (Figure 2-8 (d)). Reacting with two HF molecules, SiF_4 forms H_2SiF_6 . This process can be summarized as:

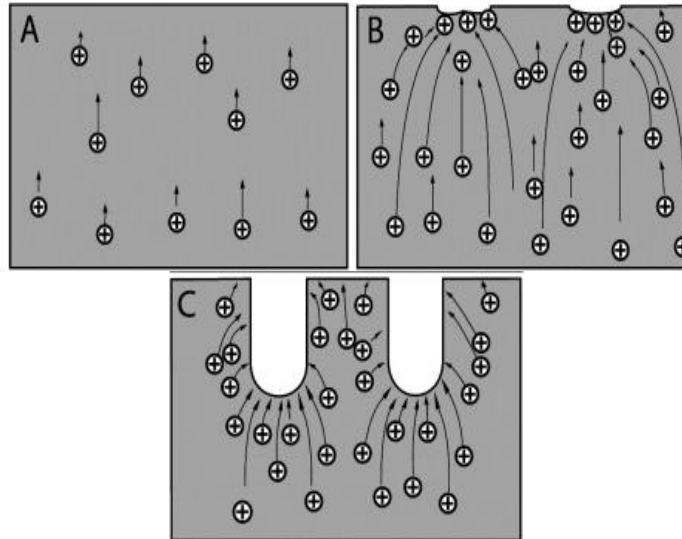


Figure 2-9 : Schematic drawing of the principle for the formation of the nano-/macroporous silicon network. Formation process includes the following stages: (A) migration of charge carriers in the bulk silicon to the electrolyte interface, (B) random pore nucleation and (C) pore formation and propagation. From [47].

This reaction continues and happens to other surrounding silicon atoms and causes the removal of silicon atoms and the formation of small silicon islands (Figure 2-9). Because of the quantum confinement effect, passivation occurs in these very small silicon islands. Hence, the energy of both electrons and holes become quantized. The appearance of bound states for holes lowers the valence band maximum and for electrons heightens the conduction band minimum. This results in a widening of the silicon band gap. Hence, the potential barrier prevents further entry electrical holes to these regions from the bulk silicon (Figure 2-10), which results in removal of silicon atoms from the pore tips rather than from other parts of PSi. By continuing the etching process, the pores therefore become deeper.

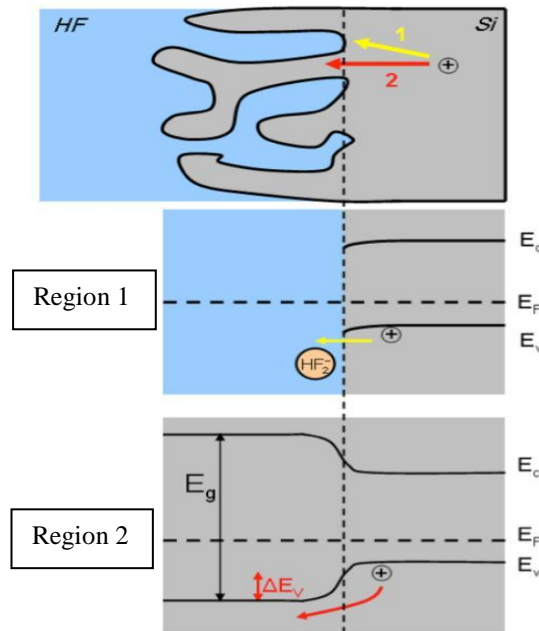


Figure 2-10 : illustration of modification of the silicon bandgap during porous silicon formation as a result of the quantum confinement effect. See [46].

According to pore geometries PSi can be categorise in 3 different groups: microporous silicon, mesoporous silicon and macroporous silicon. Figure 2-11 shows the dimension and density of the pores in different type of PSi. Pore widths smaller than 2 nm are defined as micropores, between 2 to 50 nm as mesopores and larger than 50 nm as macropores. These values are calculated assuming straight, cylindrical pores in a parallel pattern. However, it should be noted that micro- and mesoporous silicon do not exhibit such a well-ordered morphology as macroporous silicon.

The most important factors influencing the type, dimensions and density of pores are the wafer resistivity, current density (which depends on the magnitude of the applied electric field) and concentration of HF solution. As a result of quantum confinement effects, the density of micropores is independent of the silicon doping density. However, the density of mesopores and macropores increase linearly with the doping density [44].

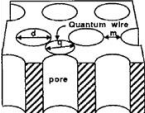

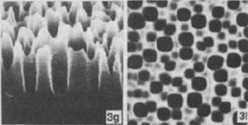
Pore diameter (nm)	Size regime	Pore density (μm^{-2})	
1	Micro	5×10^5	
2		12×10^4	
5	Meso	2×10^4	
10		5000	
20		1250	
50		200	
100	Macro	50	
200		12.5	
500		2	
1000		0.5	
2000		0.125	

Figure 2-11 : Pore diameter and density for different types of porous silicon. From [44].

The mechanism by which silicon undergoes dissolution during electrochemical anodization depends on the wafer doping density [44]. Figure 2-12 shows a linear spacing, on average, between the dopants for different resistivity of p-type silicon wafers [44]. For moderate resistivity wafers, 0.1-10 $\Omega\cdot\text{cm}$, thermionic emission within the space charge region, together with quantum confinement effects result in microporous silicon formation. For low resistivity wafers of less than 0.1 $\Omega\cdot\text{cm}$, tunneling effects occur across the space charge region, leading to the formation of mesoporous silicon.

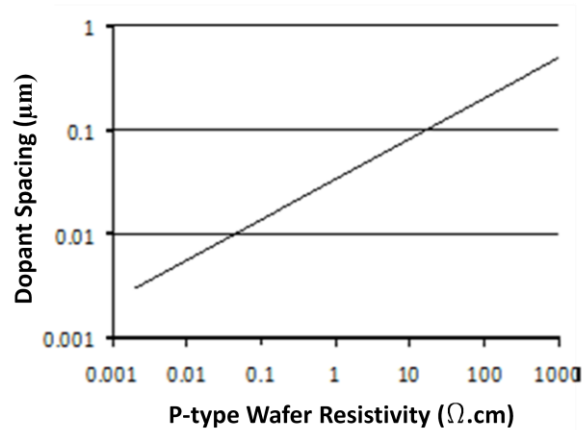


Figure 2-12 : Dopant spacing for different resistivity of p-type silicon wafers. From [48].

The ratio of voids inside the PSi is defined as porosity. The porosity of the PSi is dependent on the type of formed pores and hence is related to silicon doping density. In general, by increasing the current density, the porosity increases, and by increasing the concentration of HF electrolyte the porosity decreases [49].

2.7 Effect of ion beam irradiation on p-type silicon

The silicon fabrication process used in this thesis is based on the defects created by high energy ions in crystalline materials, at the surface and along their trajectory [30, 37, 50-52]. The defect density in silicon due to ion irradiation depends on many factors; defects can be stable or they may agglomerate into more stable divacancies and other vacancy or impurity-related centres. Many types of defects act as trap levels where charge carriers undergo recombination, so reducing the free carrier (hole) density and effectively increasing the resistivity along the ion trajectories. A simple model suggests that ion irradiation thus reduces the electrical hole current flowing through these regions during subsequent electrochemical anodization, slowing down PSi formation. Higher fluence irradiation can act as an etch stop for PSi formation, completely stopping the formation of PSi [53]. If desired, the underlying multilevel silicon structure may be easily revealed by removing the PSi with KOH.

This process uses p-type silicon within a range of resistivity from $\rho \sim 0.01 \Omega\cdot\text{cm}$ (doping density $\sim 10^{19}/\text{cm}^3$), to $1 \Omega\cdot\text{cm}$ (doping density $\sim 2 \times 10^{16}/\text{cm}^3$). The lower resistivity wafers are ideal for machining different surface topography, such as patterned Bragg reflectors, concave micromirrors and holographic surfaces, since the etch rate is proportional to the fluence. Higher resistivity wafers are more suitable in silicon photonics where the lower doping density gives lower scattering losses from free carriers. While a similar process has been used to micromachine III-V semiconductors such as [54-55], in this thesis only machining and patterning of silicon is discussed.

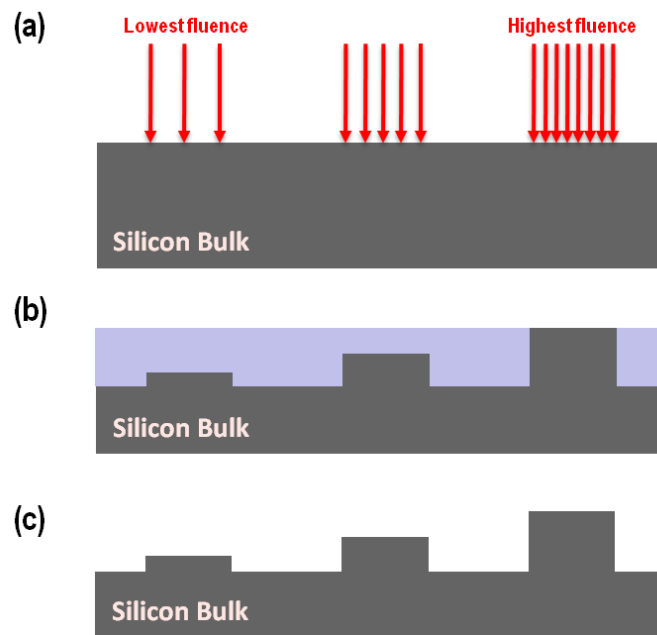


Figure 2-13 : Schematics of machining multilevel silicon structures. (a) Irradiating with various high energy ion beam fluences (b) Formation of PSi during subsequent electrochemical anodization in HF solution (c) PSi removal to reveal multilevel silicon structures.

Silicon micromachining and PSi patterning can be done using high energy protons or helium ions together with subsequent electrochemical anodization. Ion irradiation increases the local resistivity of p-type silicon by creating defects in the silicon lattice. Hence, during the electrochemical anodization in HF electrolyte, the electric hole current which is essential for PSi formation is reduced in the irradiated regions. By increasing the fluence the rate of PSi formation is

consequently reduced (Figure 2-13). At high enough fluences, the PSi formation rate is very slow and may be completely stopped. A more detailed study to improve understanding of the hole current flow and PSi formation was carried out and is described in chapter 5. The PSi can then be removed to reveal the two or three dimensional patterned silicon beneath. PBW therefore can be used to irradiate and pattern any complicated arbitrary shape on a silicon wafer.

Helium ions create defects in silicon at a much faster rate in comparison to protons, as they are heavier and hence transfer more energy during collisions. According to SRIM simulation [30], helium ions typically create ~20 times more defects than protons in silicon. In this thesis, generally for the experiments where high defect density is needed, helium ions are used. It should also be noted that the range of 2 MeV helium ions in silicon is ~7 μm , whereas the range of 2 MeV protons is ~48 μm . Hence, the choice of using protons or helium ions also depends on the required range in the silicon wafer.

2.7.1 General steps of micromachining silicon and PSi formation

Utilizing the ion beam accelerator facility at CIBA (see chapter 2.4) and the effect of ion beam irradiation on silicon (see chapter 2.5 and 2.8) various two- and three-dimensional silicon and PSi patterns can be fabricated. For this purpose the following steps are required:

1. Preparation of the desired pattern for irradiation. This depends on the mode of irradiation which can be PBW or large area irradiation. For PBW the desired pattern should be prepared as an image in a binary bitmap format for scanning through the IonScan software package [38-39] described in chapter 2.6.1 and irradiating the desired pattern. However, for large area irradiation, the desired pattern should be transferred to a resist

mask on the surface of the sample. The resist patterning can be done using standard UV lithography, e-beam lithography, PBW lithography or X-ray lithography according to the feature size and the thickness of the required resist pattern. (more detail in chapter 6.5)

2. Ion beam irradiation. PBW or large area irradiation with required ion energy and fluence is used to irradiate the prepared patterns.
3. Electrochemical anodization. After the irradiation the samples are electrochemically anodized in a HF solution. The anodization time and current density is calculated according to the desired anodization depth and porosity of the PSi. If the sample is covered with a resist pattern, the resist should be completely removed prior to anodization.
4. Removing the PSi. This step is optional depending on the application. A dilute KOH solution (56 gr/lit) can be used to remove PSi layer for revealing micromachined silicon structure beneath. Alternatively the sample can be annealed for a short time for oxidized PSi formation and removing the silicon dioxide layer with a diluted HF solution.

The above steps are used for all the fabrication work described in this thesis.

2.8 Review of previous silicon/PSi micromachining work at CIBA

This section reviews a range of PSi/silicon micromachining work previously done using various modes of irradiation [56], based around the processes described above.

2.8.1 Distributed Bragg reflectors

Large area irradiation in conjunction with multiple resist mask can be used for fabricating distributed Bragg reflectors (DBR) based on the behavior observed and described in Figure 2-13.

Patterned irradiation is achieved using standard UV photolithography to first deposit a resist layer of a few micrometers in which a certain ion energy is stopped, so that only the exposed wafer areas are irradiated. More complex photoresist patterns can be used in conjunction with multiple energy irradiation to achieve multilevel wafer patterning. Figure 2-14 shows SRIM [23] plots of two ion energies incident on different photoresist thicknesses. By suitable choice of layer thicknesses and beam energies, the defect depth distribution can be located at any wafer depth, allowing the etching rate to be defined laterally and in depth.

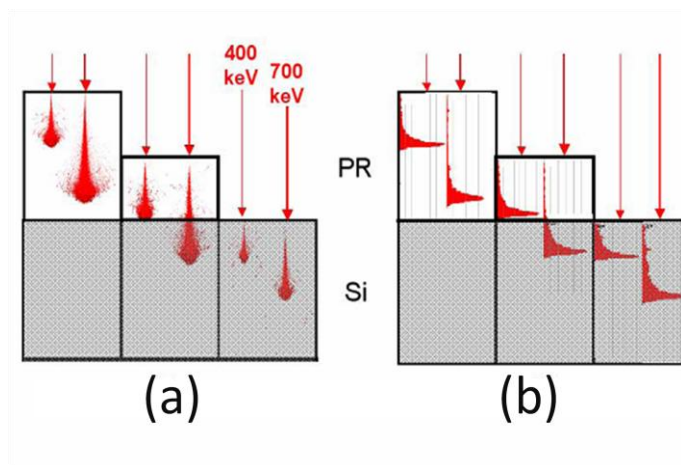


Figure 2-14 : (a),(b). SRIM [23] plots of 400 and 700 keV H_2^+ ions incident on different thicknesses of photoresist (PR) on top of a 7- μm thick Si layer (shown in gray). (a) From left to right the PR thicknesses are 7 μm , 3 μm and 0 and trajectory plots show how far each ion penetrates through the layer structure. (b) Corresponding defect density. Both beam energies are shown, with the higher energy to the right. From [40].

The ability to alter the porosity/refractive index of PSi in a periodic manner by alternately raising and lowering the etch current density during anodization is used to produce distributed Bragg reflectors, in which each layer is a quarter of the optical thickness of one incident wavelength[57-58]. By

sandwiching a half wavelength PSi layer between two such DBRs a resonant cavity is formed which can narrow and enhance the PL emitted [59]. Low resistivity (0.001 to 0.1 $\Omega\cdot\text{cm}$) p-type wafers are typically used for this as a greater range of porosity/refractive index can be produced by changing the anodization current density [44].

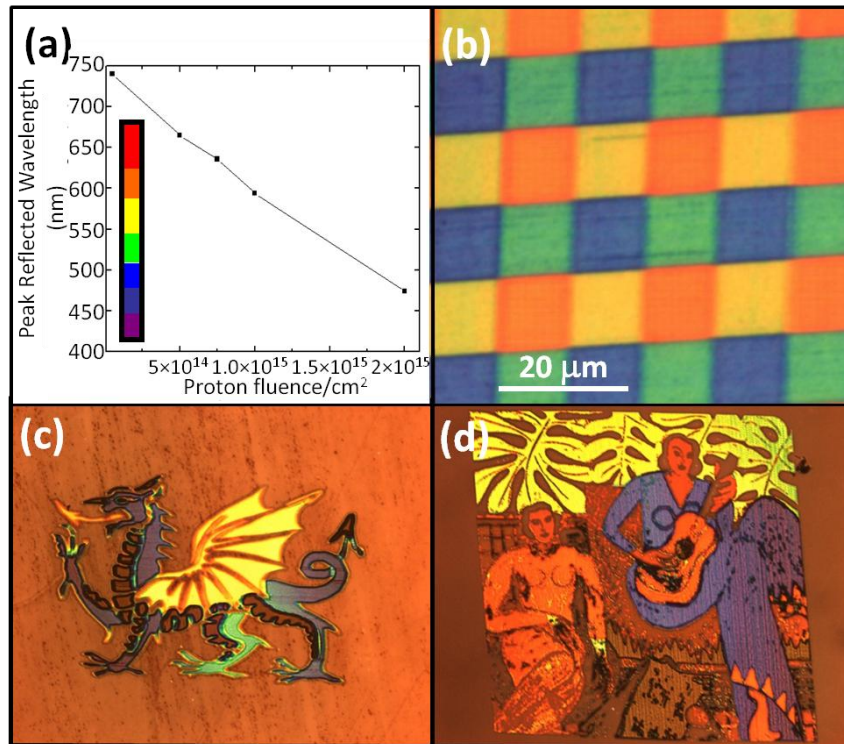


Figure 2-15 : (a) Change in peak reflected wavelength of irradiated DBR versus proton fluence. (b) Patterned DBR formed by irradiating groups of four $10 \mu\text{m}$ wide pixels with different proton fluences prior to anodization. Other examples of patterned DBR structures such as (c) Dragon and (d) Henri Matisse's painting 'La Musique'. From [60].

Patterned irradiation with MeV ions introduces an extra flexibility into DBR fabrication by allowing selectively irradiated areas to have different reflective wavelengths, owing to the reduced etch current flowing after irradiation. The reduction in anodization current at irradiated regions results in thinner layers in the porous silicon DBR. Figure 2-15 (a) shows a linear relationship between the DBR reflected wavelength and fluence, allowing local tuning of the reflected wavelengths. Figure 2-15 (b) shows an example of patterned DBR with $10 \mu\text{m}$ square pixels. Figure 2-15 (c),(d) show more complex examples of patterned

DBRs made with direct writing. When the large area irradiation facility described above is used it allows patterned DBRs with micrometer resolution over large areas.

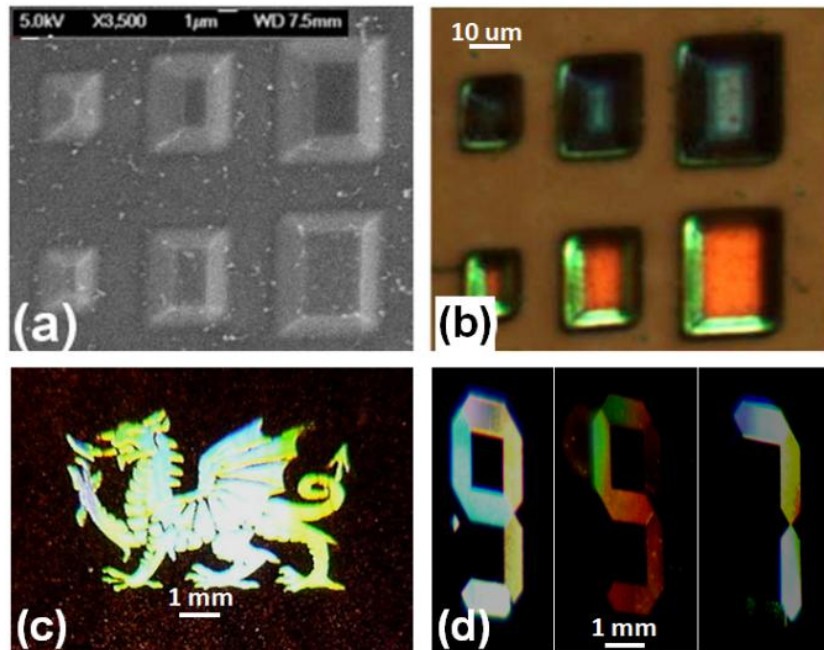


Figure 2-16 : 3D patterned DBR arrays, (a) SEM, (b) high magnification optical micrograph showing the effect of white light illumination from the top and from the left sides of such pixels. (c),(d) low magnification optical micrograph of large areas arrays of patterned 3D DBR pixels. From [61].

Irradiation not only produces a region where etching is slower and so thinner layers in the DBR, also the zone between the unirradiated and irradiated regions becomes progressively more tilted with fluence. This feature was used to produce arrays of 3D DBR pixels with tunable tilt-angles of the boundary regions, allowing different reflected wavelengths from the sides as well as the tops of the pixels[61]. Figure 2-16 (a) shows an array of such pixels where the top, flat surface and tilted sides are seen. Figure 2-16 (b) shows the effect white light illumination from the top and from the left side. A higher fluence was used fabricate the upper row than the lower row, resulting in the central reflected wavelength from the tops of the upper row pixels being more blue-shifted. Suitable side illumination produces red-shifted reflected light from the lower pixel boundary compared to the top surface, owing to the longer path length through the

tilted DBR. Figure 2-16 (c),(d) show examples of patterned DBRs, comprising arrays of pixels, each of which is fabricated utilizing the controlled tilt angle of an etched boundary. This enables ‘white’ DBRs to be produced by inducing a change in layer thickness at a boundary with etch depth, leading to a wide range of reflected wavelengths, Figure 2-16 (c). This process also enables patterned areas of DBRs showing different patterns at different tilts or with different angles of illuminated light, Figure 2-16 (d).

2.8.2 Computer generated holography

Computer Generated Holograms (CGH) are used as diffractive-optical elements for storage of digital data and images [62], precise interferometric measurements [63], pattern recognition [64], data encryption [65] and three-dimensional displays [66]. They are described mathematically by computing the phase and amplitude information of the wave propagation produced by an object, rather than physically recording it.

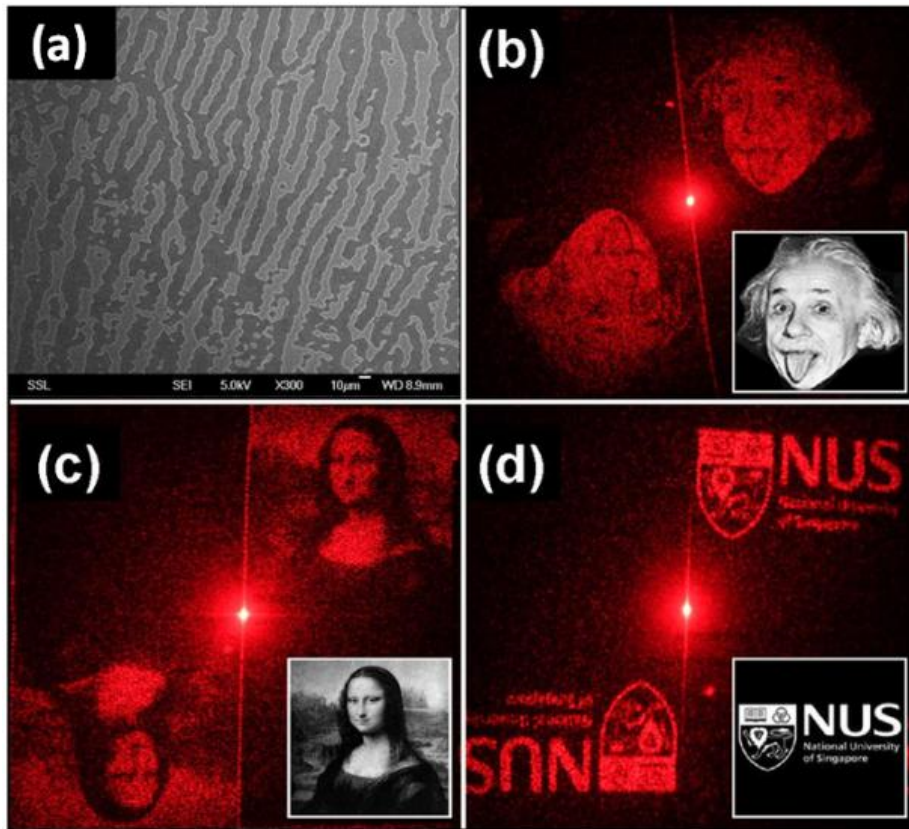


Figure 2-17 : (a) SEM image of transferred binary amplitude CGH pattern in silicon irradiated with 600 keV helium ions at 5×10^{14} ions/cm². (b) to (d) show grey scale reconstructed holograms from binary amplitude CGH on silicon. From [67].

A binary surface relief CGH pattern may be machined in silicon [67] by patterning using photolithography with suitable computed patterns, then irradiating over a large area. After anodization and removing the PSi layer a binary surface relief CGH pattern is revealed, Figure 2-17(a). Figure 2-17 (b),(c),(d) show examples of reconstructed images from such CGH patterns on silicon by reflecting a red (650 nm) laser off the CGH pattern onto a viewing screen. It is hard to record CGH patterns with variable pixel modulation of both amplitude and phase, so existing recording techniques generally modulate in an on/off binary manner, as in Figure 2-17. Since our micromachining process can variably modulate the amplitude of reflected light over a wide range by controlling the surface roughness [53], it may provide a means of modulating both reflected light intensity and phase.

2.8.3 Micromirrors – spherical surface patterning

A concave surface profile with micrometer-scale dimensions is of interest because of its ability to focus incoming light into a spot. Concave mirrors act like optical tweezers to trap/push particles with the optical gradient/scattering force [68-69] and may be used as a variable optical attenuator [70] or to produce an enhanced and localized light signal for parallel low loss optical interconnect systems [71].

Very smooth, concave mirrors [72] have been fabricated at CIBA using ion irradiation of a resist patterned as an annulus, using the same process to produce undercut structures shown in Figure 2-18 (a), but making instead use of the surface relief pattern formed on the underlying silicon substrate after anodization and PSi removal. Ion irradiation creates defects only in the exposed annuli, and so during anodization PSi only forms at the surface within the small central aperture. Since PSi formation is isotropic a curved etch front naturally forms after the top irradiated region is undercut. A large electropolishing pulse at the end of the anodization detaches the PSi layer and undercut, patterned free-standing structure from the underlying concave silicon surface. The location, diameter and height of the concave surfaces are controlled by the photoresist geometry.

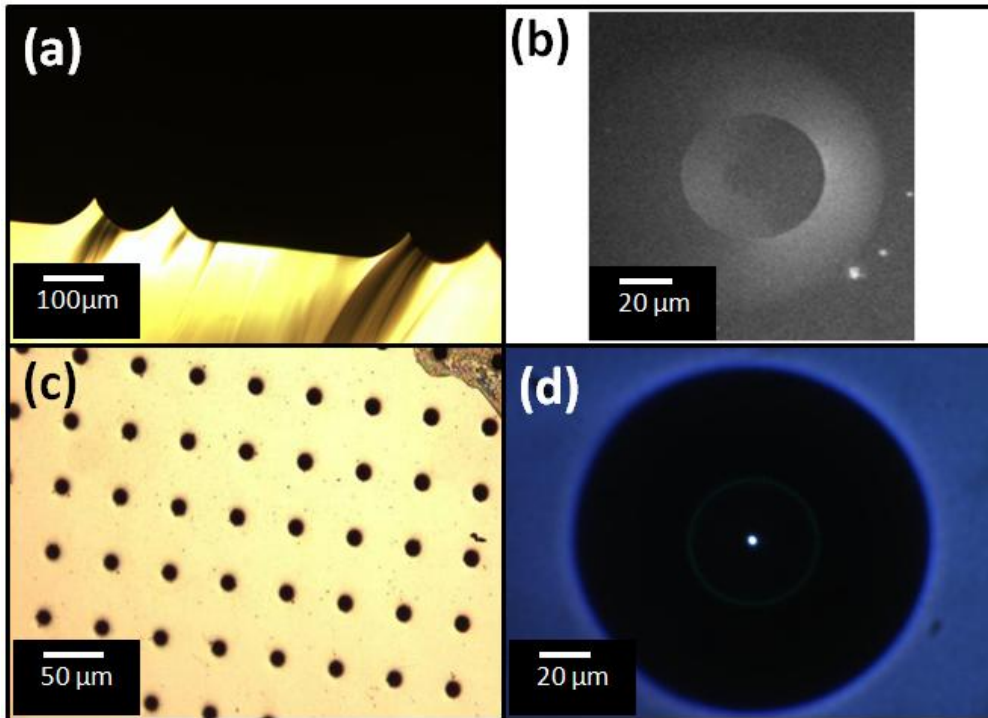


Figure 2-18 : (a) Optical, (b) SEM images of concave silicon surfaces. (c) Optical image of an array of concave surfaces with 20 μm diameter. (d) Optical image of a concave DBR mirror illuminated with white light, reflecting and focusing blue wavelengths. From [72].

Figure 2-18 (a),(b) shows optical micrograph and SEM image of a concave spherical mirror fabricated using this method. An array of such concave mirrors is demonstrated in Figure 2-18 (c). They can similarly be fabricated with a DBR at the surface, giving the ability to selectively reflect and focus particular wavelengths. A concave surface is first produced, then the P*Si* removed, followed by a second anodization step using an alternate high/low current density to achieve a thickness corresponding to one quarter of the desired wavelength. Figure 2-18 (d) shows an optical image of one of the mirrors illuminated with white light, designed to focus and reflect blue light.

2.8.4 Waveguides for silicon photonics

Several different types of silicon waveguides have been fabricated in 1–10 Ohm.cm p-type silicon using the approach described above, either with direct writing [73] or large area irradiation. Figure 2-19 (a) shows silicon-on-oxidized-porous-silicon (SOPS) strip waveguides with high-index contrast produced using

direct writing [74]. A low rms surface roughness of 3 nm was achieved after subsequent oxidation, resulting in measured propagation losses of ~1 dB/cm, the lowest reported loss for SOPS waveguides. Figure 2-19 (a) shows three such waveguides formed with different proton fluences, where the oxide cladding is seen. The core size depends on the proton fluence, so consequently the propagation loss also depends on the fluence. A fluence of $10^{15}/\text{cm}^2$ produced the largest core and so the lowest loss, though not just because of the larger size but also because of the greater likelihood of a uniform irradiation at higher fluences.

The effect of oxidation on the propagation loss and surface roughness was also studied on similar waveguides fabricated using large area irradiation with 250 keV protons, Figure 2-19 (b) [75]. A thin thermal oxide is formed around the core of the waveguide, enabling the symmetric reduction of core size and roughness on all sides. Significant loss reduction from about 10 dB/cm to 1 dB/cm was obtained after oxidation smoothening.

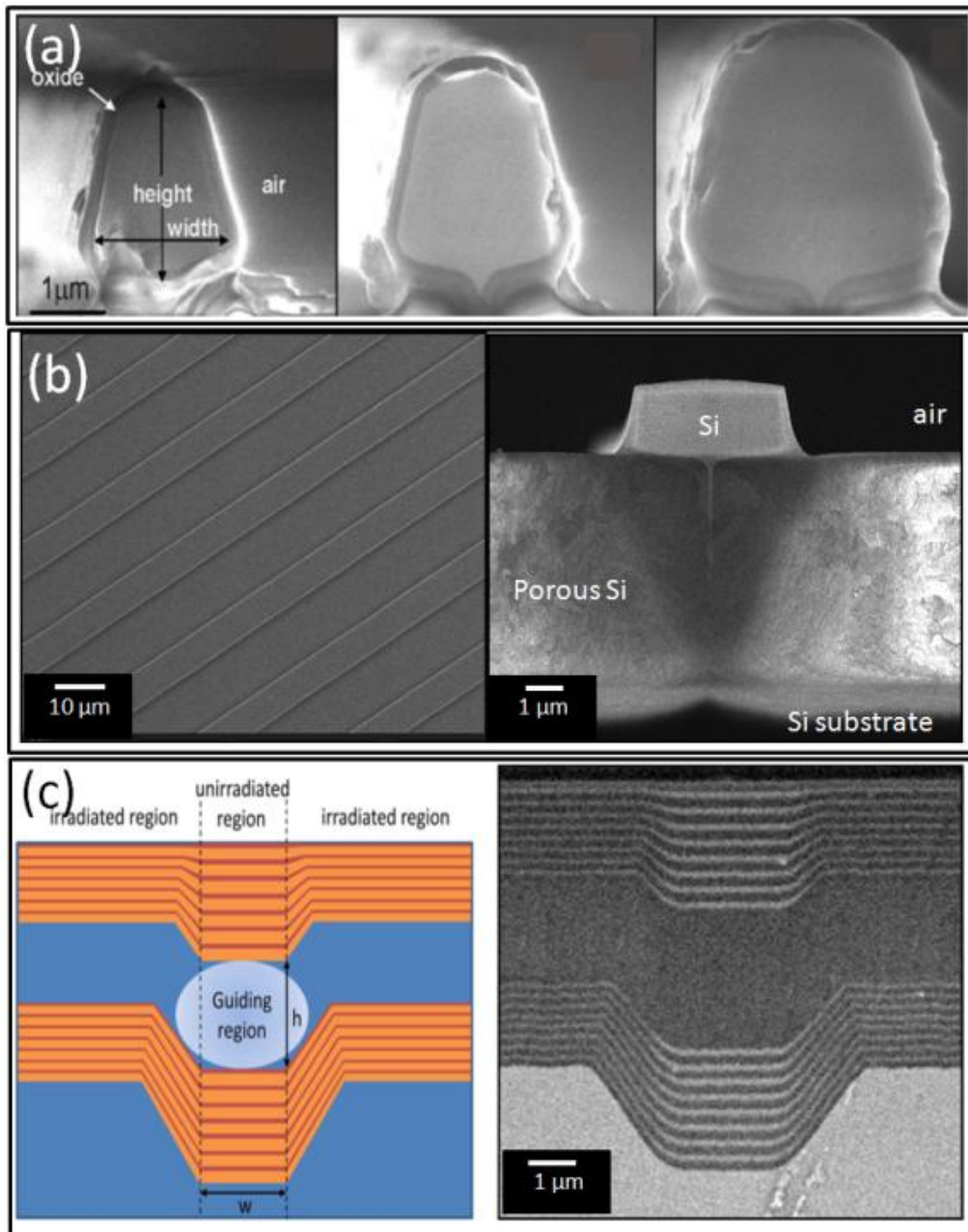


Figure 2-19 : SEM images of SOPS strip waveguides (a) direct-write irradiated with 250 keV protons fluences of 7×10^{13} , 1×10^{14} , $1 \times 10^{15}/\text{cm}^2$, increasing from left to right. (b) plan and cross section views of similar SOPS waveguides fabricated using a large area irradiation fluence of $2 \times 10^{13}/\text{cm}^2$. (c) left: schematic diagram of the fabrication process of Bragg waveguides in silicon and right: cross section SEM image of Bragg cladding waveguide irradiated with a fluence of $2 \times 10^{15}/\text{cm}^2$. From [74-76].

A single-mode Bragg cladding rib waveguide was also demonstrated in 0.02 Ohm.cm silicon [76], which consists of PSi layers with a low refractive index core that is bounded by DBRs comprising eight bilayers of alternating high and low refractive index. Irradiation acts to reduce the thickness of PSi formed, as described in chapter 2.8, creating an optical barrier needed for lateral confinement.

Single mode guiding with losses as low as approximately 1 dB/cm were obtained over a broad range of wavelengths, offering a possible method for monolithic integration of Bragg waveguides in silicon, without multiple processes of depositing alternating materials.

Chapter 3 : Electrochemical Anodization Setup

Different types of electrochemical anodization setups are used according to the desired anodization pattern and area for various applications or different silicon wafer resistivities [44]. Generally different projects involving electrochemical anodization of wafers starts with designing a suitable cell setup, followed by checking the contacts and leakage test. This chapter describes the newly-designed anodization setups which are used in the following chapters for silicon machining work.

The material which is used for designing the cell should be resistant to HF, as HF is a highly corrosive acid and can etch away most of the materials such as glass or metals. All the cells designed and used in this thesis are made out of Teflon which does not react with HF. Being resistant to HF should also be a factor in choosing the O-rings for preventing the leakage from the cell. In this work vinylidene fluoride-hexafluoropropylene (Viton) O-rings are used where required.

The anodization current is transferred to the silicon wafer through an ohmic contact on the back surface. For the open anodization cell design, where the sample is immersed completely in the HF solution, it is important to cover the ohmic contact with a material resistant to HF. Platinum is used as the electrode in all the work done in this thesis because it does not react with HF.

3.1 The immersion cell

The simplest electrochemical cell commonly used for silicon anodization is set up by immersing the sample, which has an ohmic contact on the back side, together with a platinum electrode in a Teflon beaker filled with HF electrolyte of the

desired concentration (Figure 3-1). The platinum electrode is the cathode and the silicon sample itself through its ohmic contact is the anode. Copper wire is used to transfer the current to the ohmic contact at the back of the silicon sample.

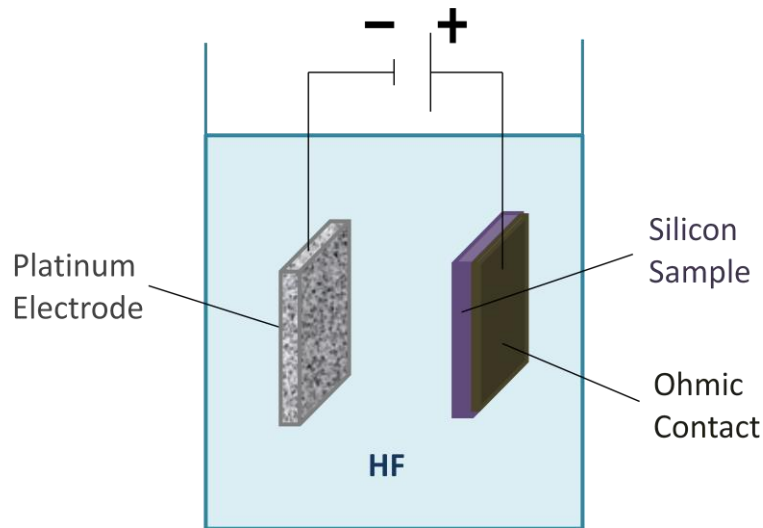


Figure 3-1 : Immersion cell anodization setup

Before the anodization step using such an immersion cell setup, an ohmic contact and a protective layer to HF on the backside of the sample should be prepared. The steps are as follows:

1. Immersing the silicon sample in 2% HF solution. There is a very thin native silicon oxide layer formed on the surfaces of silicon wafers at room temperature. By dipping the sample in a diluted HF solution (usually 2%), the oxide layer can be removed to improve the ohmic contact on the back of the sample (Figure 3-2 (a)).
2. Completely covering the backside of the sample with Gallium-Indium eutectic paint. This is done by using a copper wire as a brush to uniformly coat the backside of the sample with this conductive paint. Gallium-Indium paint has the dual benefit of uniformly distributing the current to the whole area of the sample as well as sticking the copper wire to the silicon (Figure 3-2 (b)).

3. Covering the Gallium-Indium paint and the copper wire with epoxy to prevent their reaction with HF (Figure 3-2 (c)).
4. Covering the edges of the sample with epoxy to force and limit the anodization current to the surface of the sample only (Figure 3-2 (d)).
5. Wait for the epoxy to set. However if the epoxy gets too dry it is very difficult to remove after anodization. Usually the waiting time is about 1 to 2 hours. Also it is important to use less hardener than resin when mixing the epoxy to make it softer, which makes removing the epoxy after anodization easier.

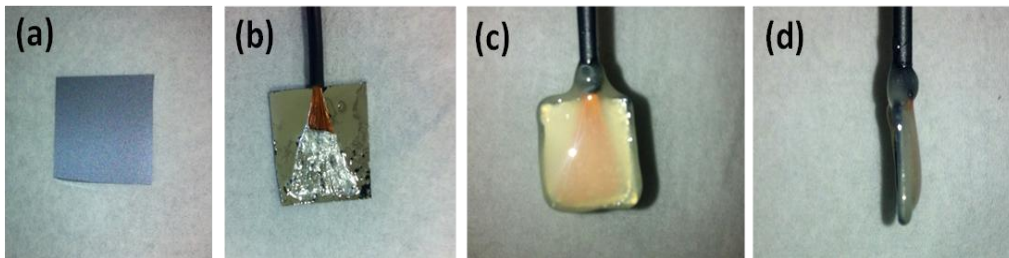


Figure 3-2 : The preparation steps prior to electrochemical anodization: (a) Removing the native oxide of the backside of the wafer by immersing in a diluted HF solution. (b) Covering the entire backside of the wafer with Gallium-Indium eutectic paint and stick a copper wire to it. (c) Coating the back surface with epoxy to protect from HF. (d) Covering all the sides of the wafer with epoxy.

Once the sample is dried and ready for anodization, it is immersed together with the platinum electrode in the Teflon beaker containing HF solution. 12% and 24% concentrations of HF solution are mostly used for various silicon machining works presented in this thesis. For preparing 12% HF, concentrated HF (48%), deionized (DI) water and ethanol is used in a ratio of 1:1:2 respectively. This concentration is mainly used because it can produce a bigger range of porosity [77]. 24% HF can be prepared by mixing concentrated HF (48%) with ethanol in a ratio of 1:1. Using this concentration the porosity is less, so for the applications that the PSi needs to remain on the sample this concentration is mostly used to minimize PSi cracking. The PSi is prone to becoming cracked when it is dried and the water evaporates from it. Preventing the cracking is more difficult for thicker

and higher porosity PSi layers. Generally PSi formed from 0.1-10 Ω .cm silicon wafers tends to crack easier than PSi formed from <0.1 Ω .cm wafers. This is simply because moderate resistivity wafers tends to form microporous silicon which naturally has higher porosity than mesoporous silicon formed by anodization of low resistivity wafers (chapter 2.7). For thin PSi layers, allowing the PSi to be slowly dried in air at room temperature helps to protect the layer from cracking.

After immersing the electrodes inside the HF solution, the electrodes are connected to a power supply. The sample is connected to the positive electrode and the platinum electrode to the negative electrode. The two electrodes are placed parallel and at the same height with a distance of about 1 cm between them. A programmable power supply is used for the experiments done in this thesis. The power supply (instrument model: Keithley 224 Programmable Current Source) is controlled through General Purpose Interface Bus (GPIB) by Labview 7.1 software which can control the anodization time accurately (milliseconds). This setup is particularly very useful when a very shallow anodization depth (small anodization time) or multilayered PSi (changing the current density alternatively at a fast rate) is needed.

Without a bias applied, silicon etching in the HF solution is negligible. The anodization current and time is set according to the experiment. Applying the bias, the anodization process begins as described in chapter 2.7.1. A little bubbling can be observed due to formation of H_2 .

After the anodization is complete, the electrodes are removed from the HF electrolyte and the platinum electrode and the sample are rinsed with both ethanol and DI water.

3.2 The O-ring cell

The immersion cell design described in the section above has the advantage of being prepared in a few minutes by using standard laboratory equipments. However, the anodization region cannot be accurately defined, and also it shows limitations in anodization of high resistivity silicon wafers and silicon-on-insulator (SOI) wafers. In the O-ring cell design the desired active area of the silicon surface is defined by the O-ring to be exposed to the HF solution. In this kind of cell around the O-ring the current density is not normal to the silicon surface and hence the current density is greater in these regions. This can lead to some non-uniformity in the PSi layer thickness [44].

In order to prevent HF leakage using the O-ring cells, the sample is pressed against the O-ring. One should be careful not to break the sample when sealing the cell. Figure 3-3 shows a cross-sectional view of a double-sided O-ring cell made in CIBA. The cell is made out of Teflon and Viton O-rings are used, both resistive to HF. In this kind of setup both surfaces of the wafer are exposed to the HF electrolyte through a circular opening in the cell. Different opening radii of 0.5 cm, 1 cm, and 1.2 cm are made for different experiments. The sample size should be bigger than the cell opening. Both sides of the cell are filled with HF solution and two platinum electrodes are immersed into them which will then be connected to the power supply. For anodizing the surface of the silicon sample the platinum electrode facing the front side of the sample should be the cathode.

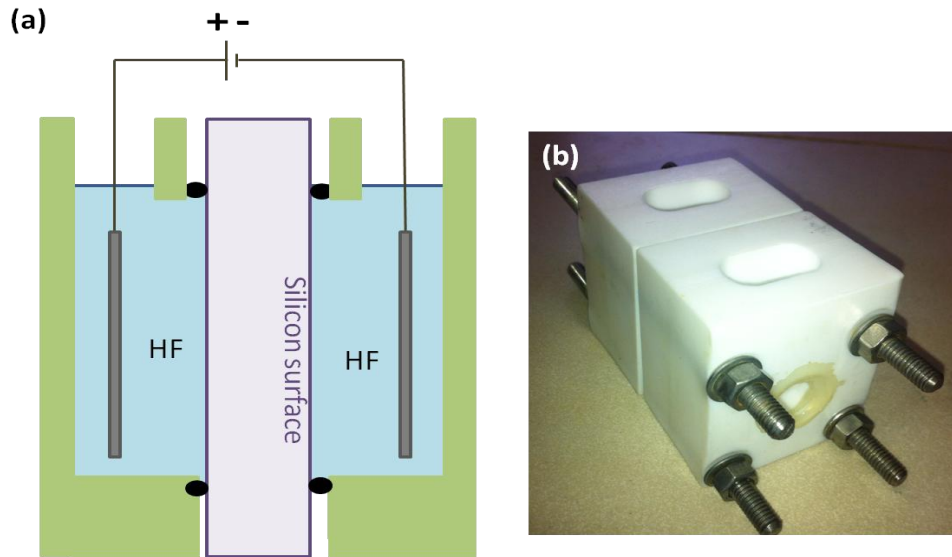


Figure 3-3 : (a) Schematic of cross sectional view of O-ring cell, the silicon wafer is placed between the cell opening and two platinum meshes are used as electrodes. (b) Designed cell.

After the anodization the cell is opened to release the sample. The sample is then carefully rinsed with ethanol and DI water.

3.2.1 Modified O-ring cell

When there is a need to anodize a high resistivity wafer, or a sample having a large area irradiated with a high fluence and hence a greatly increased resistivity, the conventional anodization setups explained in chapter 3.1 and 3.2 have limitations in etching uniformity. One solution is using a direct ohmic contact with a copper slab on the back side of the sample instead of using a setup in which the current flows through the electrolyte into the sample. The direct ohmic contact helps with forcing the current to pass through the sample with a moderate anodization voltage. The design made for this kind of cell is shown Figure 3-4. The backside of the sample can be painted with Ga-In paint prior to placing it inside the cell for improving the direct back contact.

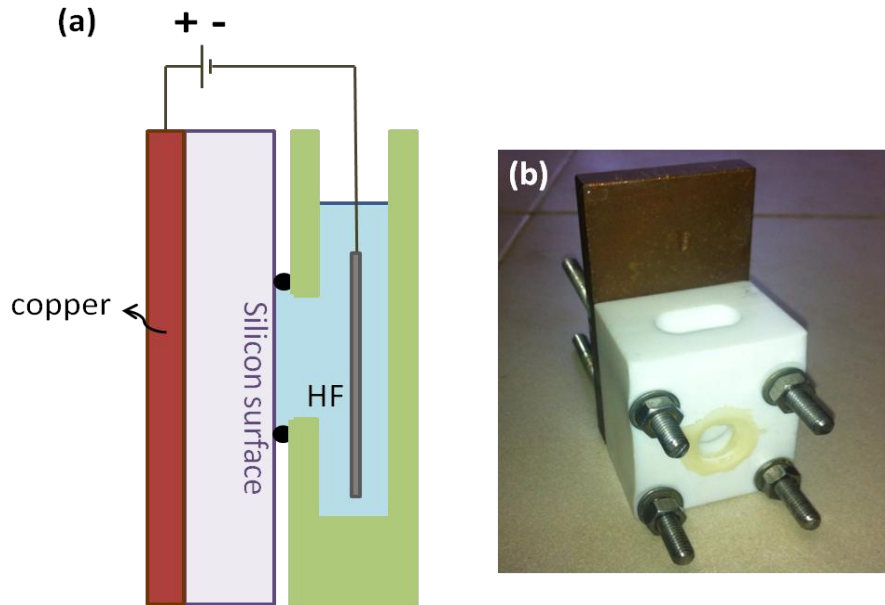


Figure 3-4 : (a) Schematic of a modified cell where a copper slab is used for giving the back contact to the silicon sample. (b) Designed cell.

Although this setup can improve uniformity of the anodization, however if the wafer resistivity or the irradiation fluence over a large area is very high, then even using the above described cell, the sample cannot be uniformly anodized and a deeply etched groove is formed around the edges of the exposed sample surface, with the rest of the sample being left unetched or only very shallowly etched (Figure 3-5 (a) and Figure 3-6). This phenomenon was explained by Astrova in Ref. [78] by preferential redistribution of the electric field at the edges of the wafer as a result of the high resistivity of the wafer. One possible solution as suggested by Astrova [78] is to prepare the setup such that the front exposed surface of the wafer to be anodized is smaller than surface of the back contact area as shown in Figure 3-5 (b). This modifies the distribution of the electric field lines, forcing them back towards the central exposed area which allows the front surface of the samples to be uniformly etched (Figure 3-5 (c)).

In addition, a conductive ring may be deposited or placed around the desired surface area with an additional positive bias applied to further force the

electrical holes towards the center of the sample. An anodization cell made of Teflon was specially designed and made for this purpose. The opening radius of the frontside is 1 cm while the backside is 5 mm.

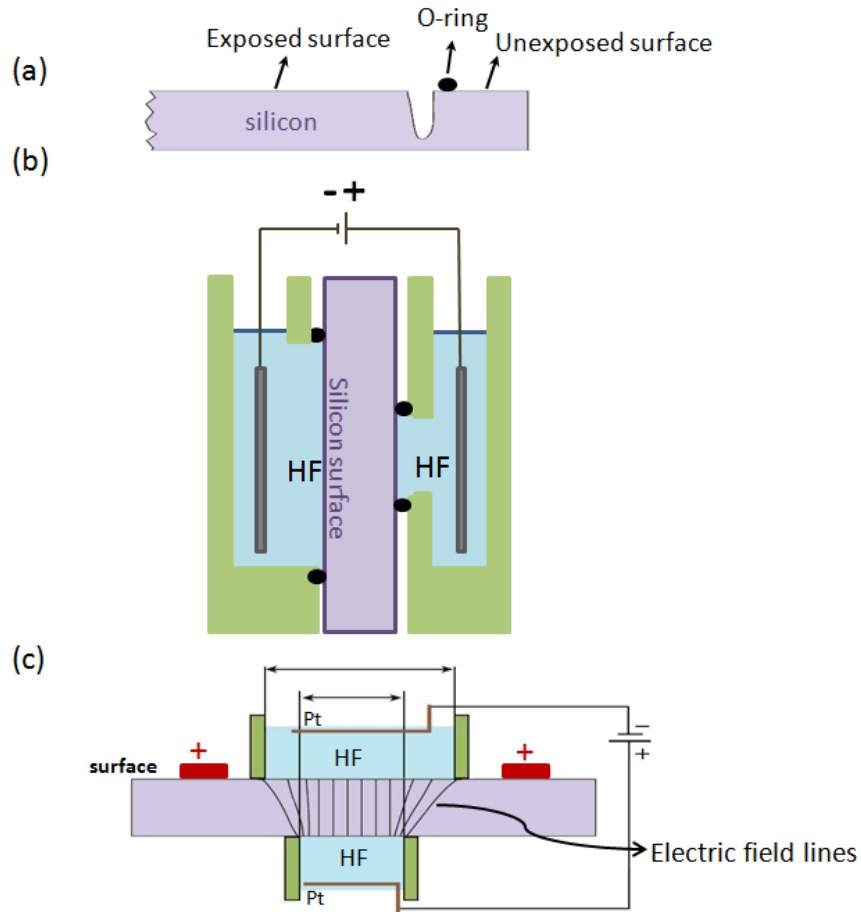


Figure 3-5: (a) Clearly pronounced edge effect in the form of a groove on the periphery of the porous region. Virtually the whole etch current is displaced to the groove region, with little etching of the central part of the sample (b) Schematic cross-sectional view of the cell designed for anodization of p-type silicon where the front opening is larger than the back side opening (c) Schematic of the cell showing the distribution of the electric field lines in the substrate. A metal ring with a positive bias can be placed on the sample surface for further improving the cell.

Using the above cell more resistive wafers can be anodized. For comparison Figure 3-6 shows two $1.5 \times 1.5 \text{ cm}^2$ areas of $0.1\text{-}1.0 \text{ }\Omega\cdot\text{cm}$ wafers irradiated with the same high fluence but anodized with different cells. The whole surface of both wafers was irradiated with a fluence of 5×10^{14} with 1 MeV helium. With the conventional anodization set up shown in Figure 3-3 the surface remains almost unetched, and only a deep groove at the boundary is observed (the left sample in Figure 3-6 (a)). However, by anodizing the sample using this modified

cell and placing a thin aluminium foil ring with a positive bias around the front opening of the cell the sample surface can be etched (the right sample in Figure 3-6 (a)). The profile of this sample after removing the PSi layer with a diluted KOH solution is shown in Figure 3-6 (b).

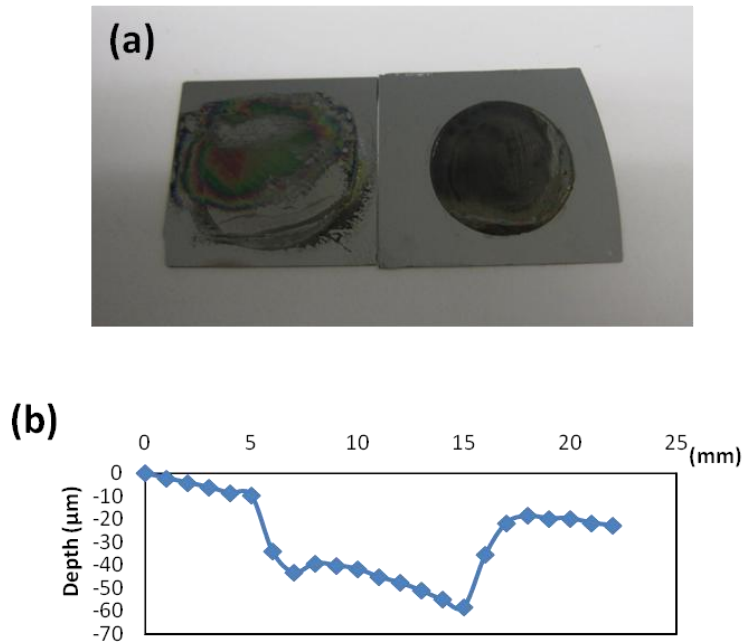


Figure 3-6 : (a) Moderate resistivity wafers irradiated with 1 MeV helium and a fluence of 5×10^{14} after anodization using conventional setup (left) and modified anodization setup (right), with 1 cm^2 opening. (b) Surface profile of the right-hand sample over its diameter after removing the PSi.

A new method for electrochemical anodization of high resistivity silicon wafers is realized by using the modified anodization setup described in Figure 3-5 (b),(c), which was not possible through other conventional anodization setups. This anodization cell is used widely in this thesis whenever the irradiation fluence is high.

3.3 Double sided cell

We have proposed an alternative method to cheaply fabricate patterned SOI wafers from bulk silicon wafers in chapter 9.2. For this purpose a new Teflon cell was designed and made. A schematic of this cell design is shown in Figure 3-7. The cell is designed to cover the irradiated regions during the anodization process. The

cell has a ring-shape front side opening with a radius of 1 cm and width of 1 mm (facing the sample surface) and a small circular backside opening with a radius of 2 mm aligned in the centre of the other side of the cell (facing the back side of the sample). A protective HF resist can also be used for coating the parts of the sample which are later covered with the cell to ensure anodization is taking place only at the desired areas. For this purpose a layer of SX AR-PC 5000/40 (Allresist Company) HF resist spin-coated at 3500 rpm (giving a film thickness of 8 μm) was used. The resist should be baked at 50°C for 25 minutes on a hotplate. As this resist is not photosensitive, it should be patterned through coating and patterning another layer of a photoresist (like AR-P 3250). The HF resist can be developed by X AR 300-74/1 (1:1 diluted with water). The results are shown and discussed later in chapter 9.2.

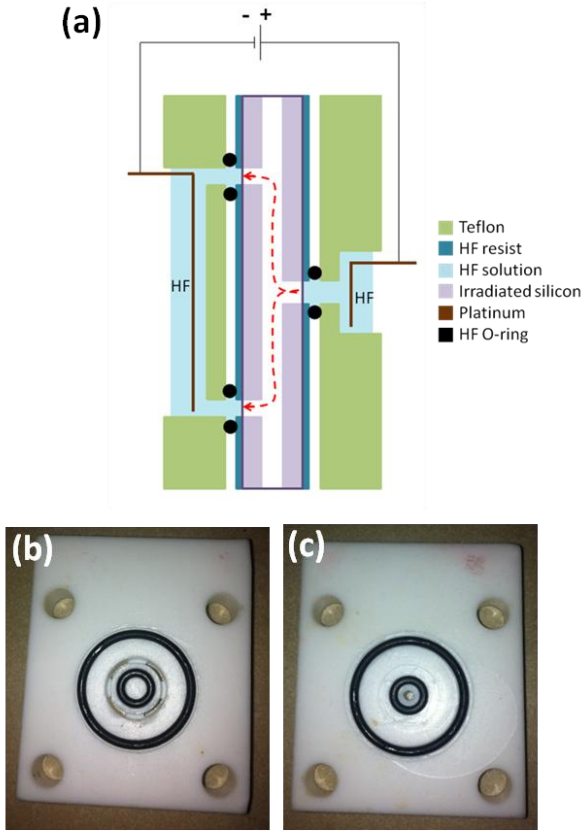


Figure 3-7 : (a) Schematic cross-sectional view of the anodization cell designed for making SOI wafers from bulk silicon wafers. Red arrows show the direction of hole current flow during the anodization. (b),(c) Frontside and backside designed slits respectively, which are added to the anodization cell in Figure 3-3 (b) where the wafer is placed.

Alternatively, with the similar process described above, another anodization cell which can be used for forming SOI out of bulk silicon wafer was designed and made as shown in Figure 3-8. The whole back side of the wafer is irradiated with a high enough fluence to stop the anodization, and the whole front surface except a ring and a small disk in the center should also be irradiated with a similar high fluence. The cell is designed to cover the irradiated parts of the front side of the wafer. It has a ring shape opening with 1 cm radius with the width of 2 mm for being filled with HF. A ring shape platinum electrode is placed inside the HF solution as an anode electrode. The cell also has a circular opening in the center of the ring with a radius of 2 mm. A copper rod can be placed in this opening for giving a direct contact to the sample. Red arrows show the direction of hole current flow during the anodization.

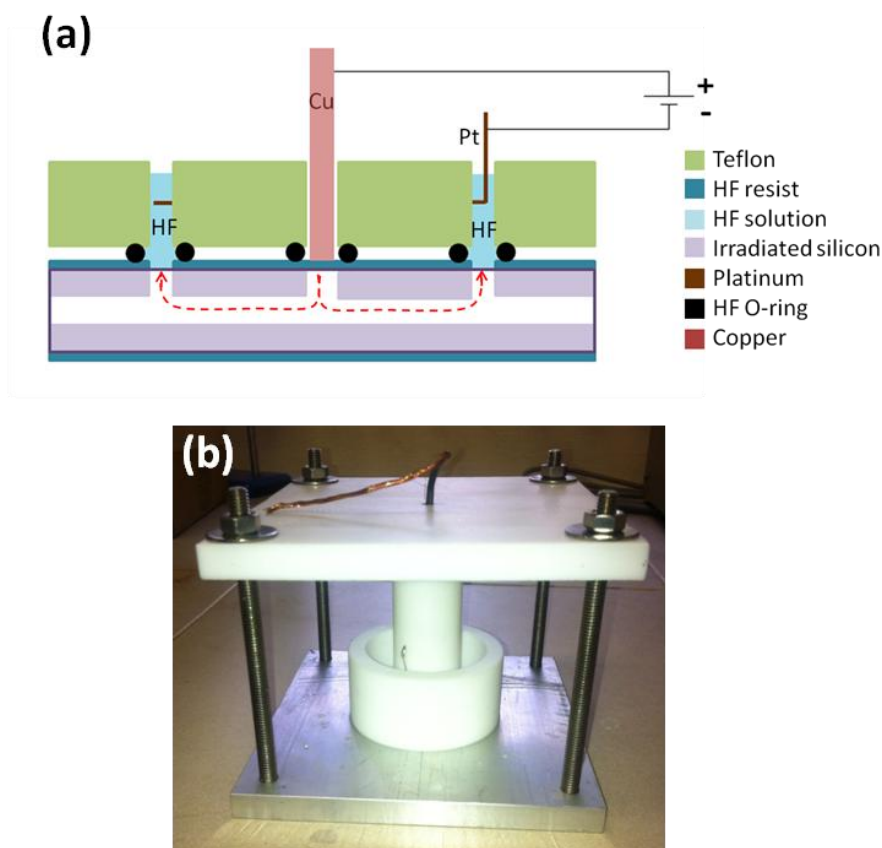


Figure 3-8 : (a) Schematic of cross sectional view of anodization cell with direct contact, specially designed for making SOI. Red arrows show the direction of hole current flow during the anodization. (b) Designed cell.

The advantage of this cell over that described in Figure 3-7 is that there is a direct, low resistance contact using the copper rode, which can be more effective for forcing the current inside the wafer with a moderate voltage.

Chapter 4 : Different Effects of Irradiation Modes on Surface Roughness

Many types of patterned PSi and silicon structures have been machined using ion beam irradiation, such as patterned distributed Bragg Reflectors [60], micro-turbines [79] and waveguides [75]. For some applications such as holographic silicon surfaces, controlling the surface roughness is desired (chapter 2.8.2) [67]. Similarly for many applications such as low loss silicon photonic components, highly reflective surfaces, high quality-factor microcavities, one needs to produce as smooth a surface as possible (chapter 2.8.3 and 2.8.4) [75, 80]. Therefore, it is important to study the underlying causes of surface roughness of silicon surfaces fabricated using our ion irradiation machining technique. Different resistivity of p-type silicon is typically used as the starting material for different applications, e.g. silicon-based photonic devices normally use low-doped material (1-10 $\Omega\cdot\text{cm}$) to minimize scattering losses due to free carrier scattering, whereas higher doped material (0.02 $\Omega\cdot\text{cm}$) is preferred for fabricating surface relief patterns with multi-level step heights, micro-mirrors and holographic surfaces since it is easier to machine a range of differing step heights by controlling the irradiation fluence.

After fabrication, the anodized silicon surface roughness can be reduced by a variety of processes. For instance, applying a large electropolishing pulse after anodization has the dual benefits of smoothing the surface as well as separating the PSi layer from the underlying silicon surface [29]. This may also negate the need to immerse the sample in KOH to remove the PSi [72]. Another procedure is reduction of surface roughness by thermal annealing in air or flowing oxygen [81-82] and subsequent silicon oxide removal by a dilute HF solution.

Very often after fabrication, small particles of silicon or PSi remain on the surface (Figure 4-1(a)). They may be removed by megasonic cleaning (Figure 4-1(b)) [83] or thermal annealing the sample for a short time followed by removing the oxide layer.

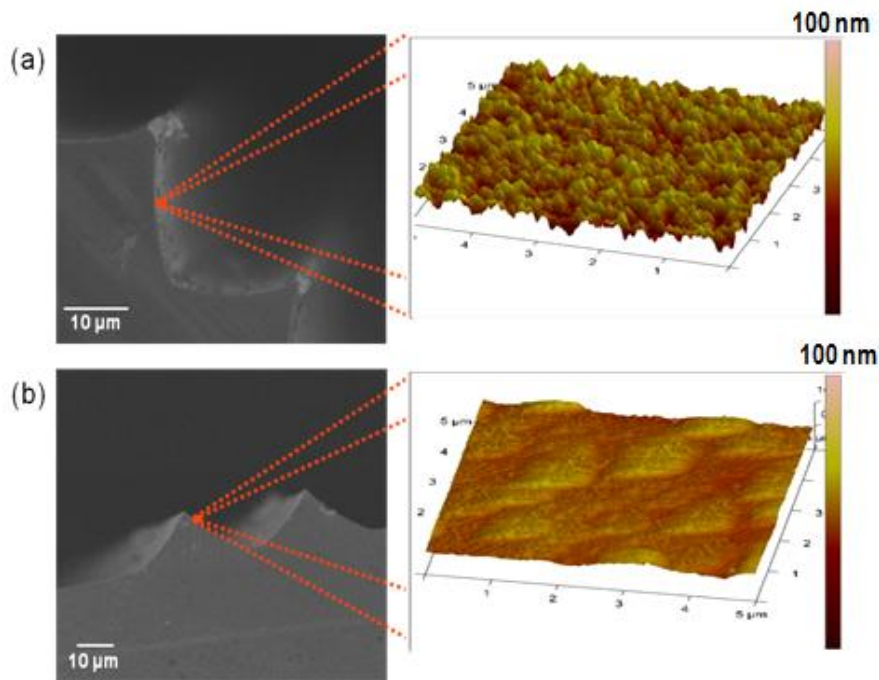


Figure 4-1 : Cross sectional SEM and AFM image of anodized silicon sample (a) before (b) after megasonic cleaning.

However, depending on the application, some of these processes may not be appropriate. For example in the formation of silicon waveguides [75] the PSi needs to remain to form an isolated cladding around the waveguide, so electropolishing is not practical in such cases. Megasonic cleaning cannot be used for cleaning the surfaces of delicate free-standing structures [84]. Thermal annealing of the wafer converts the silicon to oxidized silicon, thus reducing the remaining silicon dimensions, which may not be desired. Such smoothing also causes rounding and losing the sharp edges of silicon structures, which may not be desired. In addition, there is a maximum silicon dioxide layer thickness at which oxidation saturation occurs for each temperature, hence it limits the surface roughness reduction of relieved silicon surfaces and in general surface roughness

cannot be reduced below several nanometers if the initial roughness is high. For example, it was observed that two steps of thermal annealing at 1100°C for 6 hours followed by removing the oxide layer after each step, reduced the silicon surface roughness from 25 nm to 6 nm, and from 3.6 nm to 1.8 nm measured, over an area of $5 \times 5 \mu\text{m}^2$. Therefore, it is important to know how each different resistivity wafer behaves as a function of ion irradiation fluence and how to minimize the initial roughness of the anodized silicon surfaces produced by current densities below the electropolishing threshold.

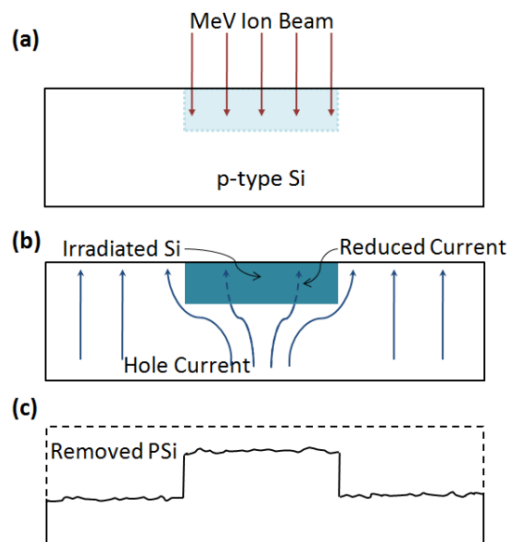


Figure 4-2 : Schematic of the effect of ion irradiation of a well-defined region. (a) ion irradiation, (b) electrochemical anodization, (c) PSi removal.

This chapter describes some important parameters that can influence the roughness of revealed silicon surfaces and compares the effect of focused and large area ion beam irradiation modes on surface roughness of silicon wafers with different resistivities after subsequent electrochemical anodization. Figure 4-2 shows a schematic of the effect of ion irradiation on the subsequent anodization process. After irradiation (Figure 4-2(a)) the increased resistivity of the irradiated region reduces the hole current density flowing through it during subsequent anodization (Figure 4-2(b)), the size of reduction depending on the fluence as described in chapter 2.7. Wafers were anodized in HF electrolyte. The thickness of

the PSi is taken to be the height difference between irradiated regions and unetched regions and was measured using a profilometer after PSi removal. A thinner PSi layer consequently forms at the irradiated area (Figure 4-2(c)) and the roughness of the exposed irradiated and unirradiated silicon surfaces is measured using an atomic force microscope (AFM). In this chapter we compare the roughness produced by focused ion beam irradiation with the roughness produced from a uniform broad area irradiation and characterize the differing behavior in terms of the way in which the focused beam is scanned over the sample surface.

4.1 Roughness of electrochemically anodized silicon surface

The surface roughness of an anodized wafer depends on the wafer doping density. The effect of the doping density on the mechanism and type of PSi formation was described in chapter 2.6.1. There are other factors influencing the surface roughness of the anodized wafers, such as anodized layer thickness and anodization current density. All these factors were studied by Lerondel [85]. The relationship between the roughness of revealed silicon surfaces and the thickness of PSi is shown in Figure 4-3. It was found that moderate resistivity wafers (0.1-10 $\Omega\cdot\text{cm}$) produce anodized surfaces with a high roughness. The roughness increases linearly with PSi layer thickness up to about 1 μm where the roughness reaches a value of 10 to 20 nm. For thicker anodized layers the roughness saturates at 20 to 40 nm. Low resistivity wafers (0.02 $\Omega\cdot\text{cm}$) produce anodized surfaces with a low roughness. The roughness exhibits a much weaker dependence on layer thickness, with values of only a few nanometers obtained for anodized layers thicker than 10 μm . Therefore, for the applications in which the silicon surface roughness is the main concern, low resistivity silicon wafer is more suitable to achieve low roughness after anodization.

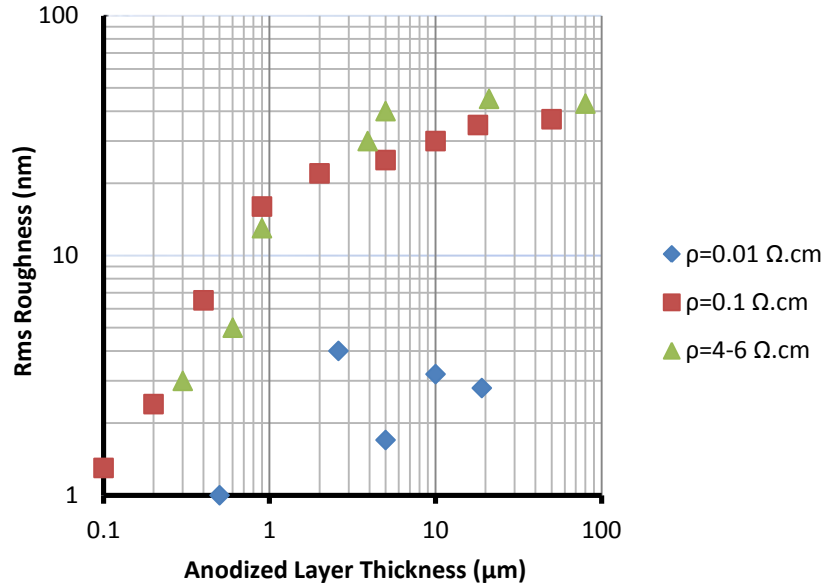


Figure 4-3 : RMS roughness plotted as a function of PSi layer thickness for three resistivities ρ of silicon substrates. From [85].

The relationship between the RMS (Root mean square) roughness and the anodization current density is shown in Figure 4-4 (a). For both cases a linear regime followed by saturation is observed. For a low anodization current density, $j < 50 \text{ mA/cm}^2$, the roughness rapidly increases with decreasing j . At a high current density, $j > 100 \text{ mA/cm}^2$, the roughness is independent of j . The current density saturation occurs before reaching the electropolishing regime (typically about 500 mA/cm^2). Figure 4-4 (b) shows the relationship between anodized PSi layer thickness and roughness for two different current densities of 20 and 100 mA/cm^2 used during the anodization. It can be seen that both the anodization current density and the PSi layer thickness (anodization depth) affect the roughness independently and should be considered when fabricating smooth silicon structures.

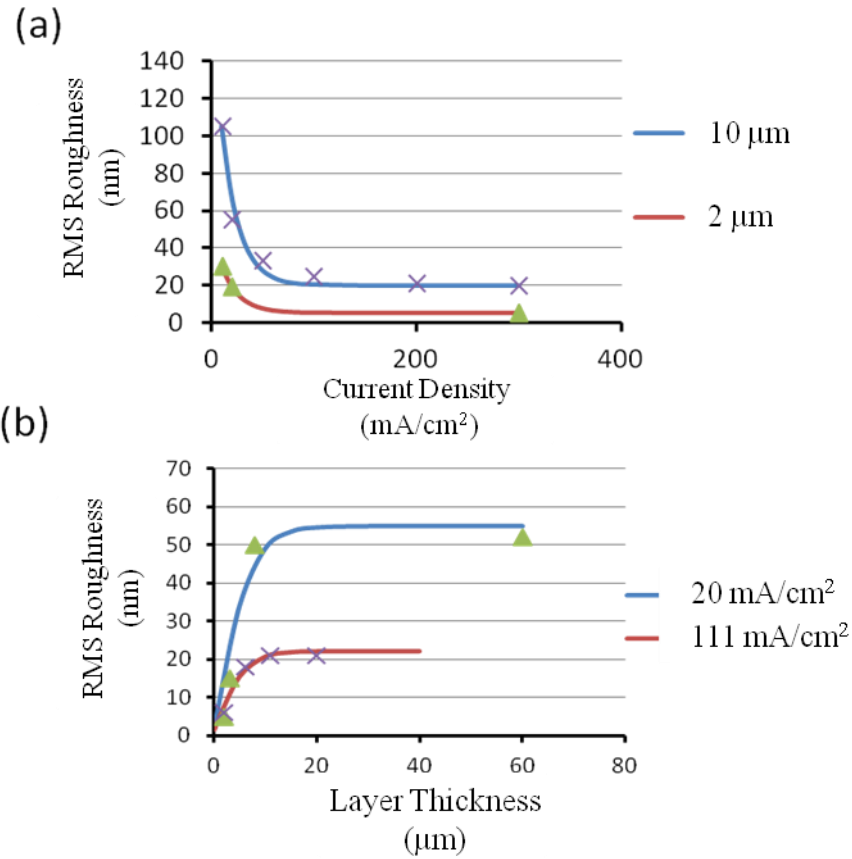


Figure 4-4 : (a) rms roughness as a function of the current density used in PSi formation for 0.01 Ω .cm wafers (25% HF was used). Comparable decreases for the two layer thicknesses are observed. (b) rms roughness as a function of PSi layer thickness anodized at two different current densities. Although saturation is obtained in both cases the limiting value is reduced by a factor of 3 at a high current density. From [85].

4.2 Focused ion beam irradiation roughness studies

PBW is a very flexible technique, enabling high spatial resolution and direct fluences to be used in the same area. Different fluence irradiations are produced by repetitively scanning the focused beam a differing number of frames over each area, chapter 2.5.1. By varying the fluence, the local resistivity may be controllably varied over a given pattern. One of the main limitations of PBW is non-uniform irradiated areas if the beam current fluctuates.

The process of PBW using MeV ion beam irradiation of selected areas differs in several respects from other forms of irradiation using focused beams of charged particles. In focused ion beam irradiation systems using keV ions, or e-beam lithography using keV electrons, the beam current is typically very stable,

and the focused beam may be rapidly scanned over the sample surface using electrostatic scanning. Any small, slow fluctuations in beam current are uniformly distributed over the sample surface so the area is uniformly irradiated. In comparison, focused MeV ion irradiation has two limiting characteristics.

First, fluctuations of the focused beam current arise from the small variations in accelerator terminal voltage, typically some tens of Volts for the highly-stabilized Singletron accelerator [86]. Even though this is typically a factor of ten times more stable than the more commonly used Van de Graaff accelerator, it still results in a minimum level current fluctuations of 2 to 5% with typical frequency components of 50 Hz and 400 Hz [87].

Second, most nuclear microprobes use magnetic scanning to deflect the focused MeV ion beam over the sample surface, since it is difficult to achieve the high field strength needed to scan the beam electrostatically. Magnetic scanning requires the beam to be slowly scanned to avoid hysteresis effects distorting the patterned area. Over the period of a single scanned frame of typically one minute the beam current fluctuates many times, so the fluence is not uniformly distributed. Furthermore, for the commonly-used high excitation quadrupole triplet lens configuration [88] with highly asymmetric demagnifications, the horizontal scan direction requires a higher magnetic field owing to the greater lens demagnification in this direction. Even slower scan speeds in the horizontal direction are consequently required to minimize hysteresis effects in the stronger magnetic field compared with the vertical direction. In most microprobes the beam is therefore raster-scanned rapidly in the vertical direction and slowly scanned across the surface in the horizontal direction.

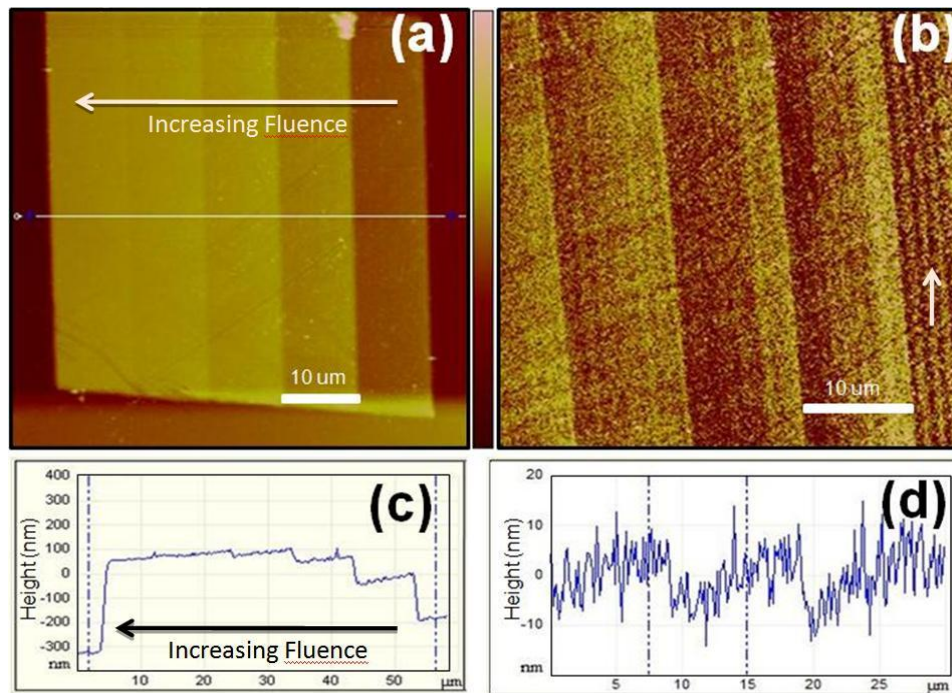


Figure 4-5 : (a),(b) AFM images of two different sets of five adjacent 10 μm wide irradiated bars. The vertical direction of the focused beam during irradiation is shown by the white arrows. (c),(d) AFM line profiles across each pattern in (a) and (b) respectively. The vertical scales are 800 nm and 40 nm respectively.

To study the effect of PBW on the surface roughness of our machined silicon structures, a 2 MeV proton beam of about 1 pA, with a range of 48 μm in silicon, was focused to a beam spot of 200 nm to irradiate small areas of 0.02 Ω cm p-type wafers with different fluences. This wafer resistivity exhibits a slightly reduced PSi formation rate at fluences of about $5 \times 10^{14}/\text{cm}^2$ and this reduces to typically 20% after a fluence of about $5 \times 10^{15}/\text{cm}^2$ (shown later in Figure 4-8(a)), hence this is the fluence range used to observe the effects on surface roughness. After the irradiation, the wafers were electrochemically anodized in an electrolyte containing HF(48%): water: ethanol in the ratio of 1:1:2. The roughness of the irradiated areas was measured and characterized using an AFM and SEM after the removal of PSi.

Figure 4-5(a),(b) shows AFM images of 2 sets of five adjacent 10 μm wide bars irradiated on 2 different wafers. In Figure 4-5(a) the fluence ranges from 1 to $5 \times 10^{15}/\text{cm}^2$ in increments of $1 \times 10^{15}/\text{cm}^2$ from right to left whereas in Figure 4-5(b)

the fluence ranges from 3 to 5×10^{15} in increments of $0.5 \times 10^{15}/\text{cm}^2$ from right to left. The two wafers were then etched at a current density of $95 \text{ mA}/\text{cm}^2$ for 90 and 30 seconds respectively to achieve different etch depths. The PSi was then removed with KOH, producing a thicker surface relief pattern at more highly irradiated areas because the rate of anodization progressively slows down with increasing fluence. In Figure 4-5(b), fluctuations in the beam current during irradiation result in pronounced vertical stripes, clearly observed for the lower fluences at the right side of the image. While well-resolved step heights are observed in Figure 4-5(a) between the larger fluence intervals, the smaller steps in Figure 4-5(b) are almost lost in the large roughness associated with the vertical stripes.

AFM roughness measurements were carried on each sample over $5 \times 5 \mu\text{m}^2$ area. The line profiles across each set of five bars are shown in Figure 4-5 (c),(d), and RMS roughness values are plotted in Figure 4-6(a), labeled as 4-5a and 4-5b respectively. The more deeply-etched sample exhibits higher roughness, consistent with [85] where the roughness of different resistivity wafers versus anodization depth and many other factors was studied. However, for both samples the RMS roughness of the irradiated surfaces initially increases sharply for low fluences, compared with the unirradiated background roughness, then decreases with higher fluences.

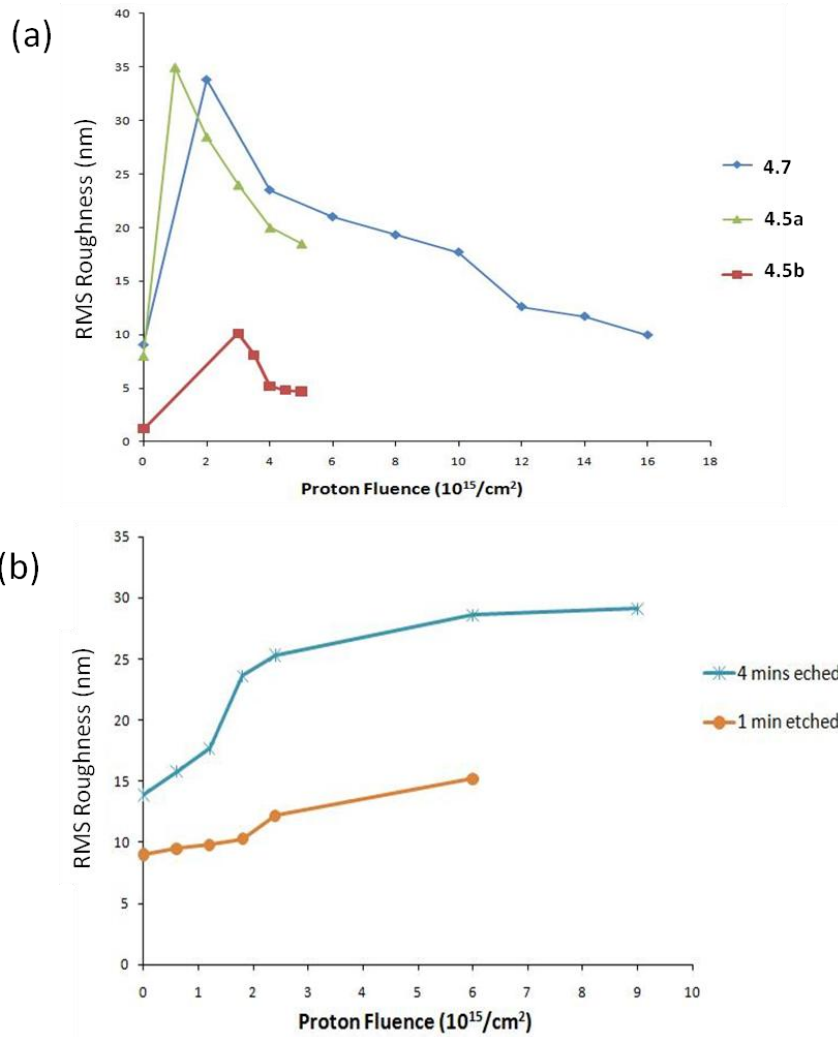


Figure 4-6 : (a) Plot of RMS roughness versus fluence for the three samples shown in Figures 4.5 (a), (b) and 4.7, labeled 4.5a, 4.5b and 4.7 respectively. The AFM rms roughness values are extracted from $5 \times 5 \mu\text{m}^2$ areas. (b) Plot of the rms roughness vs fluence for two samples irradiated using uniform broad beam ion irradiation. Zero on horizontal axis means the rms roughness measured from the unirradiated background.

In Figure 4-7(a),(b) SEM images of a different irradiated pattern are shown. Here the sample was anodized at $12 \text{ mA}/\text{cm}^2$ for 4 minutes and the PSi subsequently removed, producing a checkerboard silicon surface relief pattern. The higher roughness of all the irradiated surfaces compared with the unirradiated region is obvious, in spite of the greater etched depth of the unirradiated regions. An AFM image and linescan across this structure is shown in Figure 4-7(c),(d) and roughness measurements recorded from different regions with different fluences are plotted in Figure 4-6(a), labeled as “4.7”. Again a rapid increase in roughness for low fluence irradiation is observed, then a decrease at higher fluences.

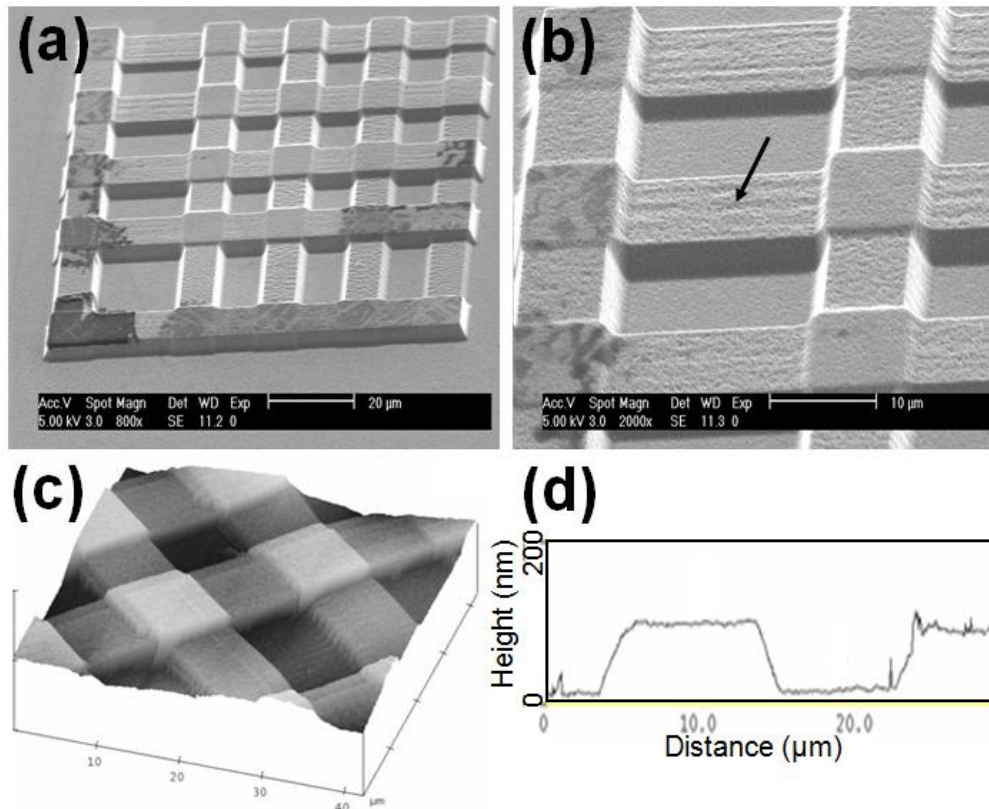


Figure 4-7 : (a),(b) SEM images of an irradiated pattern with five vertical bars with fluences of 2, 4, 6, 8, and 10×10^{15} protons/cm² and overlapped with another five similarly irradiated horizontal bars. The horizontal and vertical bars are each $10 \mu\text{m} \times 100 \mu\text{m}$ in dimensions. Each bar is spaced at $10 \mu\text{m}$ from each other except for the two bars with the highest fluence which were spaced at $20 \mu\text{m}$ for identification purpose. The vertical direction of the focused beam during irradiation is shown by the black arrow. (c), (d) AFM image and linescan across this structure.

For comparison, Figure 4-6(b) shows roughness measurements for the same wafer resistivity irradiated using a broad beam MeV ion irradiation facility [40] where the fluence is very uniformly distributed across the wafer surface. Each measurement corresponds to one wafer irradiated with a certain fluence in a small area defined by a surface photoresist pattern, then anodized under similar conditions for 1 minute or 4 minutes. Here we are not concerned with comparing the absolute magnitude of roughness, which depends on many other factors related to anodization, only the trend with increasing fluence in different modes of irradiation. In Figure 4-6(b) the RMS surface roughness gradually increases with fluence, as expected where the dominant mechanism determining the roughness is the reduced anodization current resulting from increased local resistivity [85].

4.2.1 Factors limiting roughness for focused beam irradiation

For all samples irradiated with a focused beam the roughness first increases sharply after a low fluence irradiation and then decreases at higher fluences, in contrast with the behavior observed for broad beam irradiation. This is important as it imposes a limitation on the ability to fabricate smooth surfaces using focused beam irradiation. Here we discuss the underlying cause of this behavior and how it may be reduced if not completely eliminated. We attribute the roughness behavior of the samples irradiated by a focused beam to two factors related to the small fluctuations of the focused beam current during irradiation and the way in which the focused beam is scanned over surface.

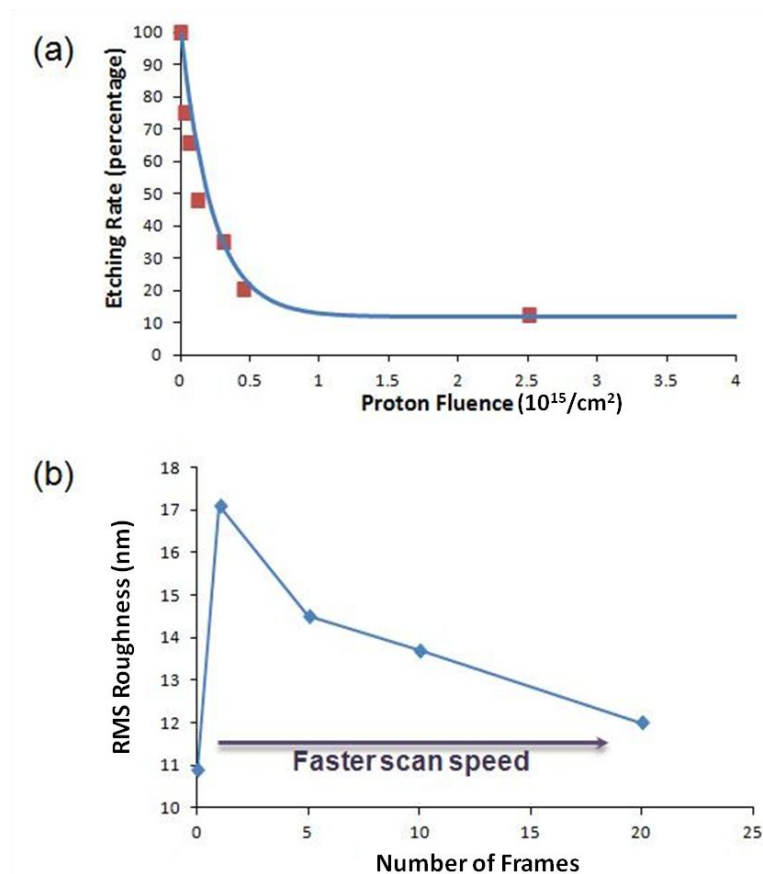


Figure 4-8 : (a) Reduced PSi formation rate versus fluence. (b) Measured RMS roughness of an irradiated area versus number of frames used to achieve the same fluence in each case. Zero on horizontal axis means the RMS roughness was measured from the unirradiated background.

One limiting factor is demonstrated in Figure 4-8(a), which shows the PSi formation rate versus fluence, obtained by taking the ratio between the PSi

formation rate at an irradiated region compared to that at the unirradiated background. The formation rate changes rapidly at low fluences, so the anodization rate at each location, and hence the roughness, is very sensitive to any fluctuations in the low fluence range. The formation rate reduces at higher fluence so the same level of fluctuations in the beam current has a reduced effect on the anodization rate, resulting in a surface with lower roughness. This effect is visible in Figure 4-7(b), where stripes along the vertical direction are detected as thickness variations along the edges of the horizontally-running bars, caused by the fluctuating beam current during irradiation. These are clearly visible at the low fluence irradiated areas but are not detected when these areas are crossed by orthogonal bars where higher fluence results in smaller fluctuations of the anodization rate.

The second limiting factor leading to the greatly increased surface roughness caused by these vertical stripes observed in the Figure 4-5 and Figure 4-7 is the local variations in fluence resulting from the slow scan speed across the horizontal direction. To indicate the importance of making the scan speed as fast as possible relative to the beam current fluctuations, four areas, each of $50\mu\text{m}\times 50\mu\text{m}$, were irradiated with the same fluence of $1\times 10^{15}/\text{cm}^2$ and the same beam current, but with differing scan speeds, hence different numbers of frames. No account of hysteresis effects produced by the more rapid beam scanning is taken here. The sample was then anodized at $40\text{ mA}/\text{cm}^2$ for 200 seconds, the PSi was removed and the roughness measured with AFM. The results are plotted in Figure 4-8(b). The surface roughness of the irradiated areas clearly reduces for faster scan speeds, i.e. increasing number of frames, owing to better averaging out of the beam current fluctuations.

4.2.2 Removal of large-scale variations in anodization rate

A non-uniform etching rate may occur over lateral scales of tens or hundreds of microns due to the influence of the irradiated areas. While this is not a strong influence on the roughness since this effect occurs over larger lateral scales, it is nevertheless a problem for our process of machining a range of different surface heights using different fluences. Such non-uniform rate of anodization is present in the structures shown Figure 4-5 where the surface of each irradiated bar is sloping. A related problem was described in Ref. [44], arising where a surface mask was used to define certain areas for anodization. A simple explanation for this effect is that the anodization current which is prevented from reaching the surface at the irradiated regions is deflected to a region where it can reach the surface. This produces a current gradient across the irradiated regions. Figure 4-5(d) shows an extreme version of this effect in which the small step heights which should occur between the adjacent different fluences are masked by the slope produced by the deflected hole current. A solution to this problem is shown in the irradiated pattern in Figure 4-7 where there are gaps between each irradiated region. The anodization current which is deflected away from the irradiated regions flows to a nearby unirradiated surface, so is not laterally deflected across a large distance nor influenced by other irradiated areas. This results in flat irradiated surfaces as can be seen in Figure 4-7(d), demonstrating that flat surfaces may be achieved by suitably designed patterns.

4.3 Large area irradiation roughness studies

Previous sections describe the surface roughness resulting after utilizing PBW as a means of patterning and machining silicon surfaces using focused high energy protons and helium. For comparison, some preliminary surface roughness studies on 0.02 Ω -cm silicon wafer of large area irradiation are also included (Figure 4-6

(b)). As previously described, PBW uses a scanned, focused beam and large area irradiation uses a large beam current incident on the wafer through a thick, patterned photoresist on the surface. Although our large area ion irradiation facility is ideal for rapid, uniform irradiation of areas up to $3 \times 3 \text{ cm}^2$ with high fluence uniformity, there is however, still an important role for PBW where it is easier to encompass a range of different fluences to produce more complex, multilevel structures. Moreover, no surface mask is required and better spatial resolution of irradiation may be achieved. On the other hand, the large area method results in significantly smoother surfaces at the irradiated regions because of the high lateral uniformity of irradiation compared with direct writing where variations in the focused beam current can strongly increase the surface roughness by causing non-uniformities of the irradiation.

This section describes more detailed studies on the effects of ion irradiation on the anodized surface roughness of three p-type wafer resistivities of $0.02 \text{ } \Omega \cdot \text{cm}$, $0.5 \text{ } \Omega \cdot \text{cm}$ and $5 \text{ } \Omega \cdot \text{cm}$. The wafers are irradiated with different ion fluence depending on the desired reduction in PSi formation rate during subsequent anodization. Wafers were anodized in an electrolyte containing HF (48%):water:ethanol in the ratio of 1:1:2 for 130, 180 and 180 seconds respectively. After removing the PSi layer with diluted KOH solution, the roughness of the exposed irradiated and unirradiated silicon surfaces is measured using an AFM.

The aim of this study is to determine whether the deeply anodized, unirradiated surface, or the irradiated surface which was anodized with a lower current density is rougher. Figure 4-9 shows the measured RMS surface roughness and anodized layer thickness of the irradiated areas of $1 \times 1 \text{ mm}^2$ as a function of 1

MeV helium ion (range 3.5 μm in silicon) fluence for the three wafer resistivities. Ion irradiation slows down the rate of anodization in each case, shown in Figure 4-9(b). However, Figure 4-9(a) exhibits a more subtle dependence of the resultant surface roughness of the irradiated areas on the fluence. For the moderate resistivity wafers, the roughness decreases with fluence, consistent with the anodized layer thickness being the dominant factor [85]. However, for the low resistivity wafer, the roughness increases with fluence, so even though the anodized layer is thinner at the irradiated regions it has a rougher surface compared with the thicker, unirradiated background. At high fluences the roughness drops sharply simply because the anodization rate is reduced to almost zero.

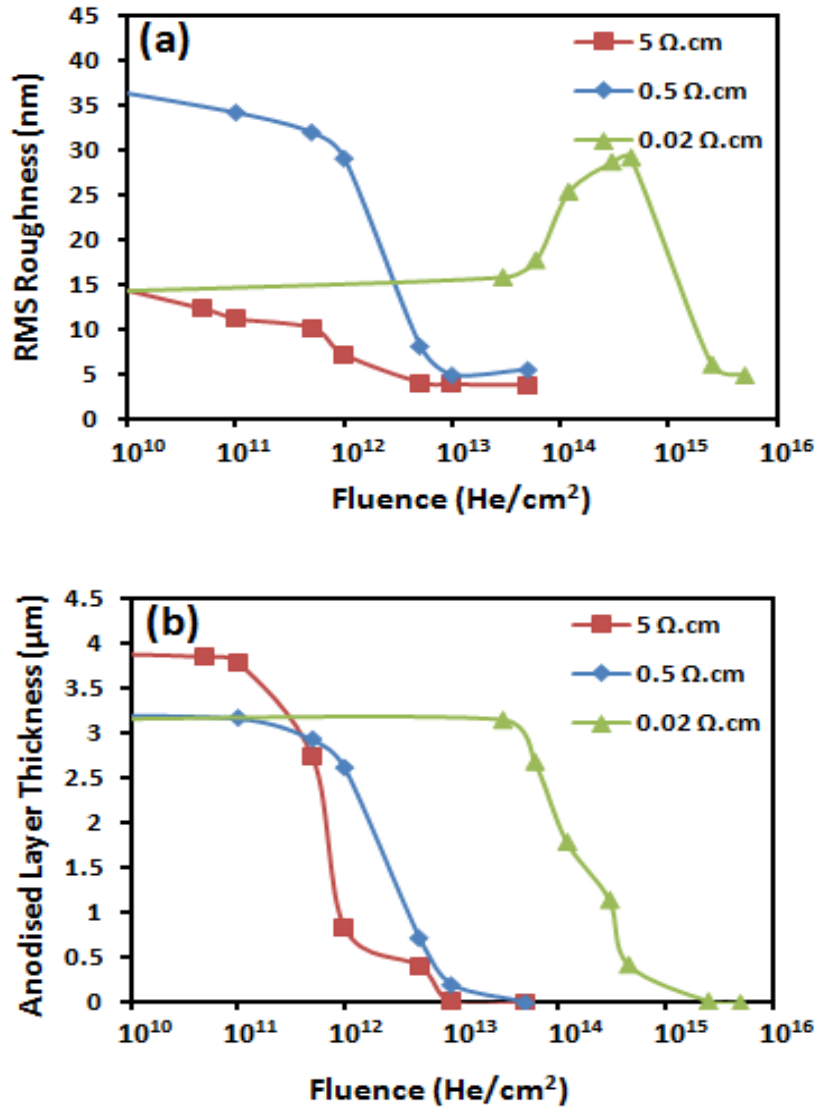


Figure 4-9 : RMS surface roughness versus helium ion fluence for three wafer resistivities, anodized using a current density of 50 mA/cm². (b). Anodized depth versus helium ion fluence for three wafer resistivities.

Although rather counter-intuitive, the observation of increasing roughness with fluence for the low resistivity wafer can be explained by considering the change in resistivity within the irradiated regions due to increasing ion fluence, shown in Figure 4-10. The defect distribution produced by 2 MeV helium ions is calculated using the code SRIM [23], and the effect of each defect on the reduced carrier density as described in Ref. [29]. Three zones of resistivity of p-type silicon are indicated, whereby mesoporous, microporous or macroporous silicon tends to form during anodization, see chapter 2.6 [44]. The horizontally-running

arrows show the range of fluences over which variations in roughness and anodization rate are observed in Figure 4-9. Irradiation of the moderate resistivity wafers (0.5 Ω .cm and 5 Ω .cm) results in the increased resistivity of the irradiated regions still lying within the range for which microporous silicon tends to be produced. However, irradiation of the low resistivity (0.02 Ω .cm) wafer results in the resistivity increasing from the regime where mesoporous silicon tends to form into the more resistive region in which microporous silicon tends to form, with its associated high roughness. Hence, for low wafer resistivities the increased resistivity of the irradiated regions is the dominant factor determining the surface roughness, rather than the anodized layer thickness.

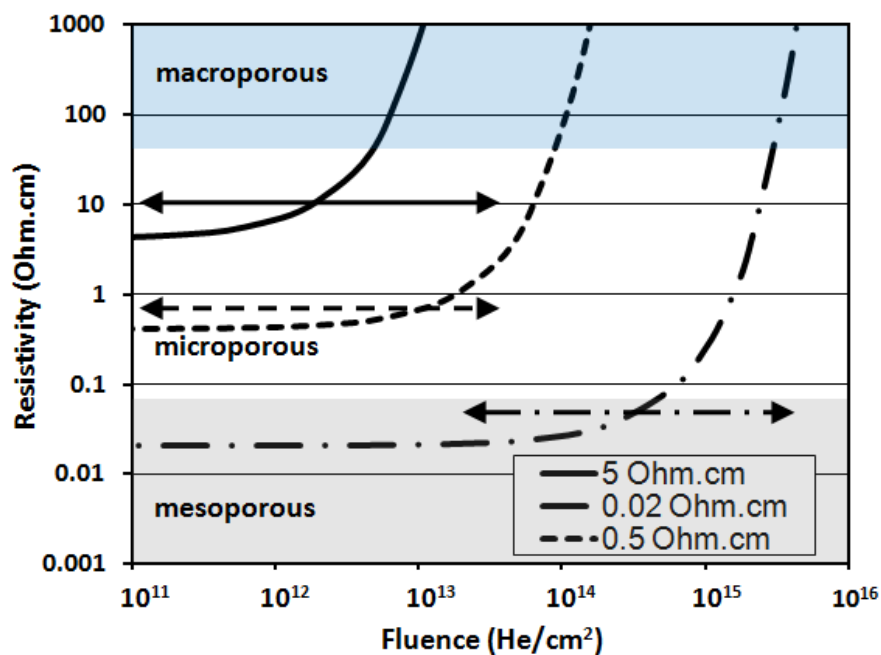


Figure 4-10 : Calculated change in resistivity versus MeV helium ion fluence for wafer resistivities of 0.02 Ω .cm, 0.5 Ω .cm and 5 Ω .cm.

To confirm this hypothesis for the increased resistivity of low resistivity wafers strongly modifying their anodization behaviour and properties of the resultant P*Si*, Figure 4-11 shows previously published data [89] for the variation on photoluminescence (PL) intensity for the 0.02 Ω .cm wafer as a function of helium ions fluence. For this purpose, the P*Si* removal stage is left out. A strong

increase in PL intensity is observed at fluences of 10^{13} to $10^{15}/\text{cm}^2$, similar to the range of fluences over which the surface roughness increases. This is compatible with our hypothesis since mesoporous silicon produced during anodization of low resistivity wafers does not produce intense PL owing to a low density of nanometer-size silicon crystallites which emit PL by quantum confinement. In comparison, intense PL is produced by microporous silicon which has a high density of nanometer size silicon crystallites, so as the resistivity of the irradiated areas rises, so does the PL emission as more microporous silicon is formed, even though the anodized layer becomes thinner.

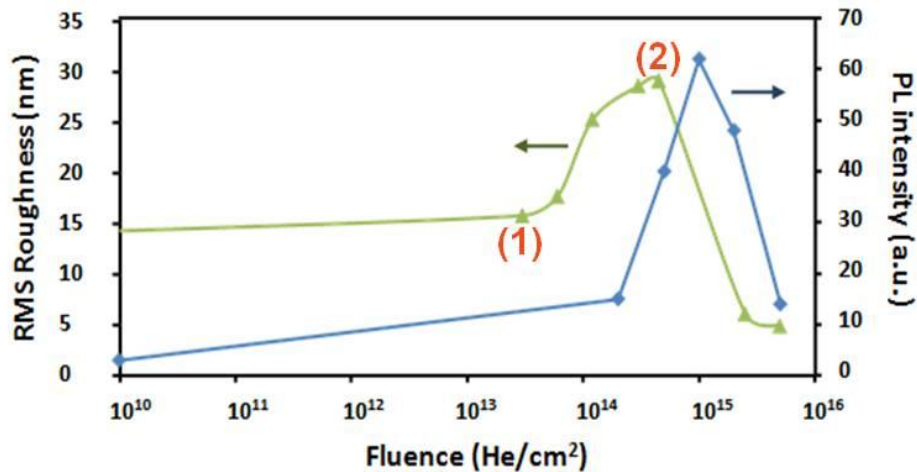


Figure 4-11 : Variation of PL intensity versus helium ion fluence for 0.02 $\Omega\cdot\text{cm}$ wafer resistivity, data reproduced from Ref. [89]. Roughness data for the same material from Figure 4-9 (a) is overlaid for comparison.

Figure 4-12 shows AFM images of $5\times 5 \mu\text{m}^2$ areas of silicon surfaces for two different points of the roughness plot for the 0.02 $\Omega\cdot\text{cm}$ wafer labeled as (1) and (2) in Figure 4-11. It can be observed that the profile of the silicon surface beneath the different types of PSi is different, which gives rise to the wide range of silicon surface roughnesses beneath the PSi layer.

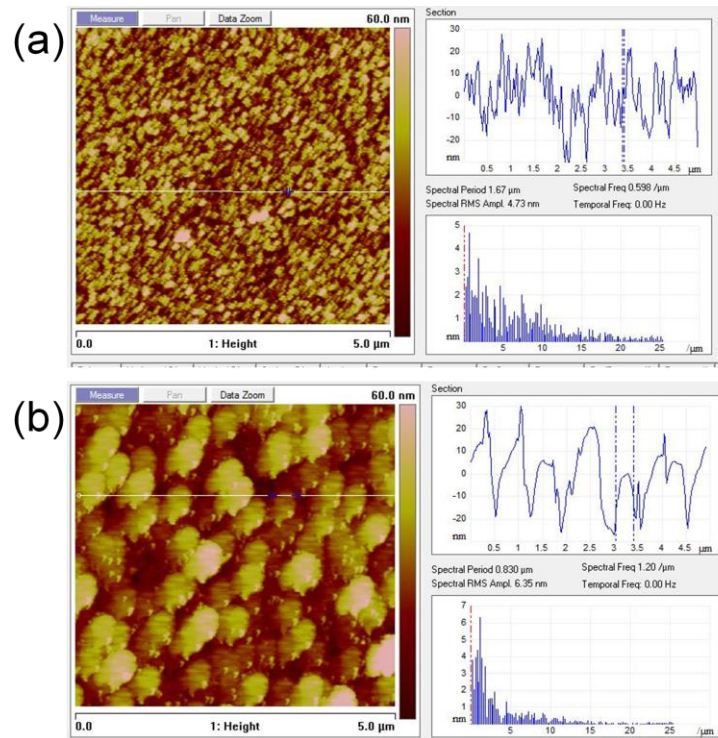


Figure 4-12 : AFM image and line profile of silicon surface relief pattern (a) from point (1) of roughness plot of Figure 4-11 which is irradiated with relatively low ion fluence and tends to form mesoporous silicon and (b) from point (2) of Figure 4-11 which is irradiated with relatively high ion fluence and tend to form microporous silicon.

4.4 Summary

In this chapter, the effects of focused ion beam irradiation on the surface roughness of electrochemically anodized silicon were studied and compared with uniform large area irradiation. The main factor responsible for the large roughness associated with focused beam irradiation is the slow speed of magnetic scanning. With a focused beam the surface roughness is large at low fluences because this regime is fundamentally more sensitive to any fluctuations in fluence and also because it is difficult to uniformly irradiate a given area with low fluences and a slow scanning speed. At higher fluences the roughness decreases because irradiation becomes more uniform and also because the sensitivity to non-uniformities is reduced. A faster beam scanning speed averages out any non-uniformities in the irradiated fluence, resulting in lower roughness.

Larger scale effects of non-uniform anodization were observed across patterned areas owing to lateral deflection of the hole current away from the irradiated regions. It was shown how this may be prevented by incorporating gaps in the irradiated pattern through which the displaced hole current may reach the surface.

These roughness studies are important in understanding the basic mechanism and effects of ion irradiation of p-type wafers and they define the different behaviour of surface roughness and PL intensity which can occur. It was demonstrated that modified resistivity is an important aspect in determining the properties of the resultant anodized PSi and underlying silicon surface, which is important to our understanding of the silicon micromachining process used in the following chapters of this thesis.

Chapter 5 : Diffusion Funnelling and Core Formation in Silicon

One of the main focuses of this thesis is developing a form of ion irradiation coupled with electrochemical anodization to produce true 3D silicon structures at the micro- and nanometer scale. An important fundamental aspect of this work is to study and model the effects of patterned ion irradiation on the motion of current flowing through irradiated wafers, particularly those aspects which result in the formation of an end-of-range core.

This chapter briefly describes a previously unknown phenomena in which low fluence ion irradiation can induce a diffusion funnelling mechanism, leading to a highly concentrated current density at the irradiated region which can dominate the total current flowing under certain conditions. At higher fluences a solid silicon core starts to form at the ion end-of-range and by increasing the fluence these cores expand and extend towards the surface, following the higher defect distribution. This fundamental study is useful in understanding the mechanism of formation of 3D silicon structures which will be described in the next chapter.

Furthermore, a wide range of ion beams of different energies and fluences are used across many fields of semiconductor materials science, engineering and processing, including fabrication, analysis, implantation and modification. In most of these processes, the residual defects introduced by ions are unwanted, though are essential for some sputtering processes. In addition to demonstrating a new current transport process during electrochemical anodization, the study in this

chapter is important in showing a new mechanism for current flow in any ion irradiated semiconductor where any residual defect-induced doping gradient may introduce an increased diffusion current which can be sufficiently concentrated by the funnelling action to dominate the total current flow.

5.1 Defect enhanced funneling of diffusion current in silicon

During electrochemical anodization of silicon in a dilute HF electrolyte, a drift current induced by an external bias results in PSi formation [44, 49]. The defect density in silicon due to ion irradiation depends on many factors; typical defects produced are divacancies and other vacancy or impurity-related centres [37, 50, 90-91]. High fluence irradiation in p-type silicon reduces the effective acceptor concentration to zero [92], resulting in reduced current flowing through these regions during subsequent electrochemical anodization by partially or fully depleting them, slowing down or completely stopping the formation of PSi (described in chapter 2.7).

In this thesis a form of defect engineering in p-type silicon is described and used, which utilizes ion induced vacancies to form an acceptor doping gradient around the irradiated region [93-95]. During subsequent electrochemical anodization the doping gradient results in a portion of the hole current diffusing towards the region of the minimum doping density, which may be at the surface or within the bulk of the wafer, depending on the energy of the incident ions. The following section shows that funnelling of the diffusion component produces a large, localized hole current density which can dominate the total current flow and thus the anodization behaviour at low fluences.

5.1.1 Experimental results of current flow around irradiated areas

Here we consider an unusual irradiation regime in which ion scattering results in the lateral extent of the defect distribution across the end-of-range region being larger than the irradiated line width on the wafer surface. Thus, at a narrow irradiated region, *fluence* is not the most useful measure of the effect of a given number of ions on the resultant anodization behaviour. Here, we define a more useful parameter for this work, *line fluence*, which is used in this thesis for cases of narrow irradiated regions. The *line fluence* Ψ is given by the number of ions used for irradiating a line of zero width per centimetre of line length. This definition is independent of the irradiated line width on the surface of the wafer. Here we mainly consider p-type silicon of $0.4 \Omega\text{-cm}$ ($N_A = 4.8 \cdot 10^{16} \text{ cm}^{-3}$), typical of that used in the 3D micromachining work in the next chapter but also give an example of diffusion current funnelling in a lower wafer resistivity of $\rho = 0.02 \Omega\text{-cm}$ to show that this mechanism occurs in a wide range of wafers.

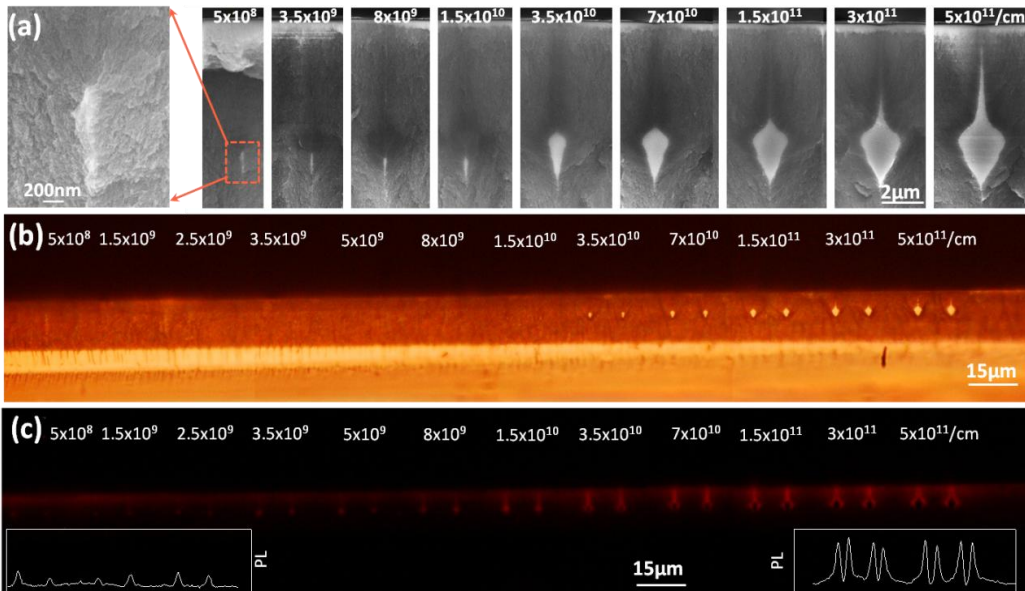


Figure 5-1 : (a) Cross-section SEM showing lines irradiated with 500 keV protons with different line fluence in $0.4 \Omega\text{-cm}$ p-type silicon, which was subsequently anodized to a depth of $10 \mu\text{m}$ at $40\text{mA}/\text{cm}^2$ and then cleaved perpendicular to the lines. A higher magnification of the lowest Ψ is shown at the left. (b),(c) Optical and photoluminescence images of the same array of lines. The insets in (c) show the PL intensity across the lowest and highest Ψ cores. PL collected with a Nikon Eclipse microscope with excitation wavelength of 330-380nm, for an exposure time of 50 ms.

Figure 5-1 shows the effect of different Ψ of 500 keV protons focused to 200 nm. This proton energy is well above the Bragg peak of the nuclear energy loss, so the maximum defect density occurs towards the end-of-range, typically several microns below the surface. The effect of irradiation along the full ion trajectory is seen in Figure 5-1 (a). At $\Psi = 3.5 \times 10^{10}/\text{cm}$ the onset of formation of a solid silicon core at the end-of range depth is observed; this effect in different resistivity wafers has been used in a variety of applications in silicon photonics [29, 73-74, 84] and it will be used in 3D fabrication described in the following chapters. At higher Ψ the core expands and extends towards the surface, following the higher defect distribution. A dark, faint region is observed surrounding and above these cores, interpreted as higher porosity PSi produced by the increased current density due to the current deflected around the cores [29]. Higher porosity silicon emits fewer secondary electrons than the surrounding lower porosity silicon as it is more insulating, as a result appears dark in a SEM image. For $\Psi < 3 \times 10^{10}/\text{cm}$ the core size reduces to a narrow vertical line, above which is another faint, dark region (Figure 5-1 (a)) which is similarly interpreted as higher porosity PSi.

This behaviour is observed down to $\Psi = 5 \times 10^8/\text{cm}$, i.e. two orders of magnitude less than the minimum Ψ required to form a core. The same silicon cores are clearly seen in Figure 5-1 (b) and enhanced photoluminescence is observed in Figure 5-1 (c) from all dark, faint regions in Figure 5-1 (a), surrounding and above the end-of-range cores for high Ψ and from the end-of-range regions at low Ψ . Enhanced photoluminescence is consistent with these regions having a higher porosity [44] and its observation from low Ψ end-of-range regions is consistent with a component of the anodization current being funnelled into regions of high defect density.

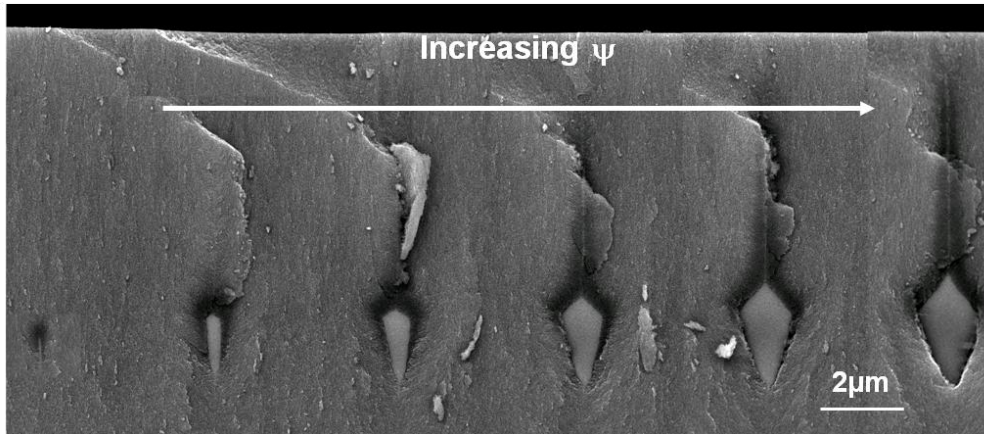


Figure 5-2 : Cross-section SEMs of 0.02 Ω .cm p-type silicon line irradiated with 500 keV protons, with a range of Ψ .

Figure 5-2 shows cross-section SEM images of a 0.02 Ω .cm wafer which was similarly irradiated with a range of Ψ changing from $2 \times 10^{10}/\text{cm}$ to $6 \times 10^{11}/\text{cm}$. A lower wafer resistivity provides a more graphic example of the effect of current focusing as it exhibits a wider range of porosity with enhanced anodization current density (see Figure 5-3), hence the dark regions at the end-of-range and along the ion trajectories are more clearly observed in Figure 5-2.

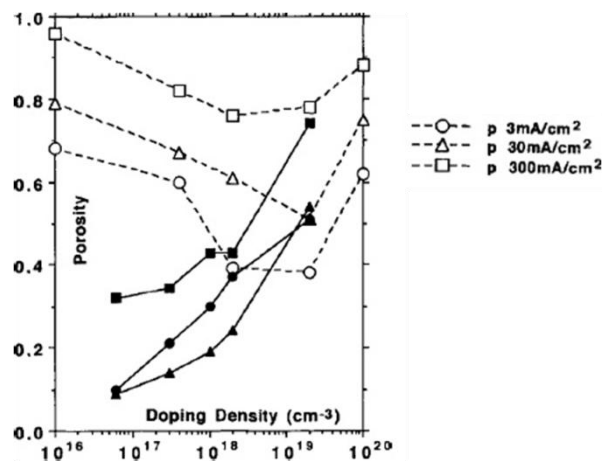


Figure 5-3 : Porosity as a function of doping density for p-type (open symbols) and n-type (filled symbols) silicon electrodes anodized in 1:1 ethanoic HF at different current densities (as indicated). From [44].

Another sample of 0.02 Ω .cm wafer was similarly irradiated 1 MeV protons (range 16 μm). After low-fluence irradiation and anodization the wafer was left for two weeks under ambient conditions, causing the PSi to gradually oxidize. Those regions with the highest porosity immediately after anodization

become sufficiently oxidized to be removed by brief immersion in dilute HF, leaving the lower porosity regions intact. Figure 5-4 shows irradiated lines with a low Ψ where hollow regions are observed at the end-of-range, which may contain a silicon core at a slightly higher Ψ , just above the onset of core formation. The latter case will be discussed in more detail in chapter 5.2.

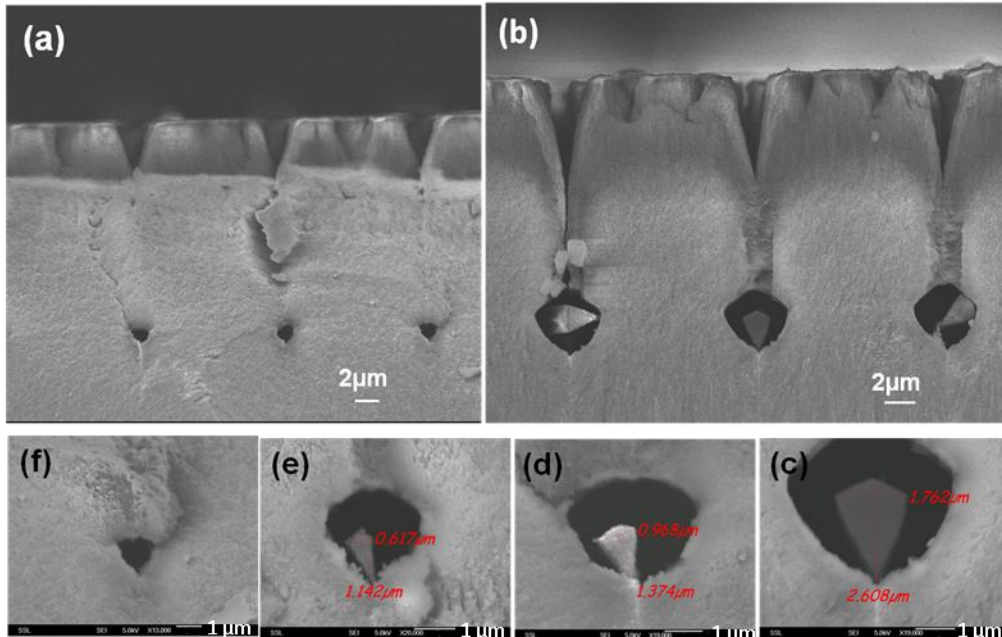


Figure 5-4 : Cross-section SEMs of line irradiated in 0.02 Ω .cm p-type silicon irradiated with 1 MeV protons, with (a),(b) $\Psi = 3 \times 10^{10}/\text{cm}$, $1.8 \times 10^{11}/\text{cm}$ and (c)-(f) zoom-in view of $\Psi = 3 \times 10^{10}/\text{cm}$, $\Psi = 6 \times 10^{10}/\text{cm}$, $\Psi = 9 \times 10^{10}/\text{cm}$ and $\Psi = 1.8 \times 10^{11}/\text{cm}$ respectively.

5.1.2 Current flow around irradiated areas

To understand the processes occurring during anodization of irradiated wafers, it is first necessary to consider the two types of current flow, namely drift and diffusion current. This section briefly discusses their different influences during anodization but a more detailed study requires computer simulation as described in the following section.

The effect of ion irradiation can be considered as a modification of the effective fixed charge profile, resulting in a positive electric potential at an irradiated region, Figure 5-5 (a), giving rise to a built-in electric field, $E_{\text{built-in}}$, which varies in magnitude and direction around the irradiated region. The resultant

doping profile induces a hole diffusion current which moves towards the highest defect density, i.e. minimum doping density.

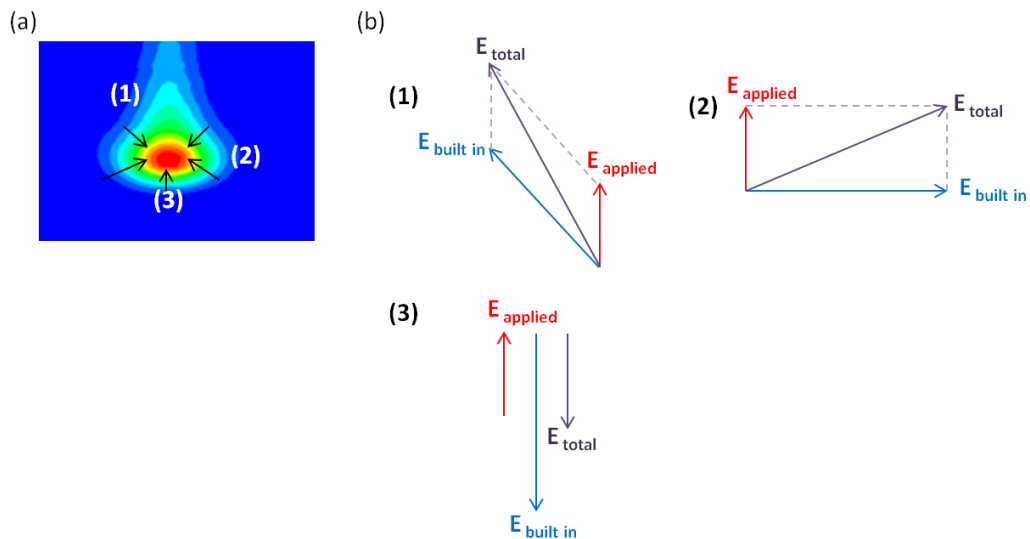


Figure 5-5: (a) Simulated electric potential using the COMSOL package [96]. Black arrows show the direction of the diffusion component of current. (b) Directions of the applied electric field and built in electric field at three different locations around the irradiated region labelled as (1)-(3) in (a). The magnitude and direction of the resultant electric field experienced by the anodization current is important in understanding the shape of the formed core.

The resultant force on the drift current is the vector sum of E_{applied} , and $E_{\text{built-in}}$, Figure 5-5 (b). Even at low fluences the built-in field is still significantly larger than the applied field, E_{applied} , so the drift component is strongly influenced by it. The resultant anodization current is the sum of the drift and diffusion components, which together determine the shape of the core. In the following section detailed simulations of these components are presented.

5.1.3 Simulation of current flow around silicon irradiated areas

To better understand the experimental results described in the following sections for high energy protons and other ongoing work using 30 keV helium ions, a simulated study of hole current flow through and around ion irradiated areas in 0.4 $\Omega\cdot\text{cm}$ p-type silicon was carried out in collaboration with Professor Ettore Vittone, University of Torino, to characterize the behaviour of the drift and diffusion components of the current flow during anodization. However, these simulations

are not a complete guide as they take no account of the actual interface region between the silicon and the HF electrolyte where the electrochemical anodization occurs, or the time evolution of the etch front.

The effects of ion irradiation were modelled for single and multiple line irradiations of different fluences. The average two dimensional vacancy density per single ion, $v_G(x,y)$, generated by a point focus of 30 keV He ions is shown in Figure 5-6 (a), calculated by convoluting the vacancy density from a delta-like point source using SRIM2010 [23, 30], assuming a displacement energy of 20 eV. The maximum vacancy density occurs at, or very close to, the surface for low ion energies close to the Bragg peak of the nuclear energy loss.

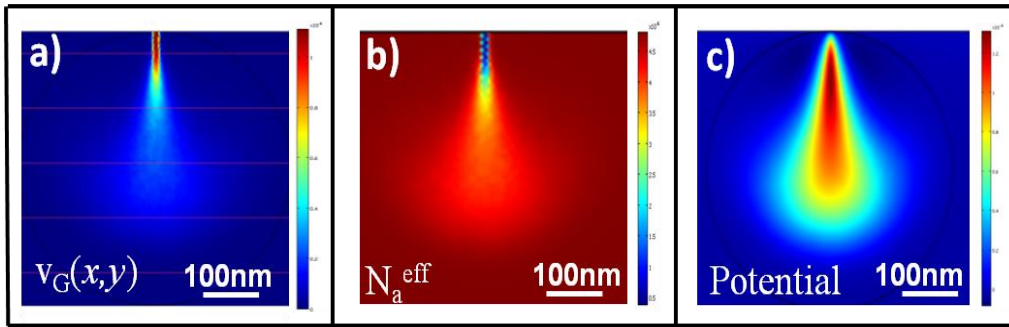


Figure 5-6 : (a) SRIM simulation map of the average vacancy distribution $v_G(x,y)$ per 30 keV He ion in silicon. (b) map of N_A^{eff} for a line irradiation for $\Psi = 4 \times 10^8 / \text{cm}$. This, and all following plots in $0.4 \Omega \cdot \text{cm}$ p-type silicon. (c) map of electric potential for $\Psi = 1 \times 10^7 / \text{cm}$.

The two dimensional vacancy density generated by a fluence Ψ is given by $V_G(x,y) = v_G(x,y) \cdot \Psi$. We assume the vacancy distribution in the irradiated silicon reduces the acceptor concentration N_A by a fraction, f , of the vacancies behaving as donors [27, 35], so compensating the native acceptor concentration, giving an effective acceptor concentration N_A^{eff} [97], according to:

$$N_A^{\text{eff}} = N_A - f \cdot \Psi \cdot v_G(x,y) = N_A - f \cdot V_G(x,y) \quad (1)$$

Equation (1) is based on the assumption of a linear relationship between the density of traps generated by ions with a donor nature and the density of

vacancies. To vary N_A^{eff} in the simulations one could change either f or Ψ ; we use a fixed value of $f = 10^{-4}$ and vary Ψ , for easier comparison with the experimental results. This f value is consistent with that extracted from previous studies by other groups on the effect of ion irradiation on the electrical properties of silicon, e.g. [90, 93].

A map of N_A^{eff} for $\Psi = 4 \times 10^8/\text{cm}$ is shown in Figure 5-6 (b) follows that of the vacancy density but with the minimum N_A^{eff} at the surface where the maximum defect density is located. Note that N_A^{eff} remains positive, i.e. no inversion of doping type, for values of Ψ typical of those where strong current funnelling observed in Figure 5-7.

Evaluation of the two-dimensional hole current map flowing around irradiated regions under the influence of an applied potential V_{applied} was performed by solving the Poisson's and continuity equation using finite element method-based commercial package [96]. The simulation only deals with majority carriers and we assume negligible recombination of holes in the irradiated region. The top and bottom boundaries were considered ohmic and of the Dirichlet type, with a constant positive potential, V_{applied} , at the bottom surface and the top surface grounded. For the $0.4 \Omega \cdot \text{cm}$ wafer, a total current density comprising the sum of the drift and diffusion currents, of $40 \text{ mA}/\text{cm}^2$ flowing through a $500 \mu\text{m}$ thick wafer is assumed. In our simulations the thickness of the domain is $10 \mu\text{m}$, so an equivalent value of $V_{\text{applied}} = 1.6 \times 10^{-5} \text{ V}$ is used. The effect of ion irradiation is mainly a modification of the effective fixed charge profile, inducing a local reduction of the hole concentration and generating a partially/fully depleted region at low/high Ψ . Figure 5-6 (c) shows the map of the positive electric potential at an irradiated region for $\Psi = 1 \times 10^7/\text{cm}$, from which one expects the hole drift current to be repelled during anodization.

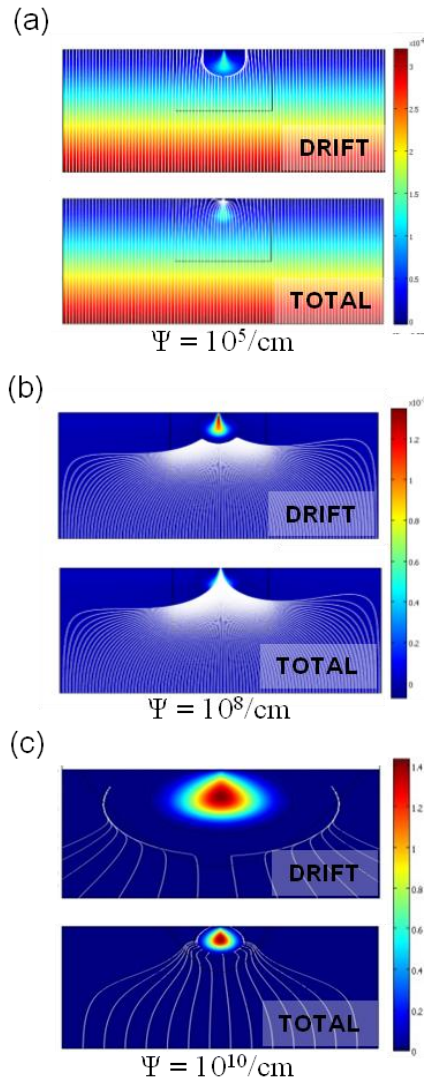


Figure 5-7 : Maps of potential (color scale on the right) and current streamlines for the (upper) drift component and (lower) total current flow for increasing values of (a) $\Psi = 10^5/\text{cm}$, (b) $10^8/\text{cm}$, (c) $10^{10}/\text{cm}$.

Figure 5-7 shows simulations for (upper) the drift component and (lower) total hole current (sum of the drift and diffusion components) for different Ψ . Changes in mobility due to additional ion-induced scattering centres are included but found to vary little for the low Ψ over which diffusion funnelling is observed (from 3.2×10^{10} to $\sim 2.3 \times 10^{10}$ up to $\Psi = 1 \times 10^9/\text{cm}$). As expected, the drift current is repelled from the irradiated region over a wider extent with increasing Ψ , due to a larger induced positive electric potential. At the lowest fluence shown the total current is very weakly funnelled at the surface, with this effect disappearing at depths greater than ~ 100 nm. At $\Psi = 1 \times 10^8/\text{cm}$, the total hole current is highly

concentrated towards a narrow surface region because the diffusion component is funnelled over both a larger lateral and depth range into a highly localized current density which dominates the anodization behaviour. At $\Psi = 1 \times 10^{10}/\text{cm}$ the anodization behaviour changes; current transport through the irradiated region reduces to zero, setting an upper limit on fluence beyond which funnelling of diffusion current is not observed.

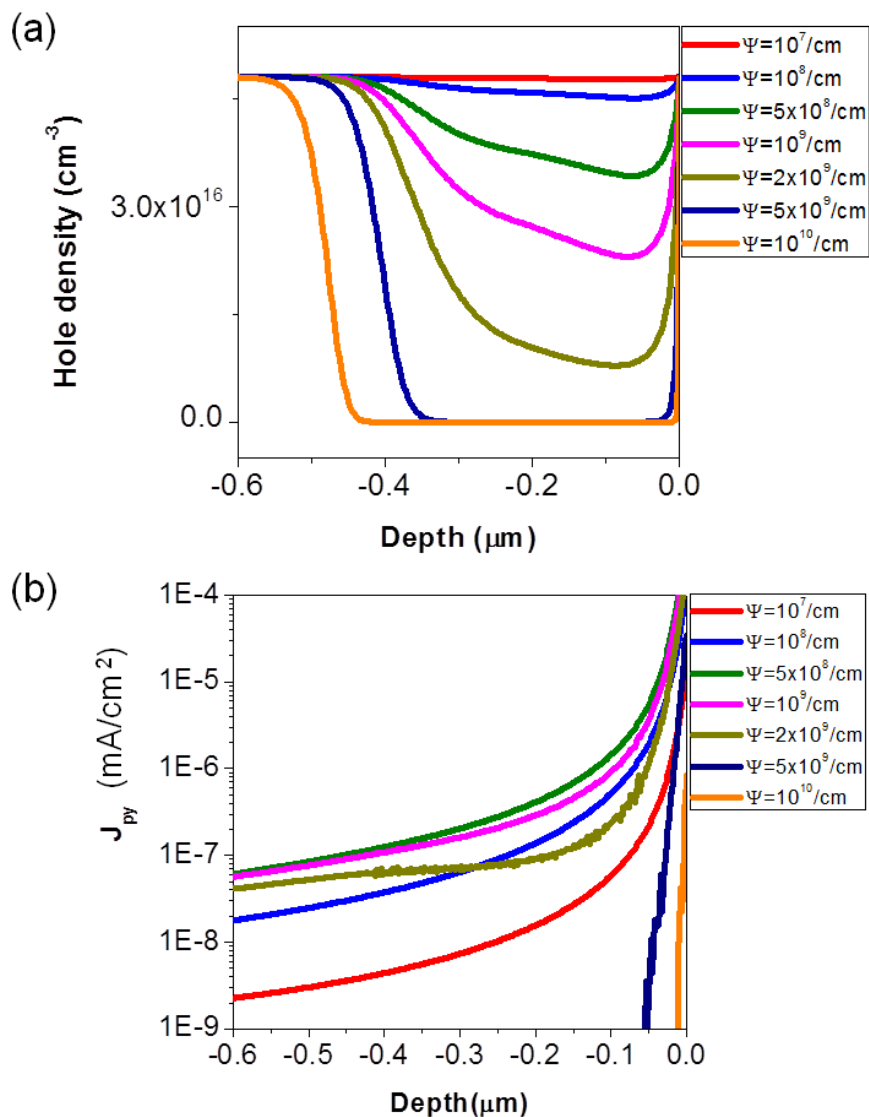


Figure 5-8 : (a) Hole density and (b) total current density versus depth below the surface, for different Ψ .

Figure 5-8 (a),(b) respectively plot the hole density and total anodization current density (vertical component) versus depth below the surface at the

irradiated line centre, giving a good insight into the mechanism which drives the current funnelling observed in the experimental and above simulated results. In Figure 5-8 (a), the hole density changes from high to low on moving towards the surface, with a gradient which increases with Ψ (up to $\Psi \leq 2 \times 10^9/\text{cm}$). One observes a clear correlation between the hole density gradient and an increasing total anodization current density with increasing Ψ . Clearly, the gradient of the hole concentration is responsible for funnelling the diffusion component of the hole current towards the maximum defect density, at the surface in this case. At higher Ψ the irradiated depth is largely depleted of holes and current transport through this region rapidly reduces to zero.

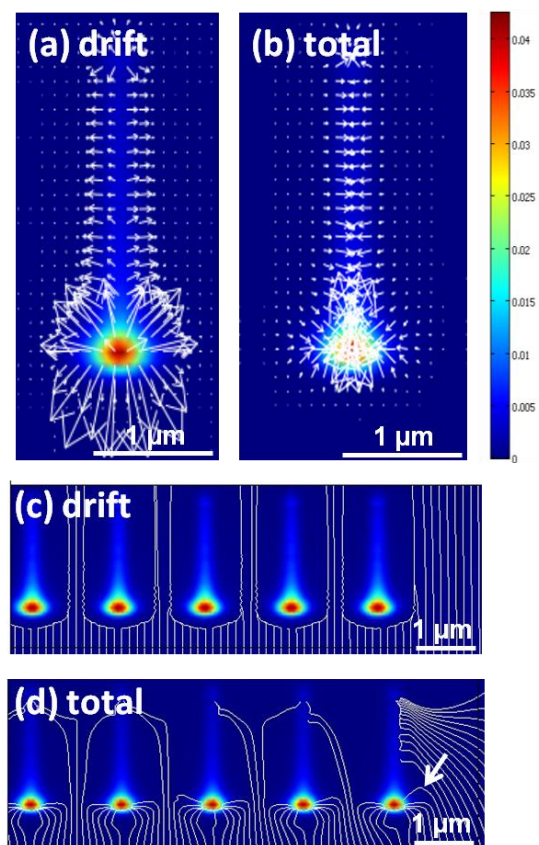


Figure 5-9 : Simulations for single line irradiation with 250 keV protons in 0.4 $\Omega\cdot\text{cm}$ silicon for $\Psi = 4 \times 10^{10}/\text{cm}$, showing (a),(b) magnified maps of potential with superposed arrow plots of the drift and diffusion components of the anodization current where the lengths of the arrows are proportional to the modulus of the current components, (c), (d) low magnification maps of the five rightmost cores in an array of eight irradiated lines, with line period of 1.7 μm , encompassing the outermost core at the right side to the central two at the left side, for $\Psi = 6 \times 10^8/\text{cm}$.

Figure 5-9 shows simulations for 250 keV protons in 0.4 $\Omega\cdot\text{cm}$ silicon (range $\sim 2.4 \mu\text{m}$) under the same anodization conditions as above. This proton energy is well above the Bragg peak for nuclear energy loss, hence the defect density reaches a maximum beneath the surface at the end-of-range, along with the minimum hole density and the maximum electric potential, with weaker effects present along the initial portion of the ion trajectory where the defect density is about ten times lower. Figure 5-9 (a),(b) show arrow plots of the drift and diffusion components around a single line irradiation. The repulsion of the drift current away from the defect induced potential at the end-of-range region, countered by the diffusion current flow towards the minimum N_A^{eff} is clear. Similar, weaker effects along the initial ion trajectory are observed.

Figure 5-9 (c),(d) show the drift and total hole current flow around five irradiated lines. The total hole current flowing close to the cores is funnelled in to them, even reversing direction of flow from upwards to downwards as arrowed, an effect not observed when the maximum defect density is at the surface. Hole current flowing further away from the end-of-range regions may 'escape' being funnelled into them, only to be funnelled towards the columns where the doping gradient is smaller. These simulations confirm the current funnelling effect at the end-of-range regions for high energy ions for low Ψ and along the portions closer to the surface for high Ψ , showing the results observed in Figure 5-1 and Figure 5-2 for the dark SEM contrast, enhanced photoluminescence are consistent with a higher porosity silicon produced the funnelling of the diffusion current.

5.2 Factors influencing the core shape

At regions where Ψ is high enough to form an intact core at the end-of-range, many factors can influence the core size, such as the wafer resistivity, ion energy,

fluence, beam size and anodization current density. It is important to be able to predict the size and the shape of buried cores for many of the applications described in the next chapters. This section focuses mainly on the influence of the ion beam energy and fluence on the core size for different wafer resistivities. For simplicity, all the samples in this chapter are etched with the same current density of 60 mA/cm^2 in an electrolyte containing HF (48%):water:ethanol (1:1:2).

5.2.1 Effect of ion energy on the core shape

Figure 5-10 shows SRIM [23, 30] results for the (a) proton range in silicon and (b) defect distribution for 10,000 simulated protons in each case versus lateral position across the end-of-range core region for different proton energies of 50 keV, 250 keV and 1000 keV, typical of those used in these studies. Use of higher energies allows deeper irradiation, with cores formed further beneath the surface. The further ions travel through matter, the more they are scattered in small-angle collisions with the sample electrons. The larger scattering at higher proton energies results in defects distributed over a wider distance away from the beam axis, so larger core sizes are expected at higher energies. This should be considered when wanting to fabricate small size cores of tens or few hundreds of nanometers.

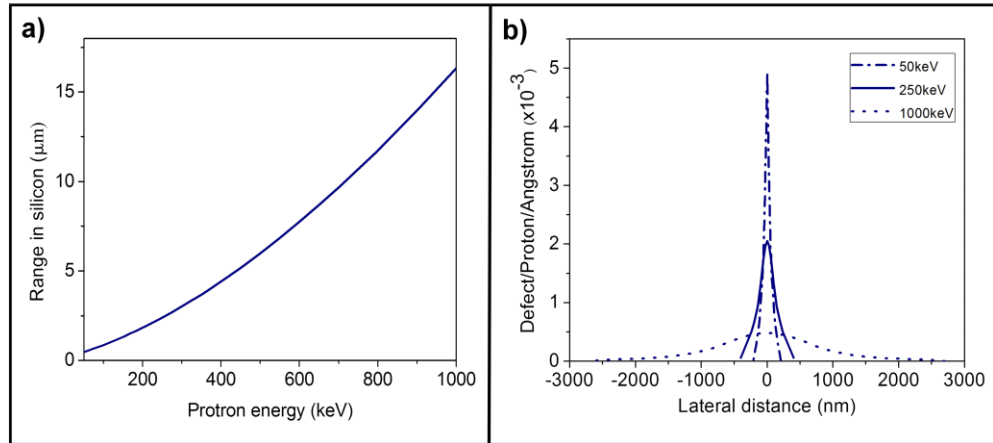


Figure 5-10 : Plot of proton range versus energy in silicon (b) Plot of defect density versus lateral distance across the end-of-range core for different proton energies in silicon.

5.2.2 Effect of ion fluence on the core shape

The standard definition of fluence, the number of ions incident upon a given surface area in units of ions/cm², is ideal for irradiating large areas where the effects of irradiation are laterally uniform and the defect depth distribution may be calculated using codes such as SRIM. Indeed we have used this approach to model the ion induced defect density as a function of depth and will use this to model the effects of ion fluence on anodization of large areas where the lateral extent of the irradiated area is bigger than the end-of-range scattering (chapter 5.2.4) [29]. However, as described in chapter 5.1.2 for studying the unusual irradiation regime in which ion scattering results in a lateral extent of the defects across the end-of-range region is significantly larger than the irradiated line width on the wafer surface (Figure 5-10 (a)), fluence is not the most relevant factor in determining the core size. As the surface width of an irradiated line becomes similar to, or less than, the end-of-range lateral scattering, the peak defect density decreases even though the fluence remains the same. Hence, the number of ions used for irradiating a line of zero width per centimeter of line length, Ψ , is a more useful parameter. This definition is independent of any variations or uncertainty in the irradiated line width on the surface and it simplifies the experimental aspects of

fabricating small cores since the only parameter is the total number of ions used, and the line length. For example, Figure 5-11 shows cross sectional optical images of cores formed in 0.4 Ω .cm p-type silicon using PBW with 1 MeV protons and surface line width and irradiated Ψ of (a) 500 nm, $3 \times 10^{10}/\text{cm}$, (b) 1000 nm, $1 \times 10^{10}/\text{cm}$. Smaller core sizes of $\sim 2 \mu\text{m}$ are formed with 1 MeV protons in Figure 5-11 (b) because Ψ is lower than in Figure 5-11 (a), even though the irradiated line width is greater.

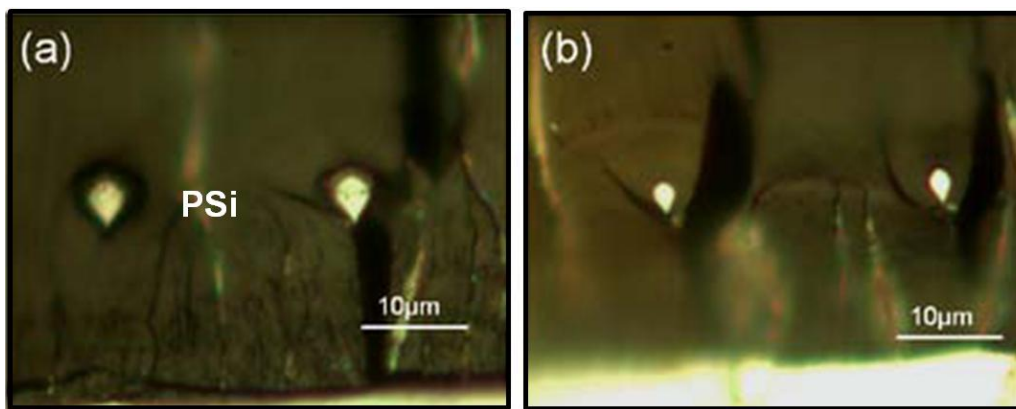


Figure 5-11 : Cross-section optical micrographs showing core sizes for surface line width and irradiated Ψ of 1 MeV protons of (a) 500 nm, $3 \times 10^{10}/\text{cm}$, (b) 1000 nm, $1 \times 10^{10}/\text{cm}$.

Figure 5-12 shows cross-section optical images of cores produced in the same resistivity by irradiation with increasing Ψ of 1 MeV protons using PBW and a beam focused to a spot size of 200 nm. By increasing the Ψ from $1.5 \times 10^{10}/\text{cm}$ to $1.2 \times 10^{11}/\text{cm}$ the width of the core increases from about 1 μm to 5 μm respectively. At the same time the core cross-section elongates, as shown in Figure 5-12 (b), as the defect density all along the irradiation path increases to the level where it significantly deflects the flow of hole current. Hence smaller core size is expected at lower Ψ .

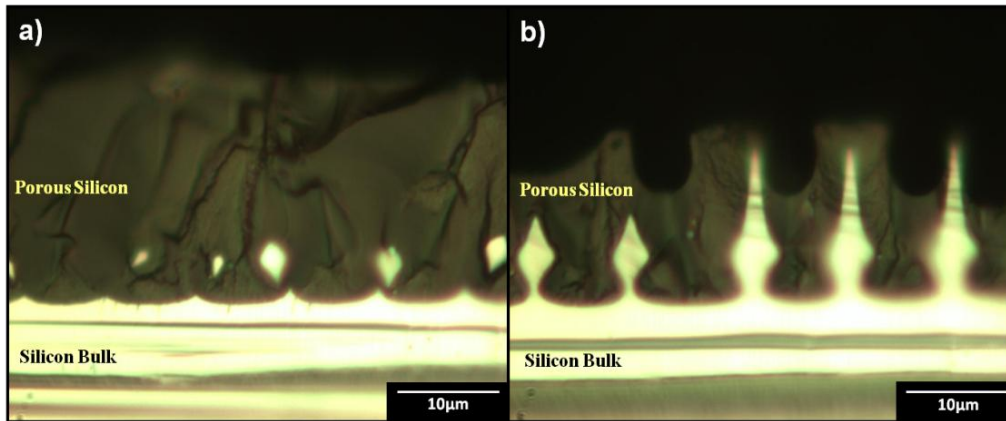


Figure 5-12 : Optical images showing wire cross-sections buried in PSi in 0.4 Ω .cm wafer after irradiation with 1MeV protons with a Ψ of (a) $1.5 \times 10^{10}/\text{cm}^2$, $3 \times 10^{10}/\text{cm}^2$, (b) $6 \times 10^{10}/\text{cm}^2$ and $1.2 \times 10^{11}/\text{cm}^2$.

5.2.3 Effect of wafer resistivity on the core shape

To study the effect of different wafer resistivity on the core shape, a 0.02 Ω .cm p-type silicon was irradiated with different line fluences, Ψ . Figure 5-13 shows cross-section SEM images of cores formed for increasing Ψ from (a) $1 \times 10^{11}/\text{cm}^2$ to (h) $2.4 \times 10^{12}/\text{cm}^2$. A higher Ψ is used compared to Figure 5-12 because a lower wafer resistivity typically needs a higher Ψ to form a solid core. With increasing Ψ both the width and the height of the core increase.

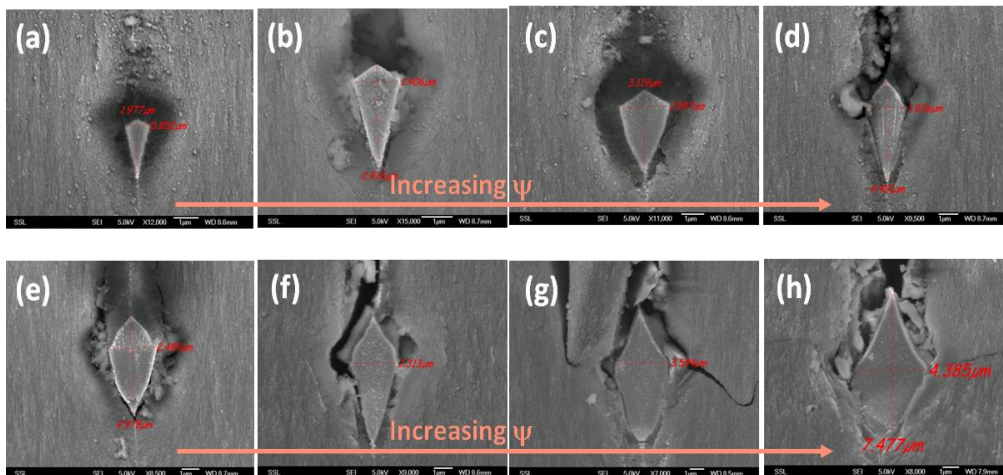


Figure 5-13 : (a)-(h) Cross-section SEMs of cores formed in 0.02 Ω .cm p-type wafer by 1 MeV protons with Ψ of $1 \times 10^{11}/\text{cm}^2$, $2 \times 10^{11}/\text{cm}^2$, $3 \times 10^{11}/\text{cm}^2$, $5 \times 10^{11}/\text{cm}^2$, $6 \times 10^{11}/\text{cm}^2$, $8 \times 10^{11}/\text{cm}^2$, $1.5 \times 10^{12}/\text{cm}^2$, $2.4 \times 10^{12}/\text{cm}^2$ respectively.

While there are minor differences in the shapes and curvature of the cores in the higher and lower resistivity wafers in Figures 5-12 and 5-13, overall one

observes a similar trend for irradiation using high energy protons of 1 MeV in both cases.

The wafer resistivity influences the core shape more significantly for the formation of small diameter cores of the order of tens or hundreds of nanometers. To fabricate small cores, a low proton energy seems preferable, also it requires a lower fluence to achieve a given peak defect density. This is because the decreased scattering at lower ion energies results in a smaller, denser defect distribution. In addition, the anodization current density also plays an important role in the resultant core shape and size. By increasing the anodization current density the core size becomes narrower and shorter. Here for the simplicity's sake, the same current density is used for comparison of the shape of the cores formed in 0.04 and 0.02 $\Omega\cdot\text{cm}$ p-type silicon.

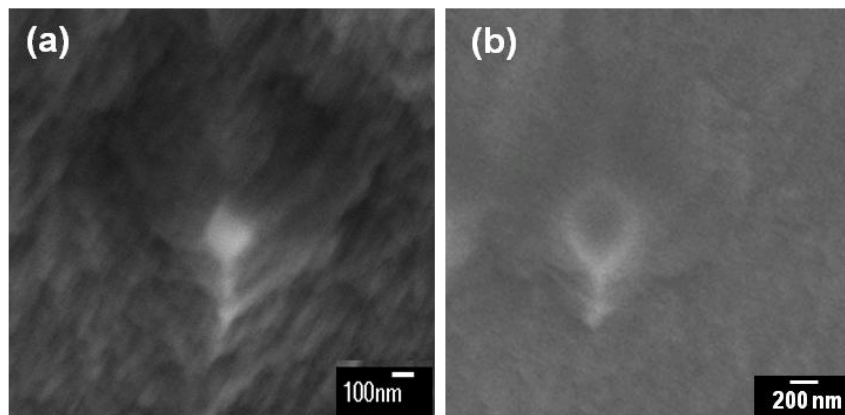


Figure 5-14 : Cross-section SEM images showing cores formed in 0.4 $\Omega\cdot\text{cm}$ p-type silicon wafer irradiated with 250 keV protons using (a) $\Psi=1\times 10^{10}/\text{cm}$ and (b) $\Psi=3\times 10^{10}/\text{cm}$.

An example of cores irradiated using PBW in 0.4 $\Omega\cdot\text{cm}$ p-type silicon with 250 keV protons (with range of $\sim 2.5 \mu\text{m}$) with Ψ of $1\times 10^{10}/\text{cm}$ and $3\times 10^{10}/\text{cm}$ can be seen in Figure 5-14. The samples were anodized for 4 minutes. A circular core with long tail is observed in this resistivity wafer. Figure 5-14 (a) shows that for the lower fluence the core size is $\sim 200\text{nm}$.

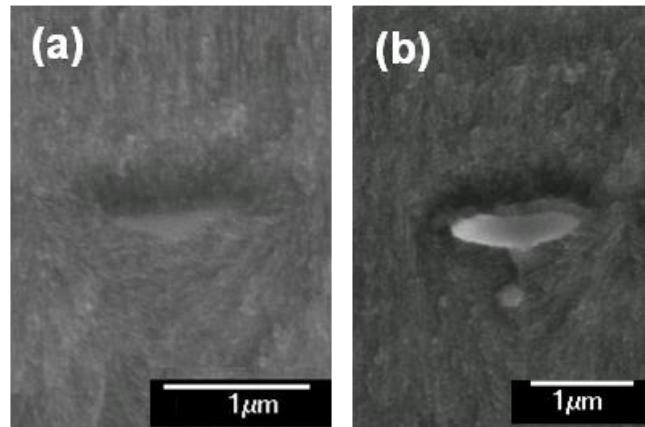


Figure 5-15 : Cross-section SEM images showing cores irradiated with (a) $\Psi=2\times 10^{10}/\text{cm}$ and (b) $\Psi=5\times 10^{10}/\text{cm}$ 250 keV protons in 0.02 $\Omega.\text{cm}$ p-type wafer.

Figure 5-15 shows SEM images of the cores formed with 250 keV protons in 0.02 $\Omega.\text{cm}$ wafers with $\Psi=2\times 10^{10}/\text{cm}$ and $\Psi=5\times 10^{10}/\text{cm}$. For lower fluences no core formation is observed, and instead high porosity regions at the end-of-range due to diffusion current funneling is observed (see chapter 5.1). Comparing Figure 5-14 and Figure 5-15, it is observed that smaller cores can be formed in a 0.4 $\Omega.\text{cm}$ wafer compared to 0.02 $\Omega.\text{cm}$ wafers. This can be explained by the more pronounced effect of the diffusion component of the anodization current passing through the cores for 0.02 $\Omega.\text{cm}$ wafers, which make them rapidly disappear in the vertical dimension. This also explains why no tails are observed at cores formed in this wafer resistivity.

5.3 Formation of extended cores

In this section the formation of cores irradiated with a beam ranging in width from several microns to a few tens of microns is discussed. This is important in defining how best to fabricate extended width surfaces with this micromachining approach. Since in this regime the surface width of the irradiated line is greater than the end-of-range lateral scattering, the standard defined fluence in units of ions/cm² is appropriate for such wide cores. Irradiation of broad line widths can be done

through scanning several adjacent lines using PBW or using a surface mask with wide openings together with large area irradiation.

3D silicon structures with a width of a few to tens of microns are of great interest for fabricating silicon-based source for irradiation, 3D micro-antennae and other components for TeraHertz wavelength regime [98-100]. In addition, being able to control the shape of the silicon cores is important and can open up new possibilities and flexibility for the fabrication of silicon photonic crystals or waveguides.

Similar to the observations made for small core formation, by controlling the wafer resistivity, ion energy, irradiation line width, irradiation fluence and anodization current density, different core shapes can be obtained. For simplicity here we only focus on the effect of the irradiated width and irradiation fluence using PBW on 0.02 Ω .cm wafers, since one can more readily produce buried, extended width features in a lower resistivity material.

5.3.1 Evolution of surfaces due to high energy protons

Previously, the effect of anodization depth and fluence on wide areas irradiated with 2 MeV protons was studied [61]. The range of 2 MeV protons in silicon is ~ 50 μm , with a uniform rate of defect production for the first 40 μm of penetration, so ideal for studying the evolution of the irradiated shape versus anodization depth and fluence within a region of uniform defect density. Figure 5-16 (a)-(c) and (d)-(f) show the effect of anodization depth for two different 6 μm wide line areas irradiated with 2 MeV protons with a fluence of $2 \times 10^{15}/\text{cm}^2$ and $4 \times 10^{15}/\text{cm}^2$. As a result of the dependence of etching rate on fluence, there is a boundary zone between the irradiated and unirradiated portions which becomes progressively more tilted with etch depth and with increasing fluence. Figure 5-16

(g) shows the measured boundary tilt angle ϕ versus anodization depth for different fluences. For all fluences, ϕ increases approximately linearly with depth until it reaches a constant value, and for increasing fluence, ϕ also increases at a particular etch depth. Under conditions of a high fluence, shallow anodization depth and wide irradiated area, an anodized surface with a flat top is generally observed, whereas for a low fluence, deeper anodization depth or narrow irradiated area a triangular shape is more likely to be observed as all these conditions favour the anodization fronts from either side meeting in the middle of the irradiated region.

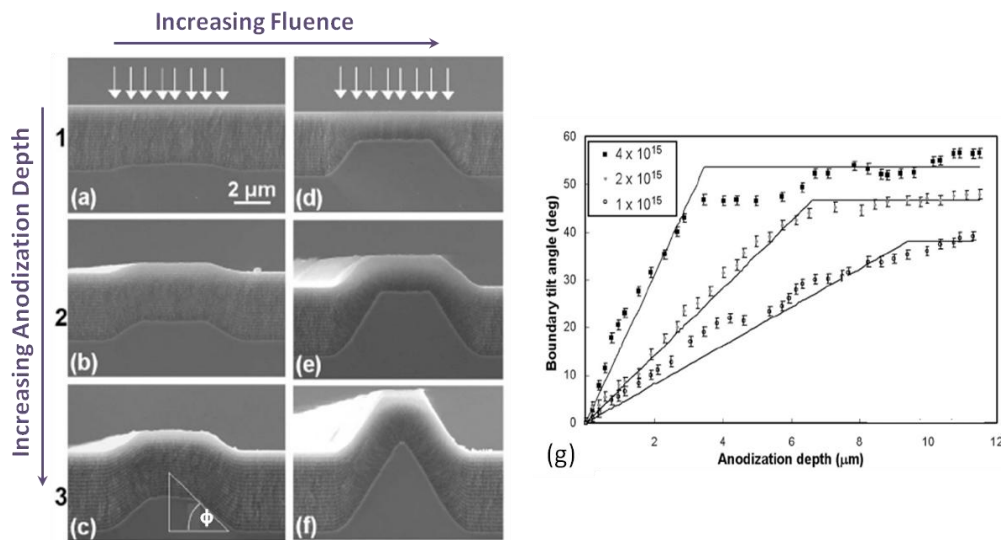


Figure 5-16 : Cross-sectional SEMs of DBRs forms by irradiating $6 \mu\text{m}$ wide line, 2 mm in length with fluence of [(a)-(c)] $2 \times 10^{15} \text{ cm}^{-2}$ and [(d)-(f)] $4 \times 10^{15} \text{ cm}^{-2}$. (g) Measured ϕ versus anodization depth of the unirradiated background for fluences of $1 \times 10^{15} \text{ cm}^{-2}$, $2 \times 10^{15} \text{ cm}^{-2}$ and $4 \times 10^{15} \text{ cm}^{-2}$. From [61].

In the following section all irradiated samples are etched deeply to completely undercut the irradiated regions. However, the above relationships between the fluence and ϕ are still useful in predicting the shape of the upper portion of the irradiated core.

5.3.2. Evolution of core shape

Low Fluences

As described earlier, current funnelling dominates at the low fluence regime, where the diffusion current is funnelled from undamaged regions to damaged regions along the doping gradient. This similarly explains the dark shadow regions in the SEM and the respective enhanced PL shown in Figure 5-17 irradiated with 1 MeV protons and a low fluence of $4 \times 10^{14}/\text{cm}^2$ with a irradiated line width of 20 μm using PBW. These regions follow the shape of the high defect end-of-range regions, where the porosity of the PSi is higher than surrounding regions. The porosity is highest at the centre of the irradiated region which refers to the highest defect density region, hence appearing darker in SEM images, and exhibiting the most enhanced PL in Figure 5-17.

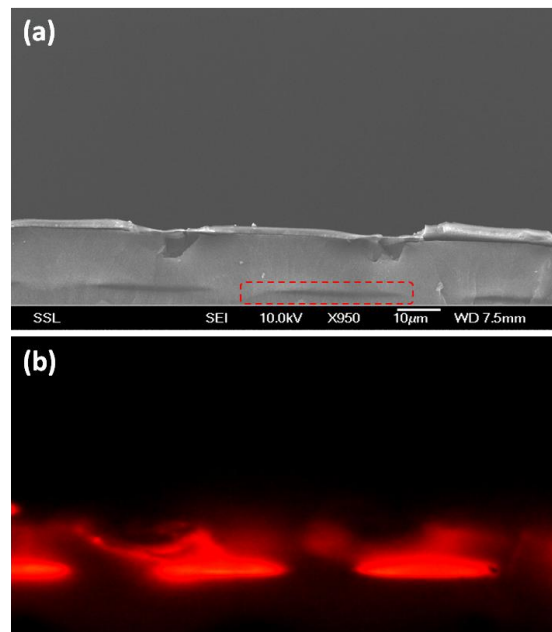


Figure 5-17 : (a) Cross-section SEM (b) PL images of the same array of lines showing high porosity observed owing to the current funnelling at the low fluence regime of $4 \times 10^{14}/\text{cm}^2$. The dashed box in (a) shows one of the end-of-range regions from which intense PL is observed in (b). PL was collected with a Nikon Eclipse microscope with excitation wavelength of 330-380nm, for an exposure time of 120 ms.

This effect is similar to that observed in chapter 5.1.2 for narrow irradiated regions and can also be explained by simulation of anodization current shown in

Figure 5-18 for a wide irradiation region. It can be observed that funnelling of the diffusion component produces a large, localized hole current density across the full width of the wide irradiated region which can dominate the total current flow and thus the anodization behaviour at low fluences.

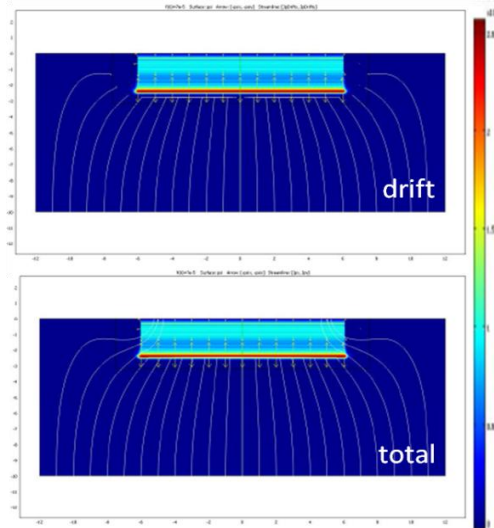


Figure 5-18 : Simulated drift and total current flow for a wide irradiation region of 12 μm , for 250 keV protons, generated using COMSOL [96].

Moderate/High Fluence

At higher fluences a range of different core shapes are formed at the same energy. Figure 5-19 shows cross sectional SEM images of 0.02 $\Omega\cdot\text{cm}$ p-type silicon, irradiated with 1 MeV proton fluences from $3 \times 10^{14}/\text{cm}^2$ to $8 \times 10^{15}/\text{cm}^2$. Three different widths, 5 μm , 10 μm and 17 μm were irradiated. For each width, by increasing the fluence the shape of the core changes. A schematic predicting the change in core shape with increasing fluence is shown in Figure 5-20.

The lower fluences used here compared with those used in Figure 5-16 are because the irradiated surface region has a low defect density per incident proton, hence requiring a fluence typically ten times higher than that where the end-of-range region undergoes anodization.

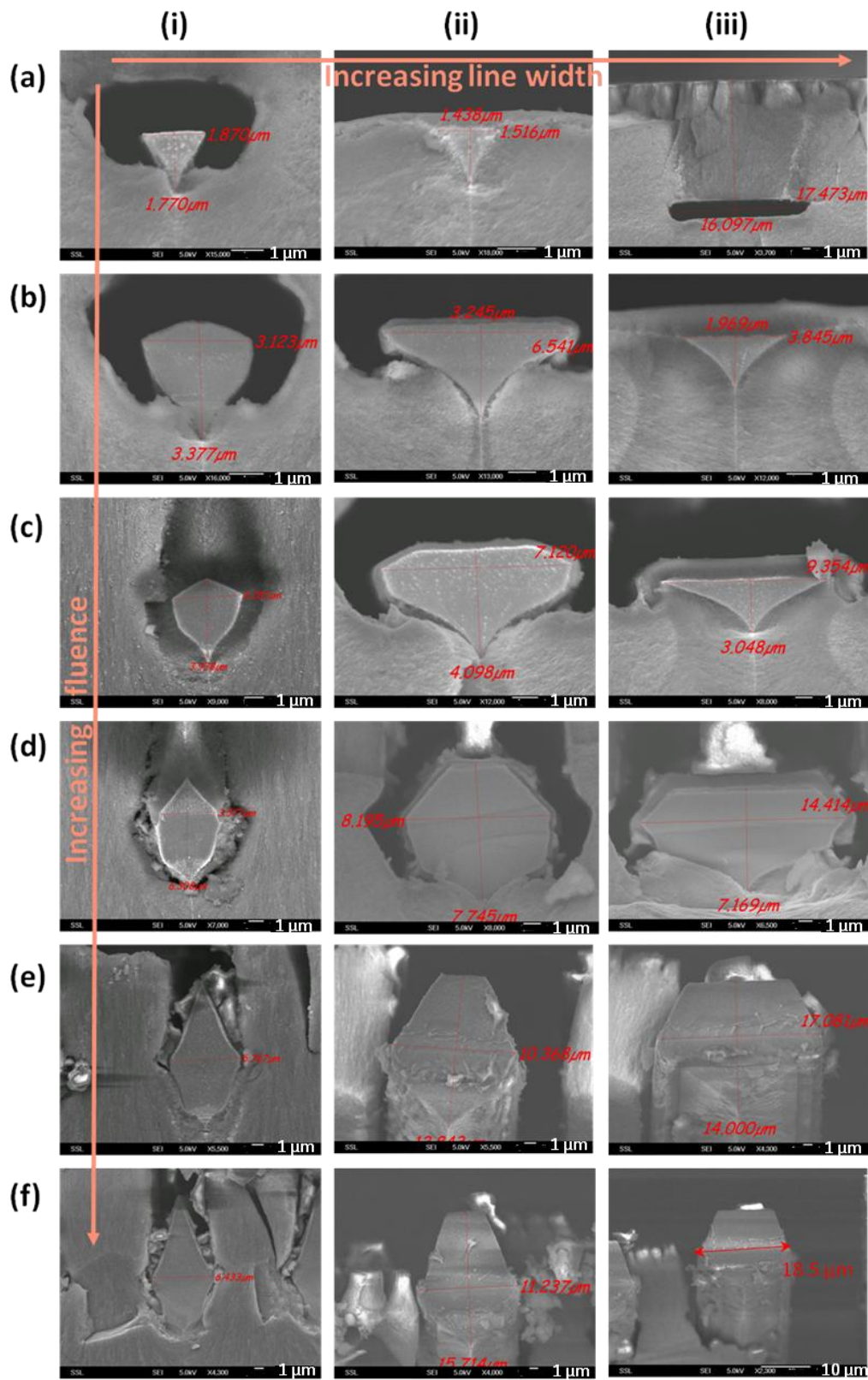


Figure 5-19 : Cross-section SEMs showing core formation by irradiating with 1 MeV protons and design widths of (i),(ii),(iii) 5 μm , 10 μm and 17 μm with increasing proton fluencies of (a)-(f): $3 \times 10^{14}/\text{cm}^2$, $6 \times 10^{14}/\text{cm}^2$, $1 \times 10^{15}/\text{cm}^2$, $2 \times 10^{15}/\text{cm}^2$, $5 \times 10^{15}/\text{cm}^2$, $8 \times 10^{15}/\text{cm}^2$ respectively.

At a moderate fluence, at the onset of core formation, some anodization current can still pass through the irradiated region and funnel into the high defect

end-of-range region above the later-formed core, hence the top surface is flat. Most current is deflected around the irradiated region, hence etching away the lower sides, producing a small triangular shape, Figures 5-19 (a) and 5-20(a). This shape is comparable to the long tail observed at low fluences in Figure 5-1, for irradiation of a narrow region in higher resistivity material. For a wider irradiation, the bottom angle, θ , of the formed core increases since current is more strongly deflected through a larger angle around the irradiated region.

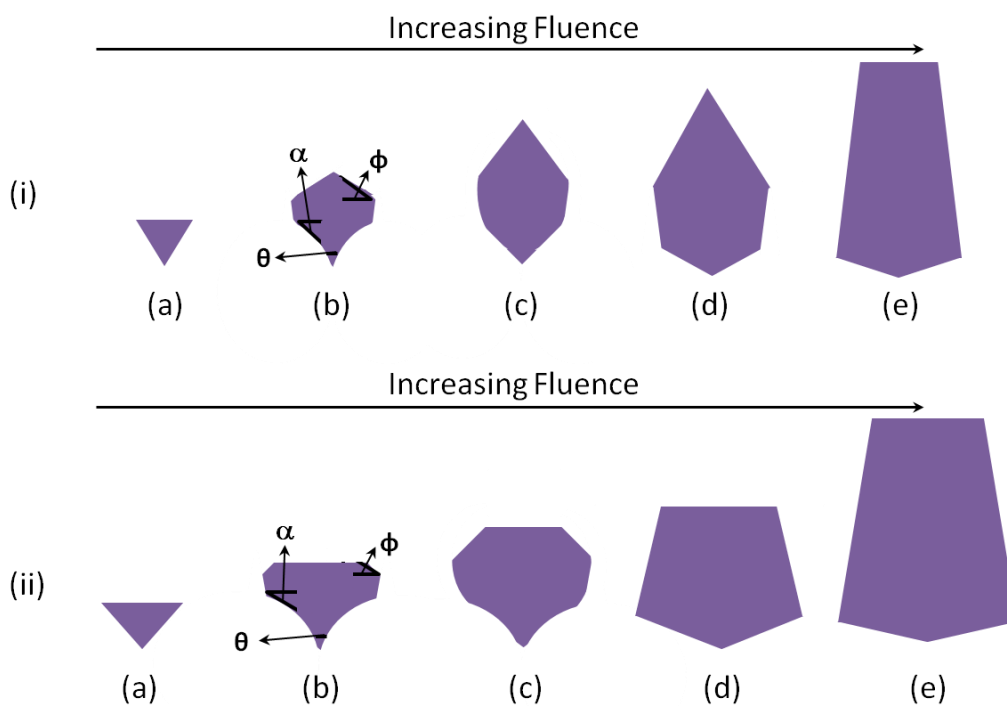


Figure 5-20 : Change in the extended core formed by increasing the fluence using high ion energy for (i) narrow (ii) wide irradiation regions. Depending on the irradiation width and depth, cores with sharp or flat top regions may be observed. The angles θ and ϕ both increase with fluence at a fixed width irradiation.

By increasing the fluence, the built-in core potential increases, so reducing the likelihood of diffusion current passing through this barrier. Consequently more current is deflected around the irradiated region, resulting in the cores becoming taller, i.e. the angle ϕ increases in Figures 5-19 and 5-20, as in previous results in Figure 5-16. The only difference is here the sample is completely undercut and the

anodization depth is fixed for all the irradiated fluences, and hence it is comparable with the saturated ϕ in the Figure 5-16 (g).

In Figures 5-19 and 5-20, the angle α also increases with fluence, for the same reasons as described for the angle ϕ ; since more current is deflected round the core region, it tends to also extend in the downwards direction. Faceting on the lower surface is observed in some cases, i.e. there are two distinct angles of the surfaces of the lower core (Figure 5-20 (c)). The most likely explanation for this is that at the extremes of the irradiated regions, the defect density is lower owing to lateral scattering, and also the built-in core potential being less at the outer edges of the irradiated width. The reduced core potential at the ends allows current to flow more vertically, i.e. less deflected compared to the angle directly beneath the irradiated central region.

Another noteworthy aspect of these results is that the cores tend to be thinner for wider irradiations, for the same fluence. For example, compare Figure 5-19 (b),(c) for 10 and 17 μm wide areas. In (b) it is seen that the width makes a difference between a solid core remaining for the 10 μm wide irradiation, compared to the wider region being fully anodized. This is important for the work in the following section whereby marked differences in the PL output are observed (Figure 5-24) for 10 and 17 μm wide areas, with strong PL emitted from the highly PSi formed at the end-of-range region at the 17 μm wide region, whereas for the 10 μm wide region, since more anodization current is deflected around this region, a solid core is formed with little PL emitted.

5.4 Photoluminescence and porosity of irradiated areas

PSi which is produced from low resistivity wafers tends to be mesoporous silicon, which does not emit intense PL compared to microporous silicon. However,

Chapter 4 described how irradiation can increase the resistivity and change the PSi type from mesoporous to microporous silicon for this resistivity wafers and hence PL can be observed. PSi produced from higher resistivity wafers which form microporous silicon, can be defined by Figure 4-10, showing that irradiation can change the intensity and wavelength of the observed PL.

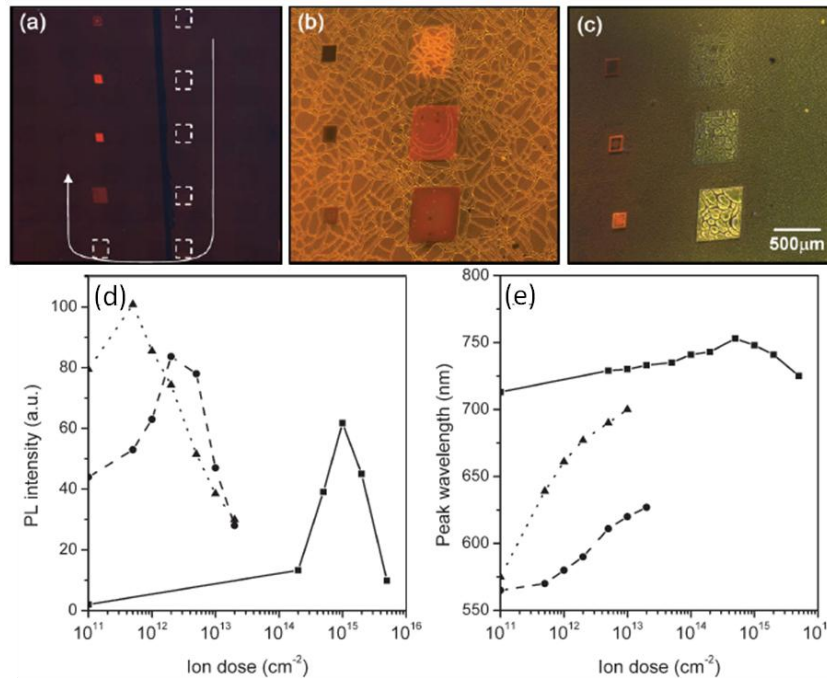


Figure 5-21: PL images of (a) 0.02, (b) 0.3, and (c) 3 Ω .cm resistivity p-type silicon wafers irradiated with a range of fluences at very large areas. The arrow points in the direction of increasing fluence for all three images. (a) Square patterns irradiated with fluences (doses) of 5×10^{12} , 1×10^{13} , 2×10^{13} , 5×10^{13} , up to $5 \times 10^{15}/\text{cm}^2$. The locations of lower fluences irradiation are outlined by dotted squares, since no visible PL is produced. In (b) and (c), irradiations of 5×10^{11} , 1×10^{12} , 2×10^{12} , 5×10^{12} , up to $2 \times 10^{13}/\text{cm}^2$ are displayed. (d) Measured PL intensity and (e) peak-wavelength emission as a function of dose from (a)-(c), for low (0.02 Ω .cm, solid line) and moderate-resistivity (0.3 Ω .cm, dotted line and 3 Ω .cm, dashed line) p-type silicon wafers. From [89].

The effect of irradiation on PL emission for very wide irradiation regions was previously studied at CIBA for different resistivities of p-type wafers irradiated with 2 MeV helium ions and was recorded in plan-view [89]. It was observed that for very wide irradiated regions, increasing the ion fluence leads to a PL red-shift and intensity change (Figure 5-21). This was explained by the fact that irradiation increases the resistivity at the irradiated area which makes it difficult for the current to bend around the end-of-range and enter the wide irradiated region closer to the surface. Hence by increasing the fluence the current

density at the irradiated regions reduces so the porosity reduces and hence a red shift in PL is observed. However, this may be different for narrow irradiated regions, where the effect of diffusion current funnelling and so the anodization current bending around the irradiated end-of-range region and back into the irradiated surface region may be observed. This section describes the observed change in PL and porosity for 0.02 Ω -cm wafers irradiated with lines up to 20 microns in width.

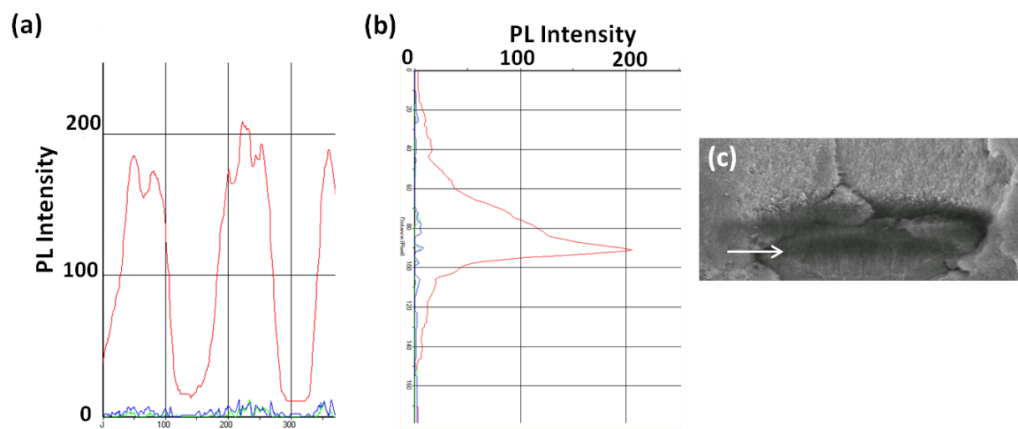


Figure 5-22 : From the irradiated region shown Figure 5-17 (a) PL intensity across and (b) perpendicular to the centre of the highest porosity (end-of-range) region for an exposure time of 30 ms. (c) Magnified SEM image of low fluence irradiated region. White arrow indicates the darkest region in the SEM referring to the highest porosity region.

For low fluence irradiation of a 0.02 Ω -cm wafer shown in Figure 5-17, where no core is formed, the porosity is highest at the centre of the high defect end-of-range region as a result of the strong current funnelling dominating the current flow. Figure 5-22 (a)-(b) show more than 20 times increase in red colour PL intensity emission at this region, indicated with an arrow in Figure 5-22 (c). This can be explained by current funnelling at the end-of-range region producing a high current density passing through a higher resistivity region compared to surrounding unirradiated regions. It is noteworthy in comparing Figures 5-21 and 5-22 that a fluence of $\sim 10^{15}/\text{cm}^2$ helium ions (equivalent to a fluence of $\sim 10^{16}/\text{cm}^2$ protons) produced the strongest increase in PL intensity from the wafer resistivity

when viewed from the surface where the end-of-range region is deeply buried, whereas in Figures 5-22, a fluence of $5 \times 10^{14}/\text{cm}^2$ protons is sufficient to produce a similar PL increase from the end-of-range region where it is directly observed in a cross-section view. Again this highlights the importance of the strong current funnelling into the end-of-range region as being one of the dominant mechanism occurring during anodization.

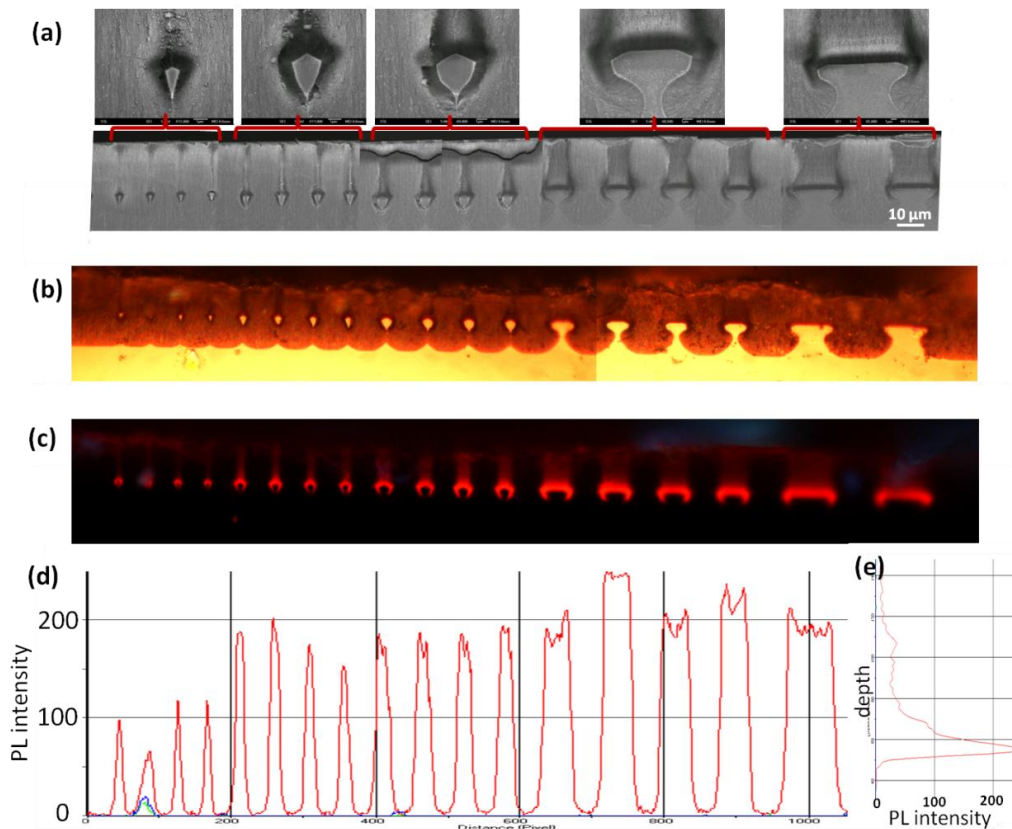


Figure 5-23 : Cross-section SEM, and magnified view of the cores, showing 0.02 $\Omega\cdot\text{cm}$ wafer irradiated with 1 MeV protons with different line width of 1, 3 μm with line fluence of $1 \times 10^{11}/\text{cm}^2$ and $3.5 \times 10^{10}/\text{cm}^2$ respectively. (b),(c) Optical and PL images of the same array of lines. PL collected with a Nikon Eclipse microscope with excitation wavelength of 330-380 nm, for an exposure time of 60 ms. (d) PL intensity perpendicular to the centre of the 10 μm core. (e) PL intensity across the formed cores.

By increasing the fluence a solid core starts to form, resulting in the anodization current bending around it as described earlier in this chapter. Figure 5-23 shows a 0.02 $\Omega\cdot\text{cm}$ wafer irradiated with 1 MeV protons, with the irradiated width changing from 1, 3, 5, 10, 17 μm . Magnified SEMs in Figure 5-23 (a) clearly show the effects of current funnelling and bending around the silicon core, hence a larger current density at these regions causing the PSi to appear darker

which is consistent with a higher porosity. The porous regions directly above the irradiated cores exhibit intense PL in Figure 5-23 (c),(d). A lower PL intensity is observed at the irradiated regions along the path of the current flow to the wafer surface. Figure 5-23 (e) shows for the 10 μm wide irradiated line, the PL emission from the zone around the core is over one thousand times greater than the background level which exhibits little PL as it is mesoporous silicon. The huge discrepancy arises because for plan-view observation (Figure 5-21) only PL emitted from the top few microns is detected, and PL produced at ion end-of-range regions at depths of tens of microns was absorbed before it reached the surface. Thus, only the effects of the weakly-damaged surface region were observed and much higher fluences are required to make the surface region sufficiently resistive to produce microporous silicon upon anodization. However, such a high fluence results in the formation of a large, extended silicon core at the end-of-range region which strongly limits current flow to the surface, thus reducing porosity and PL intensity (Figure 5-21). Even so, a twenty-fold increase in PL was observed from high-fluence irradiated large areas of hundreds of microns in diameter. A more important observation is that the brightest observed PL from the zones surrounding the silicon cores in Figure 5-23 (c) is comparable in intensity to that from similarly-prepared, unirradiated 0.4 $\Omega\cdot\text{cm}$ p-type wafer where formation of microporous silicon results in bright PL emission [44]. It is thus likely that microporous silicon is indeed formed along the ion trajectory, consistent with the wafer resistivity being significantly increased by irradiation [101].

For better understanding and proof of the higher porosity at the irradiated regions, another irradiated sample was prepared with various widths and fluences. After anodization it was left in air for a few days, then dipped in a dilute HF solution to remove the highest porosity PSi, which was converted to fully oxidized

porous silicon (FOPS). Hence, the PSi surrounding the silicon cores, which usually appears darkest in the SEM images, is removed as explained in chapter 5.1.1. The sample was left in air for another few more days to form another native oxide and so further reduce the diameter of the silicon skeleton of the remaining PSi in order to be able to define the next highest porosity region of the irradiated areas, Figure 5-24 (a). The corresponding PL image and intensity linescan is shown in Figure 5-24 (b),(c). It is observed that the PSi surrounding the removed FOPS emits the highest PL intensity, which is expected as a result of current bending around the end-of-range regions. The two end-of-range regions at the right side of the image emit PL which is more than 200 times higher than the surrounding, Figure 5-24 (d). Figure 5-24 (e) shows a SEM of the region from which the PL image was recorded, and Figure 5-24 (f) shows a SEM of the same region before dipping the sample in HF for removal of the FOPS. The darkest region in the Figure 5-24 (f) shows where large current funnelling effect into the highest resistivity region results in highly PSi which was removed during the initial oxidation process. However more PSi at a depth also corresponding to the end-of-range region still remains, which we interpret as having a high porosity, which is however slightly lower than that at the removed region, Figure 5-24 (e). Hence this region emits the highest PL intensity in Figure 5-24 (c),(d). The third highest porosity is right at the edge of the removed region, which is logical as being the boundary between PSi which is removed, and that which remains.

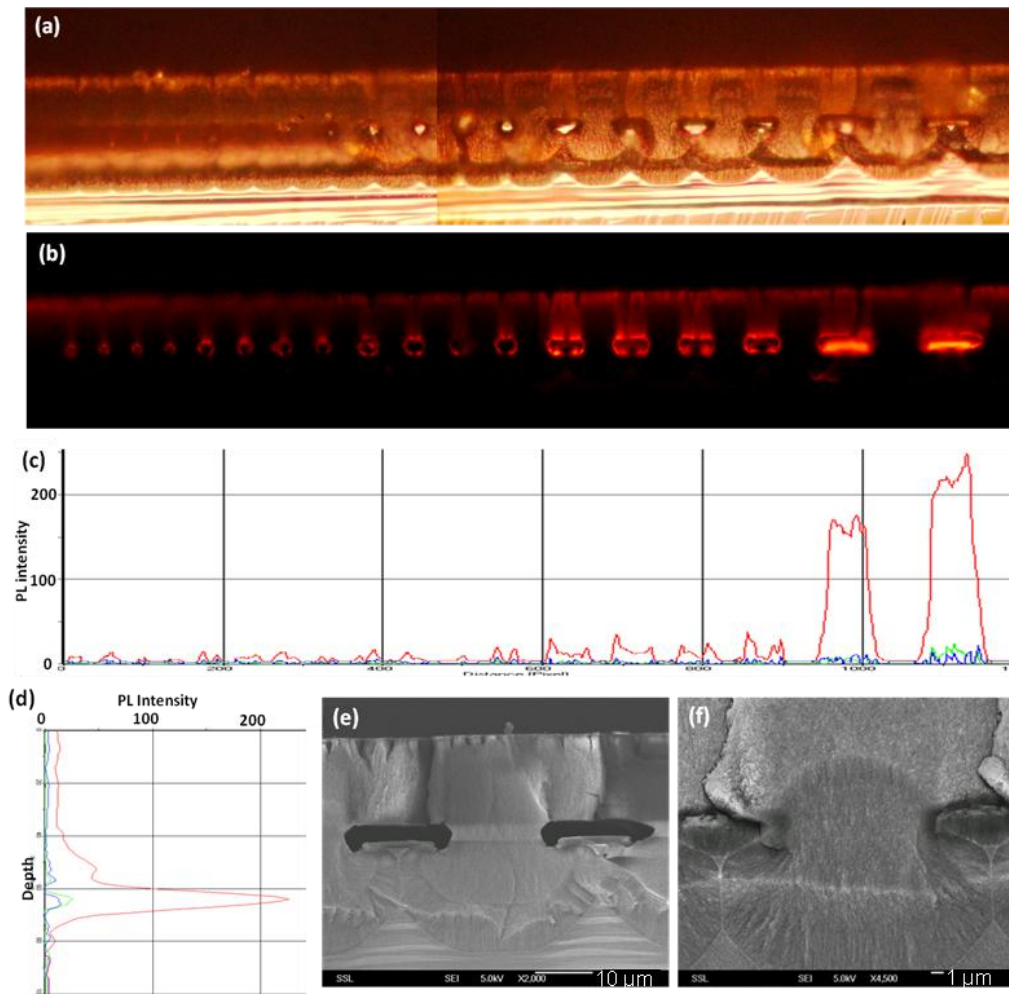


Figure 5-24 : (a)-(c) Optical micrograph and PL image and intensity linescan collected for 30 ms across the top of the formed core in $0.02 \Omega\text{-cm}$ wafer irradiated with 1 MeV protons with different line width of 1, 3 μm with line fluence of $5 \times 10^{10}/\text{cm}$ and $1.5 \times 10^{10}/\text{cm}$ and line width of 5, 10, 17 μm with the same fluence of $5 \times 10^{14}/\text{cm}^2$ respectively after the removal of FOPS formed at the highest porosity regions. (d) PL intensity perpendicular to the centre of the 17 μm core, and (e) showing the respective SEM. (f) shows the same region before removing FOPS.

Another important observation is that unlike the wide irradiated areas shown in Figure 5-21 [89], here the hole current can bend around the irradiated regions as the irradiated area is smaller, hence with increasing fluence the PSi along the irradiated region becomes more porous. Figure 5-25 (a)-(d) show 1 μm wide area irradiated with increasing Ψ of $1 \times 10^{11}/\text{cm}$, $2 \times 10^{11}/\text{cm}$, $5 \times 10^{11}/\text{cm}$ and $8 \times 10^{11}/\text{cm}$. With increasing Ψ , current funneling is enhanced and the porosity of the PSi along the irradiated region increases. Hence in Figure 5-25 (c), (d) the PSi is so porous that it has cracked and been unintentionally removed along the irradiated region during anodization. The same effect is observed for a wider

irradiated region of 10 μm , which still allows the hole current to bend around it and to reach the surface at the irradiated region, Figure 5-25 (e)-(i). So greatly enhanced PL intensity is expected to be observed in both top view and in a cross-section view. This effect can also be seen in Figure 5-21 (a)-(c) at the edges of the irradiated regions where the current density is higher than at the central region of the large irradiated areas. These detailed studies are important for better understanding the fundamentals effects of ion irradiation on the anodization process.

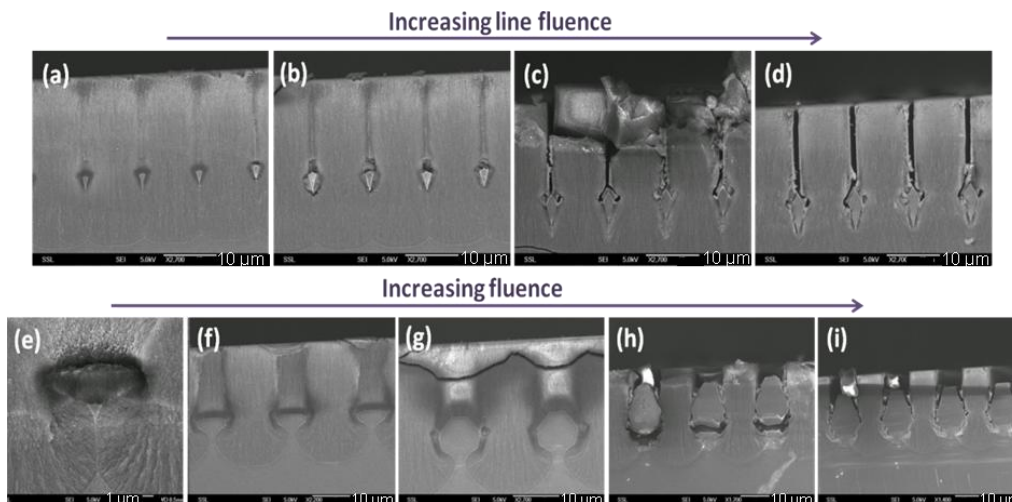


Figure 5-25 : Cross-section SEMs of 0.02 $\Omega\text{-cm}$ wafer showing (a)-(d) 1 μm irradiated line Ψ of $1 \times 10^{11}/\text{cm}$, $2 \times 10^{11}/\text{cm}$, $5 \times 10^{11}/\text{cm}$ and $8 \times 10^{11}/\text{cm}$ respectively, and (e)-(i) 10 μm irradiated line with fluence of $3 \times 10^{14}/\text{cm}^2$, $6 \times 10^{14}/\text{cm}^2$, $2 \times 10^{15}/\text{cm}^2$, $5 \times 10^{15}/\text{cm}^2$ and $8 \times 10^{15}/\text{cm}^2$ respectively.

5.5 Summary

In summary, this chapter has explained a current transport mechanism observed during electrochemical anodization of low/moderate-fluence ion irradiated p-type silicon in which a hole diffusion current is highly funneled along the gradient of the modified doping profile towards the maximum ion induced defect density, so dominating the etching behaviour. This phenomena is observed for high energy ions (>250 keV protons), where the maximum defect density occurs several microns beneath the surface, resulting in funneling into these sub-surface regions during anodization, and in different resistivity wafers. It was also observed that a

large increase in the porosity of highly-doped p-type silicon is induced at the end-of-range depth of high-energy ions after subsequent electrochemical anodization. This occurs under certain conditions of irradiation geometry and fluence, owing to the dual effects of an increased wafer resistivity and a locally increased current density during anodization, allowing the creation of highly porous, sub-surface zones with diameters down to hundreds of nanometers. These zones emit PL with an intensity more than three orders of magnitude greater than the surrounding mesoporous silicon, comparable to that produced by microporous silicon. Furthermore, they can be selectively removed after oxidation, allowing the formation of micro- and nano-scale buried, hollow channels within PSi.

In addition, different parameters influencing the core shape and size for both narrow and wide irradiated lines were characterized and studied. The most important factors determining the shape and the size of the cores after irradiation and subsequent electrochemical anodization are the ion energy, fluence, irradiation width, resistivity and anodization current density.

This understanding of the factors influencing core formation, including the characteristic shapes which can be produced, opens a new process for fabricating components for 3D silicon machining and silicon photonics. The studies described in this chapter are the basis of much of the 3D silicon fabrication, described in the following chapters.

Chapter 6 : Three-Dimensional (3D) Silicon

Machining

One of the main focuses of this thesis is developing a technique capable of 3D machining within bulk silicon. There is a wide spectrum of scientific and technological disciplines in which precisely machined, 3D micro- and nano-scale structures are required in silicon-based materials. For example, in silicon photonics utilizing the near and mid-infra red regions [102-105], conventional silicon waveguide structures are fabricated in SOI (silicon-on-insulator) wafers, which do not readily allow 3D waveguides between circuitry at different depths within the wafer. Therefore the ability to controllably fabricate 3D lines and wires is highly desirable for coupling between circuits at different depths, and allowing better 3D integration and packing density of photonic devices with each other and with microelectronic components. It would also allow new options for the design and fabrication of high-aspect ratio, multilevel microstructures in silicon for optoelectronic and in micro- and nano-electromechanical systems [106-108] and in fabricating photonic crystals [109]. Common techniques for 3D silicon fabrication are briefly described in chapter 1. These techniques, however, require multiple or unconventional processes and show limitations in fabrication of complex 3D geometries. To overcome these limitations, there is a need to develop a simple, direct, and cost efficient technique capable of fabricating arbitrary, curved multilevel 3D micro/nano-structures in bulk silicon. Such a technique developed using high energy ions, typically protons or helium, in conjunction with electrochemical anodization will be discussed in this and the following chapters.

6.1 Principles of 3D silicon machining using ion irradiation

Previous chapters discussed the unique characteristics of high energy protons and heliums inside silicon where the localized defects density at their end-of-range is significantly higher than along their penetration path. In light of this advantage, we have developed a technique using ion beam irradiation capable of fabricating true-3D structures in bulk silicon in a single etch step. This process is an important development in fields such as silicon photonics and MEMS.

Ion irradiation causes damage to the crystalline silicon, mainly in the form of vacancy-interstitial pairs, i.e. Frenkel defects [23, 35-37]; however, this is not a concern for using the fabricated structures for fields such as silicon photonics, as these defects can be completely recovered by thermal annealing after the fabrication process. Hence, the low fluence used for this micromachining process has no effect on the optical properties of silicon. While agglomeration of the ions used for irradiation may occur, the fluence is very low ($\sim 10^{14}/\text{cm}^2$) compared with, for example, Smart-Cut silicon (10^{16} to $10^{17}/\text{cm}^2$), and only within the patterned areas, so we do not consider that this limits the performance of the photonic structures fabricated using this approach. Similarly, the low fluence ensures that the silicon lattice is only lightly damaged, the fluence being several orders of magnitude lower than that at which noticeable amorphisation occurs. The use of this ion irradiation-based process to fabricate low loss waveguides has been verified by measuring the propagation losses of micrometer width waveguides made in this manner, with losses of ~ 1 dB/cm obtained [74-75].

Chapter 2.7 discussed the effect of ion irradiation on p-type silicon and chapter 5 described in detail the flow of hole current during the electrochemical anodization and the formation of silicon cores for different high energy ion

fluences. In brief, using ion beam irradiation for silicon machining gives the ability to selectively form PSi inside a bulk silicon wafer, due to the unique characteristic that high-energy protons and heliums create significantly more localized defects at their end-of-range than along their penetration path (close to the surface). As an example, Figure 6-1 (a) shows SRIM simulation[30] of the trajectories of 1 MeV protons in silicon, which is a typically used energy in this chapter for 3D silicon fabrication. The beam tends to remain well-collimated, with little lateral scattering until the ions slow down close to their end-of-range. 1 MeV protons have a range of $\sim 16 \mu\text{m}$ in silicon, with a FWHM (full-width-at-half-maximum) of the lateral distribution of $\sim 2 \mu\text{m}$. The defect generation rate is more than ten times higher at the end of range compared to the trajectory closer to the surface [20]. By controlling the fluence within each point of an irradiated area, the resistivity can be controlled and increased locally for selective PSi formation [29], as shown in Figure 6-1 (b). If the fluence is high, during the electrochemical process the flow of electrical holes from the back surface bends around the high defect regions to the front surface. As a result PSi forms around these regions, leaving the core region intact, with a size and depth mainly depending on the proton fluence and energy. The detailed mechanism was described in chapter 5.2.

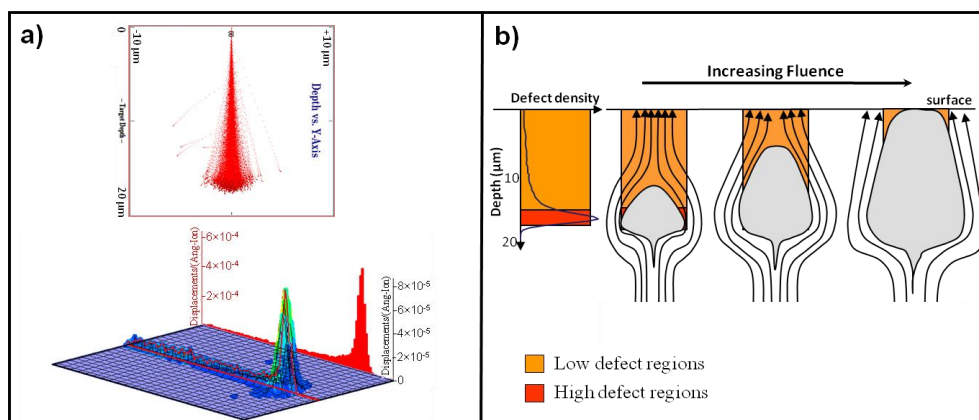


Figure 6-1: (a) SRIM simulation[30] of (top) trajectories versus depth and (bottom) defect distribution for 1MeV protons in silicon. (b) schematic showing the damage profile and deflected hole current around high defect region during anodization. At suitable fluences, the total hole current bends round the high defect region and flows through the lower defect region.

6.2 Fabrication process of free standing 3D silicon structures

The schematic of the 3D fabrication process used in this thesis is shown in Figure 6-2. Typically two different energies are used for making free-standing 3D structures and their supports. For the sake of easy explanation here we describe the process with 1 and 2 MeV protons which are the energies typically used in these experiments. Supporting walls for the final free-standing structures are defined using 2 MeV protons (range of $\sim 48 \mu\text{m}$) with a high Ψ , typically $1.2 \times 10^{12}/\text{cm}$, which is enough to completely stop anodization at the irradiated regions of a $0.4 \Omega\cdot\text{cm}$ wafer. In this process, single energy (1 MeV) proton irradiation (range of $\sim 16 \mu\text{m}$ in silicon) with a low Ψ of the order of $1 \times 10^{10}/\text{cm}$ can be used to create end-of-range cores at a single depth. Focused beam irradiation may be of any shape, such as lines or circles. During anodization in Figure 6-2 (b), current flows through those regions above and below the end-of-range core region, resulting in PSi formation. No current flows through the core or the supports, leaving the irradiated regions intact. The last step is using a very dilute KOH solution to release the free-standing 3D silicon structures, Figure 6-2 (c).

The core size depends on many factors including the wafer resistivity, ion energy, fluence, beam size and anodization current. The influences of some of these factors are studied in detail chapter 6.

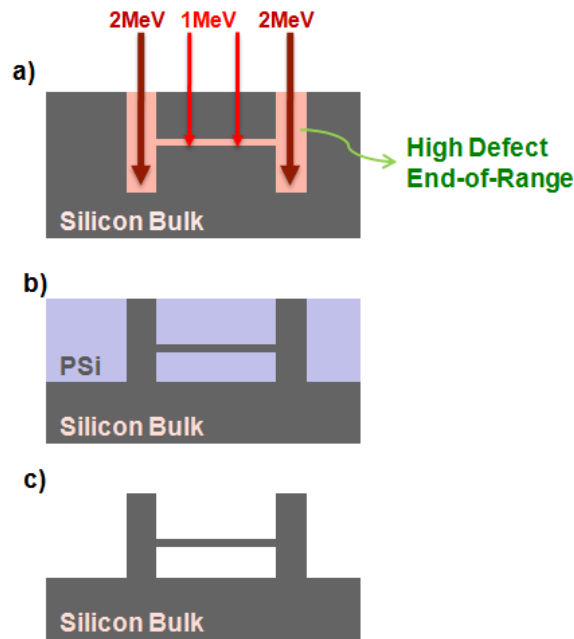


Figure 6-2 : Schematics of the processes involved in fabricating free standing 3D structures using (a) as an example, 1MeV proton irradiation for wires and 2MeV protons with a high Ψ for supporting walls, (b) anodization to produce PSi around the cores and (c) removal of the PSi leaving a free-standing structure.

6.3 3D silicon machining using PBW

PBW, described in chapter 2, is a flexible technique for machining arbitrary shape 3D silicon structures at micro- and nano-scale. For this work, we mainly used the 10° beam line described in chapter 2.6.1 with a beam focus of a few hundreds of nanometers.

Using PBW we have successfully fabricated arrays of long wires in 0.4 Ω .cm wafers using the approach in Figure 6-2 by irradiating lines of 500 μ m length with 1 MeV protons and $\Psi = 1 \times 10^{10}/\text{cm}$, illustrated in Figure 6-3 before and Figure 6-4 after removing the PSi. A long supporting wall mid-way along their length and shorter ones at different spacings were included by using a Ψ of $1.2 \times 10^{12}/\text{cm}$ of 2 MeV protons with the aim of studying how long such free-standing wires could be made. Wafers were then electrochemically anodized in an electrolyte containing HF (48%):water:ethanol (1:1:2) for 12 minutes with a current density of 60 mA/cm^2 , giving an etch depth of about 27 μ m. During the electrochemical process, the flow of electrical holes from the back surface bends

around the high defect regions to the front surface. As a result PSi forms around these regions, leaving the core region intact, with a size and depth depending on the proton fluence and energy (Figure 6-3). However, the fluence is high enough to stop the PSi formation on top of the supporting walls in this resistivity material.

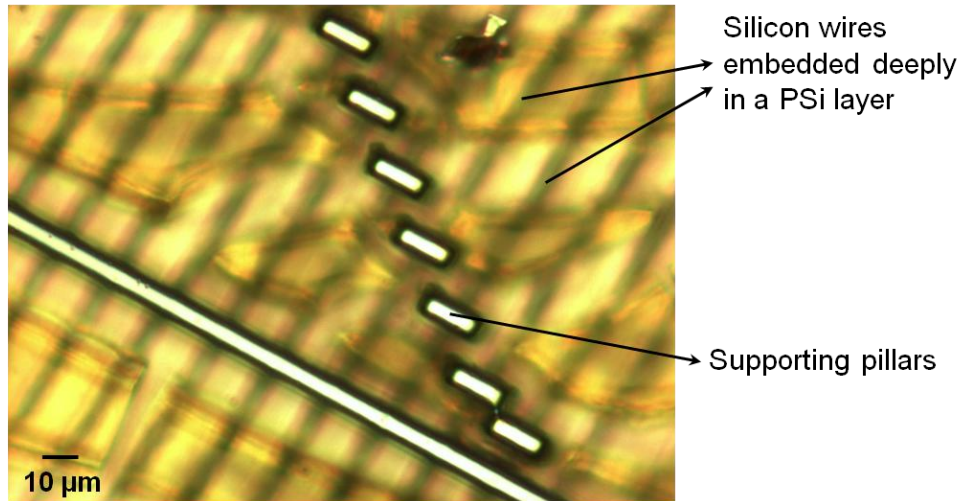


Figure 6-3 : Optical image of embedded silicon wires in PSi layer. The supporting walls appeared bright as they are not etched hence not embedded in PSi and they are very smooth. The fluence used for irradiating them is high enough to form the PSi on top of these regions. Figure 6-4 (a) shows the same sample after removing the PSi.

Very dilute KOH solution can be used for removing the PSi and making the wires completely free-standing. Figure 6-4 shows SEMs of free-standing silicon wires after removing the PSi. None of the wires shown in Figure 6-4 (b) have broken, showing that free-standing wires with diameter of about 1 μm can be produced over 400 μm long.

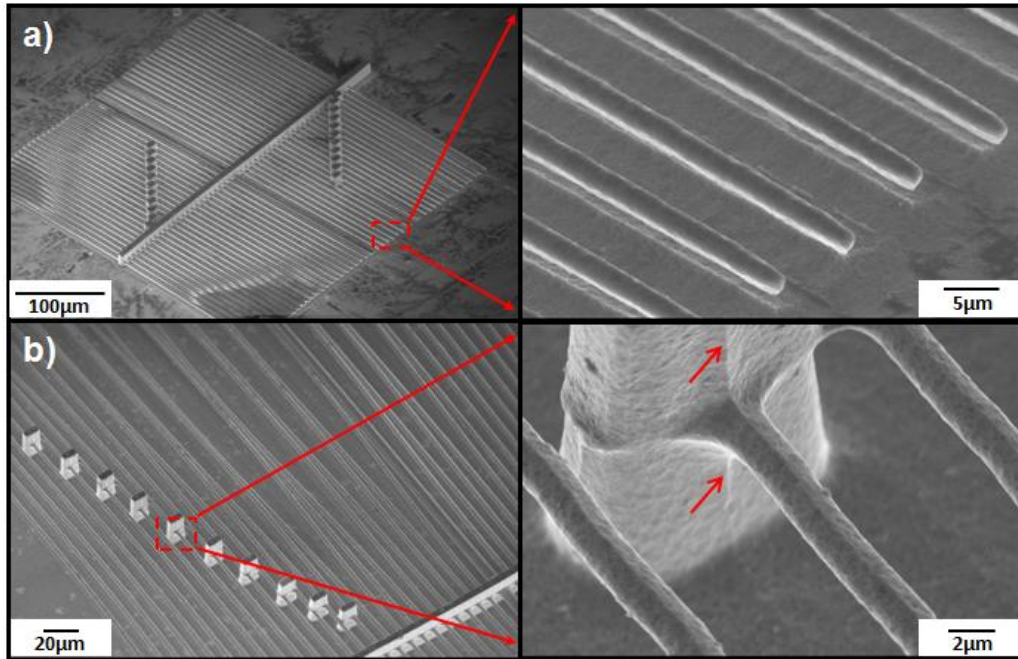


Figure 6-4 : SEM images of 3D machined arrays of free standing cores forming various shapes, supported by heavily irradiated silicon walls in a 0.4 Ω .cm wafer. (a),(b) show wires and their close-up views.

The higher magnification SEMs in Figure 6-4 (a),(b) respectively show the end of the wires suspended above the etched silicon surface and details of where the wire joins the support. Note a widening of the wire where it meets the support and the slight protrusion at the support in the vertical direction, both above and below the wire, indicated by arrows. Above the wire the protrusion is attributed to the lower defect density formed above the core by the 1 MeV proton irradiation. This is not high enough to stop anodization above the wire, but enough to produce a slight decrease in etch rate at the support wall where the defect density is already high. The protrusion below the wire reflects the depth beneath the core of about 3 μ m at which the hole current flowing to the surface starts to bend around the wire, reducing the current density at the supporting wall. In the higher magnification SEM in Figure 6-4 (b), the protrusion of the underlying silicon surface reflects the reduced etch rate associated with the core formation.

6.3.1 Dimensions of the free-standing silicon wires

Different parameters influencing the cores' shape and diameter were described in detail in chapter 5.2. Figure 6-5 shows free-standing wires fabricated with the same method and irradiation and anodization conditions as the wires produced in Figure 6-4. The only difference is the irradiated Ψ of the wires is varying: (a) $2 \times 10^{10}/\text{cm}$, (b) $4 \times 10^{10}/\text{cm}$, (c) $8 \times 10^{10}/\text{cm}$, (d) $1 \times 10^{11}/\text{cm}$, (e) $2 \times 10^{11}/\text{cm}$, (f) $4 \times 10^{11}/\text{cm}$. As viewed from the top, for these fluences the width of the end-of-range core size changes from 3 μm , 3.9 μm , 4.4 μm , 5.2 μm , 5.5 μm to 6.3 μm respectively. The vertical elongation of the cores is also clear by increasing the Ψ of the wires. The change in the free-standing wires' cross-sections is consistent with what was described in chapter 5.2.

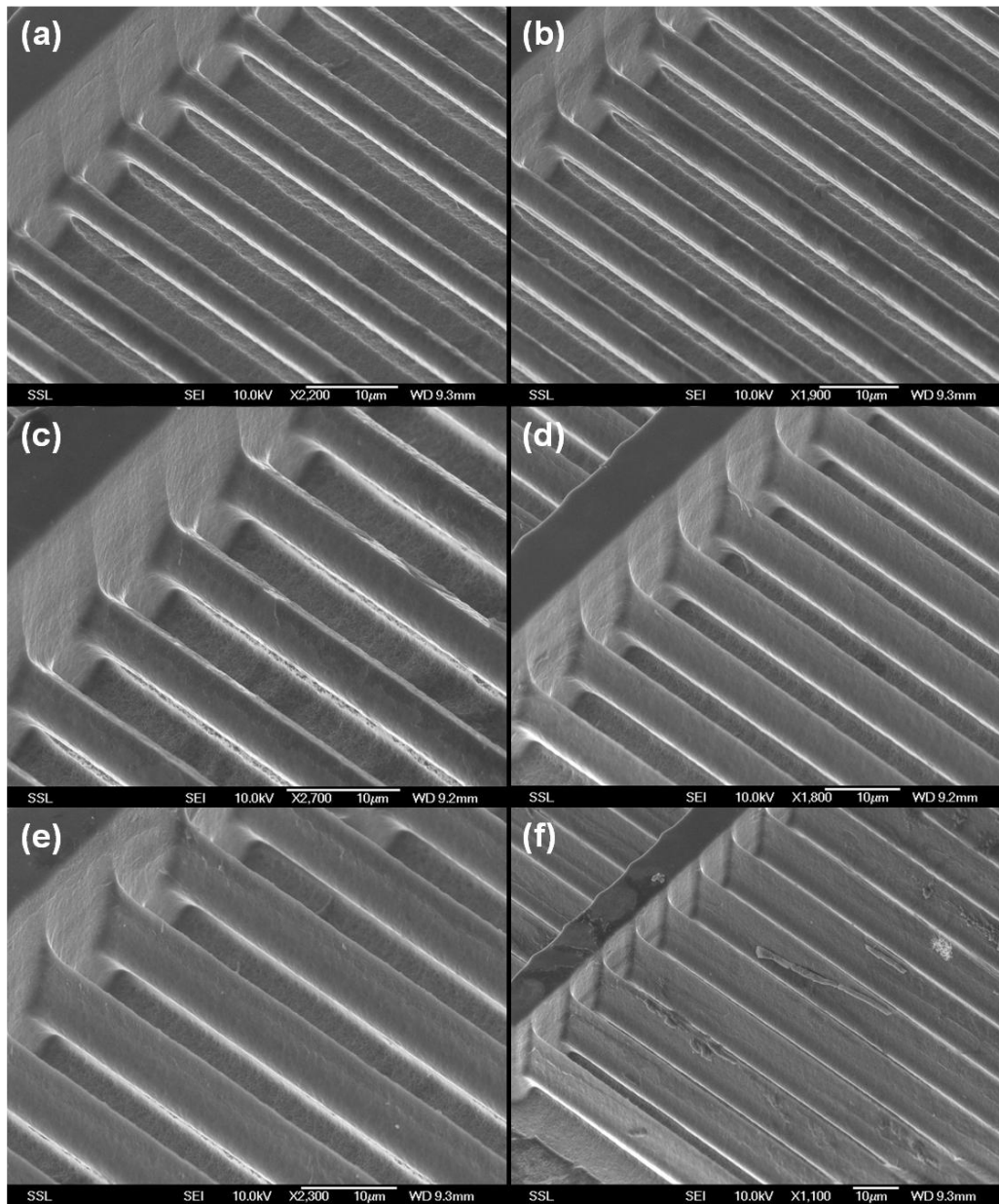


Figure 6-5 : Free-standing silicon wires formed in a 0.4 Ω .cm wafer and irradiated with: (a) $2 \times 10^{10}/\text{cm}$, (b) $4 \times 10^{10}/\text{cm}$, (c) $8 \times 10^{10}/\text{cm}$, (d) $1 \times 10^{11}/\text{cm}$, (e) $2 \times 10^{11}/\text{cm}$, (f) $4 \times 10^{11}/\text{cm}$.

6.3.2 Reducing the wire size by thermal annealing

After the fabrication process, the cores can be made narrower and smoother by oxidation. Figure 6-6 (a), (b) show SEM images of free-standing silicon wires formed in a 0.02 Ω .cm wafer using 500 keV protons before and after oxidation respectively. The core was annealed at 1100°C for 3 hours in air. The silicon dioxide layer surrounding the core was subsequently removed by a dilute HF solution.

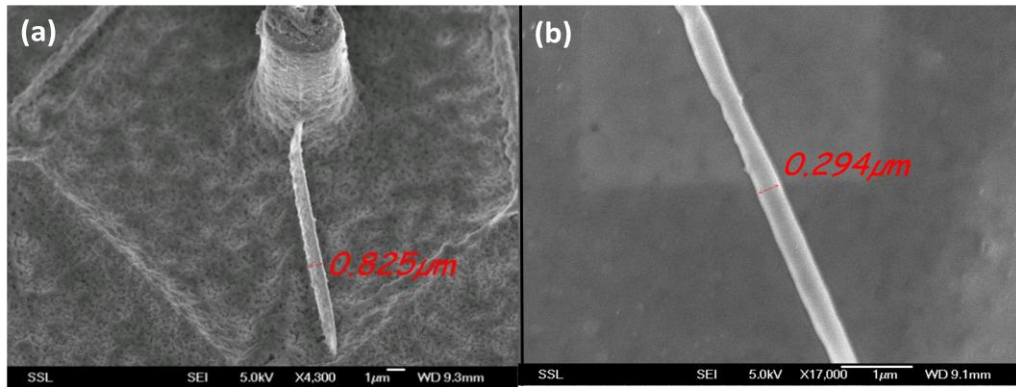


Figure 6-6 : Silicon wire (a) before (b) after oxidation.

Repeating the oxidation and removing the surrounding PSi layer can make the wire become even narrower and smoother. Figure 6-7 shows SEM images of different free-standing 3D wires after oxidation in air for 1100°C for 3 hours and removing the PSi with diluted HF solution. The starting core diameters in Figure 6-7 (a)-(c) before oxidation were 480 nm, 550 nm and 620 nm respectively. Figure 6-7 (a) shows a successful smooth free-standing nano-wire with a diameter of less than 100 nm fabricated using our machining techniques together with post annealing and removing the silicon dioxide.

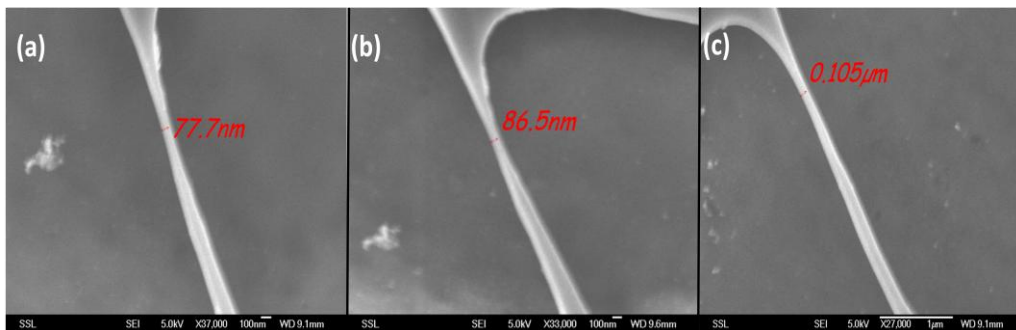


Figure 6-7 : 3D silicon nano-wires achieved after oxidation and removing the PSi.

Starting from smaller wire dimensions by using lower proton energies, or a lower fluence, or increasing the anodization current and/or using higher resistivity wafers as described in chapter 5.3.2, followed by thermal oxidation, is a promising route for obtaining free-standing nano-wires with diameters of tens of nanometers or less.

6.4 Fabrication of complex 3D silicon structures using PBW

Using proton beam writing for selective irradiation gives the ability to directly fabricate arbitrary patterns, not necessarily just lines as described above. Figure 6-8 (a) shows a simple free-standing wheel supported by a pillar, fabricated using 1 MeV protons and a Ψ of $1.5 \times 10^{10}/\text{cm}$ as an example to show the further capability of this technique for fabricating more complicated structures in 0.4 $\Omega\cdot\text{cm}$ silicon. The axle was deliberately offset from the center of the wheel so that the wheel was held in place, rather than being free to rotate, so that it could be more easily recorded as a free-standing structure. Figure 6-8 (b) shows a grid structure, formed using the same process in the same wafer resistivity except using 250 keV protons (range 2.6 μm , FWHM width at the end-of-range of 460 nm), Ψ of $1 \times 10^{10}/\text{cm}$ to produce the end-of-range cores as a grid structure, again supported by higher energy irradiations. Since the FWHM beam spread at the end-of-range is considerably smaller than for 1 MeV protons used in chapter 6.3.1, a smaller wire cross-section of 800 nm is produced.

A variety of complex shapes silicon wires and structures can be fabricated with our process. For the sake of demonstrating the ability of fabricating complex, arbitrary-shaped silicon structures using PBW, a silicon star and butterfly are fabricated using 500 keV protons which have a range of $\sim 6.1 \mu\text{m}$ in silicon, with a Ψ of $\sim 1.5 \times 10^{10}/\text{cm}$ in a 0.02 $\Omega\cdot\text{cm}$ silicon wafer.

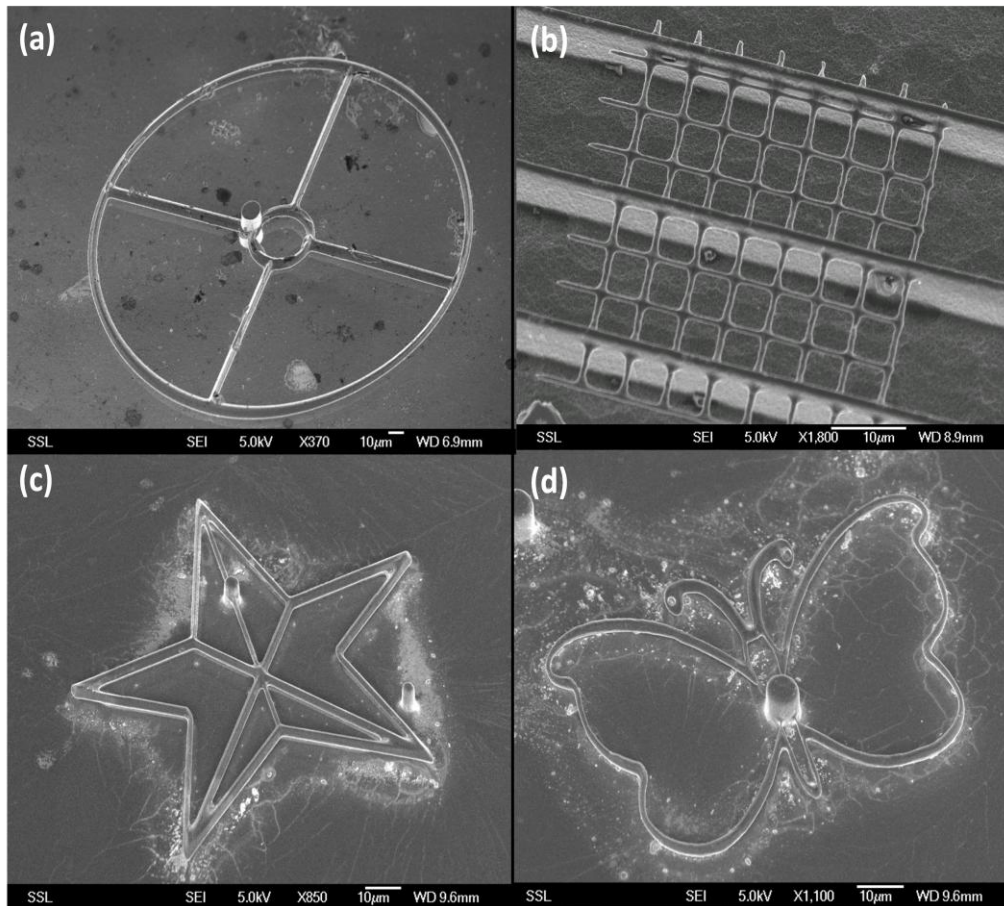


Figure 6-8 : (a) 3D machined wheel with a pillar for support. (b) grid formed by irradiation with 250 keV protons. (c) and (d) 3D star and butterfly irradiated by 500 keV protons.

Figure 6-9 shows a different type of 3D free-standing structure, a silicon spring, which can be fabricated using this approach. A silicon wafer with a resistivity of $0.02 \Omega \cdot \text{cm}$ was irradiated with a Ψ of $1.5 \times 10^{10}/\text{cm}$ using 500 keV protons. For demonstrating the effect of oxidation in reducing the core size as well as smoothing our machined structures, the sample was annealed for 3 hours at 1100°C in air. Figure 6-9(a) and (b) show high magnification views of a silicon spring before and after oxidation respectively. A lower magnification view of the silicon spring after removing the silicon dioxide layer with a diluted HF solution is illustrated in Figure 6-9(c). Oxidation not only helps to reduce the structure size, but also with removing the remaining small particles of silicon or P_{Si} that were not removed with KOH, and hence the structure and background looks much smoother and cleaner after oxidation.

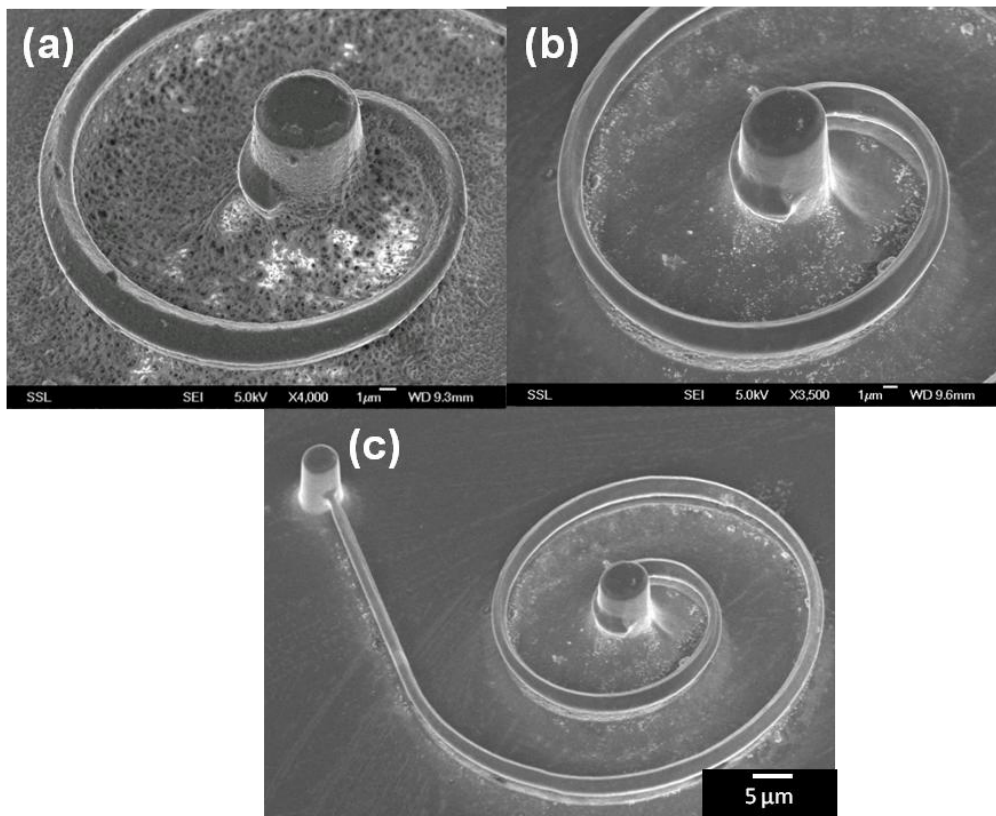


Figure 6-9: Free-standing 3D silicon spring fabricated with PBW. Silicon spring (a) before (b) after oxidation. (c) Large view of the silicon spring after oxidation.

6.5 3D silicon micromachining using large area irradiation

Although PBW described above is a useful approach for making prototypes for 3D silicon machining, the throughput is low due to the low currents when using a focused beam (chapter 2.5). Generally the required fluence for fabricating 3D structures is $\sim 10^{14}/\text{cm}^2$, for which the irradiation may take few minutes to tens of minutes depending on used ions (typically protons, H_2^+ or helium) and also the ion energy. In comparison, using our large area irradiation facility all the various structures can be irradiated at the same time using a high beam current of hundreds of nA over a sample size of up to $25 \times 25 \text{ mm}^2$. Another benefit of using large area irradiation is ensuring uniform irradiation, with no undesirable variations in fluence produced by any beam current fluctuations (chapter 2.5), which enables fabricating long uniform 3D structures. Hence, this section studies how to

implement rapid mass production of 3D free-standing silicon structures using a surface mask in conjunction with the large area irradiation facility at CIBA.

Using the large area irradiation setup the sample can be rapidly irradiated. However, the large beam current used during the irradiation can melt and change the shape of the thermoplastic resist polymer patterns (e.g. PMMA) due to increasing the temperature of the sample and resist by irradiation. This problem was solved by placing the sample on a specially-designed thermoelectric heat pump or Peltier device (5.3W, model CP1.0-31-08L) which is connected to a copper stick, to transfer the heat from the sample to outside of the chamber and hence cool the sample. This method proved efficient in cooling down the sample to prevent the resist melting or becoming distorted during irradiation.

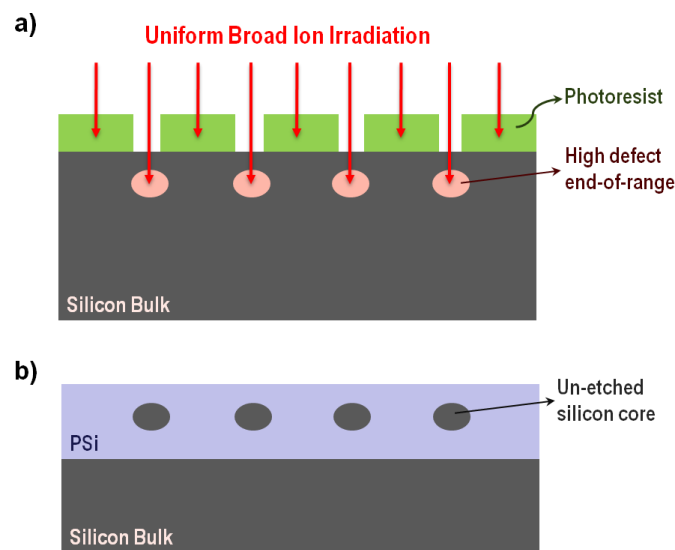


Figure 6-10 : Schematics of the processes involved in fabricating free-standing 3D structures using (a) broad uniform irradiation over a sample covered with a desired resist pattern. The resist is thick enough to stop the incoming ions completely. (b) anodization to produce PSi around the cores, leaving the cores intact. The PSi can be removed if desired, to make free-standing 3D structures.

In order to mass produce 3D silicon structures, a surface mask with desired patterns on top of a wafer together with our large area irradiation facility is required. A schematic of this process is shown in Figure 6-10. A moderate Ψ is used to create end-of-range defects in the desired area of the wafer. The effect of

irradiation and the subsequent electrochemical anodization is the same as that described in chapter 6.1 and 6.2. Depending on the desired structure size and depth in silicon, UV lithography, e-beam lithography or X-ray lithography may be used for mass production of 3D silicon structures and were all considered here. While structures typically larger than 2 μm can be mass produced using UV lithography, e-beam and X-ray lithography are ideal for smaller structures with small spacing between them. Since the pattern resolution of e-beam lithography is dependent on the resist thickness, only low energy irradiation which produces shallow end-of-range defects, is possible using this approach. However, mass production of 3D silicon structures deep inside the bulk silicon is possible by using a thick X-ray lithography patterned resist mask and high energy ion irradiation.

6.5.1 UV-lithography

For obtaining 3D silicon structures having micron-scale dimensions or larger, UV-lithography can be used to pattern the surface of the wafer with the desired patterned resist mask prior to the irradiation step. The resolution of the resist structures depends on the thickness of the resist layer. The thicker the resist layer becomes, the larger the minimum structure size is. In most of our 3D silicon machining work, the resist should be thick enough to stop the high energy ions (typically 500 keV- 2 MeV protons and heliums) in the silicon regions covered with the resist. Depending on the end-of-range of the ions used, which is determined by ion type and energy, different resist thickness can be used.

For demonstrating this ability, standard UV lithography was used to pattern 30 μm lines on a 20 μm thick photoresist covering a 0.02 $\Omega\cdot\text{cm}$ wafer. Large area irradiation was then used to irradiate the sample with 1 MeV protons and a fluence of $8 \times 10^{13}/\text{cm}^2$. The photoresist was thick enough to stop the

incoming ions completely, creating defects only in the uncovered silicon regions. Figure 6-11 shows a cross-section SEM after removing the photoresist and subsequent electrochemical anodization.

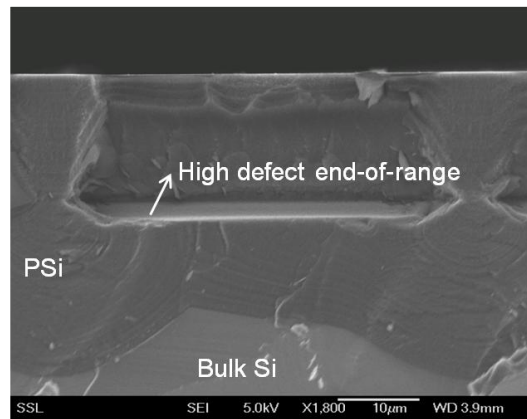


Figure 6-11 : Silicon machining using UV lithography pattern in conjunction with large area irradiation.

Although UV lithography is an easy and flexible method for fabricating large patterns to be transferred into silicon, an alternative method is needed when the required structure size is smaller. For cases where small structures with small gaps between them are required, using e-beam and X-ray lithography are good alternatives and hence will be described in the following sections.

6.5.2 E-beam lithography

Fabricating smaller cores (hundreds to few tens of nm) with smaller gaps between them is desired for some applications, for instance for fabricating single mode silicon waveguides which requires core sizes of about 300 to 400 nm[110], or being able to couple light between adjacent waveguides, or into resonator structures, both of which require gaps of hundreds of nanometers or less. E-beam lithography can be employed for high resolution patterning and/or small features. One limitation of using e-beam lithography is the limited thickness of the resist (described in chapter 2.1), therefore when using e-beam patterned masks, only low energy ion irradiation can be used, which is ideal for making nano-structures (chapter 5.2.1), but a limitation for fabricating structures deep inside the wafer.

To show the ability of 3D silicon machining using large area irradiation through e-beam mask pattern, a 0.4 $\Omega\cdot\text{cm}$ wafer was first patterned using e-beam lithography to pattern a 1000 nm thick PMMA (polymethyl methacrylate) layer with line widths of 90 nm Figure 6-12 (a). A resist-coated wafer was then irradiated with a Ψ of $1.3\times 10^9/\text{cm}$ using 100 keV H_2^+ . When H_2^+ ions impact on the surface they break into two 50 keV protons, which have a range of about 470 nm in silicon and 820 nm in PMMA. The PMMA layer is therefore thick enough to stop 50 keV protons, so the only wafer portions irradiated are through the 90 nm wide exposed areas. Anodization is performed using a dilute HF, with a current density of 40 mA/cm^2 for 1 to 4 minutes. To prepare samples for cross-section SEM, line lengths of several hundred microns were irradiated and the wafer was cleaved after anodization. Figure 6-12 (a) shows the resist pattern prior to irradiation on top of the silicon wafer and Figure 6-12 (b) illustrates the pattern transferred to the silicon sample beneath after irradiation and anodization. The resultant structure is a set of silicon cores formed within the PSi with diameter of few hundred nanometer. The cores vary in size even though the Ψ is constant, and this observation is important to the understanding of what core size is achieved by a given line fluence. Core sizes of ~ 200 nm are produced at large spacing between the irradiated regions, they decrease in size gradually by decreasing the spacing and disappear totally for line periods less than ~ 700 nm, where the etch rate starts to reduce from its unirradiated rate, as deduced by the silicon/PSi interface becoming shallower. We interpret this observation as follows: as the cores become closer together the etch current is forced to flow through the cores, resulting in them being progressively etched away. This emphasizes the importance of the location of a feature within an irradiated area in determining its final size. Figure 6-12 (c) shows a plan view SEM of similar structures, with the PSi removed. For

such narrow wires as observed here the usual removal process with diluted KOH destroys the silicon wires due to the large bubbling involved. Instead, first the PSi was oxidized and then removed using dilute HF, which involves little bubbling. This enabled removal of the PSi and observation of the remaining cores as free-standing nanoscale wires without being destroyed.

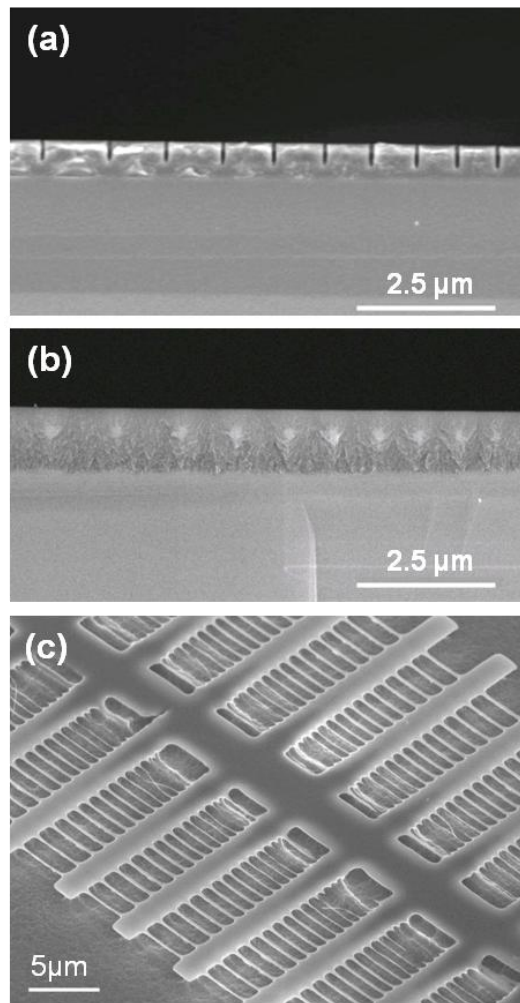


Figure 6-12 : Cross-section SEMs of (a) 1 μm thick e-beam patterned PMMA resist on top of 0.4 $\Omega\text{-cm}$ wafer, and (b) silicon cores formed inside the PSi after irradiation with $\Psi=1.3\times 10^9/\text{cm}$ using 50 keV protons and anodization. (c) shows plane view SEM of free-standing wires after removing the PSi.

Figure 6-13 shows cross-section SEMs of arrays of cores where a different approach is taken to fabricate very small gaps between the silicon cores. Larger periods and higher line fluences were used to make the resultant cores large enough so that they are not dissolved away under the flow of etch current through them at small gap sizes. The flattening of the upper core surface is because the

current flowing through the core etched the upper portions away. As the period is reduced from 650 nm to 550 nm, for a fixed Ψ , the gap size reduces. As the Ψ is increased, for a fixed period, the gap size also reduces, so producing a very small gap is just a question of finding the best combination between these two parameters. Gaps of about 50 nm are indicated in Figure 6-13 (c). For a period of 550 nm, on increasing the line fluence the core height reduces, again due to the flow of current forced through the small gap, resulting in more flowing through the core region, so producing a thinner core. This effect is not observed for the 650 nm line period, as this does not result in such small gaps. This sort of small gaps between the nanowires can be used for nanostencil mask fabrication which is described in chapter 8.4.

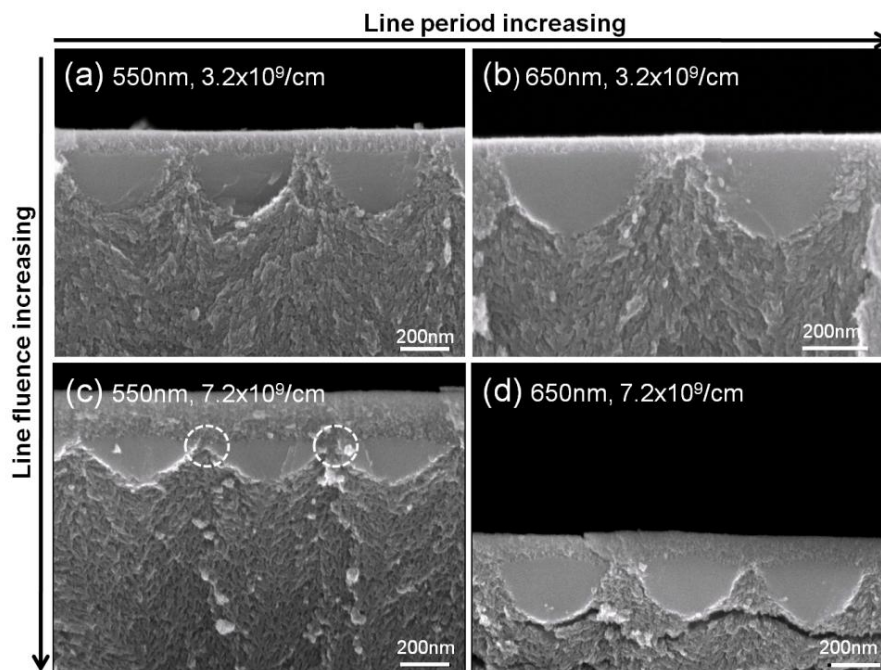


Figure 6-13 : Cross-section SEMs of individual cores in 0.02 $\Omega\cdot\text{cm}$ wafers irradiated with 50 keV protons with varying period and line fluence.

6.5.3 X-ray lithography

As described above, by using e-beam lithography in conjunction with large area irradiation, fabrication of small structures which are deep inside the silicon wafer is not possible, as the thickness of the resist limits the ion energies, therefore 3D

nano-structures cannot be produced deeper than $\sim 1 \mu\text{m}$ inside the bulk silicon. Also, using UV-lithography which enables thick resist patterns, limits the dimension of the structures to micrometer sizes.

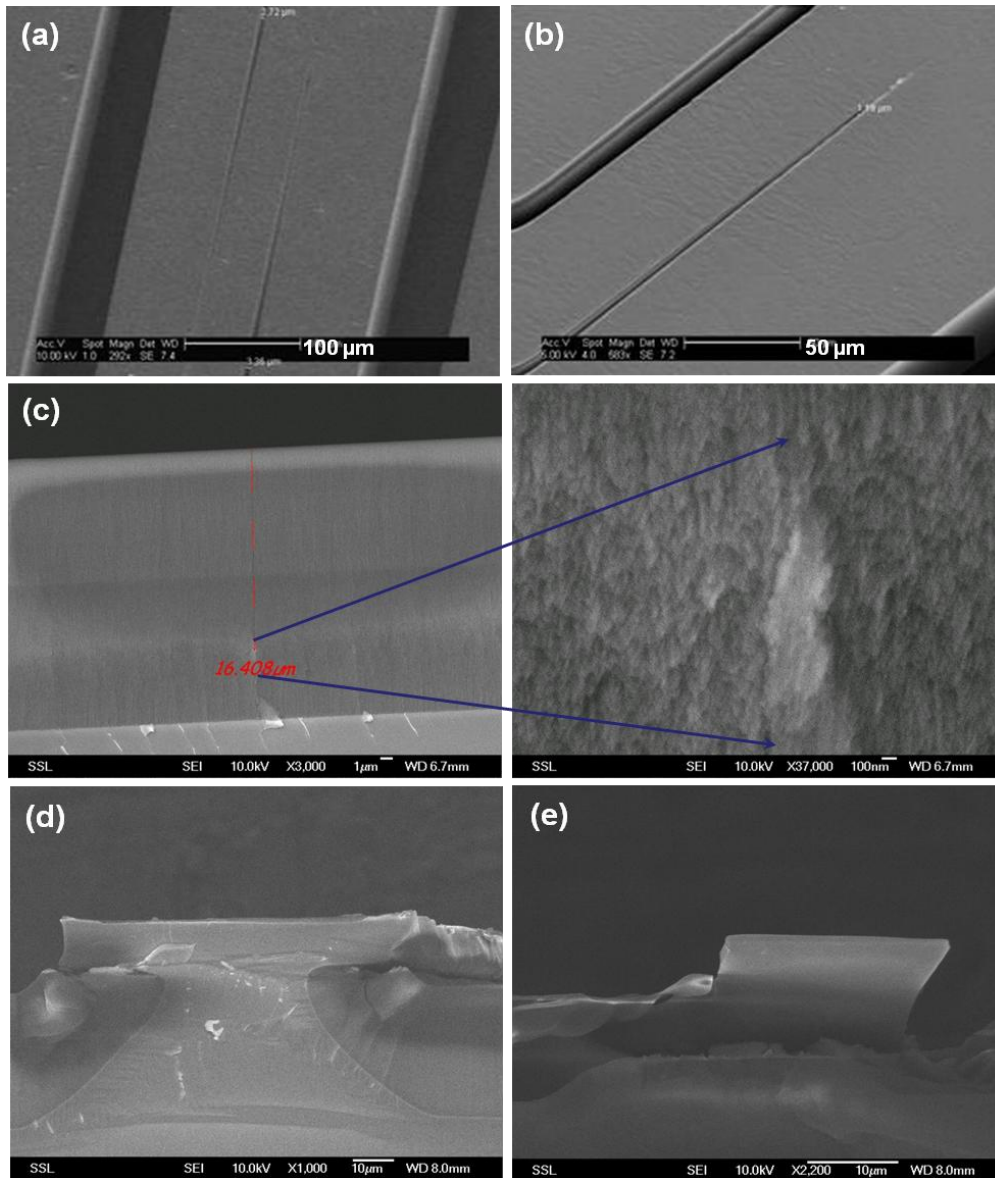


Figure 6-14 : (a),(b) show SEMs of a 150 μm thick PMMA layer patterned using X-ray lithography. (c) Cross-section SEM images of a core formed 16 μm deep inside the sample irradiated with 1 MeV protons and a Ψ of $1.6 \times 10^{10}/\text{cm}^2$ after anodization. (d),(e) Cross-sectional SEMs of larger cores formed using X-ray lithography patterns and large area irradiation facility with fluence of $1.2 \times 10^{15}/\text{cm}^2$ and $8 \times 10^{14}/\text{cm}^2$ respectively. The wide silicon region in (d) needs to be etched for longer time to be completely undercut.

A solution to this problem was explored using X-ray lithography for patterning PMMA layers prior to the irradiation step, which enables patterning thick resists with feature sizes ranging from a few hundred nanometers to hundreds of microns. X-rays penetrate much deeper in the material than an

electron beam while staying well collimated, hence can be used for fabricating high aspect ratio structures.

To make an X-ray mask with openings ranging from hundreds of nanometers to a few hundred μm , two existing gold stencil X-ray masks having line openings of 40 μm and 120 μm were overlapped and stuck together and used for making high aspect ratio PMMA patterns. The two masks were aligned using an optical microscope, and were purposely slightly offset from being parallel to achieve small, tapered openings in the final mask, with the width changing along the mask. This setup could be later improved by making a new X-ray mask with accurate design and dimensions. This X-ray mask was used to pattern a thick PMMA layer with a thickness of 150 μm . After exposing the PMMA with an X-ray fluence of $\sim 3.5 \times 10^{13}/\text{cm}^2$ using the Synchrotron radiation facility at the Singapore Synchrotron Light Source (SSLS), the samples were developed for 2 hours at 30°C and rinsed in DI water for 30 minutes at the same temperature, Figure 6-14 (a), (b). PMMA line patterns changing from 200 nm to 100 μm were achieved. The samples were irradiated using large area irradiation facility with 1 MeV protons with a Ψ of $1.6 \times 10^{10}/\text{cm}$ and $3.5 \times 10^{10}/\text{cm}$. The samples were then 20 μm anodized. Figure 6-14 (c) shows cross-section SEM images showing a small core with a few hundred nanometer width formed in the depth of 16 μm inside the bulk silicon surrounded by the PSi layer. The PSi was then removed with diluted KOH solution and the sample was anodized for another 20 μm . This was done mainly because after the first etching the wide irradiated structures were not completely undercut, and in order to prevent the PSi cracking because of the layer thickness, the PSi formed after the first anodization step was removed. Figure 6-14 (d), (e) shows a patterned area about 50 μm wide which was transferred to the silicon after irradiation with fluence of $1.2 \times 10^{15}/\text{cm}^2$ and $8 \times 10^{14}/\text{cm}^2$ respectively.

While appearing on the surface in these images, this patterned area was buried at the end-of-range of the proton irradiation, showing that large buried surfaces can be machined using this approach.

6.6 Summary

This chapter has demonstrated the ability of using localized defects created at the end-of-range of high energy protons for machining complex true-3D silicon structures within bulk silicon after subsequent anodization process. PSi can then be removed if desired, to make free-standing 3D silicon micro/nano-structures in bulk silicon. This process can be an important development in fields such as silicon photonics and M/NEMS.

While proton beam writing gives more flexibility in designing the structures during the irradiation step, rapid mass production of 3D silicon structures is possible using a patterned resist mask on the sample surface, prepared by UV lithography, e-beam lithography or X-ray lithography, in conjunction with large area irradiation.

Chapter 7 : Curved and Multilevel 3D Silicon Structures

This chapter presents the ability of our new developed 3D silicon machining technique to fabricate complex, curved, multilevel 3D silicon structures using a single etch step in bulk silicon. The general ideas underlying this machining technique were discussed in chapters 5 and 6. This chapter focuses on further developing this unique technique for fabricating curved, multilevel, free-standing 3D silicon structures using a gray-scale surface mask and/or multiple energy exposure. Developing this state-of-the-art method to achieve 3D integrated systems can improve device performance and packing density as well as providing the ability of fabricating custom-shaped structures. Such highly compact 3D systems-on-a-chip offer abundant possibilities and applications for developing future micro/nanotechnologies in many different fields.

7.1 Fabrication of curved 3D silicon structures

3D silicon structures can be achieved by moderate fluence irradiation and subsequent electrochemical anodization of the wafer in dilute HF solution. The localized defects created at the end-of-range region tend to remain unetched, whereas surrounding regions are etched, leaving a small diameter core surrounded by PSi, which can be removed afterwards if desired. In a similar manner, 3D silicon microstructures which are curved in the vertical plane can be micromachined, with the addition of a thin, patterned gray-scale resist mask with sloping edges on the wafer's surface prior to the irradiation step. This process is described in Figure 7-1.

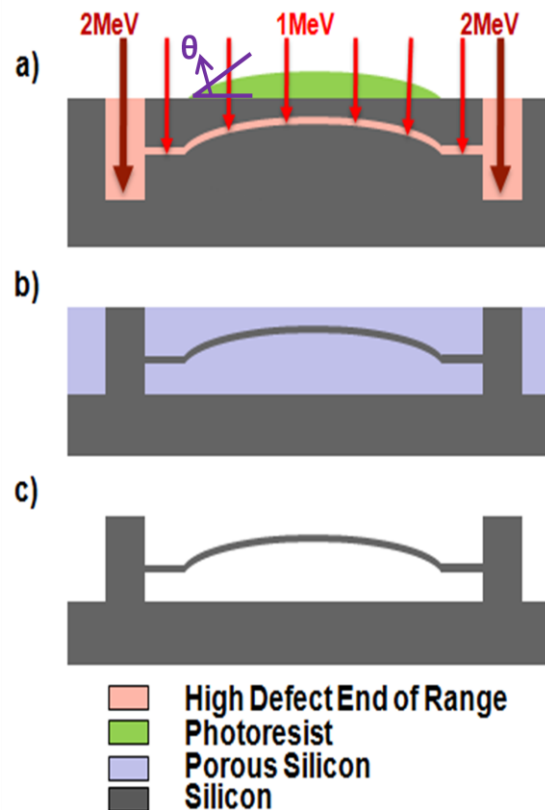


Figure 7-1 : Schematics of the processes involved in fabricating curved free-standing 3D wires using (a) 1MeV proton irradiation for wires and 2MeV protons with a high Ψ for supporting walls, (b) anodization to produce PSi around the cores and (c) removal of the PSi leaving a free-standing structure.

The top resist on the sample must be thin enough so that protons can pass through and reach the underlying silicon. Because of the resist thickness, the end-of-range of the protons in the silicon is modified according to the profile of the resist. Such spatial variations of the end-of-range results in 3D silicon microstructures which are curved in the vertical direction.

Another consideration for this work is the angle θ of the resist with the silicon surface. Figure 7-2 shows a failed example where θ was too sharp. A 0.4 Ω .cm silicon wafer was covered with 8 μ m thick SU-8 resist lines of 5 μ m width. The width of the sloping edge is \sim 1 μ m, so $\theta \sim 83^\circ$. The sample was irradiated with a parallel line pattern using PBW with 1 MeV protons and $\Psi=1 \times 10^{10}/\text{cm}$ to form curved 3D wires, while a Ψ of $1.2 \times 10^{12}/\text{cm}$ of 2 MeV protons was used to create supporting walls for free-standing wires. After irradiation and removing the resist

from the wafer, the sample was electrochemically etched followed by removing the PSi using dilute KOH solution. Here, the curved wires are broken because of the large θ . The red line in Figure 7-2 (b) indicates the location of the resist line during irradiation, showing the 3D wires are broken at base of the resist line.

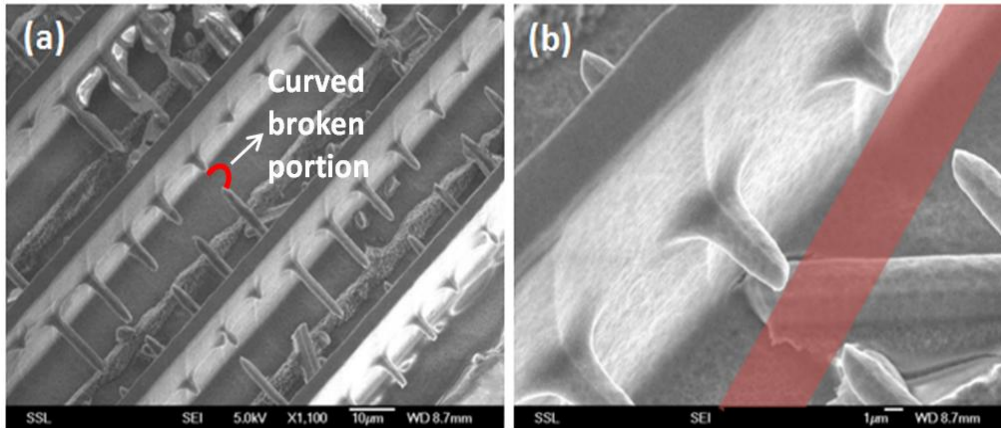


Figure 7-2 : (a) SEM images of an example failure in fabrication of curved 3D wires due to the sharp angle (θ) between the resist pattern and the wafer surface. The red curved line shows an example of the place of the curved wires which are broken and removed. (b) magnified view of such failure with the red line indicating the location of the resist line pattern during the irradiation.

To overcome the problem of breaking of the 3D free-standing structures owing to the large θ , the patterned resist should have smooth edges and a more gradual slope. Two methods for making such a resist pattern were studied: thermal reflow of PMMA after UV lithography, and two-photon lithography of SU-8.

7.1.2 UV lithography followed by thermal reflow of PMMA

Thermal reflow of a thermoplastic polymer can be used for fabricating resist patterns with smooth edges [111]. A silicon wafer was first patterned with 8 μm thick squares of PMMA resist using standard UV lithography (Figure 7-3 (a)), and it was then placed on a hot plate at 200°C for 30 mins. Figure 7-3 (b) shows an optical image of the resist with sloping edges after the thermal reflow process.

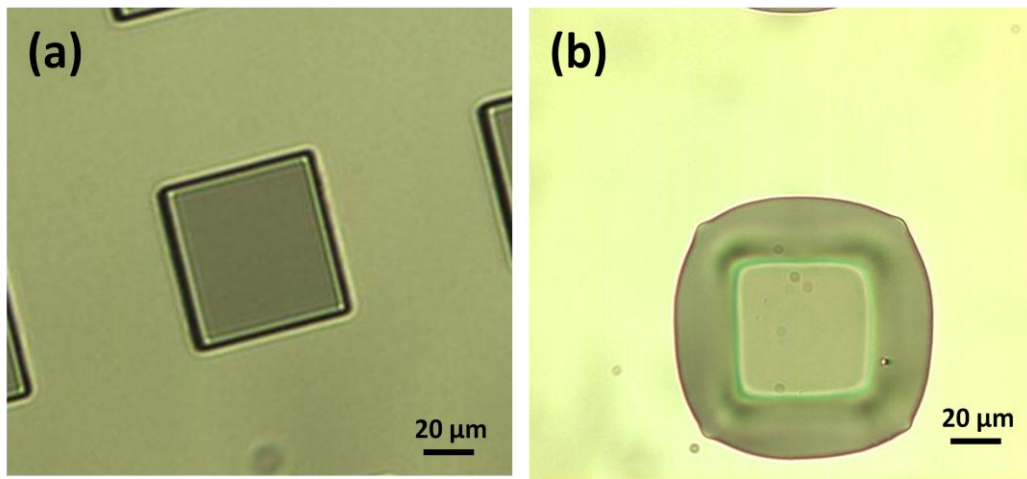


Figure 7-3 : PMMA resist pattern (a) before (b) after thermal reflow.

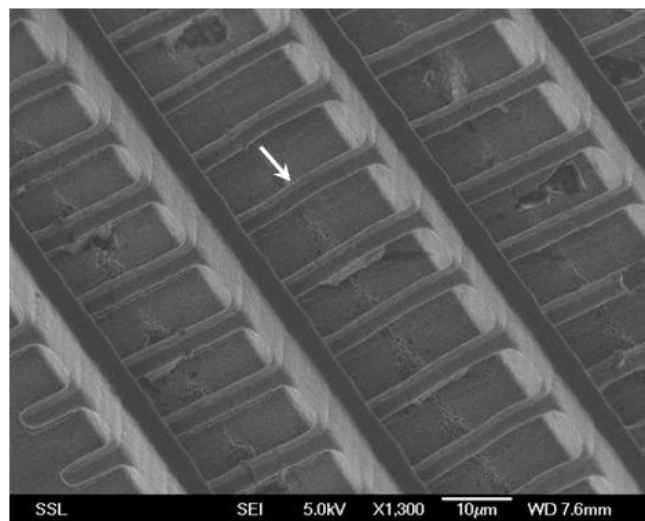


Figure 7-4 : SEM of curved wires fabricated via PBW of lines over the resist pattern shown in Figure 7-3 (b). The arrow indicates in the bend in the wires following the resist profile on the surface of the wafer.

The resist pattern shown in Figure 7-3 (b) has sloping edge with a width of $23 \mu\text{m}$ and height of $8 \mu\text{m}$, giving an angle of $\theta \sim 19^\circ$ between the resist and silicon surface. This pattern was used for fabricating curved 3D silicon wires. The sample was irradiated with a parallel line pattern using PBW with 1 MeV protons and a Ψ of $2 \times 10^{10}/\text{cm}^2$ to form curved 3D wires, while a Ψ of $1.2 \times 10^{12}/\text{cm}^2$ of 2 MeV protons was used to create supporting walls for free-standing wires. Figure 7-4 shows the successful fabrication of curved 3D silicon wires following the shape of the resist on the wafer's surface after the irradiation, anodization and PSi removal. The white arrow in Figure 7-4 shows the bend in the wires. This approach is cheap, but limited in what surface profiles can be achieved.

7.1.3 Two-photon lithography

Two-photon lithography (TPL) is a very flexible technique for fabrication of gray-scale resist masks. Another approach explored for fabricating resists with smooth edges was utilizing TPL for patterning a SU-8 resist on silicon wafers. This process is done at the CIBA photonics laboratory. Ultrafast laser pulses, with a centre wavelength of 800 nm and pulse width of approximately 150 fs, are generated by a mode-locked Ti:Sapphire oscillator and can selectively polymerize a small focal volume inside the photoresist [112]. By scanning the stage in all three dimensions, an arbitrary 3D polymer structure can be fabricated. For this purpose, the 3D design of the mask is first sliced in AutoCAD into layers of 2D bitmaps, which are then patterned by the laser, with different layers at different height levels. The distance between each layer is set at 0.6 μm to avoid the "step" shape sidewall profile. Although the 800 nm wavelength is far from the absorbance peak of SU-8 which is located near 400 nm, at the tiny focal volume, a peak power as high as 150 kW is achieved, allowing the SU8 to be polymerized by simultaneously absorbing two photons. The gray-scale mask profile is finished after laser irradiation which is followed by post-baking the wafer at 95°C for 10 minutes before a final development and iso-propyl alcohol (IPA) rinse. The SU-8 should be thin enough to let the ions pass through and reach the wafer beneath.

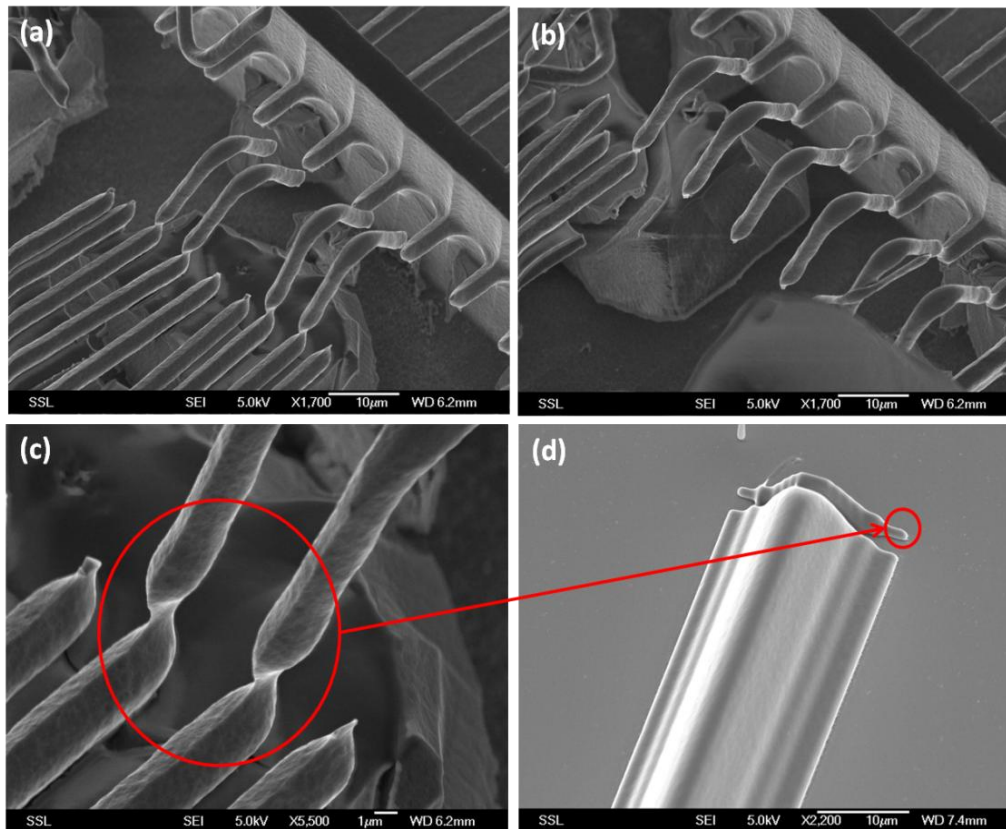


Figure 7-5 : Example of a failed fabrication of curved 3D wires due to the step at the edge of the resist pattern, $\Psi=1\times 10^{10}/\text{cm}$. (d) shows the resist line used on the sample to modify the end-of-range defects.

Figure 7-5 (a)-(c) show curved wires fabricated by PBW of lines over the resist pattern shown in Figure 7-5 (d), with 1 MeV protons and $\Psi=1\times 10^{10}/\text{cm}$. The irradiated lines are orthogonal to the resist lines on the silicon surface. There is a small, discontinuous resist step at the boundary of the resist pattern, see Figure 7-5 (d). Many of the curved wires of width of $\sim 1\ \mu\text{m}$, produced using this Ψ have broken because of this discontinuous resist step. However, we believe micrometer wide, curved lines can be successfully fabricated after optimizing the gray-scale mask patterning.

Using the same resist patterned in Figure 7-5 (d) thicker curved wires were produced by irradiation with 1 MeV protons with a high Ψ of $5\times 10^{10}/\text{cm}$ as shown in Figure 7-6. Because of the discontinuous resist step at the boundary, a high Ψ was used to produce a thick wire width of $5\ \mu\text{m}$ in Figure 7-6 to ensure that the

cores of the curved portion sufficiently overlapped with that of the bottom, flat portion, i.e. discontinuities in the curved surface are less critical.

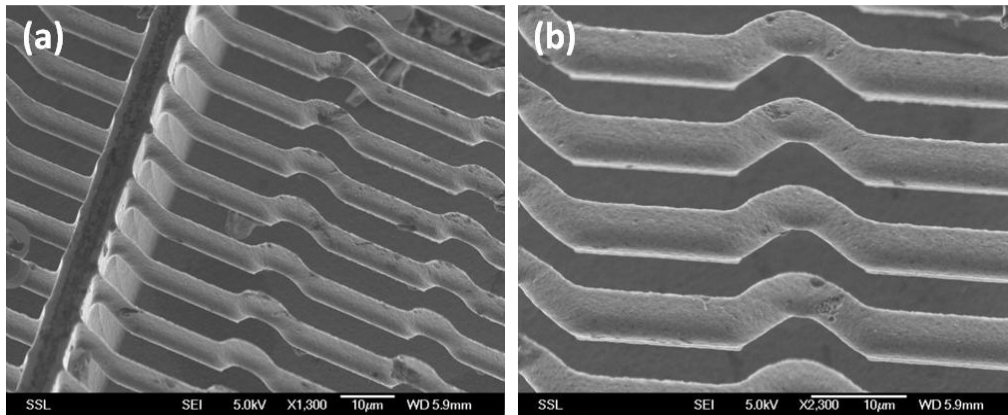


Figure 7-6 : Curved 3D free-standing silicon wires, $\Psi=5\times 10^{10}/\text{cm}$.

After fabrication the cores can be made narrower and smoother by oxidation. Figure 7-7 (a) shows the same free-standing 3D silicon wires fabricated in Figure 7-6 with a Ψ of $5\times 10^{10}/\text{cm}$, while Figure 7-7 (b) shows cross-sectional SEM images of another set of even thicker wires fabricated with a Ψ of $8\times 10^{10}/\text{cm}$. Figure 7-7 (c),(d) illustrate the cores formed respectively in Figure 7-7 (a),(b) after oxidation at 900°C for 4 hours in air. The effect of oxidation in reducing the 3D silicon cores' size and roughness is clear. If required, the silicon dioxide layer surrounding the core can be removed by a dilute HF solution.

TPL, which can fabricate complex resist patterns, enables the fabrication of complex 3D silicon structures by transferring the resist patterns to the silicon sample beneath after irradiation and anodization.

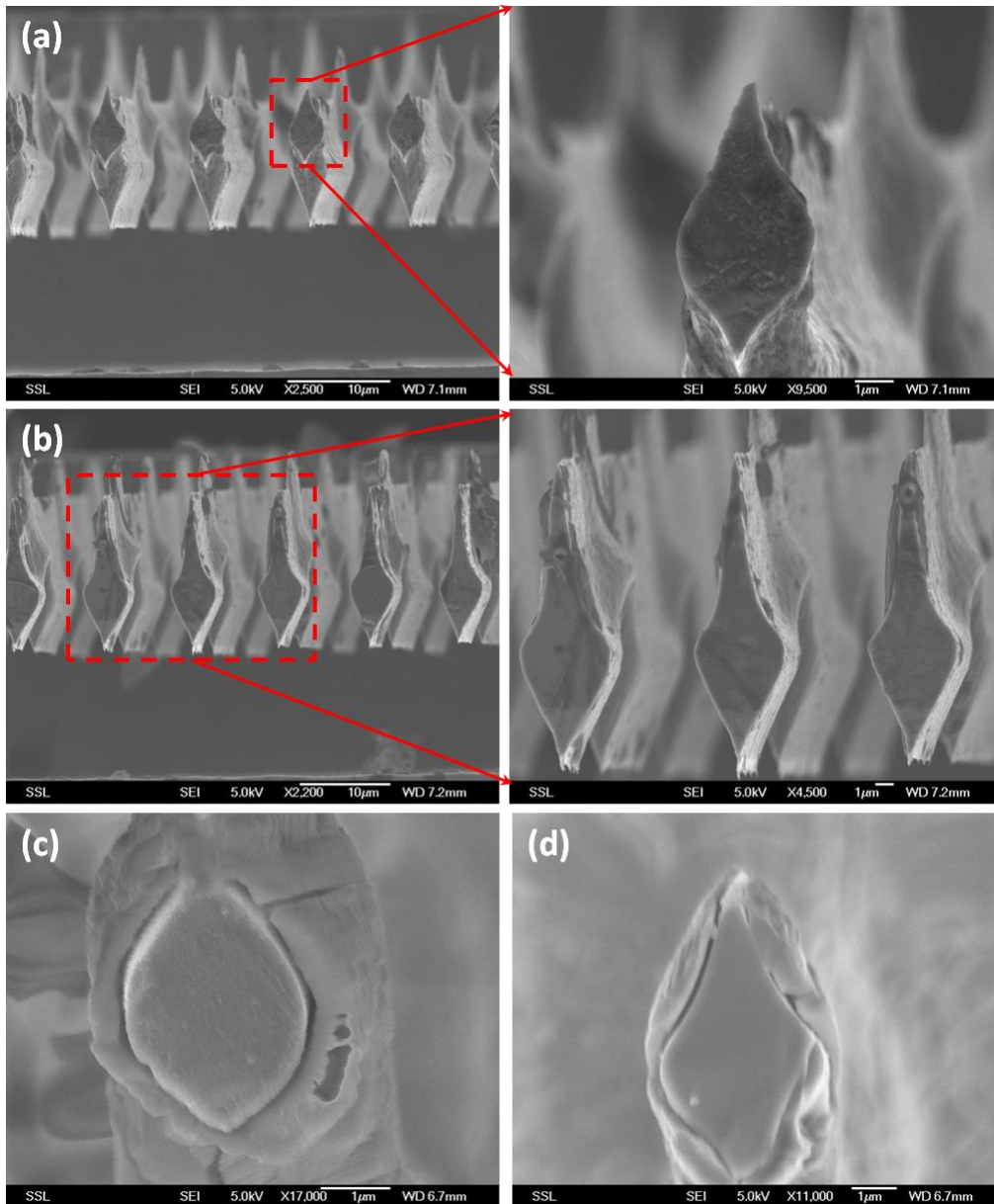


Figure 7-7 : Cross-sectional SEMs of free-standing silicon cores fabricated with (a) $5 \times 10^{10}/\text{cm}$ and (b) $8 \times 10^{10}/\text{cm}$ protons. (c),(d) show the cores after oxidation respectively.

7.2 Multilevel 3D wires

Multiple energy proton irradiation or multilevel resist pattern can be used to create localized defects at different depths within the silicon wafer to fabricate multilevel free-standing 3D silicon structures. This process is schematically described in Figure 7-8 using two different ion energies. After anodization the high defect core regions, produced by different proton energies, remain intact while the surrounding low defect regions between the cores form PSi. The Ψ of the highest

proton energy is the only factor which influences the formation of the deepest cores. However, the layers of cores closer to the surface, formed by lower energy irradiations, are additionally influenced by the defects produced by irradiation of the deeper structures, which increases the resistivity along the path. This additional increment in resistivity should ideally be low enough to not significantly influence the formation of the PSi along the low energy proton trajectory.

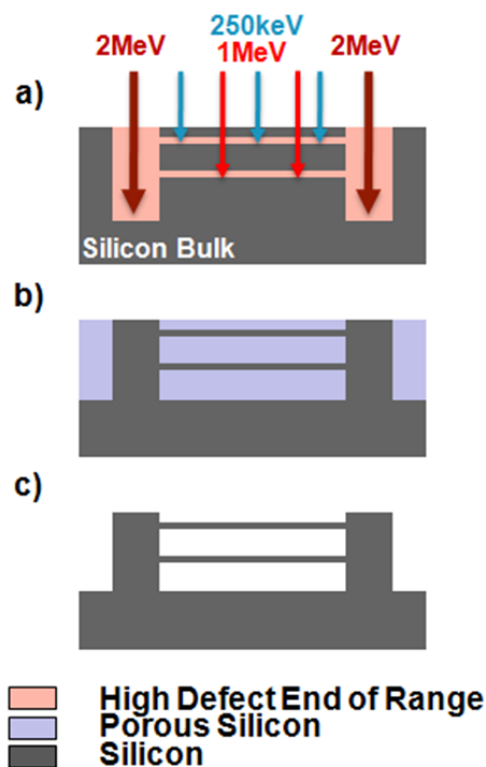


Figure 7-8 : Schematics of the processes involved in fabricating multilevel free-standing 3D wires using (a) 250 keV and 1 MeV proton irradiation for wires and 2 MeV protons with a high Ψ for supporting walls, (b) anodization to produce PSi around the cores and (c) removal of the PSi leaving a free-standing structures.

7.2.1 Fabrication of two-level silicon structures

An array of two-level silicon wires running in orthogonal directions was fabricated in 0.4 Ω .cm wafer with a period of 10 μ m, Figure 7-9 (a). Line irradiations using 250 keV protons with $\Psi=1 \times 10^{10}/\text{cm}$ and $\Psi = 7 \times 10^{10}/\text{cm}$ were used to fabricate shallow wires, while orthogonal line irradiations using 1 MeV protons with $\Psi=$

$1 \times 10^{10}/\text{cm}$ and $\Psi = 5 \times 10^{10}/\text{cm}$ were used to fabricate deeper wires, resulting in four different combinations of fluences within the array, indicated as [c] to [f]. Supporting walls were formed by irradiation using a 2 MeV proton Ψ of $1.2 \times 10^{12}/\text{cm}$. After anodization and PSi removal, orthogonal free-standing lines at different depths were revealed, Figure 7-9 (b).

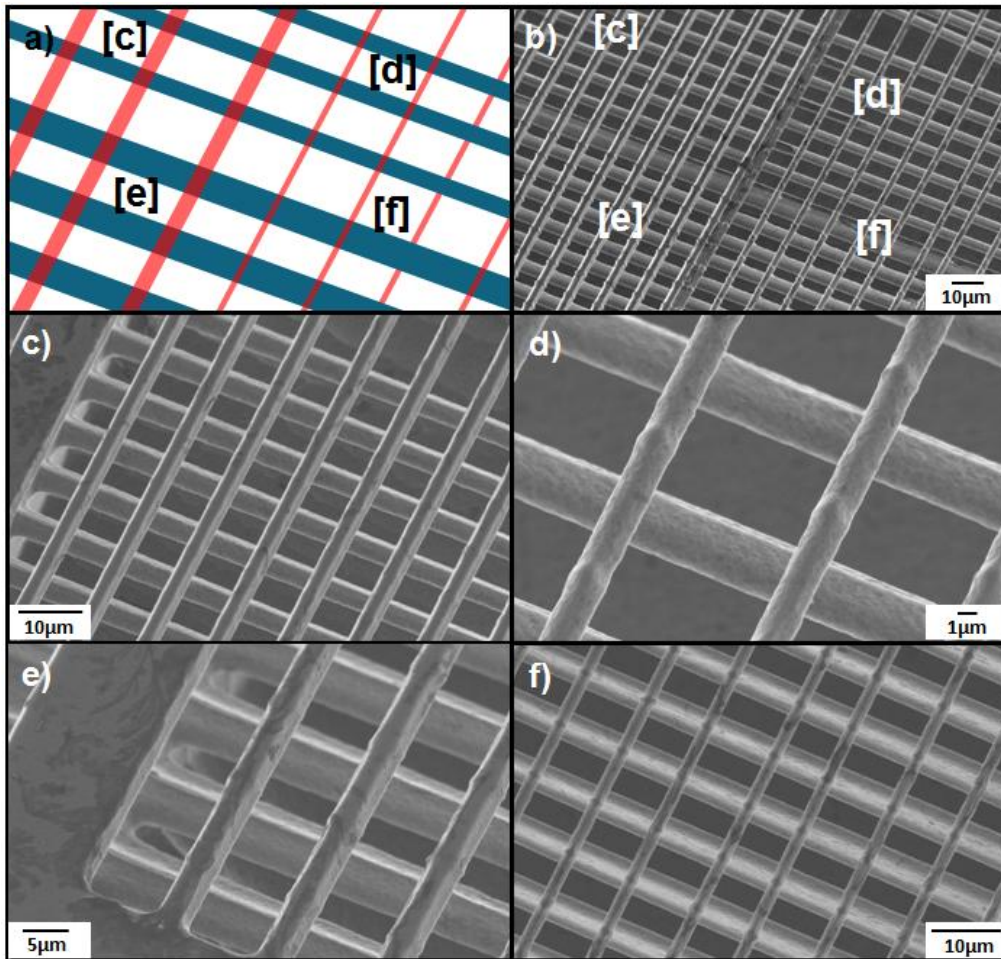


Figure 7-9 : (a) A schematic of a two level silicon wire array created with four irradiation combinations of Ψ and energy, where the thin/thick lines indicates a low/high fluence. Deep wires (shown in blue) are formed by irradiation with 1 MeV protons with a low Ψ of $1 \times 10^{10}/\text{cm}$ in portions [c,d] and high Ψ of $5 \times 10^{10}/\text{cm}$ in portions [e,f]. Shallow wires (shown in red) are formed by irradiation with 250 keV protons with a low Ψ of $1 \times 10^{10}/\text{cm}$ in portions [d,f] and a high Ψ of $7 \times 10^{10}/\text{cm}$ in portions [c,e]. (b) SEM showing the resultant 3D line array. (c)-(f) SEMs showing close up view of each combination, with same lettering as in Figure 7-9 (a),(b).

Higher magnification SEMs of the four different Ψ combinations within this array are shown in Figure 7-9 (c)-(f), corresponding to the same letters indicated in Figure 7-9 (a),(b). Wires irradiated at lower energy and lower Ψ are thinner due to the lower lateral scattering and the smaller extent of the core region.

Since both of these factors are important, the wire widths are similar in Figure 7-9 (c) even though they are formed with a factor of seven difference in Ψ . Small bumps on the shallow wires at overlapping regions are observed in Figure 7-9 (d),(f) owing to the additional defects produced by the orthogonal, high-energy irradiation, as discussed above. This effect is less pronounced in Figure 7-9 (c),(e) where the shallow wires were irradiated with a Ψ high enough to act as an etch stop, so additional irradiation of the deeper layer has little effect.

A limitation of this process is that the ability to reduce the period is limited by the difficulty of forcing the anodization current through a more densely irradiated array. Hence, while Figure 7-9 shows results obtained using a period of 10 μm , it becomes increasingly more difficult to fabricate smaller periods. We can overcome this limitation by using a lower resistivity wafer, such as was used in previous studies in chapter 5 and 6 [53, 113-115]. The higher wafer doping level makes it easier to leave sufficiently conducting paths for the hole anodization current to flow through a more densely packed structure.

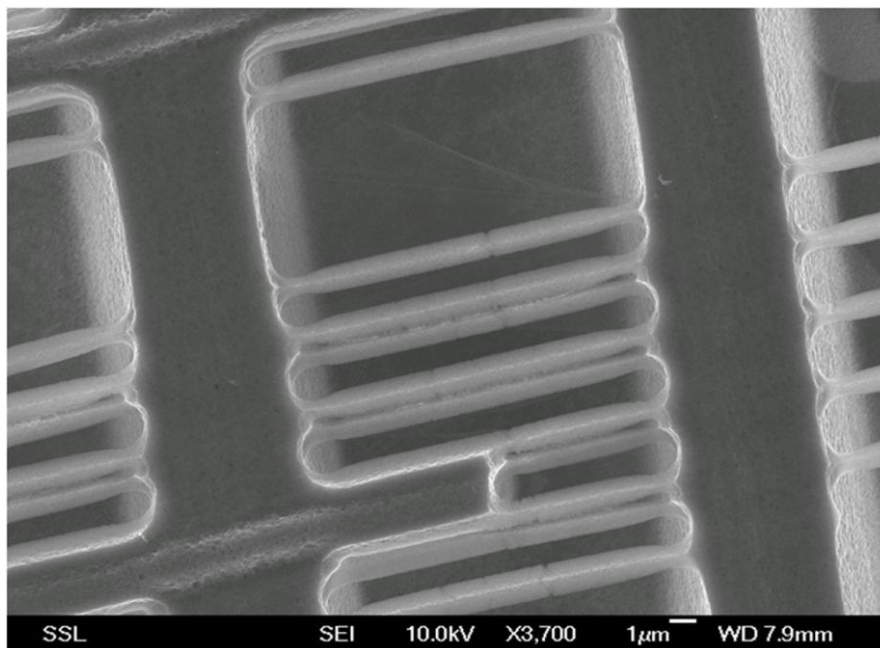


Figure 7-10 : Two-level array of parallel wires fabricated using 0.02 $\Omega\cdot\text{cm}$ silicon wafer.

Figure 7-10 shows a two-level array of parallel wires fabricated with the same process using 250 keV and 215 keV protons in 0.02 Ω .cm silicon. The two levels of wires were irradiated at the same surface locations, each with a Ψ of $4 \times 10^{10}/\text{cm}$ and a period of 3 μm . After anodization and removal of the PSi, free standing wires, supported by a wall fabricated at 1 MeV protons with a Ψ of $3 \times 10^{12}/\text{cm}$ are produced.

PBW is thus a unique technique which gives the ability of fabricating multilevel 3D silicon structures with any complex shape and any arbitrary angle between the different levels after a single etch step.

7.2.2 Fabrication of multilevel silicon structures

Though changing the energy by altering the accelerator terminal voltage is possible, it is time-consuming as for each of the energies, the beam needs to be re-optimized and re-focused.

Another approach is to use a multilevel resist pattern on the wafer surface to change the ion end-of-range depth for fabricating multilevel 3D silicon structures. This enables fabrication of many different levels of silicon structures using a single ion energy and irradiation, depending on the number of different levels of the resist pattern. All resist steps should be thin enough to let the ions pass through and form the end-of-range cores in the wafer beneath. This principle is similar to chapter 7.1 for fabricating curved 3D wires, however, here PBW is used to write lines perpendicular to the resist gradient instead of parallel to it. Figure 7-11 shows a general schematic of using a gray-scale resist pattern to form many different levels of 3D silicon structures in bulk silicon using a single ion energy and a single etch step.

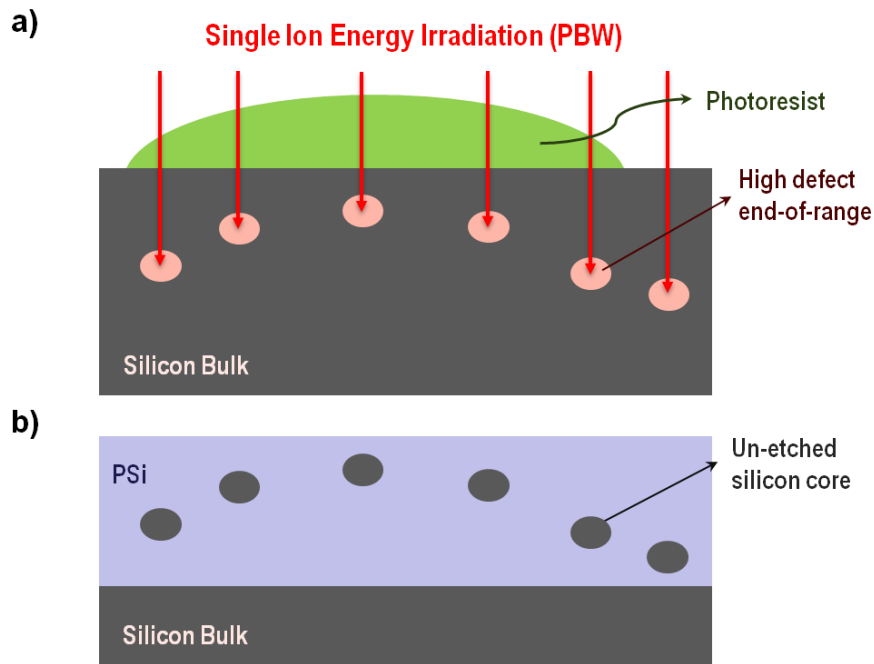


Figure 7-11 : Schematic showing fabrication of multilevel 3D silicon structures using a single ion energy. (a) the beam is scanned in line orthogonal to the page, resulting in (b) end-of-range cores at different depths.

Figure 7-12 shows an example of multilevel silicon wires all fabricated with 1 MeV protons. UV lithography of a line and spacing pattern of PMMA together with thermal reflow process similar to the process described in Figure 7-3 was used. An array of parallel lines was irradiated over it using PBW with 1 MeV protons and Ψ of $2 \times 10^{10}/\text{cm}$ to form wires, and a Ψ of $1.2 \times 10^{12}/\text{cm}$ of 2 MeV protons to create supporting walls for the free-standing multilevel 3D wires. The gradient of the resist thickness is used to change the penetration depth of ions. The arrow in the Figure 7-12 indicates the increasing depth of silicon wires as the resist thickness reduces. The wires closest to the surface of the wafer were irradiated through the thickest flat part of the resist, while the deepest wires were irradiated through the part that was not covered with any resist. Sloping edges of the resist caused the gradual change in the depth of the wires between these regions.

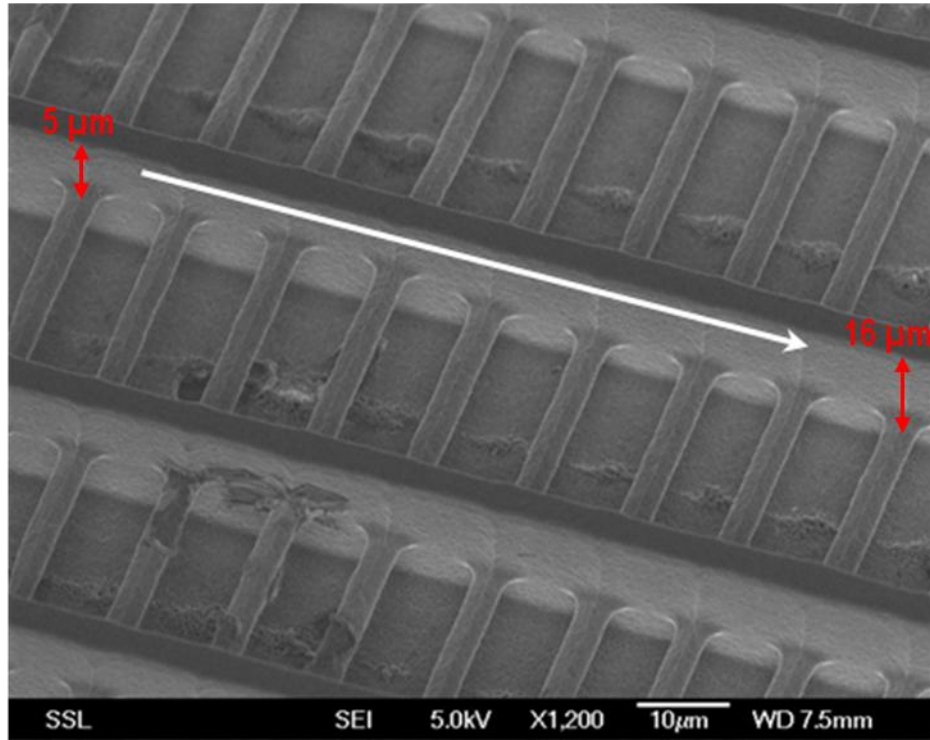


Figure 7-12 : SEM image showing the change in the depth of the free-standing multilevel silicon wires following the resist profile on the surface of the wafer. The white arrow is indicating the increase in depth of the wires.

7.3 Summary

This chapter has demonstrated the ability of using localized defects created at the end-of-range of high energy protons for machining curved and multilevel true-3D silicon micro/nano-structures within bulk silicon after subsequent anodization and removing the PSi. While multiple energy exposure can be used for fabricating multilevel 3D silicon structures, a multilevel/gray scale mask can improve this process using a single ion energy.

Extending this work for making multilevel 3D silicon structures can play an important role and open up a new process in development of M/NEMS, tissue engineering and 2D/3D silicon-based photonics[109], e.g. flexible fabrication of woodpile photonic crystals or obtaining densely packed multilevel silicon waveguides.

Chapter 8 : Micro- and Nano-Scale Applications of 3D Silicon Machining

This chapter describes applications of 3D machined silicon structures. Most of these projects are still ongoing, and undergoing further development and refinement with various collaborators. Hence, in this chapter the focus is mainly on presenting what can be achieved with our 3D machining technique across a range of applications. Each section presents a different application of the newly developed 2D and 3D silicon machining technique. The high end-of-range defect generation rate of an energetic ion, typically protons and helium is widely used for these processes.

8.1 Fabrication of silicon lines with nano-sized tips

Here we use the newly-developed technique, described in chapters 6 and 7, for 3D silicon machining. Irradiation was performed using the large area irradiation facility in conjunction with coating the sample with a mask comprising a patterned photoresist. Instead of simply stopping ions, a photoresist with a gradually varying thickness at the edges can be used to change the depth of end-of-range of ions and bring them nearer to the silicon surface. The modified end-of-range defect depth profile was then used to fabricate silicon lines with nano-sized tips. The basic principle is similar to that used in chapter 7.1, but with a lower resistivity wafer.

The sample was irradiated with 450 keV protons. Figure 8-1 (a) shows a SRIM [116] simulation plot of the defect generation versus depth by 450 keV protons (range $\sim 5.1 \mu\text{m}$ in silicon), with a defect generation rate more than 10 times higher at the end-of-range compared to along the trajectories. An example of

a photoresist pattern with sloping sidewalls used as a surface mask is shown in Figure 8-1(b). Figure 8-1 (c),(d) show schematics of such a patterned photoresist with sloping sidewalls which act to vary the end-of-range of protons laterally across a silicon wafer. The flat part of the photoresist is thick enough to completely stop the incoming protons from reaching the underlying silicon, Figure 8-1 (c). However, protons are able to penetrate through the thinner sloping sidewalls of the photoresist to reach the silicon underneath. The end-of-range defect profiles, both in the vertical and lateral sense, follow that of the sloping photoresist sidewalls.

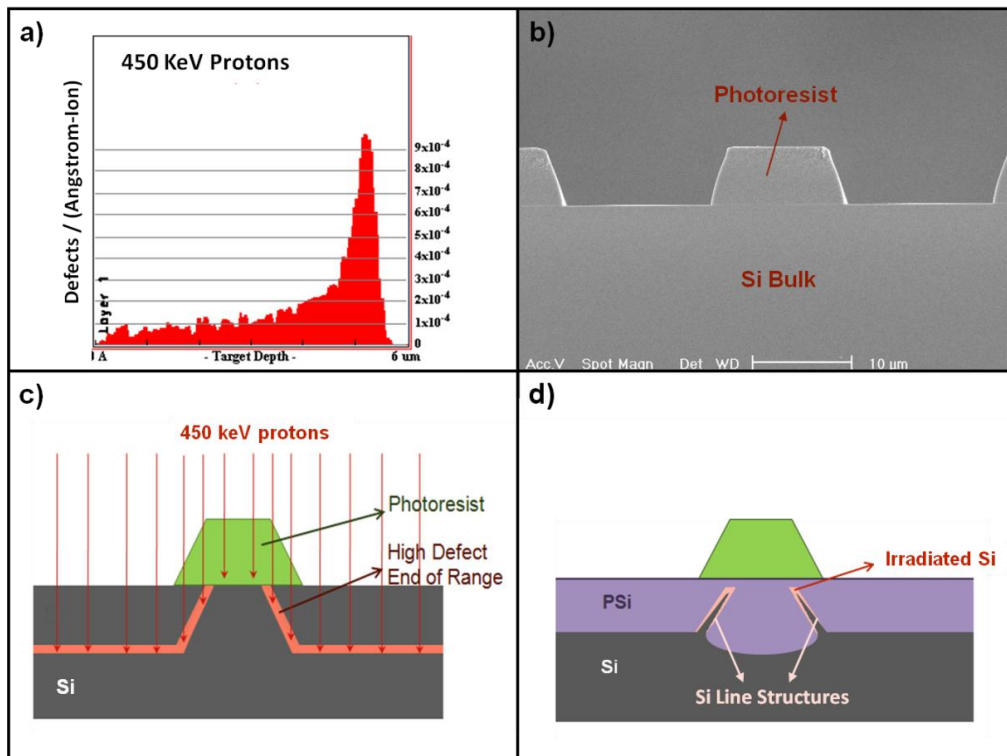


Figure 8-1 : (a) SRIM plot showing defects versus depth for 450 KeV protons in silicon. (b) A cross sectional SEM image of a photoresist with sloping sidewalls on silicon. (c) - (d) schematics showing the fabrication of silicon lines with nano-sized tips. (c) shows how photoresist with sloping sidewalls may change and bring the end of range of ions nearer to the silicon surface. (d) shows the anodization process and how with continued anodization, sharp silicon tips forms as PSi continues to form inwardly.

After irradiation, the resist is removed and PSi formed via electrochemical anodization. Regions of silicon which were shielded by the thick, flat resist are not irradiated and undergo PSi formation normally while all other irradiated regions have a reduced PSi formation rate. The regions under the sloping sidewalls of the

photoresist in particular, have the lowest PSi formation rate since the end-of-range region is nearer to the wafer surface and so the defect generation close to the surface is much higher. Sloping silicon line structures following the sloping resist sidewall profiles are hence formed. With continued PSi formation, the initial exposed silicon line structures nearer to the surface continues to form PSi (orange region in Figure 8-1 (c)) inwardly giving rise to silicon line structures with very narrow tips since regions closest to the surface are most anodized and hence thinnest.

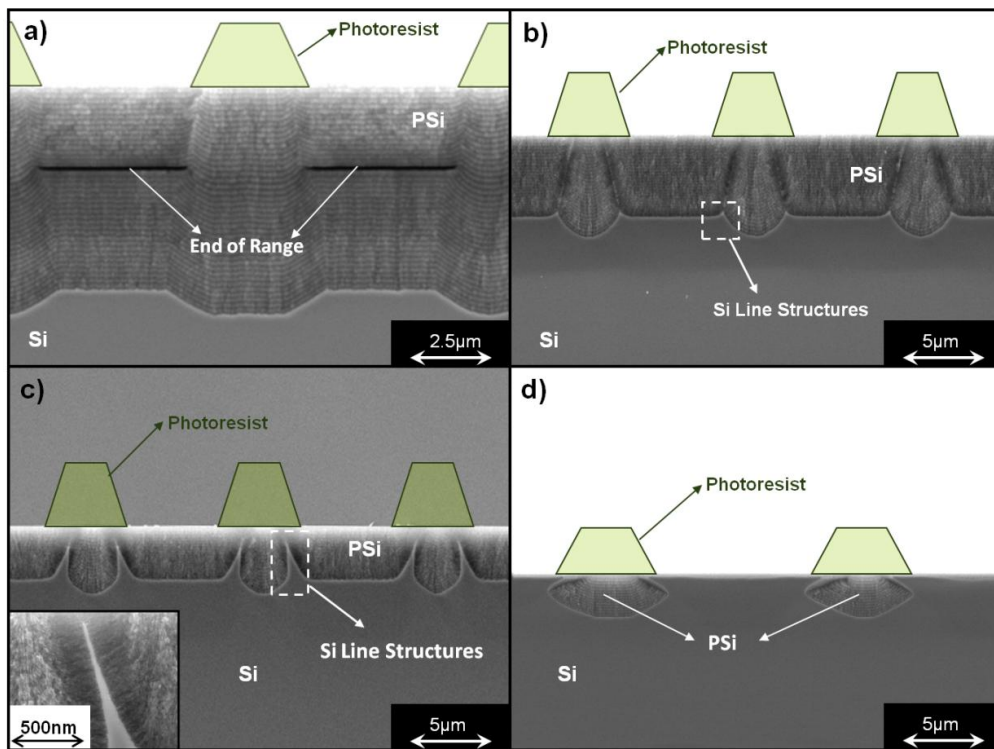


Figure 8-2 : (a)-(d) show cross sectional SEM images of multilayer PSi irradiated with fluences $2 \times 10^{13}/\text{cm}^2$, $2 \times 10^{14}/\text{cm}^2$, $1 \times 10^{15}/\text{cm}^2$ and $2 \times 10^{16}/\text{cm}^2$ respectively. Green trapezium indicates the locations of the photoresist during the irradiation. In (d) the fluence was high enough to completely stop PSi formation.

Figure 8-2 (a)-(d) show cross sectional SEM images of PSi multilayers which have $5 \mu\text{m}$ wide, $6 \mu\text{m}$ thick photoresist lines patterned on the surface of a $0.02 \Omega.\text{cm}$ wafer and irradiated by a uniform broad 450 keV proton beam with increasing fluences. Formation of a multilayer here serves the purpose of tracking the progression of the PSi formation in time and depth. With a low fluence of

$2 \times 10^{13}/\text{cm}^2$ (Figure 8-2 (a)), the end of range defects under the sloping part of the photoresist are not enough to substantially slow PSi formation, hence no line structures are observed. This sample was anodized more deeply so that PSi forms past the end-of-range of $5.1 \mu\text{m}$. It may be observed here that each PSi layer at the irradiated region is slightly thinner than that of the unirradiated region before the end-of-range. However, beneath this region the PSi layers formed are the same thickness as those at the unirradiated parts, since the hole current flowing is now the same at all locations.

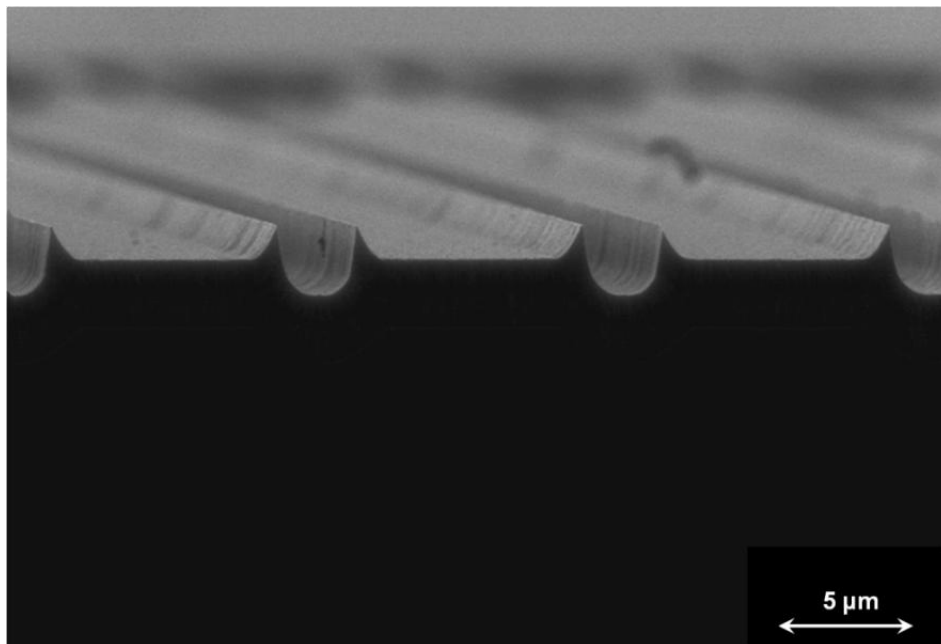


Figure 8-3: Silicon line structures after the removal of PSi with KOH.

Samples in Figure 8-2 (b) and (c) were fabricated in similar fashion except that anodization was stopped just before a depth of $5.1 \mu\text{m}$ and the fluences were higher. In Figure 8-2 (b), the sample was irradiated with a fluence of $2 \times 10^{14}/\text{cm}^2$, just high enough for the silicon line structures to start forming (white dashed box). In Figure 8-2 (c), a higher fluence of $1 \times 10^{15}/\text{cm}^2$ produces pronounced silicon lines with very fine tips. The inset of Figure 8-2 (c) shows that the tip width is smaller than 100 nm . It may also be seen here that the PSi formation over the

irradiated regions are slower (hence thinner) than at the areas shielded by photoresists.

Figure 8-3 shows these silicon line structures after the removal of PSi with KOH. These narrow silicon line structures may well be used for nano-imprinting lithography [117-118] and the grooves between every two silicon line structures may be used as nano/micro channels for nano/micro fluidics devices [119]. Figure 8-2 (d) shows a sample which was irradiated with the highest fluence of $2 \times 10^{16}/\text{cm}^2$, where PSi ceases to form not only at the end of range, but even along the initial part of the proton trajectory. Hence, PSi only forms at areas which were shielded by the resist.

8.2 Buried porous silicon channels

To further utilize and combine the abilities to modify the depth distribution of end-of-range defects of ions with a sloping photoresist as well as to completely stop PSi formation, this section describes forming buried PSi channels by utilizing a patterned multileveled photoresist, with subsequent irradiation and anodization.

Figure 8-4 shows schematics for fabricating buried PSi channels.

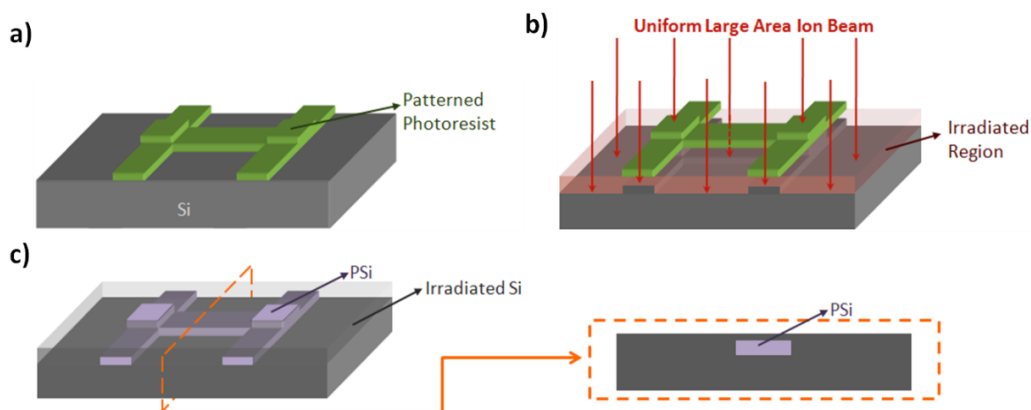


Figure 8-4 : (a)-(b) Schematics showing the processes used to achieve buried PSi channels formation. (a) shows a multilevel photoresist pattern on silicon. (b) shows how ions are completely stopped by the thickest PR step while their end of range is brought nearer to the surface by the second PR step. (c) shows the formation of the buried PSi channel.

Figure 8-5 (a) demonstrates an example of a patterned multilevel photoresist, having two level resist steps. The multilevel photoresist was fabricated by first patterning 10 μm wide, 3 μm thick resist lines, and then patterning a second layer of resist lines with the same dimensions orthogonal to the first layer of resist lines. This way, a resist pattern with different thicknesses on the same sample is achieved; double layered resists (6 μm thick), single layered resist (3 μm thick) as well as bare silicon surface. Irradiation was carried out with 1.5 MeV helium ions for a fluence of $1 \times 10^{15}/\text{cm}^2$, high enough to completely stop PSi formation at irradiated regions. Helium ions are used here because being heavier than protons, their defect generation is ~ 20 times higher, resulting in a shorter irradiation time.

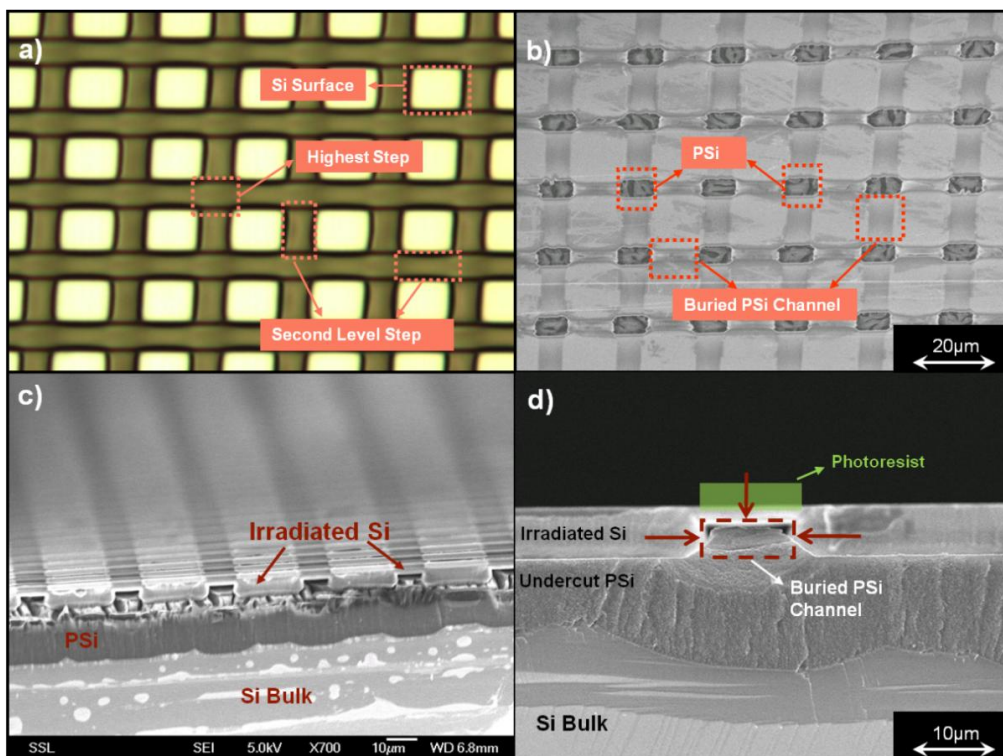


Figure 8-5 : (a) Optical image of multilevel photoresist patterned on silicon. The thickest photoresist step is where two PR lines overlap. (b) shows a plan view SEM image of the sample. PSi forms only from the regions previously covered with the thickest resist while buried PSi channels are achieved when PSi formation starts to undercut the shallowly irradiated silicon areas under the second resist step (c) A cross-section SEM image of the irradiated and anodized sample. (d) A magnified cross-sectional SEM image of the irradiated and anodized sample. Red arrows indicate the planes where PSi formation is confined. Sample in (c) and (d) were intentionally over-anodized to demonstrate PSi undercutting all irradiated regions.

The end of range of 1.5 MeV helium ions is $\sim 5.2 \mu\text{m}$ in silicon. The thickest photoresist ($6 \mu\text{m}$) step is thick enough to stop the incoming helium ions from reaching the silicon while the second photoresist step ($3 \mu\text{m}$) slows down incoming ions and reduces their end-of-range depth in silicon, resulting in the helium ions only shallowly irradiating the silicon to a depth of $\sim 2 \mu\text{m}$. Regions which are not covered with photoresist are simply irradiated with the deepest end-of-range of $\sim 5.2 \mu\text{m}$ in silicon. Upon electrochemical anodization, PSi formation commences at regions which were covered with the thickest resist since these were not irradiated. PSi continues forming and undercuts the irradiated regions under the second resist step and at the same time, PSi formation is confined at the sides as a result of the defects caused by the ions irradiating at parts of the silicon that were not covered with resist. The result is a buried PSi channel under the second resist step. This can be seen from the plan view SEM image in Figure 8-5 (b) where regions on the surface where PSi starts to form are indicated. The buried PSi channels are also observable and indicated. However, as PSi formation is not confined from the bottom, since it was not irradiated, further anodization would allow PSi formation to proceed deeper into the bulk and at the same time, undercut all irradiated regions as can be seen in Figure 8-5 (c) and (d). By simply obtaining suitable resist patterns and selecting the correct energy and ions to use, we can create buried PSi channels of different dimensions as long as care is taken not to anodize for too long which would allow PSi to form past the end-of-range of the ions. The PSi can be removed, if desired, to form hollow channels inside bulk silicon.

8.3 Arrays of buried 3D hollow channels

This section describes a method for creating hollow channels with various dimensions inside PSi and fully oxidized PSi layers, the channel can be

completely empty or have a silicon rod inside, depending on the irradiation conditions.

Chapter 5 described the hole current flowing during electrochemical anodization and the funnelling effect of the total hole current through the end-of-range irradiated regions when the fluence is low. Here we use this funnelling effect for forming hollow channels. A 0.02 Ω .cm wafer was irradiated with different line widths of 1, 3, 5, 10 and 17 μm using 1 MeV protons (range 16 μm) to a fluence of $3 \times 10^{14}/\text{cm}^2$ by PBW. After irradiation, the wafer was anodized to a depth of $\sim 35 \mu\text{m}$ using 30 mA/cm^2 . The low-fluence ion irradiation induces a diffusion current funnelling into the highly defected irradiated regions, which leads to a highly concentrated current density and formation of higher porosity PSi. As higher porosity PSi has a narrower silicon skeleton, by leaving the wafer for two weeks under ambient conditions, the higher porosity PSi was gradually but completely converted to oxidized PSi due to native oxide formation. The oxidized regions of the highest porosity parts can be removed by immersing the sample in a diluted HF solution, leaving the lower porosity regions intact. Although in this case the sample was left for many days under ambient conditions, it is likely that thermal annealing at a low temperature, e.g. 200-300°C, would cause rapid formation of oxidized PSi at the highly porous regions, but would probably be difficult to control.

Figure 8-6 shows cross-section SEMs of the sample. Hollow channels at the depth of $\sim 16 \mu\text{m}$ with different widths following the irradiated design width are observed in the PSi layer at the end-of-range regions of the irradiated lines.

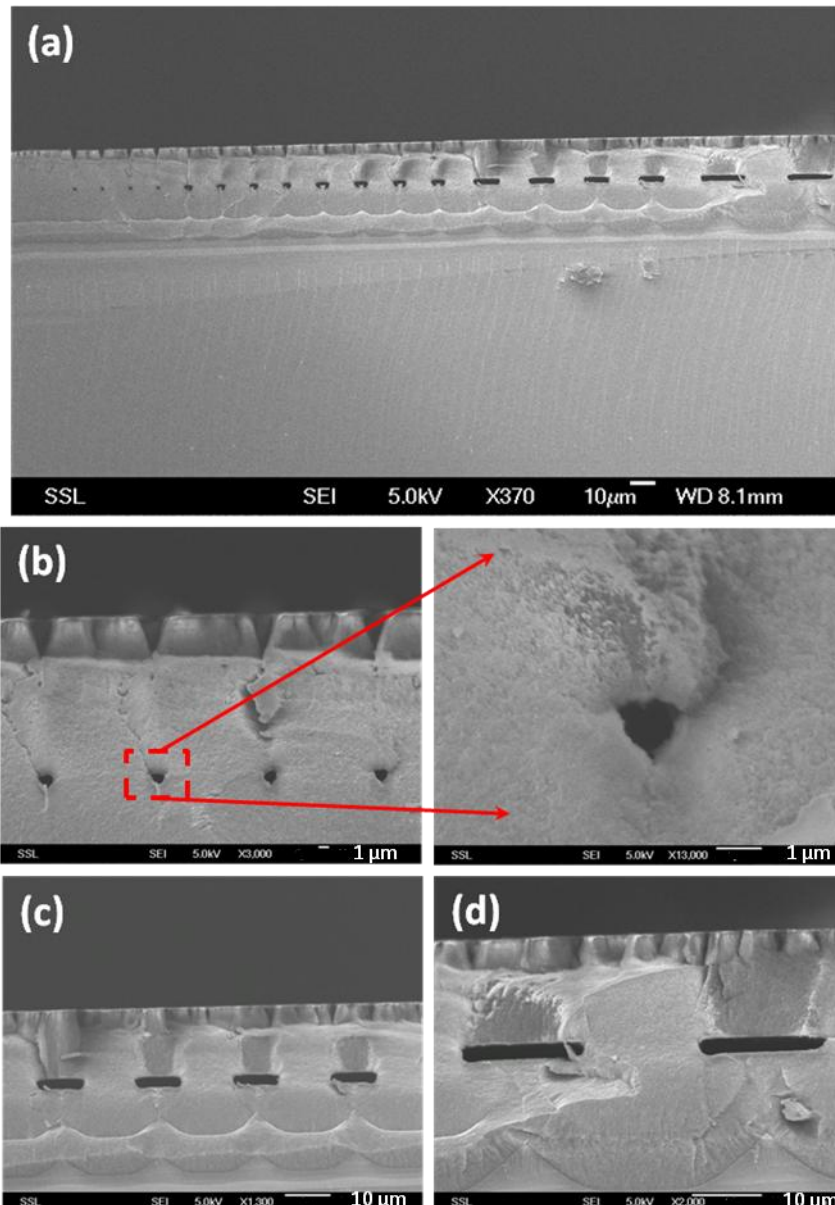


Figure 8-6 : Cross-sectional SEMs showing (a) various dimensions of hollow channels formed inside a PSi layer and magnified view of hollow channels with a width of (b) $\sim 1 \mu\text{m}$ (c) $10 \mu\text{m}$ and (d) $17 \mu\text{m}$ within the depth of $16 \mu\text{m}$ of PSi.

By slightly increasing the Ψ , a silicon core gradually starts to form, surrounded by high porosity PSi (see chapter 5 for more detail), which can be removed, leaving a silicon rod inside a hollow channel deep inside a PSi layer, Figure 8-7. The silicon rod can be completely detached from the surrounding PSi, and is free to move if desired.

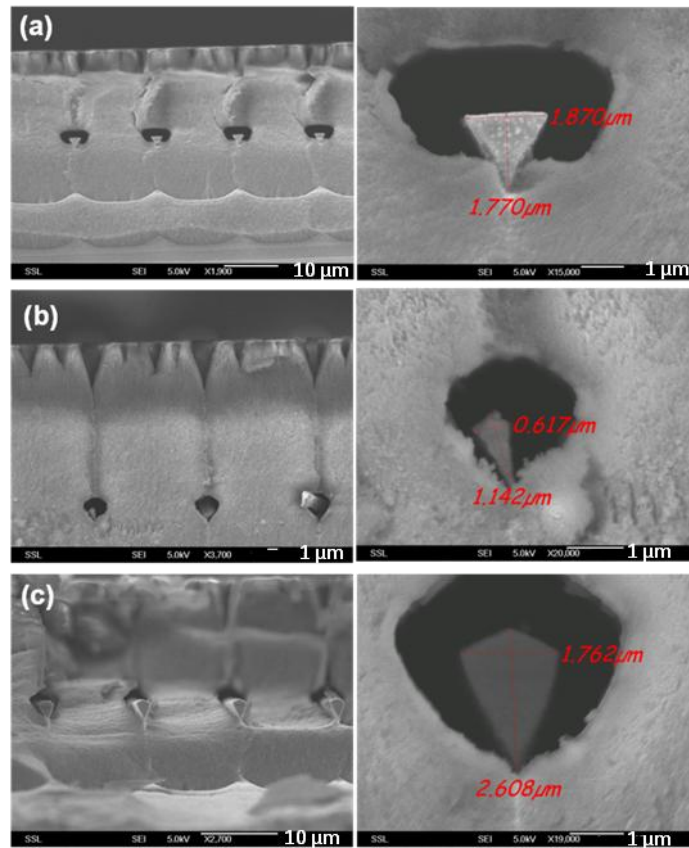


Figure 8-7 : cross-section SEM images showing a silicon rod inside a hollow channel within the PSi layer by using slightly higher line fluences (a),(b) $\Psi= 6 \times 10^{10}/\text{cm}$ and irradiated width of 5 μm and 1 μm respectively (c) $\Psi= 1.8 \times 10^{11}/\text{cm}$ and irradiation width of 3 μm .

If desired the sample can be thermally oxidized afterwards, to convert the PSi to fully oxidized porous silicon (FOPS) which has dielectric and optical properties comparable with conventionally produced silicon dioxide. For this purpose the sample was oxidized at 1100°C for 3 hours in a furnace with ambient condition. Figure 8-8 shows an example of channels in FOPS. The oxidized porous layer appears glass-like in contrast to the brown hue of the PSi layer, opening a new route to 3D microfabrication in glass. There is an optimal condition for the porosity of the PSi, oxidation temperature and the rate of increasing/decreasing temperature at which the fully oxidized PSi does not crack [120-121]. Very few cracks are observed in Figure 8-8 due to having the right porosity, about 50%, which requires an anodization current density of 30 mA/cm², see Figure 5-3. This was used for etching this sample, so PSi with the optimum

porosity can undergo full oxidation with minimal cracking due to volume expansion.[44]

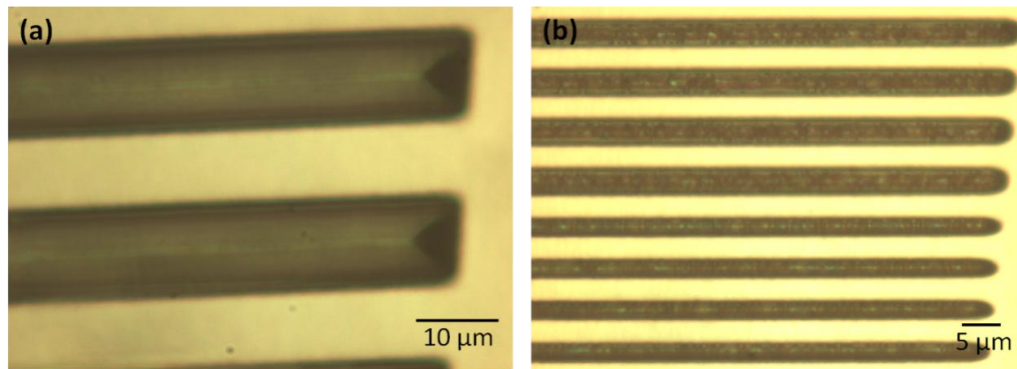


Figure 8-8 : Plane optical micrograph of an array of parallel, hollow channels (dark regions) at a depth of 16 μm inside a transparent FOPS layer.

Hence using a low irradiation fluence enables the formation of complex 3D channels with various dimensions in a desired depth of PSi and FOPS. This process can be used to obtain arrays of wide hollow channels with the width of tens of microns as well as narrow nanometer channels. In addition, by carefully controlling the fluence a silicon rod can be formed inside the hollow channel. Such designs may find applications in cell-engineering, e.g. cell sorting, or micro/nano-fluidic devices.

8.4 Precisely controlled 3D surface steps at micro and nano scale

This section describes a method for fabricating precisely controlled surface steps on silicon with step heights varying from tens of microns to a few nanometers. The patterned surface can subsequently be transferred to a polymer sheet, if desired, by using imprinting, which can open up new fields of applications for our 3D silicon machining technique.

Figure 8-9 (a),(b) shows cross-section SEMs of a 0.02 Ω.cm p-type wafer irradiated with different fluences of $5 \times 10^{14}/\text{cm}^2$ and $2.5 \times 10^{15}/\text{cm}^2$ respectively

using 2 MeV protons along a 4 μm wide line. The sample was then etched with an alternating current density of 10 mA/cm^2 and 100 mA/cm^2 for 4 seconds each layer, for 15 periods, forming multilayer PSi for better tracking the PSi formation progress. A progressive height difference between the underlying irradiated surface and that of the unirradiated background is observed, owing to a reduction in the etch current at irradiated areas due to a reduced anodization rate with fluence. This behavior can be used to fabricate a range of different components in low resistivity wafers, utilizing the different properties of the irradiated and unirradiated PSi and the underlying silicon surface relief pattern.

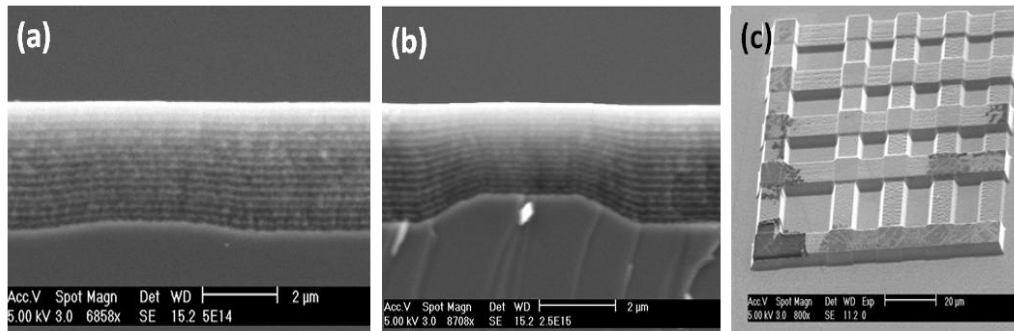


Figure 8-9 : (a),(b) Different step heights formed across a 4 μm wide region irradiated 2 MeV proton fluence of $5 \times 10^{14}/\text{cm}^2$ and $2.5 \times 10^{15}/\text{cm}^2$ respectively. (c) SEM image of checkerboard silicon surface pattern, having many different heights. Fabricated with irradiating two sets of crossing bars, each with fluences of 2,4,6,8 and 10×10^{15} protons/ cm^2 using 2 MeV protons.

For example, this irradiation and anodization process can be used for fabricating silicon surface relief structures in 0.02 $\Omega\cdot\text{cm}$ wafers, such as single/multiple step heights. This work requires the final step of removing the etched PSi, typically using dilute KOH solution [67, 72, 114]. Different ion fluences may be used to machine silicon surfaces with precisely controlled heights, and a high fluence may completely stop the etching at the irradiated regions [114]. The relationship between irradiation fluence and reduced PSi formation rate follows that shown in Figure 4-8 (a) and using this method the ‘checkerboard’ silicon surface pattern illustrated in Figure 8-9 (c) was previously fabricated by irradiating two sets of orthogonal bars with 2 MeV protons and

different fluences of $2,4,6,8$ and $10 \times 10^{15}/\text{cm}^2$ using PBW, indicating the ability to fabricate step heights in order of tens of microns.

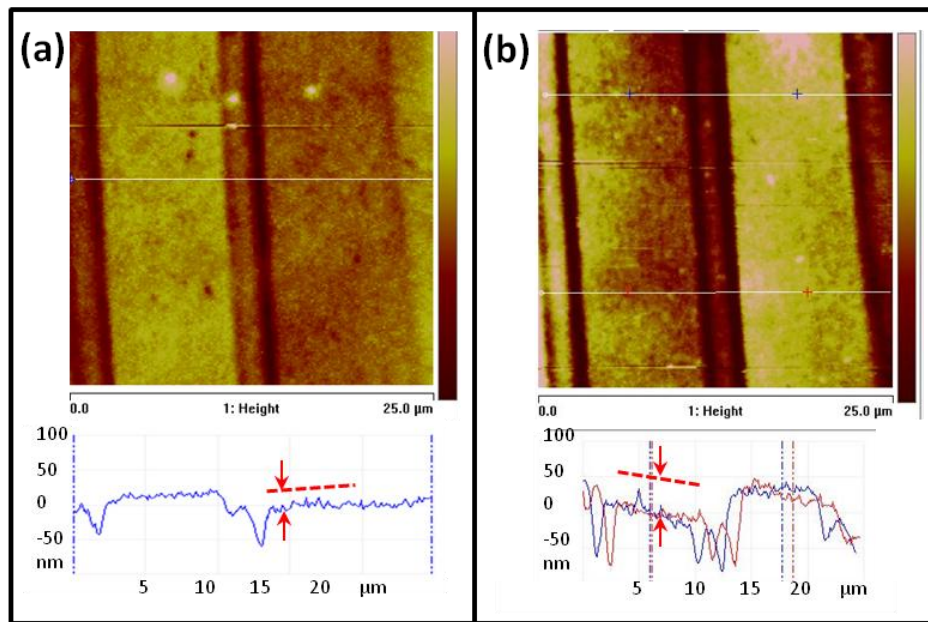


Figure 8-10 : AFM images and line profiles across adjacent 10 μm wide bars showing (a) ~ 10 nm and (b) ~ 30 nm step height.

While in this case, steps up to several micrometers are produced, by carefully controlling the fluence and anodization depth, step heights of only hundreds or tens of nanometers can be similarly machined. Figure 8-10 shows two examples of single steps produced in this fashion using 1 MeV protons after 30 seconds anodization at $90 \text{ mA}/\text{cm}^2$. A step height of ~ 10 nm was achieved by fluences of 1×10^{15} and 1.1×10^{15} protons/ cm^2 , and similarly step height of ~ 30 nm was produced by using 5×10^{15} and 5.5×10^{15} protons/ cm^2 .

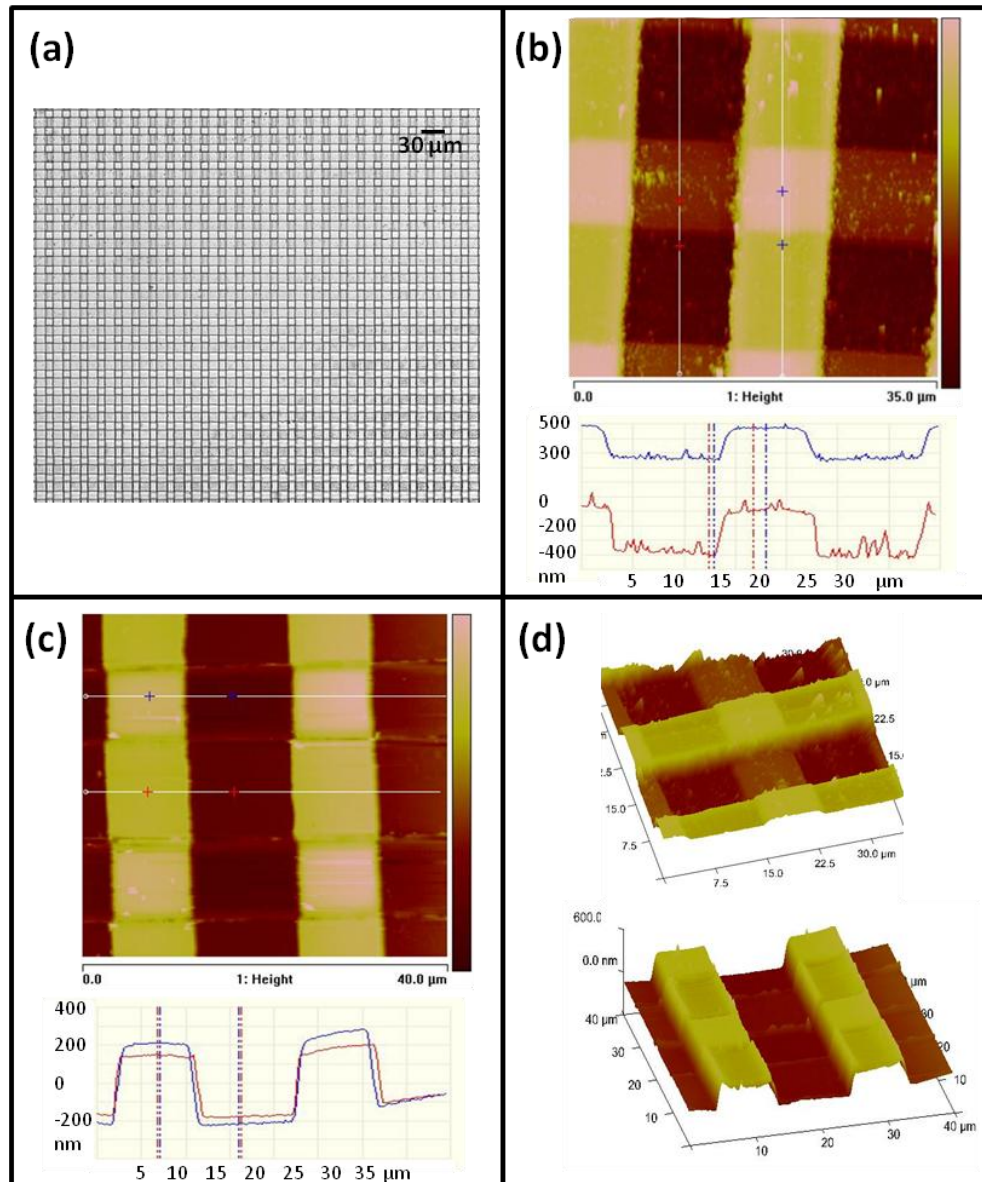


Figure 8-11 : (a) Optical micrograph, (b) before and (c) after thermal annealing AFM images and line scans of surface relief pattern of 10 μm squares of four different heights, created using large area irradiation with 1 MeV proton fluences in orthogonal directions of 1 and 1.1×10^{15} protons/cm². (d) 3D AFM images before (top) and after (bottom) thermal annealing, showing the smoothing effect of thermal annealing.

Similarly, rapid fabrication of multi-steps surface patterns with low roughness over areas of 2.5×2.5 cm² is possible using a patterned photoresist in conjunction with large area irradiation, utilizing the highly uniform fluence delivered at each area. Figure 8-11 shows an example of a range of step heights produced in this manner. This sort of four-level surface patterning was achieved using two steps of standard UV photolithography and irradiation processes, and a final anodization step and removal of the PSi layer. The wafer was first patterned

with SU-8 resist layer (5 μm thick) having 10 μm wide lines and spaces over a $1.5 \times 1.5 \text{ cm}^2$ area. The sample was then irradiated by 200 keV protons and a fluence of $5 \times 10^{14}/\text{cm}^2$. The resist is thick enough to stop these ions in the regions covered with the resist, hence only the exposed wafer areas are irradiated. After irradiation the resist is removed, and the second resist lines with the same dimensions were patterned orthogonal to the previous lines using another step of UV lithography. The sample was then irradiated with the same ions with a fluence of $1 \times 10^{15}/\text{cm}^2$, eventually giving rise to unirradiated square regions together with three adjacent square regions irradiated by fluences of 0.5, 1 and 1.5×10^{15} protons/ cm^2 , hence slowing down PSi formation at different rates. The deepest and highest regions in Figure 8-11 are produced at unirradiated and the highly irradiated areas respectively. The silicon surface in Figure 8-11 (a),(b) looks rough, largely because of small pieces of PSi sticking to the surface which are not easily removed. To remove all remaining traces of PSi and further smoothen the silicon surface, thermal annealing was used [81-82], after which the surface is much smoother, Figure 8-11 (c). Here the sample was annealed for 2 hours at 1100°C , and the silicon oxide layer was removed using a diluted HF solution.

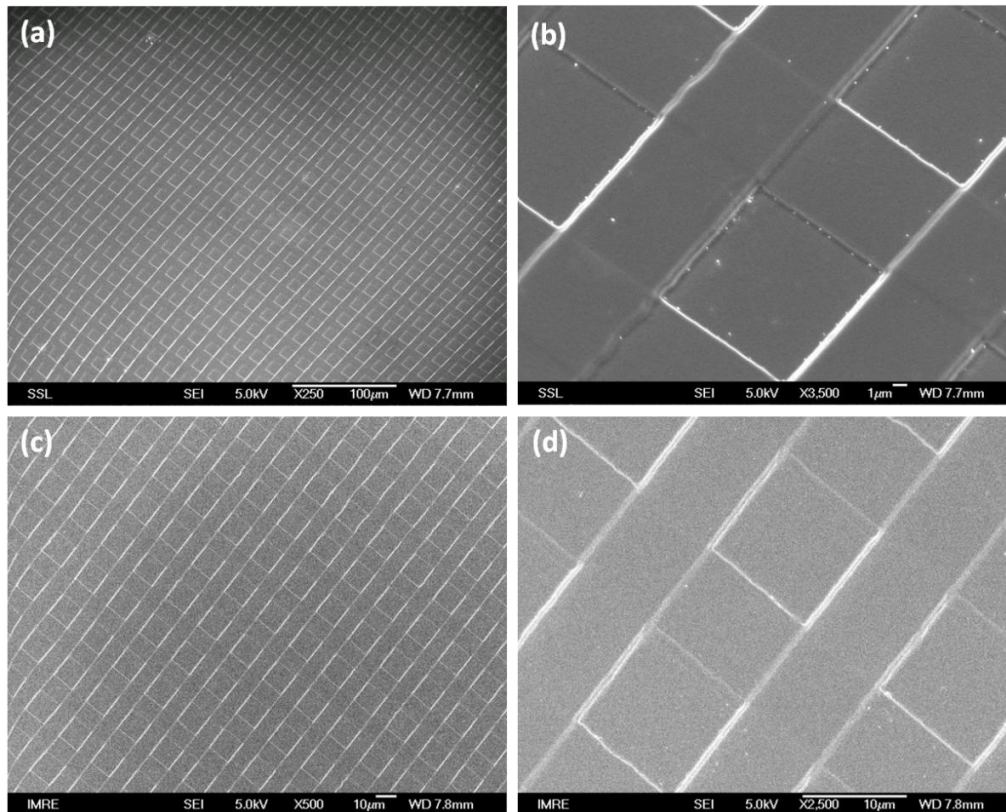


Figure 8-12 : SEM images of (a),(b) the machined four level silicon (c),(d) transferred to polycarbonate resist by nano-imprinting.

In the next stage of this work, the patterned sample was used as a mold for imprinting the pattern into a polymer. Figure 8-12 (c),(d) shows the four-level structures imprinted in polycarbonate (PC). Nano-imprinting was carried out with a commercial 4" nanoimprinter (Obducat AB Malmö, Sweden) using 125 μm thin sheets of PC as polymeric substrates. Prior to imprinting, the silicon mold is treated with 1H,1H,2H,2H perfluorodecyltrichlorosilane (FDTS; Alfa Aesar, Ward Hill, MA, USA) for hydrophobic surface treatment to obtain a fluorinated self-assembled monolayer with a very low surface energy. The PC film was then imprinted at 170°C and 50 bar pressure for 400 seconds.

Fabricating this sort of precisely controlled four-level surfaces on transparent polymer (a superpixel consists of four-level subpixels repeating over the entire large surface area) is particularly of interest for 3D imaging by placing the transparent sheet in front of a CCD camera. The steps with different heights act

as phase plates to manipulate the imaginary part of the incident beam. The following patterns with very precise phase structures on them can be utilized to influence any fields, such as laser beams or laser pulses. Having four different heights on each pixel gives the possibility for the beams to pass through different phase plates to interfere with each other in two different directions (x and y). By knowing the exact structure of the phase plate, the Fourier transform of the CCD captured interference would make possible to reconstruct the 3D image (similar to the Holographic technique). If desired, more complex photoresist patterns in conjunction with multiple energy irradiation can be used to obtain complex multilevel wafer patterning.

8.4 Free-standing silicon structures

By extending the above process, free-standing silicon structures can be fabricated simply by continued anodization which results in completely undercut silicon irradiated structures. In order to obtain a single level, free-standing film, the wafer is first patterned with a photoresist with the inverse pattern of the desired free-standing structure, then irradiated with a high ion fluence to completely stop PSi formation during subsequent anodization. Thus, PSi forms only at unirradiated regions, Figure 8-13 (a), and after etching beyond the ion penetration depth the irradiated regions start to be undercut. Once fully undercut, the surrounding PSi is removed to detach the structure from the silicon substrate. The thickness of the free-standing structure is thus controlled by the ion end-of-range depth, which depends on the ion type and energy.

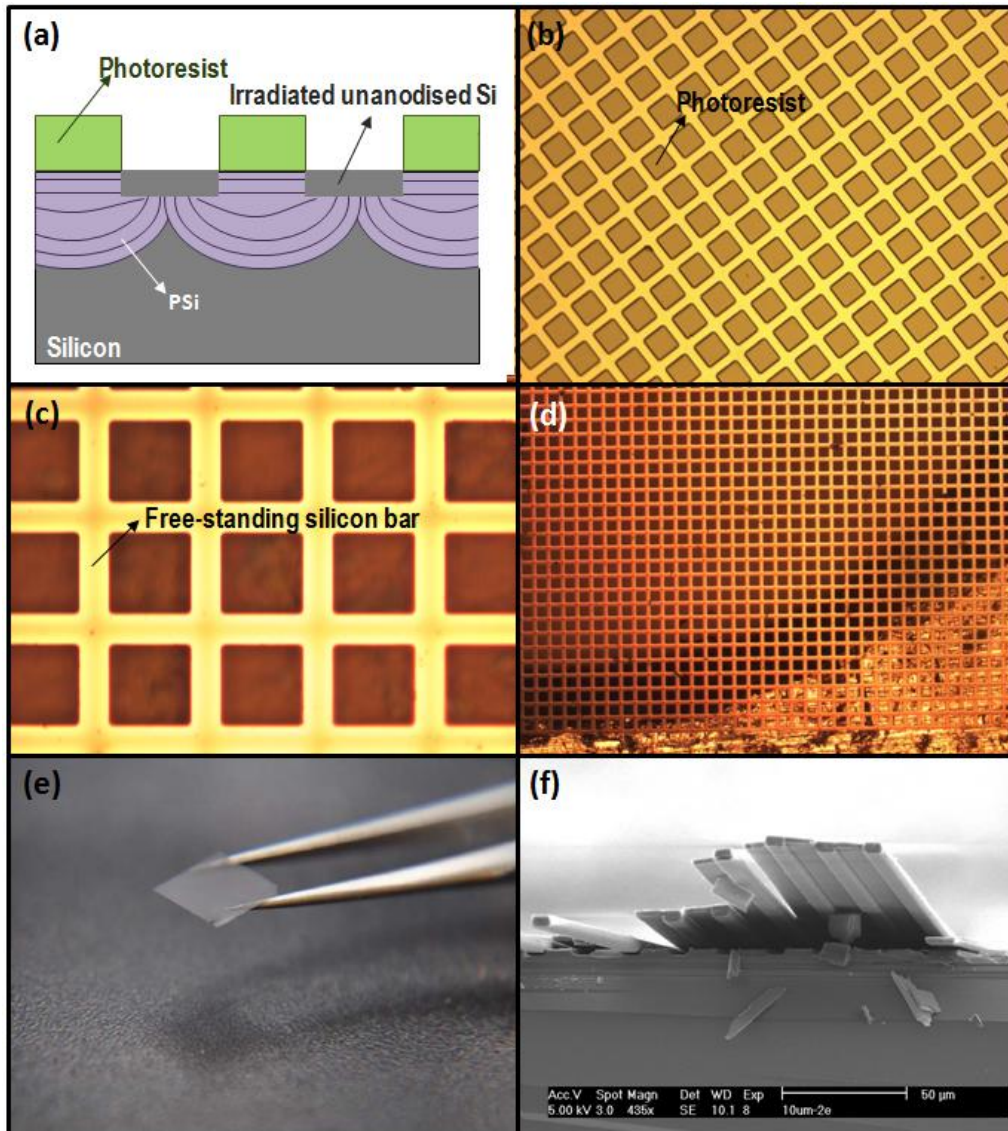


Figure 8-13 : (a) Schematic of producing undercut, detached silicon microstructures, where the PSi etch front undercuts the irradiated regions, forming curved surfaces. (b) optical micrograph of the photo resist mask pattern used for fabrication of the grid. (c)-(d) Free-standing silicon fabricated over a $5 \times 5 \text{ mm}^2$ area using this process, (c) the free-standing silicon grid resting on a tweezers. (f) SEM image of many silicon bars resting on the underlying silicon surface, though completely detached from it.

Figure 8-13 (b)-(e) show a free-standing $3.5 \mu\text{m}$ thick silicon grid fabricated using this process. The sample was first patterned with a resist squares having a period of $30 \mu\text{m}$ using standard UV lithography (Figure 8-13 (b)). The sample was then irradiated with 1 MeV helium ($\sim 3.5 \mu\text{m}$ range in silicon) with a fluence of $1.5 \times 10^{15}/\text{cm}^2$ using large area irradiation facility. This fluence is enough to almost stop the etching in the irradiated regions. Helium ions are used here to reduce the irradiation time, as the defect generation is higher than protons. Hence during the anodization process, PSi forms around these irradiated regions and

undercuts them. The PSi can then be removed by a diluted KOH solution, making the grid completely free-standing (Figure 8-13 (c)-(e)). The $5 \times 5 \text{ mm}^2$ free-standing silicon grid resting on tweezers in Figure 8-13 (e), is transparent due to being very thin. Figure 8-13 (f) shows a cross-section SEM of many 3.5 and $2 \text{ }\mu\text{m}$ thick bars, with widths of 5 and $10 \text{ }\mu\text{m}$ produced in the same manner, resting on the underlying silicon surface, though completely detached from it.

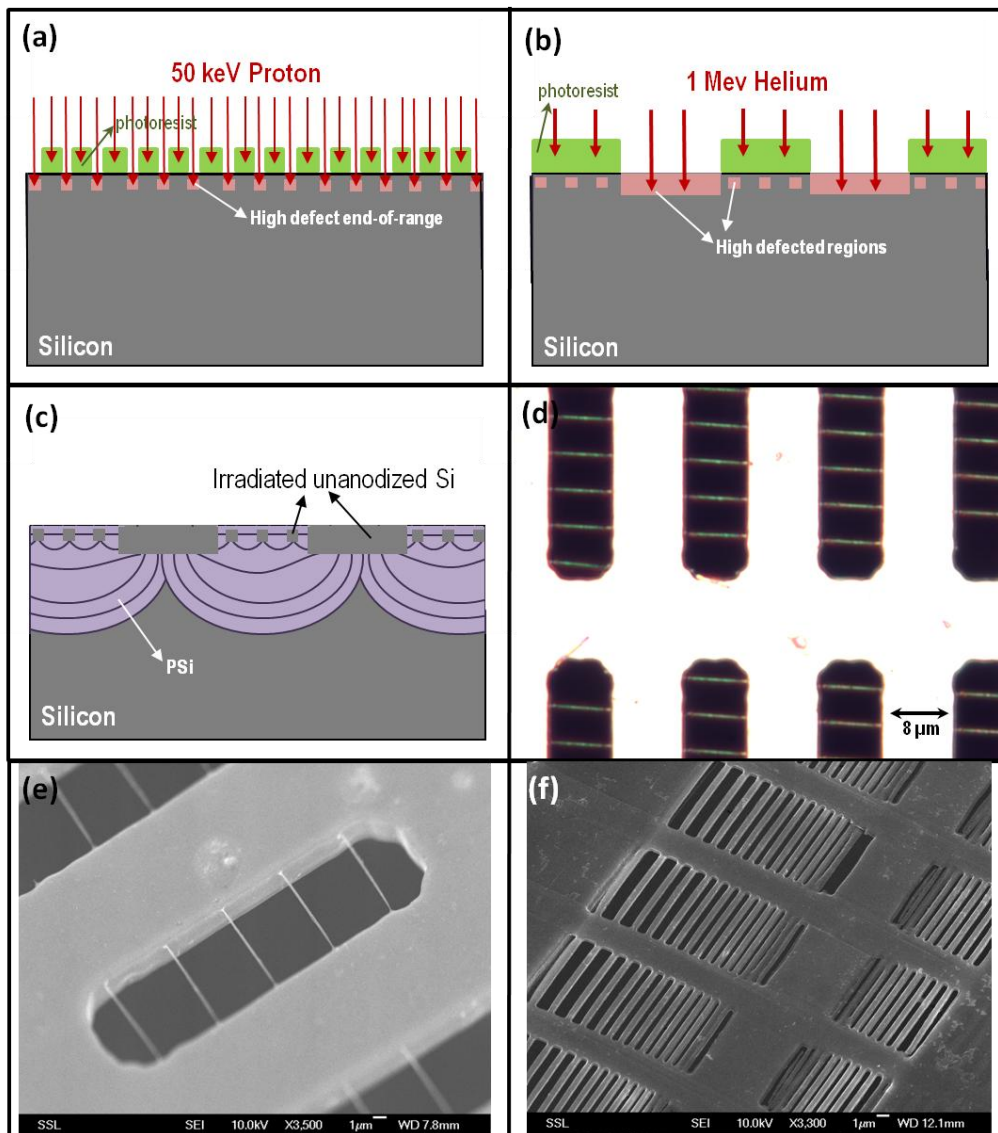


Figure 8-14 : Schematics showing fabrication process of free-standing nano-structures using large area beam irradiation setup in conjunction with a patterned photoresist mask which is thick enough to stop the incoming ions (a) low energy irradiation to produce end-of-range defects at the openings of the e-beam lithography patterned photoresist (b) higher energy ions with a high fluence to completely stop anodization at the openings of the UV lithography patterned photoresist (c) electrochemical anodization to form PSi around and undercut the high defected regions. (d),(e) Optical and SEM images showing free-standing nano-wires supported by a coarse free-standing micro-grid after the PSi is removed, making the whole structures free-standing. (f) SEM image of similarly prepared free-standing silicon structures showing the spacing between the silicon nano-wires can vary.

By further extending this ability, small, thin, free-standing structures supported by thicker structures may be fabricated by two steps of lithography and irradiation. The sample is first patterned using e-beam lithography with 100 nm lines with 5 μm spacing and was then irradiated using large area irradiation of 100 keV H_2^+ (~ 500 nm range in silicon) with a line fluence of $3 \times 10^9/\text{cm}$, forming localized defects at the end-of-range (Figure 8-14 (a)). The resist was then removed and the sample patterned with a coarse, reverse grid pattern using UV lithography with features of $8 \times 30 \mu\text{m}^2$. The sample was then irradiated with 900 keV helium ($3.2 \mu\text{m}$ range in silicon) and a fluence of $5 \times 10^{14}/\text{cm}^2$ (Figure 8-14 (b)). During subsequent electrochemical anodization, PSi forms around all the high defect density regions (Figure 8-14 (c)). Because of the small dimensions of the fine, free-standing silicon lines, here using KOH is not suitable for removing the PSi due to the aggressive bubbling involved in the removal process. Instead, the sample was thermally annealed for a short period of 30 minutes at 1000°C to fully oxidize the PSi so that it becomes FOPS, i.e. SiO_2 . The oxidized PSi was then removed by a diluted HF solution, to detach the silicon structures and allow them to float off in the solution. Figure 8-14 (d),(e) show the free-standing ~ 150 nm wide silicon wires supported by a coarse, thicker grid. Figure 8-14 (f) shows a similarly fabricated free-standing silicon thin mask based on chapter 6.5.2, where the spacing between the 250 nm silicon wires are changing from 100 nm to 1 μm .

This structure was developed for use by collaborators in X-ray optics experiments on a synchrotron, requiring free-standing nano-scale wires with spacings of a few microns. Developing this process furthermore is useful, as thin silicon films and structures are of interest for various applications, such as nanostencil masks [122-123], thin-film transistors [124], silicon solar cells [125] and light and X-ray sensors.

8.5 Combined 3D micro- and nano-scale mold for microfluidics

Since one generally cannot produce micro- and nano-scale components with the same process, fabricating a structure comprising nano- and micron-size features using standard silicon fabrication techniques is very challenging and requires many lithography and etching steps. Using our silicon machining technique, 3D structures with nano-dimensions together with micro-structures can be fabricated in a single irradiation and anodization step. This ability is used here to fabricate channels for conductivity nano-sensors used in a Lab-on-a-chip (LOC) device, designed and implemented at the Institute of Materials Research and Engineering (IMRE), which can potentially increase the detection limit of the sensors by confining the fluid flow to nanoscale channels.

Improving the detection sensitivity is the main challenge in the development of LOC technology. Recently a new LOC device has been designed and implemented at IMRE in which conductivity sensors have been employed in capillary electrophoretic systems and LOC devices. In this device, the current that is capacitatively coupled through the detector cell is measured. The design of the cell consists of a nano-fluidic channel for the ions to pass through, as cell sensing resistor, coupled with lithographically patterned electrodes close to the nano-channel to get an improved signal by confining the ions very close to the cell electrodes. In addition, an external electrophoresis electric field is applied to accelerate the ions throughout the chip and toward the detection cell, which leads to sudden squeeze of ions at the detection cell. Figure 8-15 shows the design and idea of using nano-channels, reducing the channel's size, at the detection cell for improving the detection limit.

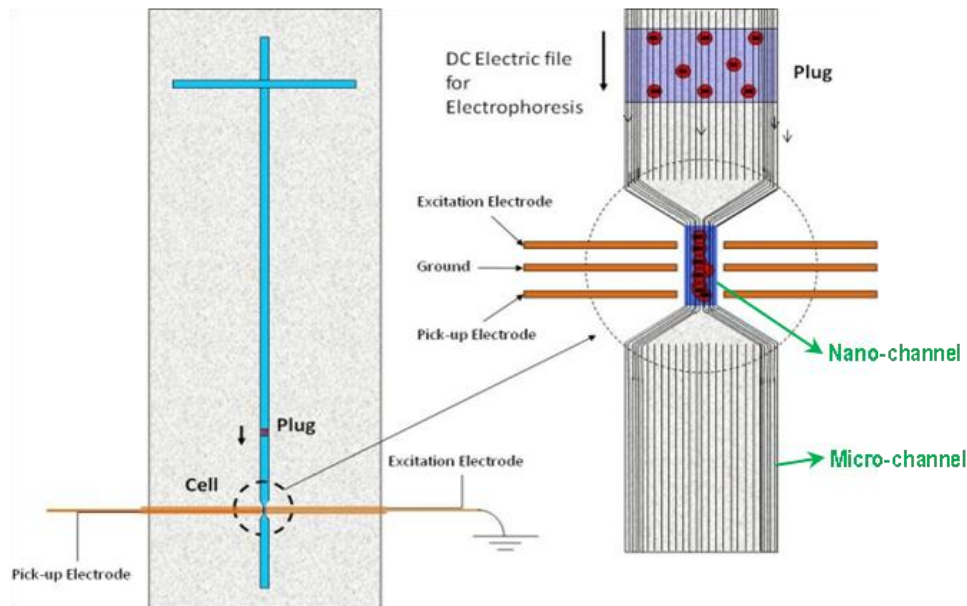


Figure 8-15 : Schematic diagram of proposed geometries of the conductivity sensor with a nano-fluidic microchip electrophoresis design and idea.

To realize microchips used for conductivity nano-sensors, 3D silicon machining together with nano-imprint lithography were used to fabricate plastic chips with 3D micro- connected to nano-fluidic channels. The silicon mold (0.02 $\Omega\cdot\text{cm}$ p-type) is fabricated using PBW with 1 MeV protons with a fluence of $2 \times 10^{17}/\text{cm}^2$ and width of 10 μm to stop the etching in the irradiated regions and to form a micro-ridge. 1 MeV protons have a range of 16 μm in silicon, allowing deep channels to be fabricated. A low line fluence of $1 \times 10^{11}/\text{cm}$ and width of 200 nm was then used to create localized defects at the ion end-of-range and to form a nano-ridge with a sharp tip. The schematic of the fabrication process is shown in Figure 8-16. After irradiation the sample is anodized to a depth of 10 μm and the P*Si* is removed using a diluted KOH solution. The cross-section view of these micro- and nano-silicon ridges are similar to what is shown in chapter 5, however, here by controlling the anodization time we avoid the undercut of the irradiated regions.

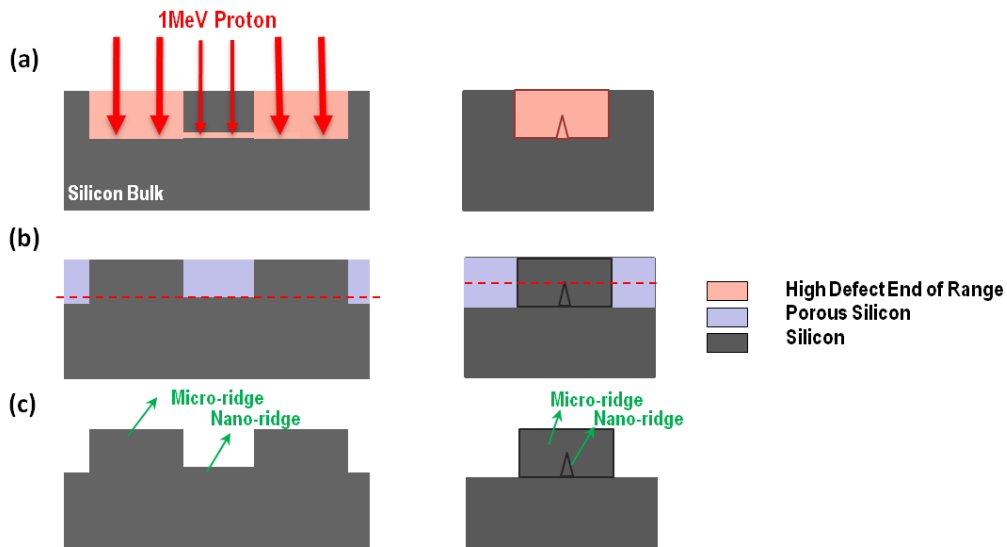


Figure 8-16 : Schematics showing silicon cross-section in two perpendicular directions (a) by using a single ion energy irradiation and vary the fluence, 3D structures with different cross-sectional dimensions, changing from tens of micron to tens of nanometers can be fabricated. The lateral dimension can be controlled by the irradiation design width. (b) PSi forms during the electrochemical anodization, leaving only high defected regions intact. (c) The PSi is removed using a diluted KOH solution.

Figure 8-17 shows an example of a 10 μm long nano-ridge being connected and placed in between a 400 μm long micro-ridge having a square cross-section of 10 \times 10 μm . In this process only a single ion energy is used.

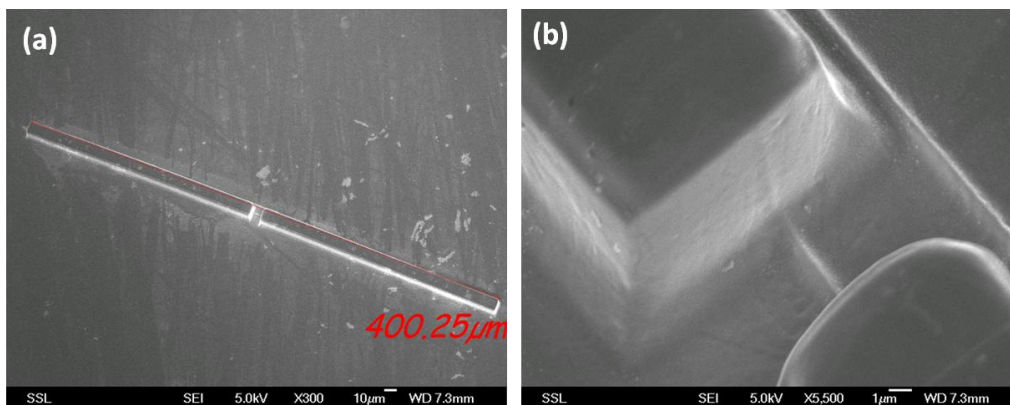


Figure 8-17: SEMs of machined structures after anodization and removal of the PSi, showing a 10 μm long nano-ridge placed in between a 400 μm long micro-ridge. A second, separate nano-ridge parallel to the actual one is for better studying the shape of the ridge.

By changing the fluence, different dimensions of nano-size channels can be fabricated. Figure 8-18 (a)-(b) shows a sample fabricated in a similar manner by 1 MeV proton irradiation with $\Psi = 2 \times 10^{11}/\text{cm}^2$ for the nano-ridge and a fluence of $2 \times 10^{17}/\text{cm}^2$ for the micro-ridge. The wafer was then used as a mold to perform nano-imprint lithography in order to obtain a plastic microchip. Figure 8-18 (c)-(d)

shows the imprinted channels in polycarbonate (PC). Sheets of $20 \times 100 \text{ mm}^2$ PC with $125 \text{ }\mu\text{m}$ thickness were used to fabricate the plastic microchips. Prior to imprinting, silicon mold surface is treated with FDTS to obtain a fluorinated self-assembled monolayer (SAM) with a very low surface energy of $\sim 11.8 \text{ mJ m}^{-2}$. Nano-imprinting using molds with non-planar 3D nano- and micro-structures requires polymer flow toward the mold surface with minimal lateral pressure gradient which may lead to defects such as side wall shifting in micro-patterns and/or incomplete filling of features. An optimized imprint was achieved using a mold-polymer assembly with the mold surface facing up against the polymer sheet having a smaller area than the mold. These together provide a uniform pressure and temperature over the polymer sheet confined within the mold surface; eliminating lateral flow at high temperature-pressure gradients which can lead to side wall shifting or defects. The nano-imprint lithography cycle consists of: 200 seconds at 170°C and 10 bar to ensure highly stabilized temperature-pressure for a further next step of 10 minutes at 170°C and 50 bar, which is just sufficient for complete filling all the features. The pressure was released after cooling just below 100°C . Upon manual separation of the stamp from the substrate, no defect was observed and the stamp patterns were transferred into the PC substrate completely. It can be observed from the SEM image of the imprinted pattern in PC shown in Figure 8-18 (c)-(d) that the replicated pattern has sharp edges, straight lines, vertical sidewalls and flat surfaces identical to the machined silicon mold.

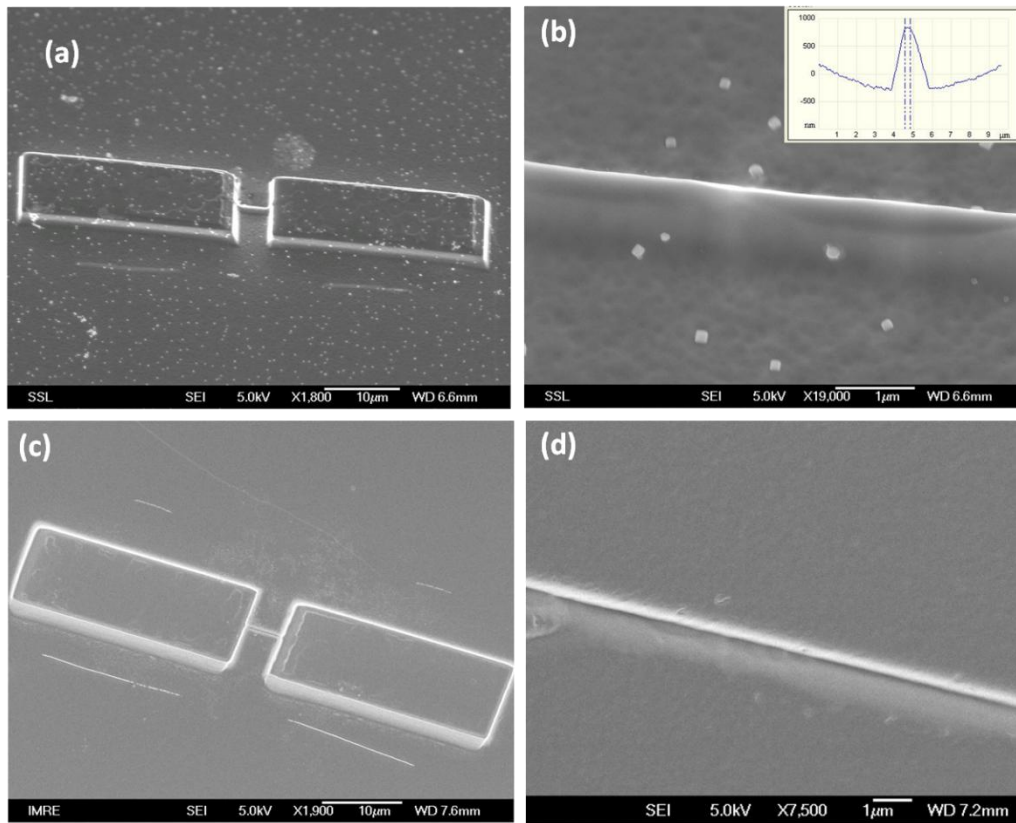


Figure 8-18 : SEMs showing (a) silicon micro-ridge connected to nano-ridge (b) high magnification of the nano-ridge, and insert shows AFM line profile across the nano-ridge. (c),(d) transferred patterns to PC after nano-imprint lithography, showing micro- and nano-channels with sharp edges and straight lines.

The final step of this work is to transfer this design to the proposed geometries of LOC device shown in Figure 8-15. The large microfluidic channels have a $50 \times 50 \mu\text{m}^2$ square cross-section designed in a standard T-cross configuration of 85 mm long separation channels and 10 mm long injection channel. The reservoirs are 2 mm diameter holes. The reservoirs are punched into the top lead and aligned against bottom reservoirs that were imprinted together with the channels to relax the requirement for alignment and to provide well defined defect free entrances for the microchannels. The imprinted nano-channel, using the silicon machined mold, will be used in the nano-detection sensor in Figure 8-15 for improving the detection limit of the ions passing through the cell. Sealing of the channels is performed by bonding a second substrate into which inlet reservoirs have been punched. Bonding of the chips is performed at 140°C and 20 bars of pressure for 10 minutes. By controlling the bonding, the wider top

part of the nano-channels can be covered, leaving only the sharp tip end the nano-channel for the liquid flow to minimize the width and height of the channel to improve the detection.

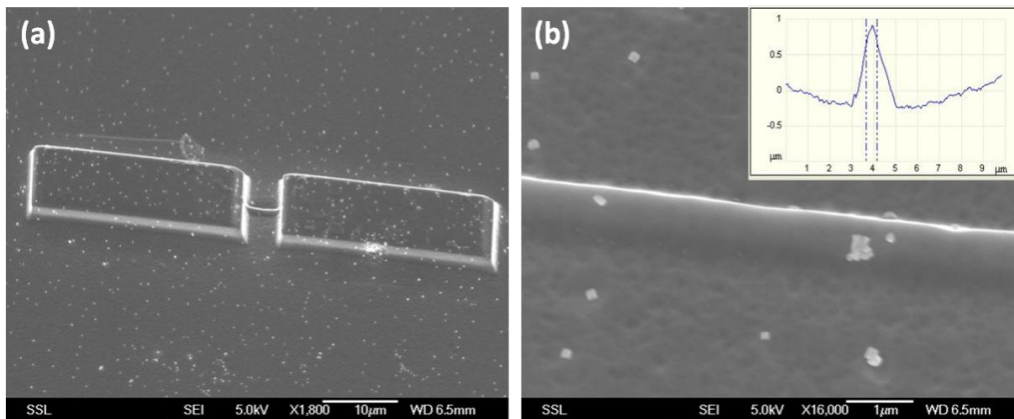


Figure 8-19 : SEM images showing sharp nano-ridge fabricated by using 1 MeV protons and $\Psi=4\times 10^{11}/\text{cm}^2$, and the same energy protons with a fluence of $2\times 10^{17}/\text{cm}^2$ was used to produce micro-ridges. (b) insert shows AFM line profile across the nano-ridge indicating a very sharp tip of the ridge.

For improving the detection limit of the cell, a sharper nano-channel was fabricated with the same technique but a different fluence. Figure 8-19 shows the silicon machined ridges, fabricated using 1 MeV protons with a $\Psi=4\times 10^{11}/\text{cm}^2$ and fluence $2\times 10^{17}/\text{cm}^2$ for the nano- and micro-ridge respectively.

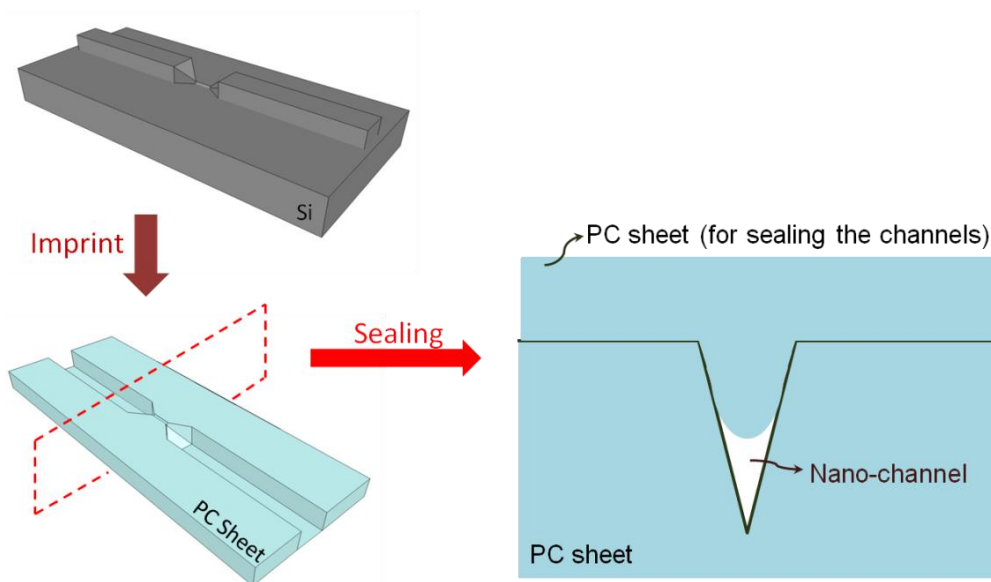


Figure 8-20 : Schematic showing imprinting and sealing of nano-channel with an identical PC sheet.

After the imprinting the channels in a PC sheet, the channels should be sealed. Sealing of the imprinted fluidic channels is by thermal bonding process using a PC sheet with similar dimensions as the fluidic chip. The two pieces are then cleaned with alcohol and DI water to eliminate any dust or particles in between. Then they are brought into contact with each other and placed between two bare cleaned silicon wafers with no patterns. A nanoimprinter can be used for bonding the sheets typically at 140 °C and 20 bars of pressure for ~10 minutes. By controlling the conditions, the wider top part of the channel can be controllably filled and sealed with PC, leaving only an empty nano-size channel (Figure 8-20). Hence we make use of the very sharp tip of the ridge fabricated using our silicon machining technique. Finding the optimum conditions for the bonding is still being investigated.

Further extending this work, for mass production of the plastic patterns, requires converting the silicon mold to a more rigid nickel mold. This is because nano-imprinting of non-planar micro and nano-structures and/or high aspect ratio features are challenging due to limitation in polymer flow to fill micro- and nano-features at different heights and resolutions uniformly and simultaneously. The visco-elastic polymer flow at high temperature and pressure demands certain parameter conditions for the nano-imprint lithography process which can damage the nano-structures defined on the brittle silicon master surface after repeated use. Therefore a process combining nano-imprinting, electroplating and metal-on-metal electroforming was employed to produce a high resolution nickel replica working mold with exact patterns as the original master and extended dimensions. Nickel electroforming is widely used in the field to produce robust, flexible and high fidelity molds for roll-to-roll nano-imprinting. A custom-built mounting jig was used to enable seamless replication of the master template via nickel

electroforming across an extended area of up to 4" wafer. Final laser-cut nickel working molds were obtained with rectangular dimensions of 4×4 cm² and 100-300 μm thickness.

Although this work was motivated by the fabrication of micro/nano-channels for LOC devices to improve the ion detections, the results show the unique ability of our machining technique. Various complex 3D silicon structures with combined cross-section dimensions changing from micron to nanometer can be fabricated using this method after only one step of irradiation and etching.

8.6 Summary

This chapter has provided several examples of current and future applications of 3D bulk and surface machining using the 3D silicon machining technique described in this thesis.

By varying the end-of-range laterally in silicon together with suitable irradiation fluence, 3D silicon lines with nano-sized tips can be fabricated. The ability to confine PSi formation to form buried PSi channels by selectively having regions on the silicon surface with two different end-of-ranges and high irradiation fluence was also demonstrated. Buried 3D hollow channels in PSi and glass-like FOPS was successfully fabricated. 3D surface patterns with precisely controlled step heights were machined by precisely controlling the irradiation fluence. Thin, free-standing silicon structures with micro- and nano-dimensions were fabricated using a resist pattern in conjunction with large, broad area uniform ion irradiation and subsequent undercutting the high defect density regions which could later be detached from the substrate by removing the surrounding PSi. Controlling the fluence allows fabrication of nano-structures together with micro-structures using

a single ion energy and anodization step. Further developing and extending the work described in this chapter is the basis of several in progress projects.

Chapter 9 : Studies of Silicon-on-Insulator Materials

Silicon-on-insulator (SOI) based photonic components utilize both the low refractive index and near atomic smoothness of the buried oxide to provide a low-loss optical confinement layer. Fabrication of many different types of photonic devices in silicon-based and SOI material has been intensively researched [102, 110, 126] with most approaches combining some form of lithography for patterning and some form of etching to remove surrounding material. Each process step introduces additional roughness [127-128] resulting in high propagation losses in SOI waveguides, though subsequent oxidation greatly helps to reduce the roughness [81, 129]. For example, in Refs. [82, 130] the propagation loss for single mode SOI waveguides was reduced from 32 to 0.8 dB/cm when the sidewall roughness was reduced from 10 to 2 nm. Hence it is very important to be able to fabricate smooth SOI structures.

Although our micromachining technique has been used for a variety of applications, as discussed in previous chapters, its use for silicon photonics was limited because SOI wafers cannot be anodized using a conventional direct current since the buried oxide layer prevents a continuous current flow across the wafer. A solution for overcoming the d.c. anodization limitation for SOI wafers was found, involving modifying the anodization setup as described in the first section of this chapter.

The second section of this chapter describes attempts to devise methods for fabricating patterned areas of silicon-on-insulator out of bulk silicon using the process of ion irradiation and electrochemical anodization. This study is important

as it is difficult to obtain high quality patterned SOI material due to the limitations of common methods for formation of patterned, buried oxide layers [131-132].

9.1 Electrochemical anodization of SOI using an alternating current

Electrochemical anodization of bulk silicon [44] gives a low surface roughness, typically 2 nm for anodized layer thicknesses of a few hundred nanometers [85]. A variety of surface-relief patterns and variable wavelength and intensity photoluminescence have been micromachined in CIBA using our micromachining technique in conjunction with electrochemical anodization (see chapter 2.8) [51, 75, 89, 133]. Using our technique either a surface relief pattern or completely undercut structures suitable for silicon waveguide formation can be produced. Chapter 2.8.4 reviewed irradiation through a thick, patterned photoresist [40] to produce silicon-on-oxidized-porous-silicon strip waveguides in bulk silicon with widths and heights from 1.5 to 3.0 μm . It was shown that after a high temperature annealing to remove the lattice damage and for oxidation smoothening, propagation losses of ~ 1 dB/cm can be obtained [75].

This machining process would be ideal for fabricating low loss SOI photonic components. However, conventional direct current (d.c.) electrochemical anodization relies on a constant current flowing to the front surface of bulk silicon and the oxide layer in SOI prevents this. Alternative approaches to anodizing SOI have been studied, such as lateral anodization across the front surface, or stain etching [44], but none produce a high uniformity or low roughness. In this section we show how this limitation can be overcome using an induced alternating current (a.c.) to anodize the device layer of SOI wafers.

9.1.1 Mechanism of electrochemical anodization of SOI using a.c.

Consider a SOI wafer as a simple parallel plate capacitor with the substrate and device silicon layers forming the conducting plates, separated by the buried silicon dioxide dielectric. An alternating potential applied across the wafer induces an alternating current across the dielectric which results in anodization of the device layer surface for the half of the alternating cycle in which the hole current flows in this direction, with hydrogen evolving from the surface during the second half of the cycle. Both wafer surfaces are anodized, though the back surface may be stopped from being anodized by replacing the HF electrolyte in this half of the cell with a non-anodizing solution. This approach is used to uniformly anodize SOI wafers with a surface roughness comparable to that obtained using conventional d.c. anodization.

9.1.2 Patterning SOI wafers using a.c. anodization cell

Figure 9-1 (a) shows patterning the SOI device layer using ion irradiation through a 10 μm thick poly (methyl methacrylate) (PMMA) photoresist. A fluence of $1 \times 10^{15}/\text{cm}^2$ of 500 keV protons was used, with a range of 7.7/6.1 μm in PMMA/Si respectively, so only the exposed wafer areas are irradiated. After removal of the PMMA layer a double-sided cell was used for a.c. anodization (Figure 9-1 (b)), with both surfaces exposed to the HF electrolyte over a wafer area of $1.2 \times 1.2 \text{ cm}^2$. This cell is very similar to the cell described in chapter 3.2. The only difference is instead of the d.c. power supply, here an a.c. voltage is used. A 50 Hz mains-coupled variable a.c. voltage supply was used with a 30 Ω series resistor to limit the induced current. The irradiated areas of the device layer remain unanodized since the high ion fluence renders them highly resistive, so all the hole current flows to adjacent unirradiated areas which are progressively anodized with time.

The PSi was then removed with a diluted KOH solution, leaving a patterned SOI device layer [Figure 9-1 (c)].

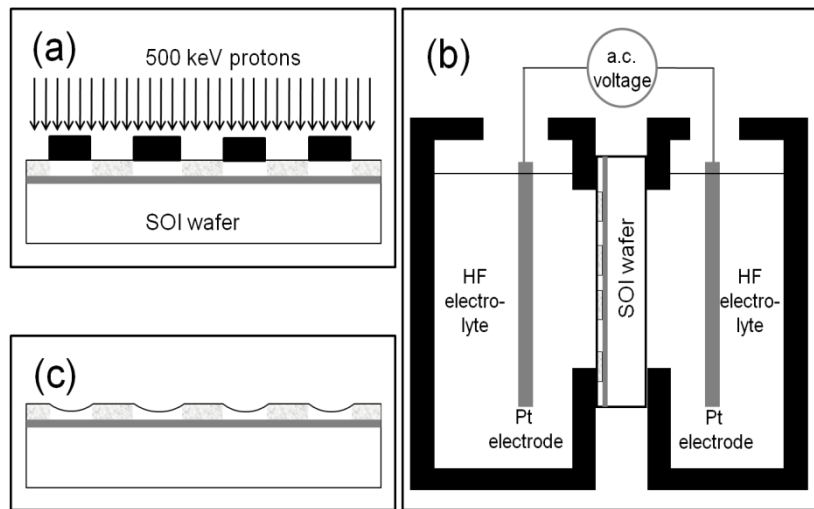


Figure 9-1 : Schematic of the a.c. anodization process. (a) Proton irradiation through a thick, patterned PMMA layer (shown in black) results in a patterned SOI device layer. (b) Teflon cell (shown in black) for a.c. anodization of SOI wafer. This cell is similar to Figure 3.3 but here a.c. voltage instead of d.c. voltage is used. (c) Removal of PSi producing a patterned SOI device layer.

9.1.3 A.c and d.c anodization of bulk silicon

The effects of a.c. and d.c. anodization using the above cell (Figure 9-1 (b)) are compared in this section. Two $2 \times 2 \text{ cm}^2$ pieces of $10 \text{ } \Omega \cdot \text{cm}$ p-type bulk silicon wafers were first patterned with a thick resist pattern having lines and spacings of 20 and $10 \text{ } \mu\text{m}$ respectively. The samples were irradiated with 500 keV protons. These samples were then anodized with the same anodization setup in a.c. and d.c. modes to depths of 250 nm using a same current density of $\sim 50 \text{ mA/cm}^2$. After removal of the PSi with KOH solution the surfaces were measured with AFM. The height profiles, recorded perpendicular to the etched lines, in Figure 9-2 exhibit similar behavior. The anodized surfaces at the unirradiated regions are convex, since deflection of the hole current away from the irradiated regions usually produces a higher anodization rate at the boundary with adjacent unirradiated regions [29]. The width of the boundaries between the irradiated lines and the

anodized regions is about 2 μm . The RMS roughness measured from $3\times 3 \mu\text{m}^2$ regions at the top, irradiated surfaces are 0.30 nm for both a.c. and d.c. modes, as one would expect since it is effectively a virgin surface. The roughness of the anodized surfaces are 0.8 nm and 0.7 nm in a.c. and d.c. mode respectively, with an error of ± 0.25 nm. This behavior agrees with Ref. [134] where it was shown that a.c. and d.c. anodization of bulk silicon produced similar photoluminescence and surface roughness, and it demonstrates that both anodization modes produced similar patterned features from ion irradiated areas.

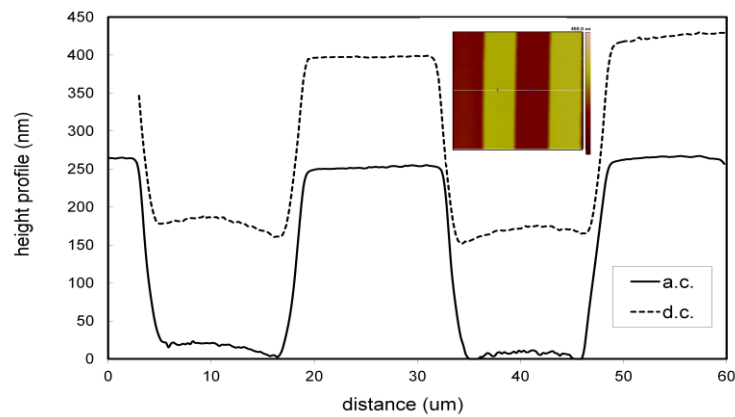


Figure 9-2 : AFM line profiles 10 Ω .cm p-type bulk silicon anodized in a.c. and d.c. modes, offset for clarity. The inset shows the AFM image of the a.c. anodized wafer.

9.1.4 Line pattern fabrication on SOI wafers using large area irradiation

A SOI wafer (ULTRASIL) with a 10 Ω .cm p-type device layer thickness of 10 μm and buried oxide thickness of 1 μm , was similarly patterned with a fluence of $1\times 10^{15}/\text{cm}^2$, then a.c. anodized to a depth of $\sim 5 \mu\text{m}$. An alternating voltage of 50 to 100 V was used to induce an a.c. current of ~ 60 mA, equivalent to a wafer impedance of ~ 2 k Ω . Figure 9-3 shows cross-section SEMs of the central portion of the anodized wafer. The gaps between the irradiated lines are all anodized to the same depth (Figure 9-3 (a)), demonstrating that the anodization rate is uniform across this central portion of the anodized surface. In Figure 9-3 (b) the anodized

surfaces have a concave profile, compared with the convex profiles in Figure 9-2. Such concave profiles are associated with heavily irradiated, closely-spaced features in highly resistive wafers [29] where the current deflected from the opposing irradiated regions creates a maximum at the central point between them, producing in a more deeply etched, concave surface.

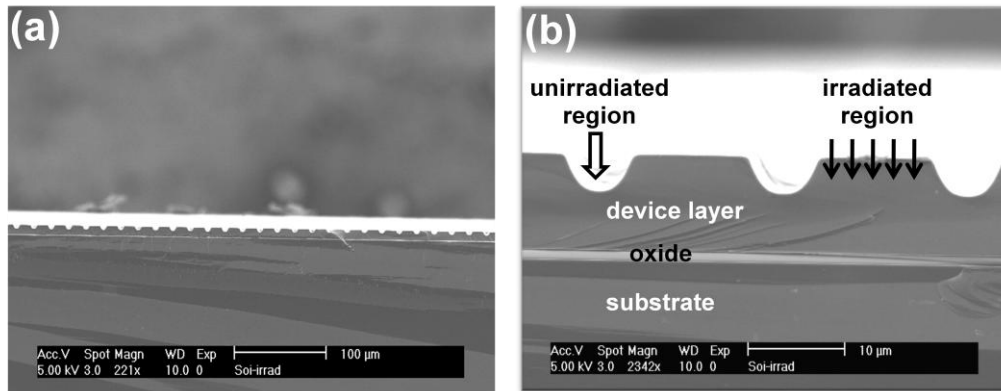


Figure 9-3 : Cross-section SEMs of the central portion of the a.c. anodized SOI wafer at different magnifications.

Further study confirmed that a.c. anodization produced uniform features across the central 6 mm width of the exposed 12 mm wide SOI surface. However, towards the cell boundary, the anodization rate varies laterally resulting in a non-uniform depth of the gaps between the etched lines [Figure 9-4(a)].

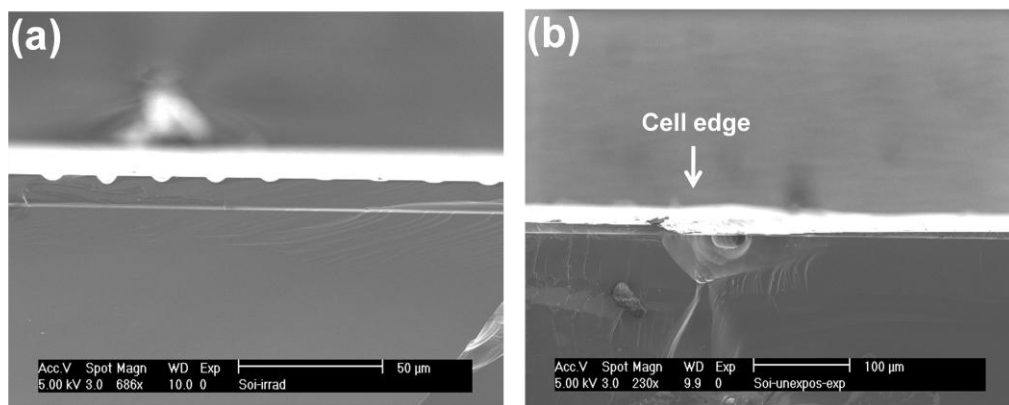


Figure 9-4 : Cross-section SEMs of the a.c. anodized SOI wafer close to the cell edge. (a) shows the non-uniform lateral anodization, (b) shows the deep groove forming at the cell edge.

Furthermore, at the cell boundary a deep groove tends to form [Figure 9-4(b)]. Since anodization occurs at a much faster rate here, care is needed during

anodization. Once the buried oxide layer at the groove is exposed, the HF electrolyte rapidly dissolves it and creates a much lower resistivity conducting path to the surface, effectively short-circuiting the wafer. The current flowing must therefore be carefully monitored and the current flow stopped when it rapidly increases. It is noted that a.c. anodization of SOI wafers exhibits similar problems as does d.c. anodization of bulk, high resistivity wafers (described in chapter 3.2.1) [135] where similar problems of groove formation and lateral non-uniformities in the anodization rate are observed.

9.1.5 Micromachining line patterns on SOI using a line focus

In Figure 9-1, the thick photoresist layer required to stop the 500 keV protons limits the minimum lateral size of the irradiated areas to about 5 μm . Here we use a novel maskless process for high-energy ion irradiation with the beam focused to a long line, up to 6 mm in length, with a width of about 1 μm . This is done by exciting the quadrupole lenses of a nuclear microprobe focusing system [136] in a particular manner so that the beam is focused in one plane but highly defocused in the orthogonal plane. This is suitable for waveguide formation of SOI without the commonly-encountered problems of PBW using a beam focused to a point (see chapter 2.6), namely beam fluctuations from one position to another and a limited scan size.

The AFM image in Figure 9-5 shows such a line irradiated in the SOI wafer material with a 10 $\Omega\cdot\text{cm}$ device layer thickness of 10 μm and buried oxide thickness of 1 μm . The line was irradiated using 2 MeV protons with a fluence of $5 \times 10^{14}/\text{cm}^2$. After a.c. anodizing the SOI device layer to a depth of 2 μm , the line width is 2.5 μm , the best achieved to date.

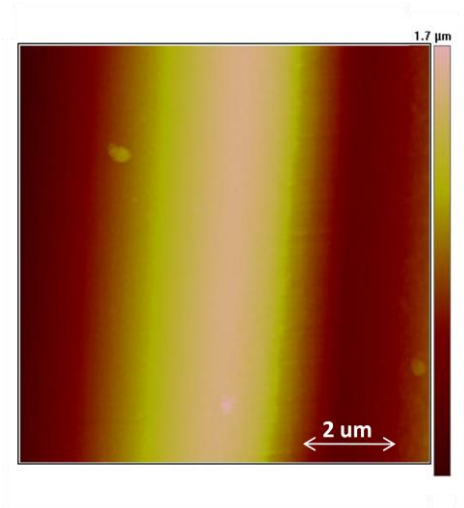


Figure 9-5 : AFM image of a single irradiated line in SOI after a.c. anodization, using a line focus of 2 MeV protons.

9.1.6 Summary

Electrochemical anodization of SOI wafers can be achieved using an induced a.c. current across the buried oxide, in addition to which a new maskless process for ion irradiation using a line focused ion beam is described. The resultant surface roughness is comparable to that obtained using conventional anodization and uniform etching across a 6 mm exposed surface area is obtained. This opens up a new route to fabricating SOI-based photonic components. The use of thinner device layers can be investigated to reduce the minimum achievable line width from its present value of 2.5 μm.

9.2 Formation of patterned SOI via ion irradiation on bulk silicon

SOI materials play an important part in fabricating high-speed and low-power logic circuits [137]. Making patterned SOI and patterned silicon/SOI in a flexible and cheap manner is another important field that needs to be studied for improving the fabrication of high performance integrated devices. However, producing high quality, patterned SOI is challenging using standard methods for forming buried oxide layers, with several previous attempts to find a suitable process for patterning SOI [131-132]. This section focuses on fabrication of partial SOI substrates via ion irradiation and anodization of bulk silicon. The PSi is converted to oxidized PSi, forming an insulator layer which is sandwiched between two silicon layers. Because of the nature of PSi, it oxidizes much faster than bulk silicon to become fully oxidized PSi (FOPS) [75]. As a result patterned (partial) SOI and silicon/SOI can be formed.

9.2.1 Principle of fabrication of patterned SOI wafer using PBW

Existing techniques for fabricating SOI structures are generally expensive or are not flexible in being able to produce patterned SOI [138]. Bonding techniques, i.e. Bonded and Etched back SOI (BESOI), SmartCut and Epitaxial Layer TRANSfer (ELTRAN) processes, form SOI by bonding oxidized surfaces of two wafers [126]. Van der Waals forces initiate and thermal annealing at 1100°C finalizes the bonding between wafers. In the BESOI process [139], etch back of the structures until the desired thickness of SOI is obtained. The SmartCut process [140] achieves splitting of a surface layer of upper wafer by implantation of hydrogen or helium ions prior to bonding and annealing, and the ELTRAN process [141] is based on the same bonding and splitting steps, only the splitting layer is PSi. SOI formed by these three bonding techniques are mono-crystalline but usually full

SOI wafers are obtained. It would require several additional steps, which would increase the cost significantly, to form partial SOI films. Separation by implantation of oxygen (SIMOX) [142] is another technique for fabricating SOI wafers, in which the buried oxide layer is obtained by oxygen implantation. The oxygen energy and dose determine the thickness and the depth of the buried oxide layer. SOI films formed by SIMOX have good crystalline quality, but the implanted oxide layer is not as perfect as a thermal oxide, which may lead to isolation problems. This process can provide full and thin SOI wafers and partial thin SOI films can be obtained by adding a photolithography step before the implantation.

Another method for fabricating patterned SOI wafers is using Full Isolation by Porous Oxidized Silicon (FIPOS) [42] method which is based on proton implantation to temporary change the silicon conductivity from p to n in the irradiated regions defined by a mask covering the wafer surface. After the electrochemical anodization step for forming the PSi, the buried PSi layer is oxidized through the openings to form buried oxide layer cladding the crystalline silicon islands defined by the prior irradiation step. Compared to SIMOX, FIPOS is a promising method due to flexibility in controlling the thickness of the layers by well-defined ion range at different energies and controlling the etching time, however it requires the formation of a PSi layer which is about half the depth of the largest surface area to be isolated, because of the isotropic etching beneath the irradiated layer. Such thick porous layers are not desirable owing to their inherent tendency to crack under their built-in stress.

9.2.1.1 Fabrication process using PBW

In this section an alternative process to fabricate patterned SOI wafers with controllable thickness of the device and buried oxide layer is discussed. This

process has similarities with FIPOS, with the advantage of making use of the high-defect density at the end-of-range of high energy ions to provide a means of limiting the thickness of the PSi layer. Figure 9-6 shows a schematic of the process which we devised. The principle is very similar to formation of multilevel 3D silicon structures described in chapter 8. Here two different energy and fluence irradiations are used to form two flat silicon surfaces forming the device and bottom layer of a SOI wafer (Figure 9-6 (a)). At each energy, parallel line regions are irradiated using PBW. The high fluence of the lower energy ions is enough to almost stop the etching in subsequent anodization step in the irradiated regions to form the device layer. Hence, the thickness of the device layer is controlled by the type and energy of the ions used for this step. A higher energy with low fluence is used to only create localized defects at the end-of-range of ions. The thickness of the buried oxide layer of the SOI wafer can be controlled by the difference between the two ion energies and the fluence of the higher energy. The wafer is then anodized to form PSi around the high defect density regions. A deliberate mis-aligning between the two levels of parallel regions helps the anodization current flow and hence the formation of PSi between the two irradiated levels. The PSi starts to form from the unirradiated space between the top irradiated lines and then starts to undercut the top layers. When PSi formation reaches the second localized highly-defective regions, these regions remain unetched and instead start to be undercut. Hence, two parallel flat silicon films separated by PSi can be formed. The sample can then be thermally annealed to convert the PSi layer to an insulating FOPS layer as well as repairing the defects created in the crystal lattice of the wafer by the ion irradiation (Figure 9-6 (c)). As a result by using PBW after anodization and annealing steps any arbitrary shape patterned SOI and patterned

silicon/SOI can be obtained. Using the above process, SOI regions can be made with sizes ranging from microns to hundreds of microns.

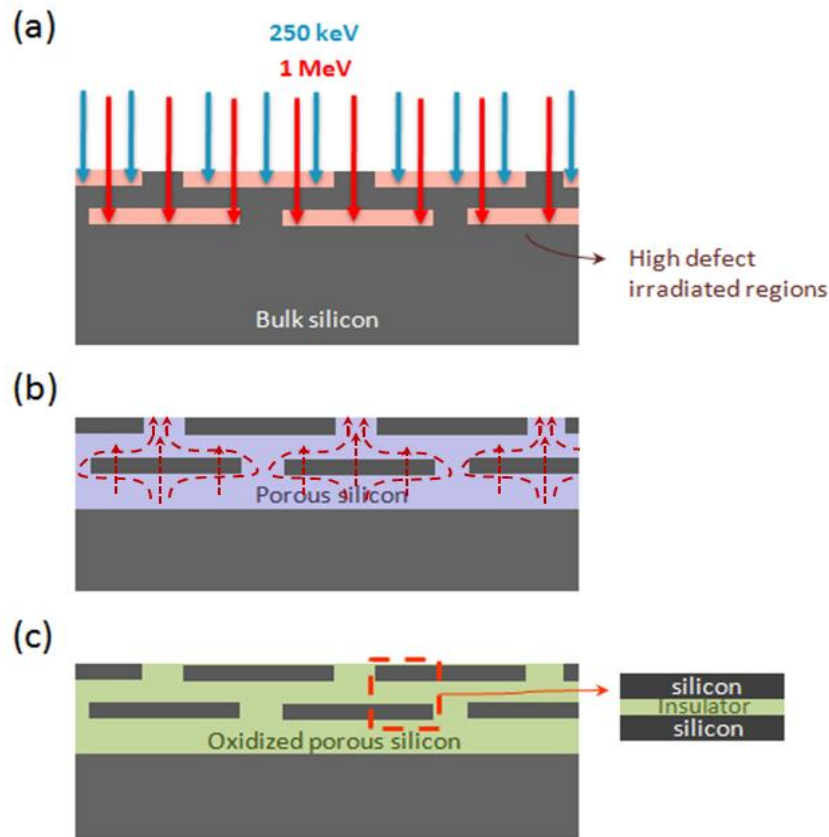


Figure 9-6: Schematics of the processes involved in fabricating patterned SOI wafer using (a) 250 keV and 1 MeV proton irradiation, (b) anodization to produce PSi around the irradiated regions, red dashed arrows show the hole current flow and (c) thermal annealing to oxidized the PSi layer.

9.2.1.2 Experimental results

PBW was used to irradiate an arrays of 3 mm long lines with a width of 30 μm with 250 keV protons (range $\sim 2.5 \mu\text{m}$ in silicon) with a high fluence of $2 \times 10^{16}/\text{cm}^2$ and 1 MeV protons (range $\sim 16 \mu\text{m}$ in silicon) with a low fluence of $1 \times 10^{15}/\text{cm}^2$ inside a 0.02 $\Omega\cdot\text{cm}$ wafer. The sample was then anodized by alternately raising and lowering the etch current density of 40 and 80 mA/cm^2 during anodization to alter the porosity of PSi for the purpose of tracking the progression of the PSi formation. Figure 9-7 shows cross section SEMs of the wafer after anodization. The red dashed arrows in Figure 9-6 (b) show the desired hole current flow during anodization. The PSi forms around the top irradiated regions, leaving them almost

unetched. For low fluences used for deeper irradiation, the built-in potential surrounding the deep end-of-range region is small, allowing holes beneath this region to diffuse and contribute to etching above these irradiated regions, resulting in P*Si* undercutting the top irradiated region followed by formation of flat top deeper regions. The formation of the deeper silicon level is very similar to what was described in chapter 6.3 for extended width regions (only here the base angle θ tends to 180°) due to the large width of the irradiated area.

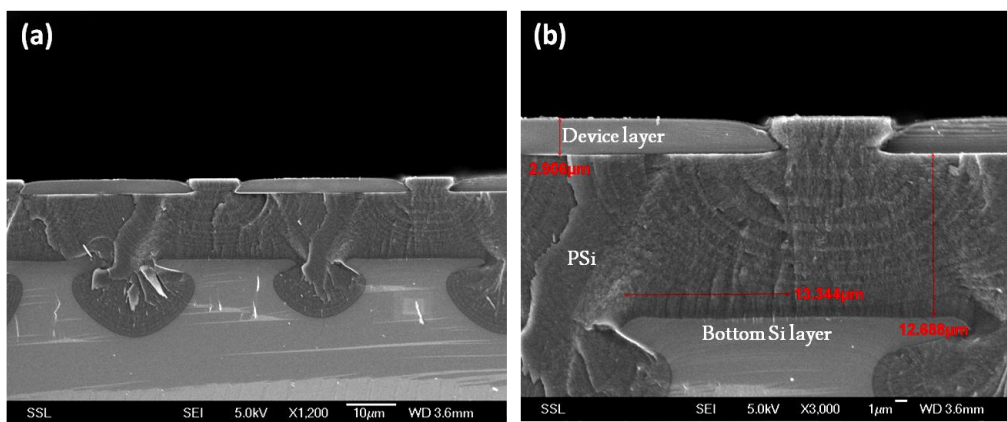


Figure 9-7 : Patterned SOI wafer formed by 1 MeV with a low fluence of $1 \times 10^{15}/\text{cm}^2$ to form the bottom layer, and 250 keV protons with a high fluence of $2 \times 10^{16}/\text{cm}^2$ to form the top layer.

With increasing fluence used for the deeper irradiated regions, the defect density above these end-of-range regions increases, making it more difficult for holes to pass through and etch the silicon between two levels of irradiation. This makes it more difficult to completely undercut the top irradiated region and hence the two levels of irradiated regions are more likely to remain connected to each other at the central part of the top irradiated region. In such cases, hole transport is easiest at the sides above the deeper irradiated regions, resulting in unetched regions with a sloping profile. Hence, a shape similar to that in Figure 5-19 iii(e) is observed. Figure 9-8 shows such an irradiated region where it can be seen that the two levels are connected to each other, and the connected area becomes wider by increasing the deeper irradiation fluence as the hole supply for etching becomes more difficult.

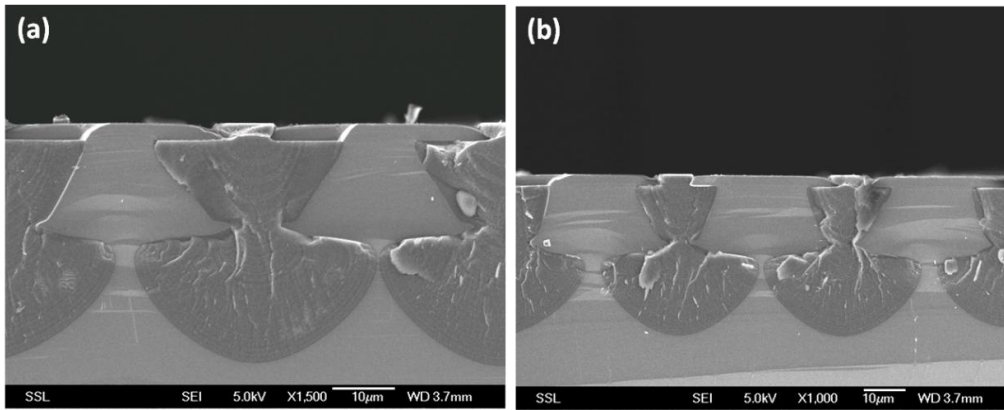


Figure 9-8 : Two levels of irradiation connected to each other by using 250 keV protons with a fluence of $2 \times 10^{16}/\text{cm}^2$ and 1 MeV protons with a fluence of (a) $2.5 \times 10^{15}/\text{cm}^2$ and (b) $5 \times 10^{15}/\text{cm}^2$.

For a better understanding of the limitations of this process, another sample was irradiated with only 1 MeV protons with exactly the same irradiation and anodization conditions as for the deeper irradiations of Figure 9-7 and Figure 9-8. Cross-section SEMs are shown in Figure 9-9. As described in chapter 5.3 these extended irradiated regions have a flat top and by increasing the fluence they become taller. However, adding another highly-irradiated region above this makes it difficult for holes to reach the top irradiated regions, hence they are more likely to be connected.

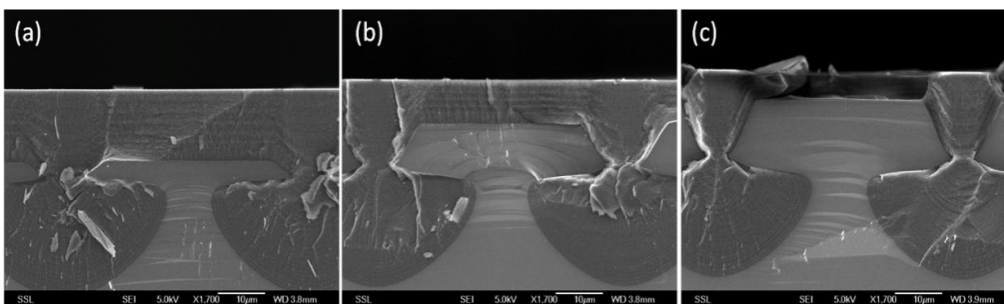


Figure 9-9 : SEM cross-sectional images showing only the bottom irradiation with the same irradiation and anodization conditions as (a) Figure 9-8, (b) and (c) Figure 9-9 (a),(b) respectively.

Figure 9-10 (a) shows another example, similar to Figure 9-7, where 30 μm lines are irradiated with 600 keV helium (range 2.2 μm) with a fluence of $1 \times 10^{15}/\text{cm}^2$ and 1 MeV protons with a low fluence of $7 \times 10^{14}/\text{cm}^2$, hence forming a larger gap between the irradiated levels. Figure 9-10 (b) shows an intermediate condition where the bottom fluence is not high enough to form a significant barrier

for the holes to make the two levels of irradiations connected, but high enough to form slightly taller unetched silicon regions with a flat top and hence a thinner PSi layer. This is assumed to happen owing both to the lower fluence used for the bottom irradiated regions and the larger gap between the two levels in comparison to Figure 9-8 (a),(b). The irradiated top silicon regions are lifted during the cleaving of the sample, it is not related to the anodization process.

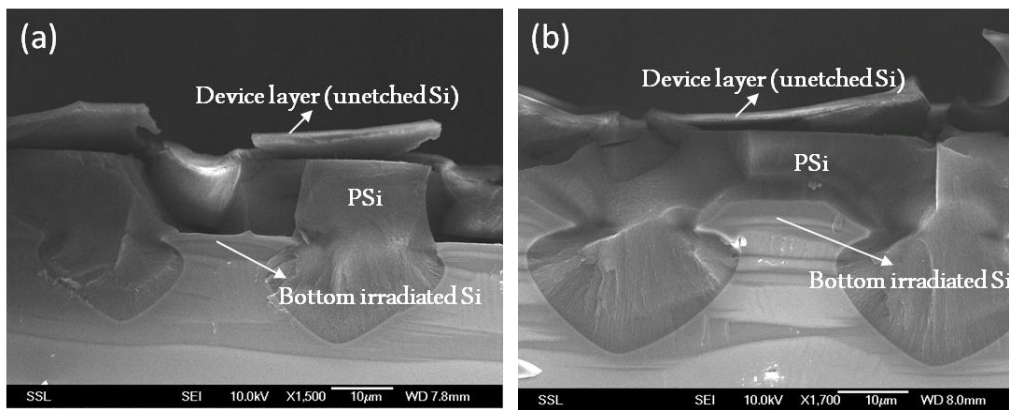


Figure 9-10 : Cross-section SEMs of 600 keV helium ion irradiation with a fluence of $1 \times 10^{15}/\text{cm}^2$ and 1 MeV protons with a fluence of (a) $7 \times 10^{14}/\text{cm}^2$ and (b) $1.4 \times 10^{15}/\text{cm}^2$. The irradiated top silicon regions are lifted during the cleaving of the sample.

9.2.2 Fabrication process using large area irradiation

Using these same principles, attempts were also made to fabricate larger area SOI wafers and patterned SOI areas. For this we used the newly-designed anodization cell described in Figure 3-7, made for this purpose which helps to cover the irradiated parts of the wafer to prevent them being etched by contacting with the HF solution. In this work both front and back sides of the samples are irradiated.

Figure 9-11 shows the process flow schematic for this work. Entire surfaces except for a few small regions of the front and back side of a wafer were irradiated with a high fluence using the large area irradiation facility. The aim is to produce an unirradiated layer which is sandwiched between highly irradiated, highly resistive layers (Figure 9-11 (a),(b)). This unirradiated layer together with the small unirradiated regions at the front and back surface provides the pathway

for the hole current to flow, Figure 9-11 (c). Hence P*Si* forms only in the unirradiated layer within the wafer, sandwiched by a top and bottom silicon layers (Figure 9-11 (d)). The P*Si* layer can easily be oxidized afterwards, resulting in an insulating FOPS layer, giving a full SOI wafer made out of bulk silicon. In addition, by controlling and allowing anodization current to flow in only specific areas within the wafer, the positions of formation of SOI within the silicon wafer can be controlled. Hence patterned designs which have silicon together with SOI on a single wafer may be achievable.

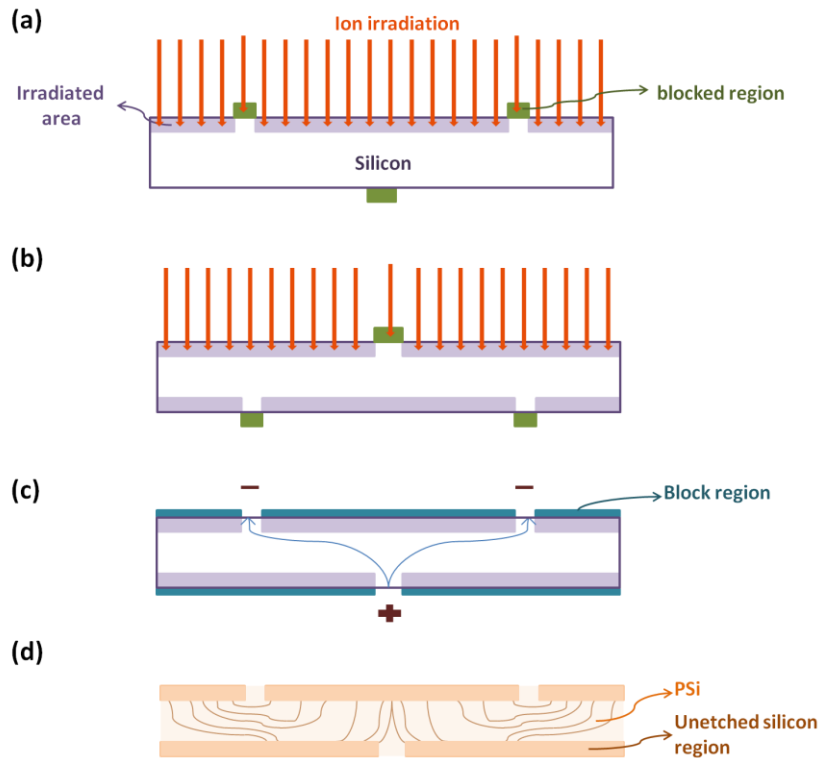


Figure 9-11 : Schematics showing the fabrication process of SOI wafer using large area high-energy ion irradiation for directing the hole current during electrochemical anodization in the sample.

To achieve a uniform P*Si* layer, the two surfaces of the wafer, except those parts covered with a ring on the front surface and a small disk on the back side are irradiated with a high fluence. The unirradiated disk at the front side is positioned right in the centre of the unirradiated ring on the back side. Using the special Teflon cell and covering the irradiated parts with HF resist further ensures that the

anodization hole current only flows from the unirradiated disk to the unirradiated ring via the sandwiched unirradiated layer within the wafer.

Figure 9-12 shows preliminary results, where both top (except a ring shape) and bottom (except a disk shape) of the sample is irradiated with 1MeV helium to a fluence of $1 \times 10^{16}/\text{cm}^2$. The irradiated parts are covered with SX AR-PC 5000/40 (Allresist Company) HF resist to further ensure they are not etched during the anodization. From Figure 9-12 (a),(b) the PSi starts to form from unirradiated ring shape region on top of the wafer and slowly starts to undercut the irradiated regions covered with the Teflon cell and HF resist (Figure 9-12 (c)). By continued etching the whole surface area can be undercut and hence forming PSi layer beneath the top irradiated layer. It should be noted that the etch rate is usually around tens of microns per minute; hence undercutting large areas requires very long anodization time. Another limitation of this work is not having access to higher energy ion irradiation and hence a very large gap of hundreds of microns remains between the two irradiated layers. The ion accelerator at CIBA can provide up to 2 MeV protons with an end of range of $\sim 48 \mu\text{m}$ in silicon, which assuming a wafer thickness of $250 \mu\text{m}$ leaves a very large gap between the two irradiated top and bottom layers and hence forming fragile PSi in this thick sandwiched layer. Next section shows a solution to these problems by using boron implantation.

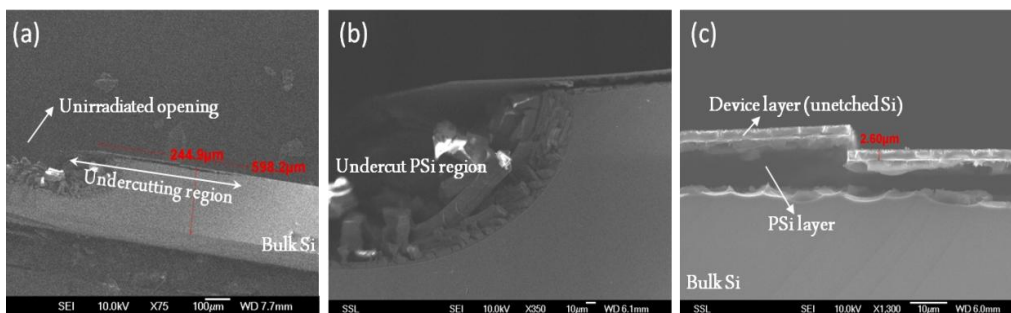


Figure 9-12 : Attempt to fabricate SOI wafer. Cross-section SEM of one side of the wafer (a) and magnified view of it (b). (c) Magnified SEM showing the undercut irradiated regions.

9.2.3 Fabrication process using boron implantation

Boron implantation makes silicon less resistive by increasing the acceptor doping density. Figure 9-13 shows the almost linear decrease in p-type silicon wafer resistivity by increasing the dopant density. After ion implantation, thermal annealing is needed for activation to remove lattice damage and locate the boron atoms on substitutional sites. Occupying lattice sites in the silicon crystal, they act as acceptors.

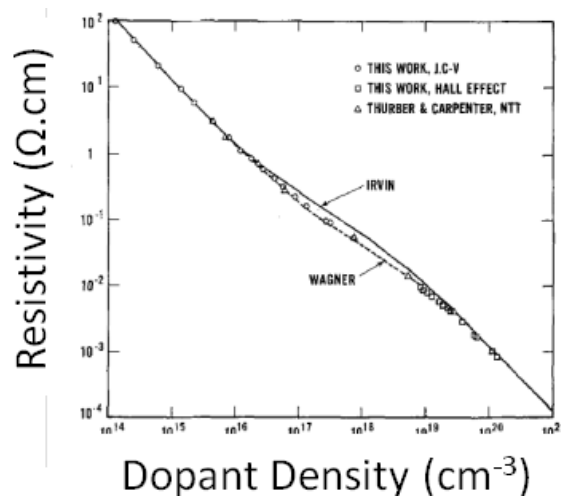


Figure 9-13 : Resistivity as a function of effective dopant density for p-type silicon at 300°K. From [143].

We investigated the use of boron implantation of bulk silicon for forming a more conductive buried layer at a depth of a few hundred nanometers in the wafer to facilitate hole current flow in the horizontal direction during anodization along this conducting path. For this work 10 Ω .cm p-type silicon wafers were implanted at the Institute of Microelectronics (IME) with different boron energies and fluences. Figure 9-14 shows an example, where the wafer was implanted with 300 keV boron to a fluence of $2 \times 10^{13}/\text{cm}^2$ to form a conducting layer which peaks at a depth of ~ 750 nm inside the bulk silicon (Figure 9-14 (a)). The sample was then covered with AZ 1518 photoresist (thickness of $2.5 \mu\text{m}$) with line patterns of $\sim 55 \mu\text{m}$ width and 1 cm long, then irradiated by 100 keV helium (range ~ 650 nm in silicon) fluence of $1 \times 10^{15}/\text{cm}^2$ using the large area irradiation facility. This energy

was chosen to make the top silicon layer above the boron implanted layer more resistive. Hence, during anodization undercutting of the irradiated lines is easier and faster as the anodization current preferentially moves horizontally along the conducting pathway formed by the boron implanted layer (Figure 9-14 (b),(c)). The sample was etched for 11 minutes with a current density of 60 mA/cm². Figure 9-14 (d) shows a high magnification cross-section SEM of the sample, where unetched silicon line and two different P*Si* layers with different porosity beneath the irradiated region are clearly observed. This can be explained by the fact that the more conductive boron layer forms mesoporous silicon, while the rest of the sample forms microporous silicon (see chapter 4.3). The stronger intensity observed at the boron implanted layer, which has a thickness of about 100 nm in this case, is because lower porosity silicon is a better secondary electron emitter.

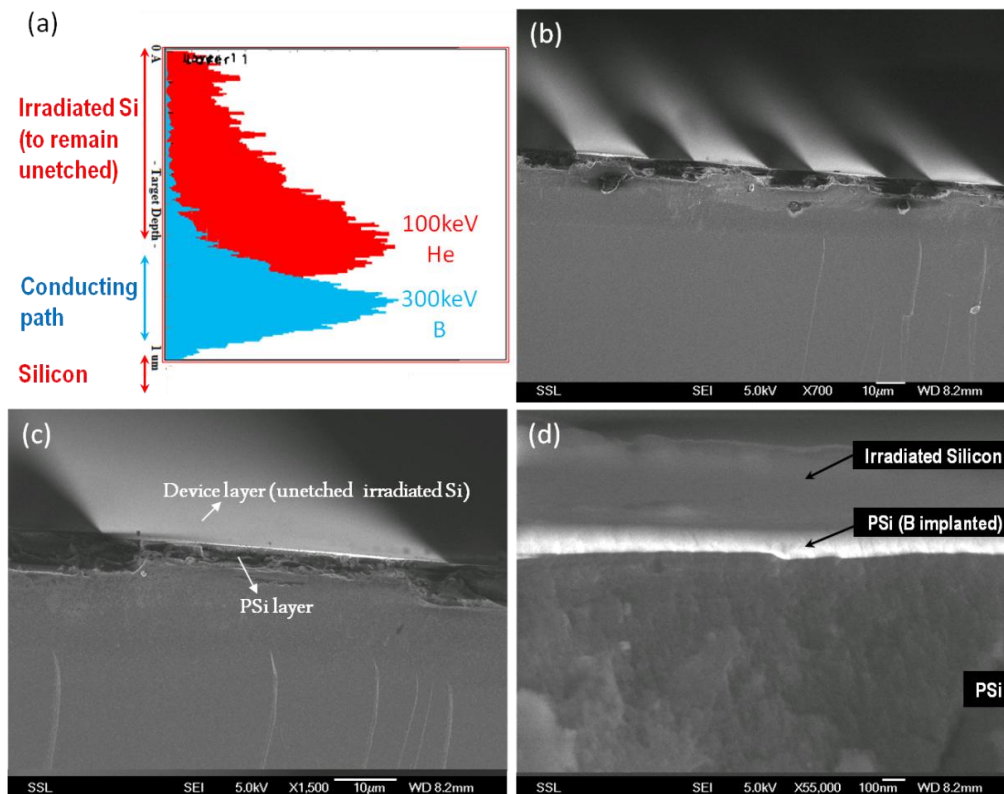


Figure 9-14: (a) SRIM simulation [23] showing the penetration depth of 300 keV boron (blue) and 100 keV helium (red). (b),(c) Tilted cross-section SEMs of silicon implanted with 300 keV boron and irradiated with a line pattern (d) High magnification cross-section SEM of the sample.

For comparison, another sample with a similar resistivity but without the boron implantation was prepared with the same irradiation fluence ($1 \times 10^{15}/\text{cm}^2$) and anodization conditions as for the sample shown in Figure 9-14. Optical cross-section images of both samples after being anodized for the same time are shown in Figure 9-15. The top region of the sample implanted with boron becomes undercut much faster owing to the more conducting pathway provided by the implanted region, while the other sample is undercut very slowly, with no mechanism to produce thin PSi layer at the base of the irradiated region.

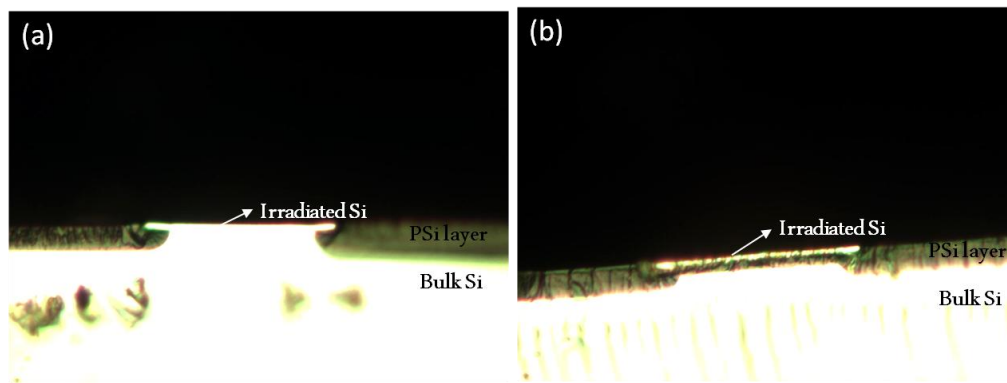


Figure 9-15 : Optical images comparing 5 Ω .cm wafer irradiated with a line pattern using 1 MeV helium (a) without boron implantation (b) with 300 keV implanted boron which allows an easy and fast undercutting of the irradiated regions by forming a conducting path.

By using ions with energies having a range deeper than the boron implanted layer, it should be possible to separate the irradiated region into two at the depth of the boron layer by forming a more conducting path for the hole current to flow during anodization. Figure 9-16 shows such an example, where the same wafer was implanted with 50 keV boron (range ~ 150 nm) to a fluence of $1.5 \times 10^{13}/\text{cm}^2$, followed by irradiation using 100 keV helium. A helium fluence of $1 \times 10^{15}/\text{cm}^2$ was used, enough to stop etching above and below the boron layer during subsequent anodization. A line irradiated pattern was achieved using a photoresist mask in conjunction with large area irradiation. Figure 9-16 (d) shows a very thin silicon layer on top of a PSi layer, corresponding to the depth of the boron implanted layer. The irradiated region under this layer slowly becomes

undercut, similar to other irradiated regions described in chapter 5.4. In the SEM image, PSi formed at the boron implanted layer appears a little brighter than other PSi regions, again explained by it having a lower porosity, hence stronger electron emission in the SEM (see chapter 2.6).

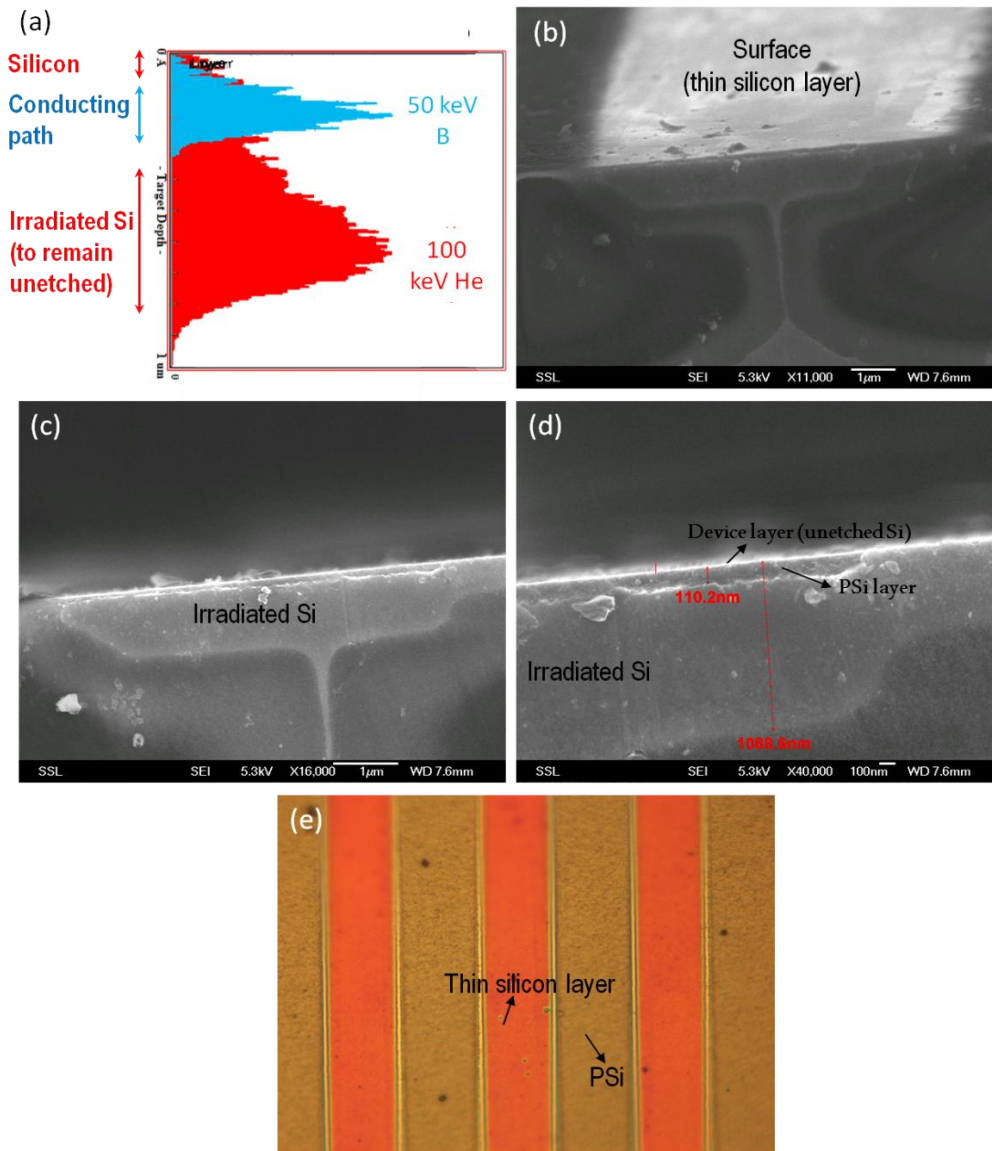


Figure 9-16 : (a) SRIM simulation [23] showing the penetration depth of 50 keV boron (blue) and 100 keV helium (red). (b) Tilted and (c),(d) normal cross-section SEMs of this sample irradiated with a line pattern. (e) Optical image showing top view of array of such irradiated lines. Silicon layers appear colourful as they are very thin.

To further explore the combined effects of boron implantation, which acts to make a layer more conducting, and high energy ion beam irradiation, which results in a more resistive layer, a wafer with the same resistivity was dual

implanted with 50 keV boron (range ~150 nm) with a fluence of $1.5 \times 10^{13}/\text{cm}^2$ and 200 keV boron (range ~550 nm) with a fluence of $2 \times 10^{13}/\text{cm}^2$. The sample was then irradiated with a fluence of $1 \times 10^{15}/\text{cm}^2$ of 100 keV helium ions. Hence, it is the same as that described above, except for an additional boron implantation which peaks at the same depth as the helium ion irradiation, Figure 9-17 (a). Figure 9-17 (b) shows that PSi has formed throughout the anodized depth, the different bands of intensity being due to at least three differing porosities produced through the layer structure owing to the superposition of the boron and helium ion depth profiles. The large features at the surface are consistent with formation of a macroporous silicon layer, since anodization current can now reach the surface through a high resistivity, thin layer, whereas in Figure 9-16, no current was able to reach the surface.

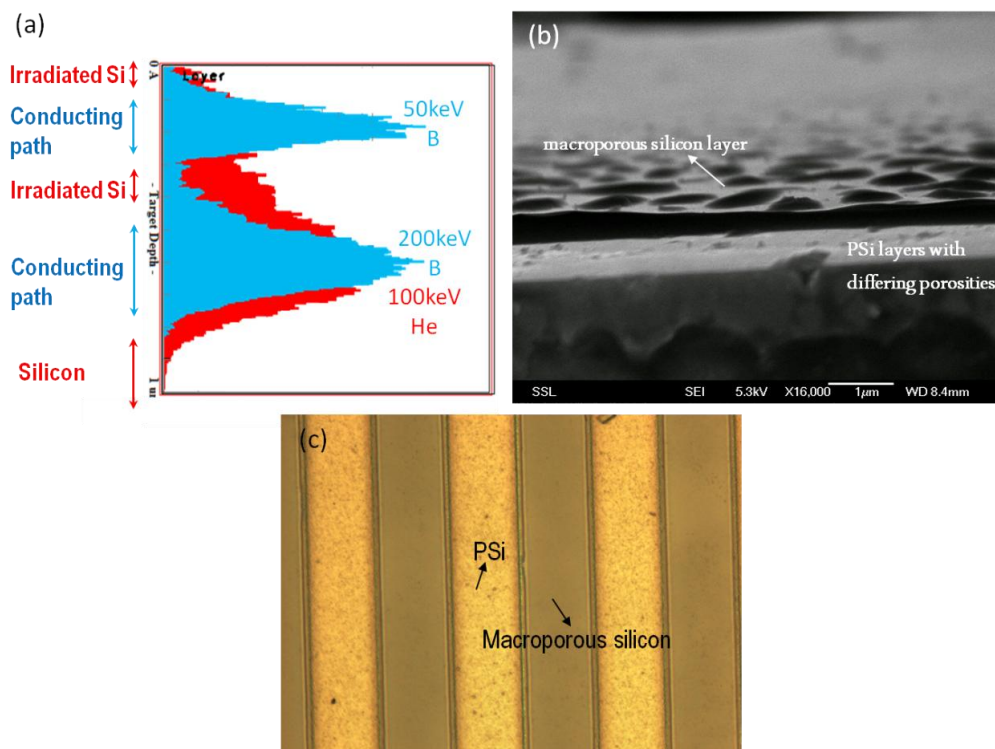


Figure 9-17 : SRIM simulation [23] showing the penetration depth of 50 and 200 keV boron (shown in blue) and 100 keV helium (shown in red). (b) Tilted cross-section SEM of silicon implanted with 50 and 200 keV boron and irradiated with a line pattern, showing a thin macroporous silicon layer formed on the top surface of the irradiated wafer. (c) Optical image showing top view of array of such irradiated lines.

9.2.4 Summary

This section has described studies of the use of two level ion irradiation followed by electrochemical anodization of bulk silicon to form patterned SOI wafer. The possibility of forming large, patterned areas of SOI wafer is demonstrated using a new design of anodization cell or by boron implantation to facilitate the desired direction of anodization current flow. Although much of this work is still in progress it does point the way forward to how these processes may be used to achieve patterned SOI wafer out of bulk silicon.

Chapter 10 : Conclusions

To date, there is no single technique capable of fabricating multilevel, truly 3D silicon structures in a convenient way. A novel innovative technique for fabricating such silicon and PSi components at micro- and nano-scale dimensions was developed in this thesis. Using this technique, free-standing, arbitrary-shape, curved, multilevel, true-3D silicon components combined at nano- and micro-scales were machined in a single etch step at different depths of bulk wafer. This process uses p-type wafers within a range of resistivity from $\rho \sim 0.01 \text{ } \Omega\cdot\text{cm}$ (doping density $\sim 10^{19}/\text{cm}^3$), to $1 \text{ } \Omega\cdot\text{cm}$ (doping density $\sim 2 \times 10^{16}/\text{cm}^3$) for different applications.

The fabrication process in this thesis is based on the defects created by high energy ions, such as 100 keV to 2 MeV protons, molecular hydrogen and helium ions, in crystalline silicon, at the surface and along their trajectory. The created defects act as trap levels where charge carriers undergo recombination, so reducing the hole density and increasing the resistivity along the ion trajectories. Ion irradiation thus reduces the electrical hole current flowing through these irradiated regions during subsequent electrochemical anodization in HF electrolyte, slowing down or completely stopping the formation of PSi for low/high fluences. For moderate fluences the anodization rate is selectively stopped only at depths corresponding to the high defect density at the end of ion range, allowing multilevel true three-dimensional silicon machining. We can controllably vary the width of 3D structures from a few tens of nanometers to tens of microns by varying the irradiation width and the ion fluence, and the depth of structures by varying the ion energy. By using a combination of multiple energy

irradiation and/or gray-scale masks, different ion penetration depths and multilevel free-standing three-dimensional silicon structures were obtained.

Two different irradiation approaches were used for the silicon machining in this thesis: PBW and large area irradiation. Although PBW is a useful and flexible approach for making prototypes for 3D silicon components, the throughput is small due to the low currents when using a highly focused beam and also the scan size is limited. A broad uniform beam in conjunction with a patterned surface mask can be used for rapid mass production of 3D silicon components over a large area, with additional benefit of uniform irradiation and hence eliminate any surface roughness caused by beam current fluctuation and stage scanning compared to using PBW. Different types of resist patterning techniques such as UV, e-beam, proton-beam, X-ray lithography and TPL were used for this purpose depending on the feature resolution and the resist thickness.

For better understanding the potential of this machining process, fundamental aspects of this work were also studied, particularly surface roughness and characterization of PSi and the effects of patterned ion irradiation on the motion of current flowing through irradiated regions. Different parameters influencing the PSi type and the roughness of revealed silicon surfaces, as well as the effect of focused and large area ion beam irradiation on the surface roughness of silicon wafers with different resistivities after subsequent electrochemical anodization were studied. Furthermore, a new mechanism for current transport during electrochemical anodization of low-fluence ion irradiated p-type silicon was observed in this thesis. Here a hole diffusion current is highly funneled along the gradient of the modified doping profile towards the maximum ion induced defect density, so dominating the etching behaviour. At higher fluences a solid 3D silicon core can form. For predicting the core shape and size, this mechanism

together with other important factors, including irradiation width, ion energy, ion fluence and the wafer resistivity, were studied. These studies are important in understanding the basic mechanisms and effects of ion irradiation of p-type silicon wafers and also defining the different behaviour of surface roughness and PSi photoluminescence intensity and wavelength which can occur. In addition to a new approach to patterning using electrochemical anodization, this study provides an important insight into how any ion irradiation process can introduce a diffusive current funneling mechanism which alters the current flow through semiconductors, relevant to many fields including radiation induced defects in satellite-based electronics, proton isolation of device areas and wafer gettering.

This machining process was applied in different fields such as photonics, microfluidics, X-ray optics, SOI technology and nanoscale depth machining. Several examples of current and possible future applications of 2D/3D bulk and surface machining using this novel silicon machining technique were described in this thesis, such as

- Free-standing, true 3D multilevel micro- and nano-scale silicon components,
- Buried PSi channels in silicon,
- Buried high porosity PSi channels in surrounding PSi material,
- Buried, hollow micro- and nano-channels in PSi and glass,
- 3D surface patterns with precisely controlled step heights of the order of few tens of nanometers to tens of microns,
- 3D silicon lines with sharp nano-sized tips having arbitrary angle with the surface,

- Thin film silicon structures at micro- and nano-scale,
- Nanostencil masks,
- Combined 3D micro- and nano-scale silicon and resist components,
- Patterned SOI wafers out of bulk silicon.

Further developing and extending the work described in this thesis is the basis of several in-progress projects in CIBA, and can open up abundant new possibilities and applications for fabricating different components for fields such as M/NEMS, photonics, optoelectronics, nanostencil lithography, micro/nanofluidics and tissue engineering. Micro- and nano-machining 3D components which may have custom shape design and improved performances and functionalities, may lead to fabrication of highly compact 3D systems-on-a-chip to develop future micro/nanotechnologies.

Bibliography

1. Franssila, S., *Introduction to Microfabrication*. 2010: John Wiley & Sons.
2. Franz Laermer and A. Schilp, *Method of anisotropically etching silicon*. U.S. Patent 5501893 Mar. 26, 1996.
3. Christopher, M.W., M. Alireza, and G. Reza, *Investigation of gray-scale technology for large area 3D silicon MEMS structures*. Journal of Micromechanics and Microengineering, 2003. **13**(2): p. 170.
4. Bühler, J., F.P. Steiner, and H. Baltes, *Silicon dioxide sacrificial layer etching in surface micromachining*. Journal of Micromechanics and Microengineering, 1997. **7**(1): p. R1.
5. Bustillo, J.M., R.T. Howe, and R.S. Muller, *Surface micromachining for microelectromechanical systems*. Proceedings of the IEEE, 1998. **86**(8): p. 1552-1574.
6. Luoto, H., et al., *MEMS on cavity-SOI wafers*. Solid-State Electronics, 2007. **51**(2): p. 328-332.
7. Steve, R. and P. Robert, *A review of focused ion beam applications in microsystem technology*. Journal of Micromechanics and Microengineering, 2001. **11**(4): p. 287.
8. Langford, R.M., et al., *Focused ion beam micromachining of three-dimensional structures and three-dimensional reconstruction to assess their shape*. Journal of Micromechanics and Microengineering, 2002. **12**(2): p. 111.
9. Chekurov, N., et al., *Dry fabrication of microdevices by the combination of focused ion beam and cryogenic deep reactive ion etching*. Journal of Micromechanics and Microengineering, 2010. **20**(8): p. 085009.
10. Henry, M.D., et al., *Ga + beam lithography for nanoscale silicon reactive ion etching*. Nanotechnology, 2010. **21**(24): p. 245303.
11. Päivi, S., C. Nikolai, and T. Ilkka, *The fabrication of silicon nanostructures by focused-ion-beam implantation and TMAH wet etching*. Nanotechnology, 2010. **21**(14): p. 145301.
12. Ayon, A.A., et al., *Characterization of a Time Multiplexed Inductively Coupled Plasma Etcher*. Journal of The Electrochemical Society, 1999. **146**(1): p. 339-349.
13. Christophersen, M. and B.F. Philips, *Gray-tone lithography using an optical diffuser and a contact aligner*. Applied Physics Letters, 2008. **92**(19): p. 194102-3.
14. Azimi, S., et al., *Three-dimensional etching of silicon substrates using a modified deep reactive ion etching technique*. Journal of Micromechanics and Microengineering, 2011. **21**(7): p. 074005.
15. Arne, S. and S. Helmut, *Fabrication of 3D nanoimprint stamps with continuous reliefs using dose-modulated electron beam lithography and*

- thermal reflow*. Journal of Micromechanics and Microengineering, 2010. **20**(9): p. 095002.
16. Waits, C.M., et al., *Microfabrication of 3D silicon MEMS structures using gray-scale lithography and deep reactive ion etching*. Sensors and Actuators A: Physical, 2005. **119**(1): p. 245-253.
 17. Gantz, K. and et al., *Development of a comprehensive model for RIE-lag-based three-dimensional microchannel fabrication*. Journal of Micromechanics and Microengineering, 2008. **18**(2): p. 025003.
 18. Rao, M.P., M.F. Aimi, and N.C. MacDonald, *Single-mask, three-dimensional microfabrication of high-aspect-ratio structures in bulk silicon using reactive ion etching lag and sacrificial oxidation*. Vol. 85. 2004: AIP. 6281-6283.
 19. Yongjin, W., et al., *Design and fabrication of freestanding pitch-variable blazed gratings on a silicon-on-insulator wafer*. Journal of Micromechanics and Microengineering, 2009. **19**(2): p. 025019.
 20. Jeon, J., H.C. Floresca, and M.J. Kim, *Fabrication of complex three-dimensional nanostructures using focused ion beam and nanomanipulation*. Vol. 28. 2010: AVS. 549-553.
 21. Hohyun, K., et al., *Silicon micro-masonry using elastomeric stamps for three-dimensional microfabrication*. Journal of Micromechanics and Microengineering, 2012. **22**(5): p. 055018.
 22. Watt, F., et al., *Proton beam writing*. Materials Today, 2007. **10**(6): p. 20-29.
 23. Ziegler, J.F., *SRIM-2003*. Nuclear Instruments and Methods in Physics Research Section B: Beam Interactions with Materials and Atoms, 2004. **219-220**: p. 1027-1036.
 24. Drouin, D., P. Hovington, and R. Gauvin, *CASINO: A new monte carlo code in C language for electron beam interactions—part II: Tabulated values of the mott cross section*. Scanning, 1997. **19**(1): p. 20-28.
 25. Tseng, A.A., et al., *Electron beam lithography in nanoscale fabrication: recent development*. Electronics Packaging Manufacturing, IEEE Transactions on, 2003. **26**(2): p. 141-149.
 26. Mackenzie, R.A.D. and G.D.W. Smith, *Focused ion beam technology: a bibliography*. Nanotechnology, 1990. **1**(2): p. 163.
 27. Breese, M.B.H., G.W. Grime, and F. Watt, *The Nuclear Microprobe*. Annual Review of Nuclear and Particle Science, 1992. **42**(1): p. 1-38.
 28. Mark B. H. Breese, David N. Jamieson, and P.J.C. King, *Materials analysis using a nuclear microprobe*. 1996, New York: Wiley.
 29. Breese, M.B.H., et al., *Hole transport through proton-irradiated p -type silicon wafers during electrochemical anodization*. Physical Review B, 2006. **73**(3): p. 035428.
 30. Ziegler, J.F., M.D. Ziegler, and J.P. Biersack, *SRIM – The stopping and range of ions in matter (2010)*. Nuclear Instruments and Methods in Physics Research Section B: Beam Interactions with Materials and Atoms, 2010. **268**(11–12): p. 1818-1823.

31. Watt, F. and G.W. Grime, *Principles and Applications of High-energy Ion Microbeams* 1987: Adam Hilger, Bristol.
32. Breese, M.B.H. and D.N. Jamieson, *The use of a magnetic quadrupole triplet as a high resolution ion energy spectrometer*. Nuclear Instruments and Methods in Physics Research Section B: Beam Interactions with Materials and Atoms, 1999. **155**(1–2): p. 153-159.
33. Breese, M.B.H., *Monte Carlo simulations of a magnetic quadrupole triplet as a high resolution energy spectrometer*. Nuclear Instruments and Methods in Physics Research Section B: Beam Interactions with Materials and Atoms, 2000. **171**(4): p. 565-572.
34. Grime, G.W. and F. Watt, *Focusing protons and light ions to micron and submicron dimensions*. Nuclear Instruments and Methods in Physics Research Section B: Beam Interactions with Materials and Atoms, 1988. **30**(3): p. 227-234.
35. Svensson, B.G., et al., *Point defects in MeV ion-implanted silicon studied by deep level transient spectroscopy*. Nuclear Instruments and Methods in Physics Research Section B: Beam Interactions with Materials and Atoms, 1995. **106**(1-4): p. 183-190.
36. Anders Hallén, et al., *Lifetime in proton irradiated silicon*. J. Appl. Phys., 1996. **79**(8): p. 3906.
37. Svensson, B.G., et al., *Divacancy acceptor levels in ion-irradiated silicon*. Physical Review B, 1991. **43**(3): p. 2292-2298.
38. Bettiol, A.A., et al., *A LabVIEW™-based scanning and control system for proton beam micromachining*. Nuclear Instruments and Methods in Physics Research Section B: Beam Interactions with Materials and Atoms, 2001. **181**(1–4): p. 49-53.
39. Bettiol, A.A., et al., *Ionscan: scanning and control software for proton beam writing*. Nuclear Instruments and Methods in Physics Research Section B: Beam Interactions with Materials and Atoms, 2005. **231**(1–4): p. 400-406.
40. Mangaiyarkarasi, D., et al., *Fabrication of large-area patterned porous silicon distributed Bragg reflectors*. Opt. Express, 2008. **16**(17): p. 12757-12763.
41. Watanabe, Y., et al., *Formation and Properties of Porous Silicon and Its Application*. Journal of The Electrochemical Society, 1975. **122**(10): p. 1351-1355.
42. Imai, K. and S. Nakajima. *Full isolation technology by porous oxidized silicon and its application to LSIs*. in *Electron Devices Meeting, 1981 International*. 1981.
43. Imai, K., *A new dielectric isolation method using porous silicon*. Solid-State Electronics, 1981. **24**(2): p. 159-164.
44. Lehmann, V., *Electrochemistry of Silicon: Instrumentation, Science, Materials and Applications*. 2002, Weinheim, Germany: Wiley-VCH.
45. Bisi, O., S. Ossicini, and L. Pavesi, *Porous silicon: a quantum sponge structure for silicon based optoelectronics*. Surface Science Reports, 2000. **38**(1–3): p. 1-126.

46. Lehmann, V. and U. Gosele, *Porous silicon formation: A quantum wire effect*. Applied Physics Letters, 1991. **58**(8): p. 856-858.
47. Ressine, A., et al., *Macro-/Nanoporous Silicon as a Support for High-Performance Protein Microarrays*. Analytical Chemistry, 2003. **75**(24): p. 6968-6974.
48. Hull, R., *Properties of Crystalline Silicon*. 1999, London, UK: Institution of Engineering and Technology.
49. Sailor, M.J., *Porous Silicon in Practice: Preparation, Characterization and Applications* 2011, Weinheim: Wiley-VCH.
50. Hallen, A., et al., *Lifetime in proton irradiated silicon*. Journal of Applied Physics, 1996. **79**(8): p. 3906-3914.
51. Polesello, P., et al., *Micromachining of silicon with a proton microbeam*. Nuclear Instruments and Methods in Physics Research Section B: Beam Interactions with Materials and Atoms, 1999. **158**(1-4): p. 173-178.
52. Rajta, I., et al., *Si micro-turbine by proton beam writing and porous silicon micromachining*. Nuclear Instruments and Methods in Physics Research Section B: Beam Interactions with Materials and Atoms, 2009. **267**(12-13): p. 2292-2295.
53. Azimi, S., Y.S. Ow, and M.B.H. Breese, *On the Dependence of the Surface Roughness of Electrochemically Anodized Silicon on Ion Irradiation Fluence*. Electrochemical and Solid-State Letters, 2010. **13**(11): p. H382-H384.
54. Menzel, F., et al., *Fabrication of microstructures in III-V semiconductors by proton beam writing*. Nuclear Instruments and Methods in Physics Research Section B: Beam Interactions with Materials and Atoms, 2009. **267**(12-13): p. 2321-2326.
55. Schulte-Borchers, M., et al., *3D microstructuring in p-GaAs with proton beam writing using multiple ion fluences*. Journal of Micromechanics and Microengineering, 2012. **22**(2): p. 025011.
56. Azimi, S., et al., *Three-dimensional silicon micromachining*. Journal of Micromechanics and Microengineering, 2012. **22**(11): p. 113001.
57. Berger, M.G., et al., *Dielectric filters made of PS: advanced performance by oxidation and new layer structures*. Thin Solid Films, 1997. **297**(1-2): p. 237-240.
58. Pavese, L., *Porous silicon dielectric multilayers and microcavities*. La Rivista del Nuovo Cimento (1978-1999), 1997. **20**(10): p. 1-76.
59. Vincent, G., *Optical properties of porous silicon superlattices*. Applied Physics Letters, 1994. **64**(18): p. 2367-2369.
60. Mangaiyarkarasi, D., et al., *Controlled blueshift of the resonant wavelength in porous silicon microcavities using ion irradiation*. Applied Physics Letters, 2006. **89**(2): p. 021910-3.
61. Mangaiyarkarasi, D., M.B.H. Breese, and Y.S. Ow, *Fabrication of three dimensional porous silicon distributed Bragg reflectors*. Applied Physics Letters, 2008. **93**(22): p. 221905-3.

62. Wilson, W.L., et al., *High density, high performance optical data storage via volume holography: Viability at last?* Optical and Quantum Electronics, 2000. **32**(3): p. 393-404.
63. Per, G., *Four-pulse interferometric recordings of transient events by pulsed TV holography.* Optics and Lasers in Engineering, 2003. **40**(5–6): p. 517-528.
64. Saari, P., R. Kaarli, and M. Rätsep, *Temporally multiplexed Fourier holography and pattern recognition of femtosecond-duration images.* Journal of Luminescence, 1993. **56**(1–6): p. 175-180.
65. Nishchal, N.K., J. Joseph, and K. Singh, *Fully phase encryption using digital holography.* Optical Engineering, 2004. **43**(12): p. 2959-2966.
66. Son, J.Y., B. Javidi, and K.D. Kwack, *Methods for Displaying Three-Dimensional Images.* Proceedings of the IEEE, 2006. **94**(3): p. 502-523.
67. Ow, Y.S., et al., *Micromachining of amplitude and phase modulated reflective computer generated hologram patterns in silicon.* Nuclear Instruments and Methods in Physics Research Section B: Beam Interactions with Materials and Atoms, 2010. **268**(9): p. 1416-1421.
68. Merenda, F., et al., *Three-dimensional force measurements in optical tweezers formed with high-NA micromirrors.* Opt. Lett., 2009. **34**(7): p. 1063-1065.
69. Merenda, F., et al., *Miniaturized high-NA focusing-mirror multiple optical tweezers.* Opt. Express, 2007. **15**(10): p. 6075-6086.
70. Lin, C.-H., S.-Y. Wen, and W. Hsu, *Variable Optical Attenuator with Tunable Nonsmooth Curved Mirror.* The Japan Society of Applied Physics, 2004. **43**: p. 7764–7768.
71. Aoki, Y., Y. Shimada, and K. Iga. *Collimation characteristics of stacked planar microlens for parallel optical interconnects.* in *Lasers and Electro-Optics Europe, 2000. Conference Digest. 2000 Conference on.* 2000.
72. Ow, Y.S., M.B.H. Breese, and S. Azimi, *Fabrication of concave silicon micro-mirrors.* Optics Express, 2010. **18**(14): p. 14511-14518.
73. Yang, P.Y., et al., *Freestanding waveguides in silicon.* Applied Physics Letters, 2007. **90**(24): p. 241109-3.
74. Teo, E.J., et al., *Fabrication of low-loss silicon-on-oxidized-porous-silicon strip waveguide using focused proton-beam irradiation.* Opt. Lett., 2009. **34**(5): p. 659-661.
75. Teo, E.J., et al., *Effects of oxide formation around core circumference of silicon-on-oxidized-porous-silicon strip waveguides.* Opt. Lett., 2009. **34**(20): p. 3142-3144.
76. Teo, E.J., et al., *An all-silicon, single-mode Bragg cladding rib waveguide.* Opt. Express, 2010. **18**(9): p. 8816-8823.
77. Mazzoleni, C. and L. Pavesi, *Application to optical components of dielectric porous silicon multilayers.* Applied Physics Letters, 1995. **67**(20): p. 2983-2985.
78. Astrova, E. and A. Nechitaïlov, *Boundary effect in electrochemical etching of silicon.* Semiconductors, 2008. **42**(4): p. 470-474.

79. Rajta, I., et al., *Si micro-turbine by proton beam writing and porous silicon micromachining*. Nuclear Instruments and Methods in Physics Research Section B: Beam Interactions with Materials and Atoms, 2009. **267**(12-13): p. 2292-2295.
80. Sugano, K. and O. Tabata, *Reduction of surface roughness and aperture size effect for etching of Si with XeF₂*. Journal of Micromechanics and Microengineering, 2002. **12**(6): p. 911.
81. Lai, L. and E.A. Irene, *Limiting Si/SiO₂ interface roughness resulting from thermal oxidation*. Journal of Applied Physics, 1999. **86**(3): p. 1729-1735.
82. Lee, K.K., et al., *Fabrication of ultralow-loss Si/SiO₂ waveguides by roughness reduction*. Opt. Lett., 2001. **26**(23): p. 1888-1890.
83. Busnaina, A.A., I.I. Kashkoush, and G.W. Gale, *An Experimental Study of Megasonic Cleaning of Silicon Wafers*. Journal of The Electrochemical Society, 1995. **142**(8): p. 2812-2817.
84. Azimi, S., et al., *Fabrication of complex curved three-dimensional silicon microstructures using ion irradiation*. Journal of Micromechanics and Microengineering, 2012. **22**(1): p. 015015.
85. Lerondel, G., R. Romestain, and S. Barret, *Roughness of the porous silicon dissolution interface*. Journal of Applied Physics, 1997. **81**(9): p. 6171-6178.
86. Visser, J., et al., *Considerations on accelerator systems requirements and limitations for μ -probe applications*. Nuclear Instruments and Methods in Physics Research Section B: Beam Interactions with Materials and Atoms, 2005. **231**(1-4): p. 32-36.
87. Teo, E.J., et al., *High quality ion-induced secondary electron imaging for MeV nuclear microprobe applications*. Journal of Vacuum Science & Technology B: Microelectronics and Nanometer Structures, 2004. **22**(2): p. 560-564.
88. Grime, G.W., et al., *The Oxford submicron nuclear microscopy facility*. Nuclear Instruments and Methods in Physics Research Section B: Beam Interactions with Materials and Atoms, 1991. **54**(1-3): p. 52-63.
89. Teo, E.J., et al., *Multicolor Photoluminescence from Porous Silicon Using Focused, High-Energy Helium Ions*. Advanced Materials, 2006. **18**(1): p. 51-55.
90. Svensson, B.G., et al., *Point defects in MeV ion-implanted silicon studied by deep level transient spectroscopy*. Nuclear Instruments and Methods in Physics Research Section B: Beam Interactions with Materials and Atoms, 1995. **106**(1-4): p. 183-190.
91. Irscher, K., H. Klose, and K. Maass, *Hydrogen-related deep levels in proton-bombarded silicon*. Journal of Physics C: Solid State Physics, 1984. **17**(35): p. 6317.
92. Yamaguchi, M., et al., *High-energy and high-fluence proton irradiation effects in silicon solar cells*. Journal of Applied Physics, 1996. **80**(9): p. 4916-4920.

93. Myers, S.M., G.A. Petersen, and C.H. Seager, *Binding of cobalt and iron to cavities in silicon*. Journal of Applied Physics, 1996. **80**(7): p. 3717-3726.
94. Peeva, A., et al., *Spatial distribution of cavities in silicon formed by ion implantation generated excess vacancies*. Journal of Applied Physics, 2004. **95**(9): p. 4738-4741.
95. Kogler, R., et al., *Alternating layers of vacancy-type and interstitial-type defects in Ge ion implanted silicon*. Applied Physics Letters, 2006. **88**(10): p. 101918-3.
96. COMSOL Multiphysics® ver. 3.5a, <http://www.comsol.com>.
97. Petris, M. *Radiation induced change of the effective doping concentration in silicon detectors*. in *Semiconductor Conference, 1999. CAS '99 Proceedings. 1999 International*. 1999.
98. Goltsman, A. and A.I. Zaghloul. *A three-dimensional antenna array for terahertz sensing*. in *Sensors, 2009 IEEE*. 2009.
99. Baehr-Jones, T., et al., *Design of a tunable, room temperature, continuous-wave terahertz source and detector using silicon waveguides*. J. Opt. Soc. Am. B, 2008. **25**(2): p. 261-268.
100. Nenzi, P., et al. *Three-dimensional micro-antenna array for millimetre and sub-millimetre-wave remote imaging*. in *Antennas and Propagation (EUCAP), Proceedings of the 5th European Conference on*. 2011.
101. Azimi, S., et al., *Defect enhanced funneling of diffusion current in silicon*. Applied Physics Letters, 2013. **102**(4): p. 042102-5.
102. Reed, G.T. and A.P. Knights, *Silicon Photonics: An Introduction* Wiley, 2004.
103. Liu, A., et al., *A high-speed silicon optical modulator based on a metal-oxide-semiconductor capacitor*. Nature, 2004. **427**(6975): p. 615-618.
104. Rong, H., et al., *A continuous-wave Raman silicon laser*. Nature, 2005. **433**(7027): p. 725-728.
105. Almeida, V.R., et al., *All-optical control of light on a silicon chip*. Nature, 2004. **431**(7012): p. 1081-1084.
106. Cleland, A.N. and M.L. Roukes, *Fabrication of high frequency nanometer scale mechanical resonators from bulk Si crystals*. Vol. 69. 1996: AIP. 2653-2655.
107. Fritz, J., et al., *Translating Biomolecular Recognition into Nanomechanics*. Science, 2000. **288**(5464): p. 316-318.
108. Craighead, H.G., *Nanoelectromechanical Systems*. Science, 2000. **290**(5496): p. 1532-1535.
109. Lin, S.Y., et al., *A three-dimensional photonic crystal operating at infrared wavelengths*. Nature, 1998. **394**(6690): p. 251-253.
110. Reed, G.T., *Silicon Photonics: The State of the Art*. 2008: Wiley.
111. Bettiol, A.A., et al., *A progress review of proton beam writing applications in microphotronics*. Nuclear Instruments and Methods in Physics Research

- Section B: Beam Interactions with Materials and Atoms, 2005. **231**(1–4): p. 364-371.
112. Yan, Y., et al., *Selective electroless silver plating of three dimensional SU-8 microstructures on silicon for metamaterials applications*. Opt. Mater. Express, 2011. **1**(8): p. 1548-1554.
 113. Ow, Y.S., et al., *Modification of Porous Silicon Formation by Varying the End of Range of Ion Irradiation*. Electrochemical and Solid-State Letters, 2011. **14**(5): p. D45-D47.
 114. Ow, Y.S., et al., *Effects of focused MeV ion beam irradiation on the roughness of electrochemically micromachined silicon surfaces*. Journal of Vacuum Science & Technology B: Microelectronics and Nanometer Structures, 2010. **28**(3): p. 500-505.
 115. Mangaiyarkarasi, D., *Fabrication of three dimensional porous silicon distributed Bragg reflectors*. Appl. Phys. Lett., 2008. **93**(22): p. 221905.
 116. Ziegler, J.F., *SRIM-2003*. Nuclear Instruments & Methods in Physics Research Section B-Beam Interactions with Materials and Atoms, 2004. **219**: p. 1027-1036.
 117. Zhao, Y., et al., *Sub-10 nm silicon ridge nanofabrication by advanced edge lithography for NIL applications*. Microelectronic Engineering. **86**(4-6): p. 832-835.
 118. Grabiec, P.B., et al., *Nano-width lines using lateral pattern definition technique for nanoimprint template fabrication*. Microelectronic Engineering, 2004. **73-74**: p. 599-603.
 119. Fekete, V., et al., *Detection enhancement in nano-channels using micro-machined silicon groove*. Journal of Chromatography A, 2006. **1130**(1): p. 151-157.
 120. Ou, H., et al., *The fabrication of thick SiO₂ layer by anodization*. Optical Materials, 2000. **14**(3): p. 271-275.
 121. Hedrich, F., S. Billat, and W. Lang, *Structuring of membrane sensors using sacrificial porous silicon*. Sensors and Actuators A: Physical, 2000. **84**(3): p. 315-323.
 122. Huang, M., et al., *Reusable Nanostencils for Creating Multiple Biofunctional Molecular Nanopatterns on Polymer Substrate*. Nano Letters, 2012. **12**(9): p. 4817-4822.
 123. Villanueva, L.G., et al., *All-stencil transistor fabrication on 3D silicon substrates*. Journal of Micromechanics and Microengineering, 2012. **22**(9): p. 095022.
 124. Wagner, S., et al., *Silicon for thin-film transistors*. Thin Solid Films, 2003. **430**(1–2): p. 15-19.
 125. Beaucarne, G., *Silicon Thin-Film Solar Cells*. Advances in OptoElectronics, 2007. **2007**.
 126. Celler, G.K. and S. Cristoloveanu, *Frontiers of silicon-on-insulator*. Journal of Applied Physics, 2003. **93**(9): p. 4955-4978.
 127. Vlasov, Y. and S. McNab, *Losses in single-mode silicon-on-insulator strip waveguides and bends*. Opt. Express, 2004. **12**(8): p. 1622-1631.

128. Cardenas, J., et al., *Low loss etchless silicon photonic waveguides*. Opt. Express, 2009. **17**(6): p. 4752-4757.
129. Sparacin, D.K., S.J. Spector, and L.C. Kimerling, *Silicon waveguide sidewall smoothing by wet chemical oxidation*. Lightwave Technology, Journal of, 2005. **23**(8): p. 2455-2461.
130. Lee, K.K., et al., *Effect of size and roughness on light transmission in a Si/SiO₂ waveguide: Experiments and model*. Applied Physics Letters, 2000. **77**(11): p. 1617-1619.
131. Ogura, A. *Partial SOI/SON formation by He⁺ implantation and annealing*. in *SOI Conference, IEEE International 2002*. 2002.
132. Cohena, G.M., P.M. Mooneya, and J.O. Chua, *Free Standing Silicon as a Compliant Substrate for SiGe*. MRS Proceedings, 2003. **767**: p. D4.6/G1.6 doi:10.1557/PROC-765-D4.6/G1.6
133. Teo, E.J., et al., *Controlled intensity emission from patterned porous silicon using focused proton beam irradiation*. Applied Physics Letters, 2004. **85**(19): p. 4370-4372.
134. El-Bahar, A. and Y. Nemirovsky, *A technique to form a porous silicon layer with no backside contact by alternating current electrochemical process*. Applied Physics Letters, 2000. **77**(2): p. 208-210.
135. Astrova, E. and A. Nechitaïlov, *Electrochemical etching of macropores in silicon with grooved etch seeds*. Semiconductors, 2008. **42**(6): p. 746-751.
136. Breese, M.B.H., D.N. Jamieson, and P.J.C. King, *Materials Analysis using a Nuclear Microprobe*. Wiley, 1996.
137. Service, R.F., *IBM Puts Fast Chips on a New Footing*. Science, 1998. **281**(5379): p. 893-894.
138. Bertrand, I., et al., *Large area recrystallization of thick polysilicon films for low cost partial SOI power devices*. Microelectronics Journal, 2006. **37**(3): p. 257-261.
139. Lasky, J.B., *Wafer bonding for silicon-on-insulator technologies*. Applied Physics Letters, 1986. **48**(1): p. 78-80.
140. Bruel, M., *U.S. Patent No. 5374564* 20 December 1994.
141. Yonehara, T., K. Sakaguchi, and N. Sato, *Silicon-on-Insulator Technology and Devices IX*, edited by P. L. F. Hemment. 1999, Pennington, NJ: The Electrochemical Society.
142. Bruel, M., *Silicon on insulator material technology*. Electronics Letters, 1995. **31**(14): p. 1201-1202.
143. Thurber, W.R., et al., *Resistivity-Dopant Density Relationship for Boron-Doped Silicon*. Journal of The Electrochemical Society, 1980. **127**(10): p. 2291-2294.